FCT Fundação para a Ciência e a Tecnologia

MINISTÉRIO DA CIÊNCIA, TECNOLOGIA E ENSINO SUPERIOR

PROJECTOS DE INVESTIGAÇÃO CIENTÍFICA E DESENVOLVIMENTO TECNOLÓGICO

RELATÓRIO FINAL

Relatório de Execução Material

REFERÊNCIA DO PROJECTO Nº POCTI/MGS/45533/2002

POCTI
Programa Operacional
Ciência Tecnologia Inovação

União Europeia – Fundos Estruturais

Governo da República Portuguesa

Data de Entrada_____ Data de Verificação_____
Nº de Registo _____ Assinatura _____

Espaço reservado à Fundação para a Ciência e a Tecnologia

Referência do projecto: POCTI/MGS/45533/2002

Título do projecto: ECODOURO - Modelling the effect of freshwater reduction and pulse discharge on the water dynamics and processes of the Crestuma Reservoir

Data de Início do Projecto: __15__/_____MAR_____/_____2003__

Duração: ____36__ Meses Prorrogado até: __15__/____SEP_____/_____2006_

Data de Conclusão do Projecto: __20__/_____DEC_____/_____2006

Identificação da instituição proponente

Nome ou designação social: Centro de Investigação Marinha e Ambiental - CIIMAR

Morada Rua do Campo Alegre, 823

Localidade Porto Código postal 4150-180 Porto

Telefone 22 608 04 70 / 71 Fax 22 608 04 79 Email cimar@cimar.org

Unidade responsável pela execução do projecto

Nome Laboratório de Hidrobiologia - ICBAS

Morada Largo Abel Salazar, 2

Localidade Porto Código postal 4099-003 Porto

Telefone 22206285 Fax 222062284 Email

Identificação do investigador responsável

Nome Adriano Agostinho Donas Bôto Bordalo e Sá

Telefone 222062285 Fax 222062284 Email bordalo@icbas.up.pt

Centro de Investigação Marinha e Ambiental
Universidade do Porto
Laboratório de Hidrobiologia

ECODOURO - Modelling the effect of freshwater reduction and pulse discharge on the water dynamics and processes of the Crestuma Reservoir

POCTI/MGS/45533/2002

Final Report

Prepared by: Adriano A. Bordalo e Sá (PI), Pedro Duarte and William Wiebe

Porto,March 2007

1. Executive summary

This report deals with the activities carried out during the project 72 months, from March 15, 2003 to September 15, 2006 under the framework of the ECODOURO - Modelling the effect of freshwater reduction and pulse discharge on the water dynamics and processes of the Crestuma Reservoir (POCTI/MGS/45533/2002). The report includes the fieldwork, data interpretation and mathematical modeling according to the seven working packages presented in the original proposal. Data is available to the public at http://ecodouro.icbas.up.pt.

The main objectives of this goal oriented research project implemented on the Crestuma Reservoir (Douro River) are: i. To evaluate the long-term effects of flow reduction on key environmental variables and processes that occur in the Crestuma Reservoir; and ii. To evaluate the effect of high frequency oscillations (freshwater pulse discharges) on the ecosystem dynamics in terms of water column stratification, water temperature and turbidity, oxygen, nutrient availability, phytoplankton biomass and primary productivity.

The original requested budget was reduced by 19%, and the evaluation commission recommended the non-acquisition of a second multiprobe CTD. Thus, the entire field survey program was changed accordingly.

The seasonal sampling was conducted at two anchor stations located about 500 m and 2,500 m from the Crestuma dam crest. Surveys were performed on December 2003 (Fall), February 2004 (Winter), May 2004 (Spring) and August 2004 (Summer). An un-scheduled survey was carried out at the onset of the program (May 2003), in order to gather basic data since no departure data (short term series) were available contrarily to what was though. This approach proved to be very useful and the obtained results were applied in the following surveys. Moreover, since no workable bathymetrics were available to the research team (only depth contours in chart format restricted to the navigational channel) several dedicated surveys were organized in order to generate bottom contour maps for the last 10 km of the reservoir, covering the two-field stations location. As a result, a costume-made GIS was created and data used to run the model.

All technical details of both the employed models (2D-vertically resolved model and the coupled biogeochemical model), including the complete mathematical formulae, are

presented in Annexes I and II. The rationale for selection of the modeled parameters are presented; the field data obtained from the 4+1 surveys were used to initialize the models.

It was found that the different flow time-scales might influence water dynamics, biogeochemistry and primary productivity. For example, during the day, longitudinal flows results from upstream forcing, with river water entering into the reservoir. A clear longitudinal flow profile emergeed, disturbed in some points by depth changes that forces upwelling of bottom water. During the night, in the absence of river flow, at it happens frequently in Spring through Fall, convective flow dominated, with surface cooled water sinking to the bottom and forcing the ascent of bottom water. Vertical flows may be larger than horizontal ones. On the other hand, the highest phytoplankton production was observed in May and September, when microalgae were using more efficiently the available light. Furthermore, phytoplankton efficiency decreased from morning to dawn.

Considering the objectives of this project, several model simulations were carried out to analyze the effects of flow variability on water column stratification and quality (cf. – Annexe III). These simulations were carried out with the same average flow magnitude and forcing conditions, in terms of water temperature, nutrients and chlorophyll concentrations, but different flow frequencies and amplitudes. Results obtained suggest that flow variability may not have a large effect on water temperature, nutrient and chlorophyll concentration and net primary production at annual time scales. However, when the time scale under analysis is reduced to seasonal and monthly, effects of flow variability become apparent, especially during the summer period and when flow is hold constant. Constant flow implies that extreme low and high values do not occur. Under this situation of “extreme” flow regulation, it appears that the synergies between river forcing and reservoir processes tend to reduce phytoplankton biomass. Therefore, from a management point of view, it is apparent that stabilizing the flow may prevent the development of phytoplankton blooms.

On the other hand, results presented and discussed in Annex IV suggest that the Crestuma reservoir has undergone some important changes over the period 1999-2005, with significant increases in nitrogen and phosphorus and a decrease in the nitrogen: phosphorus ratio i.e. the Redfield ratio. One possible change, arising from the shifts in the nitrogen: phosphorus ratio, is the apparent autumn shift towards nitrate-nitrogen limitation of phytoplankton. Apart from increasing nutrient runoff within the watershed, the

noticeable nutrient increase trend found in the Crestuma resevoir may also be explained by the reduction of chlorophyll as a result of the massive development of the invasive clam Corbicula sp. Thus, the Crestuma reservoir is now a predominantly heterotrophic ecosystem that is the source of water to 20% of the Portuguese population and feeds the Douro estuary with most of the water that reaches the Atlantic Ocean.

As a result of this project, a full functional calibrated with dedicated data model is available. During the 72 mo of the project, three young researchers were able to work and get training in the different areas covered by the program. Due to the enormous amount of data gathered, only two research papers were published. Thus, in the near future, two papers will be submitted (as a result of Annex III and Annex IV), and two additional papers are under preparation. Part of the obtained data has being used for teaching purposes at undergraduate and Master/PhD levels by the PI and the Cemas team.

2. Introduction

The Douro River flows within the largest watershed in the Iberian Peninsula, draining 98,000 km2 or 17% of this territory. The Douro is an international watershed, shared between Spain (80%) and Portugal (20%). Within the watershed, 51 large dams regulate the flow, allowing, presently, about 15 km^3 of freshwater per year to be discharged into the Atlantic Ocean at 41º08'N; 08º41'W, an equivalent to 455 m^3s^{-1}. However, because the flow regime depends not only on climatic conditions but also is controlled for hydro-electric power generation needs in both countries, as well as by irrigation needs in Spain, the daily discharge rate into the ocean ranges between zero and >13,000 m^3s^{-1} (Vieira and Bordalo 2000). The first dam on the watershed was built in 1920, but most large dams (>15m wall height) started operating in the late 1950s. The concentration of dams is particularly heavy in the last 350 km of the river main course, with a hydroelectric power dam about every 30 km. Altogether, the large dams retain up to 1100 hm^3 (13%) of water in Portuguese reservoirs and 7500 hm^3 (87%) on the Spanish side of the watershed. The scientific evaluation of the water quality, and its temporal trends, is an important task for risk assessment. This is particularly critical when dealing with an international river, i.e., a shared watershed, because the management goals of the different countries may not coincide.

The main objectives of this goal oriented research project implemented on the Crestuma Reservoir (Douro River) are:

i. To evaluate the long term effects of flow reduction on key environmental variables and processes that occur in the Crestuma Reservoir;
ii. To evaluate the effect of high frequency oscillations (freshwater pulse discharges) on the ecosystem dynamics in terms of water column stratification, water temperature and turbidity, oxygen, nutrient availability, phytoplankton biomass and primary productivity.

In order to achieve the above stated objectives, a 2-D vertically resolved coupled physical-biogeochemical model, based on an object-oriented ecological approach, was implemented.

The present final progress report deals with the activities carried out during the project 72 months, from March 15, 2003 to September 15, 2006.

3. Selection of BIC researchers

In April 2003 two vacancies for BIC fellowships associated to ECODOURO were advertised. By April 10, 19 candidacies were received and on May 7, interviews of 18 candidates were conducted. Two candidates were selected: for BIC1 – Rita Teixeira and for BIC2 - Claudia Martins.

The BIC1 is based at Laboratório de Hidrobiologia ICBAS/CIIMAR (Prime Contractor) and BIC2 at CEMAS (second project partner). BIC1 started working on May 15, 2003 and BIC2 on July 25, 2003. BIC1 was initially awarded for 18 mo but, with permission from FCT, was extended until the end of the project (36 mo).

By December 2004 BIC2 left the research team. Thus, in February 2005, a BIC fellowship associated with ECODOURO was advertised, to replace the BIC2 grant given previously to CEMAS (second project partner). By March 31, 57 proposals were received, 17 were selected for interview. Of these, only 12 candidates showed-up and were interviewed. One candidate was selected - Cátia Rabaça. The selected candidate started working in May 2005. By October 2005 BIC2 also left the research team.

4. Funding

From the original budget of 125 266€ requested to FCT, only 105 266€ were made available, according to the evaluation panel. Thus, a 20 000€ stake (initially allocated for the purchase of a multiprobe CTD) was not considered. The budget was reformulated and sent to FCT on March 15, 2003. However, the first installment was made available to the Prime Contractor only on September 1, 2003, followed by two additional installments (Table 1.1).

Table 1.1. Listing of installments from FCT and from Ciimar to Cemas.

Listagem de adiantamentos

Total: 5

Data	De	Para	Valor	%
2006-12-04	Ent. Financiadora	CIIMAR	€ 21.053,20	20.00%
2004-09-03	CIIMAR	CEMAS	€ 11.431,88	26.24%
2004-09-02	Ent. Financiadora	CIIMAR	€ 31.579,80	30.00%
2003-09-03	CIIMAR	CEMAS	€ 15.579,22	35.76%
2003-09-02	Ent. Financiadora	CIIMAR	€ 42.106,00	40.00%

Totais:
Entidade Financiadora -> CIIMAR : € 94.739,00
Coordenador -> CEMAS : € 27.011,10

5. Work Plan

According to the original proposal submitted on May 25, 2002, ECODOURO is divided into seven Work Packages (WP) as follows:

i. WP1 – Data gathering and organization;
ii. WP2 – Seasonal sampling surveys;
iii. WP3 – Time-series analysis;
iv. WP4 – Implementation of a 2D vertically resolved model;
v. WP5 – Model calibration and validation;
vi. WP6 – Data analysis and reporting;
vii. WP7 – Web page.

Due to the budget reduction, some changes were introduced, namely on WP2. The unavailability of the second multiprobe logger, which purchased was jugged unnecessary by the evaluation panel, resulted in the impossibility to perform water column mass balance of key environmental parameters, namely temperature, conductivity, dissolved oxygen, pH and turbidity according to the original plan.

WP1 – Data gathering and organization

The work planned for 3 mo was completed. The database was organized in Excel, as originally proposed. It consists of historic surface water physical and chemical data from the Portuguese Water Institute - Ministry of Environment (www.inag.pt) for three locations within the Crestuma Reservoir, namely Crestuma (1988 - 2001), Melres (1993 – 2002) and Entre-os-Rios (1993 – 2000). Also, physical and chemical data from the Porto Water Board was obtained, for a single water column station located about 1 km from the dam, covering the period 1989 – 1997. Our own data set, of monthly surveys carried out in 15 stations located in the last 30 km of the reservoir, from June 2000 to May 2001 was made available, as well as monthly (1933 – 2005), daily (1955 – 2005) and hourly (selected dates) of freshwater discharge.

The main drawback of using the above mentioned third party physical and chemical databases is the lack of control over sampling and laboratory treatment the samples, as well as the existence of blanks over the considered period, either of individual parameters for one to several months (e.g. temperature and pH) as well as the discontinuation of selected parameters (phytoplankton, etc), reducing dramatically the scientific usefulness of the data. Nevertheless, and because the Crestuma INAG survey station is a rather long data-set, it was possible to identify trends, at least as yearly averages, in key environmental parameters, such as nutrients.

In order to characterize the quality of the Portuguese side of the watershed, useful for the understanding of the water quality dynamics of the Crestuma Reservoir, data for two additional upstream reservoirs were also obtained from the INAG website (www.inag.pt). After a suitable data treatment, namely through the application of a water quality index, a research paper was published in an international journal (Bordalo et al 2006).

WP2 – Seasonal sampling surveys

This Work Package was reformulated, in order to increase the amount of data to be obtained, following the analysis and interpretation of the above mentioned data basis, specially our own. The 12 h seasonal surveys were transformed into 25 h seasonal surveys and the seasonal weekly surveys performed during 5 days, at only one station,

due to the lack of power/logging autonomy of the existing CTDs since only one new CTD was purchased as mentioned above

Moreover, an unscheduled preliminary seasonal survey was organized in May 2003 in order to gather time-series data in a single sampling station. Two 25 h sub-surveys were carried out on Sunday, May 23 and Wednesday, May 26. This corresponded roughly to periods of artificially reduced flow (Sunday), due to the modest needs in hydroelectric power generation, and to "regular" flow (Wednesday) for that period of the year.

It should be noted that the fieldwork started in May, well before the first installment was received (see #4). Further seasonal surveys were organized between 7 – 10 December 2003 (Fall), 15 – 18 February 2004 (Winter), 23-27 May 2004 (Spring), 31 August – 6 September 2004 (Summer).

May 2003 survey

The anchor station was located 2.5 km upstream the dam crest, at the premises of the Turbogás Tapada do Outeiro Power Plant (CTO) (Figure WP1.2), a private company that kindly gave the necessary permit for the use of the facilities. Three CTDs were installed at surface, 5 m and near bottom. Temperature, conductivity, dissolved oxygen, oxygen saturation, pH and turbidity data were obtained at 5 min intervals. Since only one CDT with a chlorophyll sensor was purchased (the second was considered non-essential by the evaluation team), continuous record of chlorophyll data was possible only at surface. A subsurface current meter gathered water velocity data and flow direction also at 5 min intervals. Every three hours, surface water samples were retrieved for nutrients, phytoplankton biomass (chlorophyll *a*), community respiration and primary productivity. At 15 min intervals, photosynthetic active radiation was recorded, and every 3 h, water column light profiles were obtained. Water transparency was also evaluated from Secchi disk measurements. Samples were processed immediately in a field laboratory installed on location, equipped with all required equipment and materials (Figure WP2.2). Wastes (especially toxic and/or radioactive liquid effluents) were disposed according to good laboratory practice.

Figure WP1.2. Location of the sampling stations in Crestuma reservoir (ETA - downstream; CTO – upstream).

December 2003 - fall survey

Two anchor stations were established. The first, CTO, was described above (Figure WP2.2). The second (ETA), was located at the surface water treatment plant of the public company Águas do Douro e Paiva (ADP) about 500 m from the dam crest. It should also be noted the support of ADP for this project by allowing assess to their premises. At each location, two CTDs and one current meter were deployed, respectively at surface/near bottom, and at subsurface. Since only one CTD with a chlorophyll sensor was purchased as mentioned, continuous record of chlorophyll data was possible only at the CTO station (Figure WP3.2). Additionally, every three hours, surface water samples were retrieved for nutrients, phytoplankton biomass (chlorophyll *a*), community respiration, BOD_5, primary productivity and direct bacterial counts on December 7-8 and December 10-11, for 25 h. Samples were processed immediately in the field laboratory (Figure WP4.2). At 15 min intervals, photosynthetic active radiation was recorded, and every 3 h, water column light profiles were obtained. Water transparency was also evaluated from Secchi disk measurements.

A B

Figure WP2.2. Views of CTO (A) and ETA (B) sampling stations in the Crestuma reservoir.

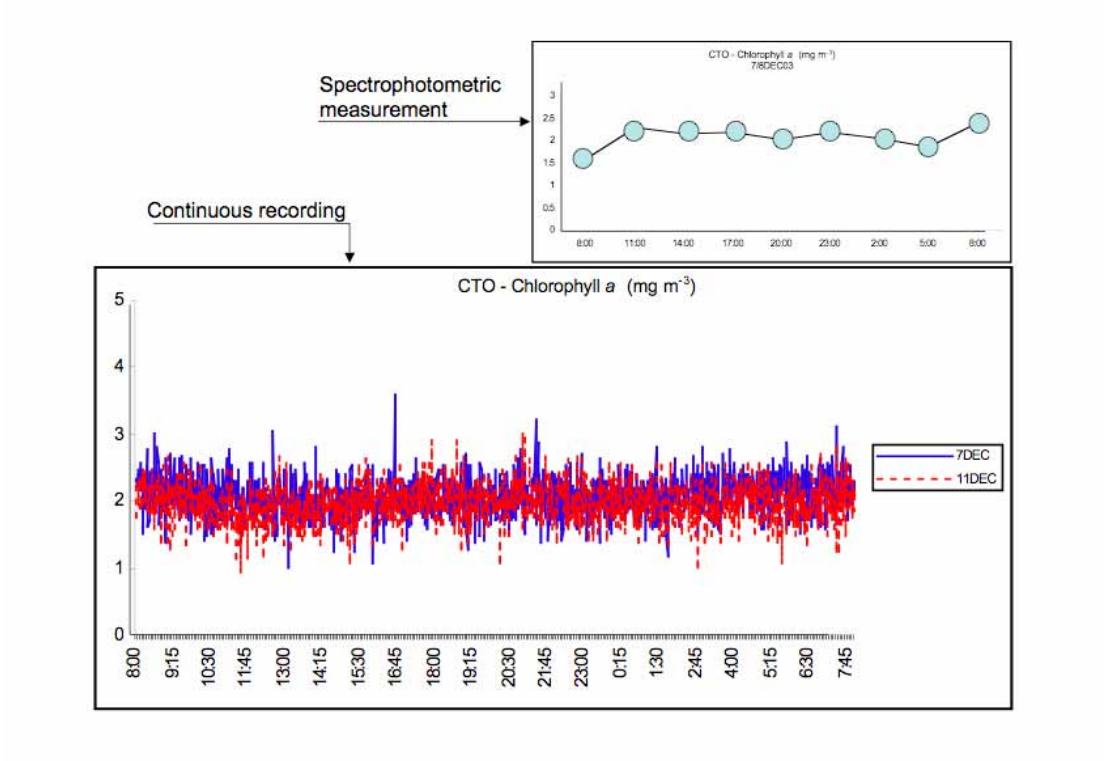

Figure WP3.2. Example of continuous 25-h chlorophyll *a* record (5 min intervals) and every 3-h measurements using the spectrophotometric method at CTO station (Fall survey).

February 2004 – winter survey

The anchor stations were established at the above-mentioned CTO and ETA locations. At each location, two CTDs and one current meter were deployed, respectively at surface/near bottom, and at subsurface. Every three hours, surface water samples were retrieved for nutrients, phytoplankton biomass (chlorophyll *a*), community respiration, BOD_5, primary productivity and direct bacterial counts on February 15-16 and February 18-19, for 25 h. Samples were processed immediately in the field laboratory installed at the CTO station (Figure WP4.2). At 15 min intervals, photosynthetic active radiation was recorded, and every 3 h, water column light profiles were obtained. Water transparency was also evaluated from Secchi disk measurements.

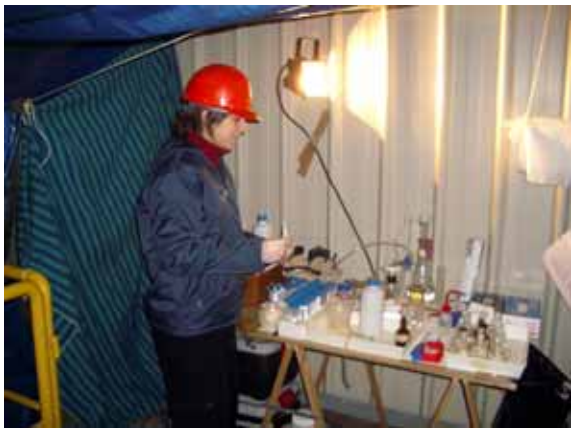

Winter survey

Spring survey

Figure WP4.2. Field laboratory installed at the Turbogás Power Plant by the Crestuma reservoir.

May 2004 - spring survey

According to the original schedule, the spring surveys were performed between 23 - 27 May. The same two anchor stations were established and equipment was deployed at CTO and ETA stations as stated above.

An example of surface and near bottom measurements of dissolved oxygen, pH and temperature at CTO stations is presented in Figure WP5.2.

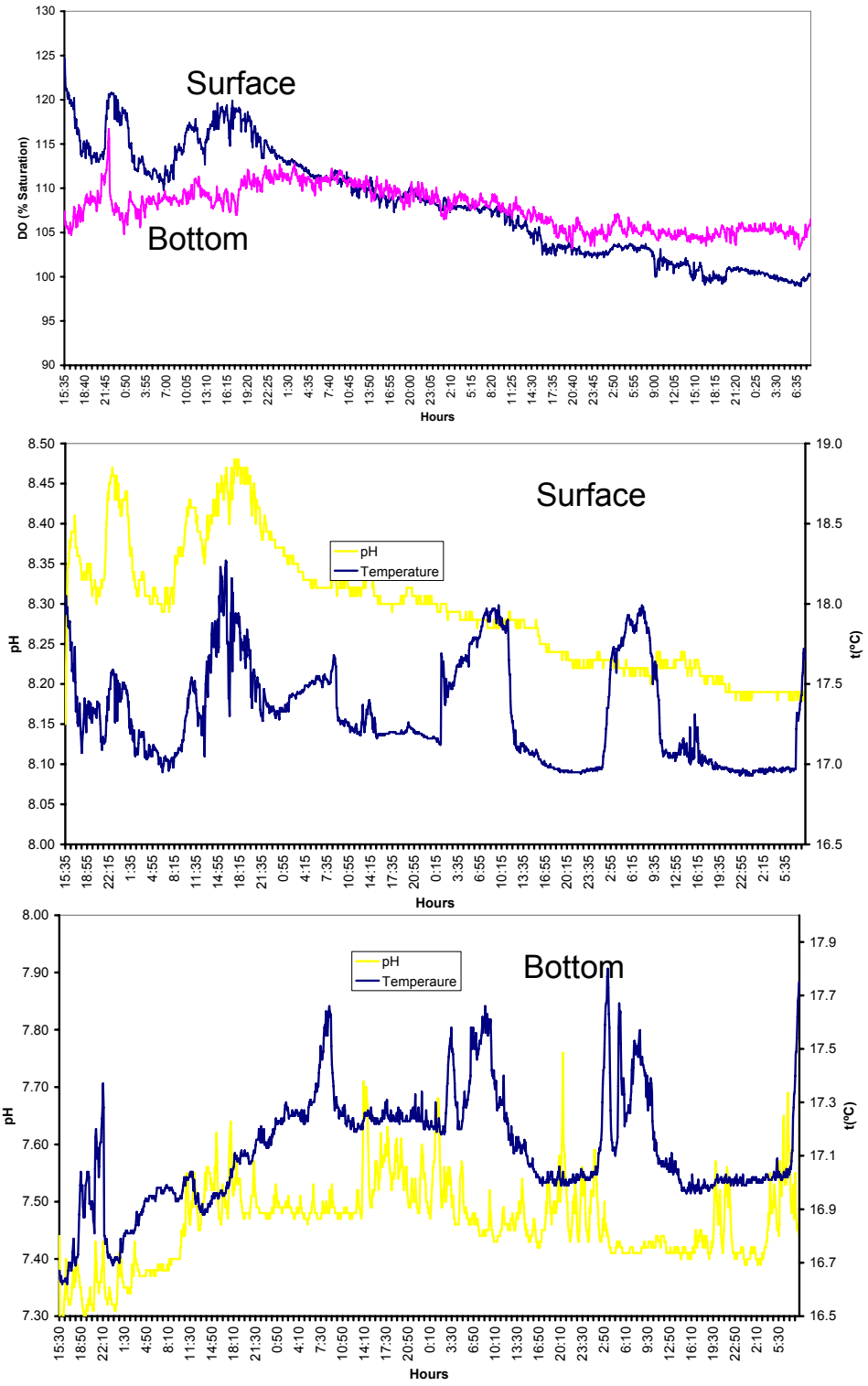

Figure WP5.2. Continuous dissolved oxygen saturation, pH and temperature measurements (5-min intervals) at CTO station during the Spring 2004 survey for 5 days.

August/September 2004 - summer survey

The last scheduled survey was carried out between 31 August and 6 September, again at the same premises as in the previous surveys (CTO and ETA, Figure WP1.2). An example of photosynthetic active radiation measurements at CTO is presented in Figure WP6.2 whereas in Figure WP7.2 the 25-h variation of surface and bottom temperatures (5-min intervals) is presented.

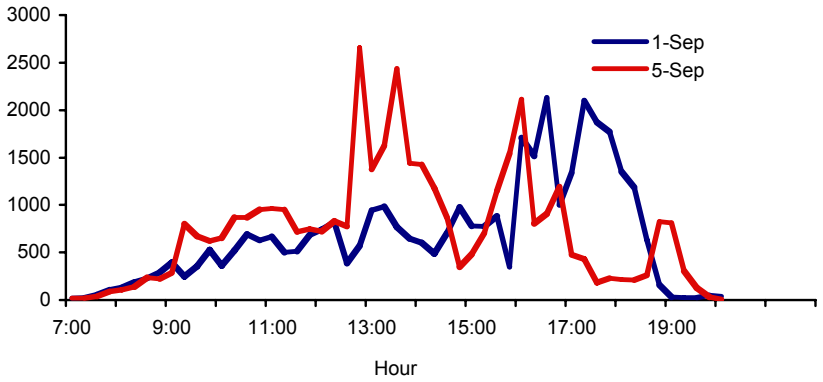

Figure WP6.2. Photosynthetic active radiation (PAR) measured at the water surface (Summer survey).

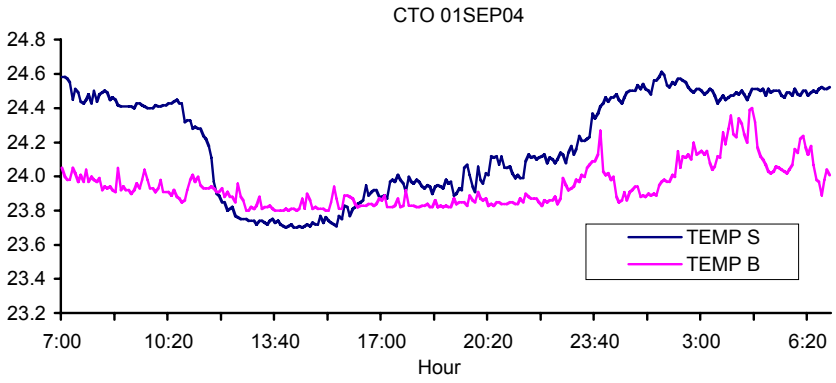

Figure WP7.2. 25-h variation of surface (S) and bottom (B) temperatures at CTO station (Summer survey).

WP3 – Time series analysis

This task consisted in chronological analysis of data from WP2 (both 25 h and 5-d surveys), and was implemented upon all the surveys were completed. The hourly discharges rates essential for the time series analysis, where requested and obtained from the Portuguese Water Institute (INAG). Several methods have been used such as auto and cross correlation and Fourier analysis, using the MatLab software. Time-series of current velocity, temperature, turbidity, pH, dissolved oxygen and chlorophyll concentrations were analysed.

The main objective of this task is answering to the following question: “How does flow variability at different time-scales influences water biogeochemistry at the Crestuma reservoir?”

In order to implement the task, 5-d datasets (see – WP2: Seasonal sampling surveys) of current velocity, dissolved oxygen, pH and fluorimetry (as a surrogate to Chl) were analysed by Fourier analysis, auto and cross correlation (Legendre & Legendre, 1998). Fourier analysis and auto correlations were carried out to break down the measured signal into constituent sinusoids of different frequencies. Cross correlations were used to compare different time series and search for time lags between them. All analyses were carried out after removing linear trends from raw data.

The 25-h datasets were analysed by graphical methods. Correlation and cluster analysis was carried out with the Statistica software to detect eventual relationships between studied variables. Separate analyses were carried out for each station and sampling date to emphasize short-term relationships between the studied variables (correlations within sampling occasions). One of the goals was to understand the potential importance of river flow on the variability of the remaining variables. Another analysis was carried out using average values for each survey and considering all sampling campaigns, in order to look for relationships between the variables at larger time scales (correlations among sampling occasions).

Production-light intensity (P/E) curves were obtained from production determinations and corresponding light intensities, using non-linear regression analysis techniques, namely the Gauss-Newton method with Statistica software. In all cases known P/E functions were tested as those of Steele (1962) and Eilers & Peeters (1988). Some parameters were

common to almost all models or could be derived from the models themselves, namely initial slope or photosynthetic efficiency (□), optimal light intensity or the light level that maximizes photosynthesis under given nutrient and temperature conditions (Eopt) as well as the maximal production rate or photosynthetic capacity (Pmax). Parameter □ may be obtained by calculating the limit of the derivative of P in relation to E as E approaches zero. In inhibition models, Eopt may be determined by calculating the light intensity that maximizes the same derivative (Duarte, *in press*). During the fitting procedure described above, Pmax, Eopt and □ were estimated.

The first part of this section will deal with time-series analysis of the 5-d datasets for each survey. Further, some comparisons were made among data from different seasons, as well as between surface and bottom data along the year but only at station CTO, due to the above mentioned lack of a second updated multiprobe logger. The second part will deal with the analysis of the shorter datasets.

December 2003 survey – surface

Temperature showed a regular temporal pattern, increasing during the morning towards a maximum at the early afternoon (Fig.3). Although dissolved oxygen (DO) patterns (.3) were similar to those of temperature, no significant correlation was found between them (maximum raw correlation coefficient (r.c.c.) was 0.48, for a time lag of almost 4h). DO saturation was generally below 90%, but always higher than 88% (**Error! Reference source not found.**.3). DO maximum occurred in the morning and showed no significant correlation with pH (maximum r.c.c. = 0.46 for a 18h lag) (**Error! Reference source not found.**.3). The DO morning maximum and the absence of correlation with pH, combined with a saturation level under 100%, suggests that photosynthesis was not compensating for net respiratory metabolism and that the ecosystem was predominantly heterotrophic.

Figure WP1.3**.** Temperature variation (left) and fast Fourier transform power spectrum (right) at station B surface level, for a 96h sampling period on December 2003.

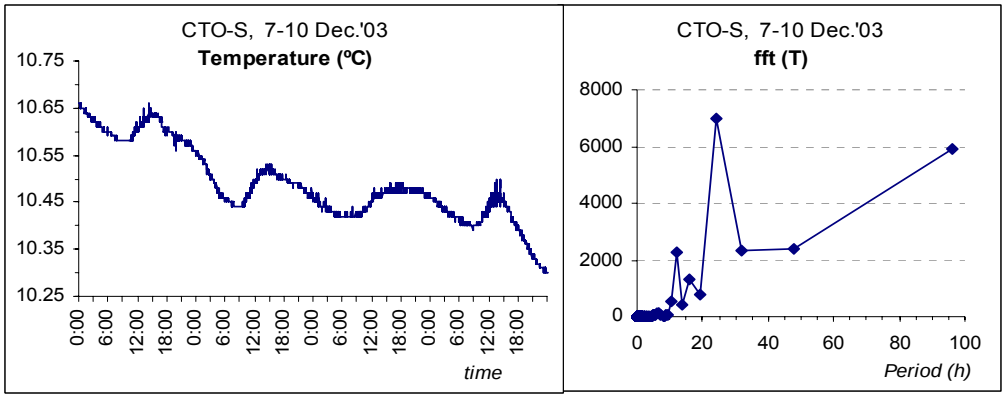

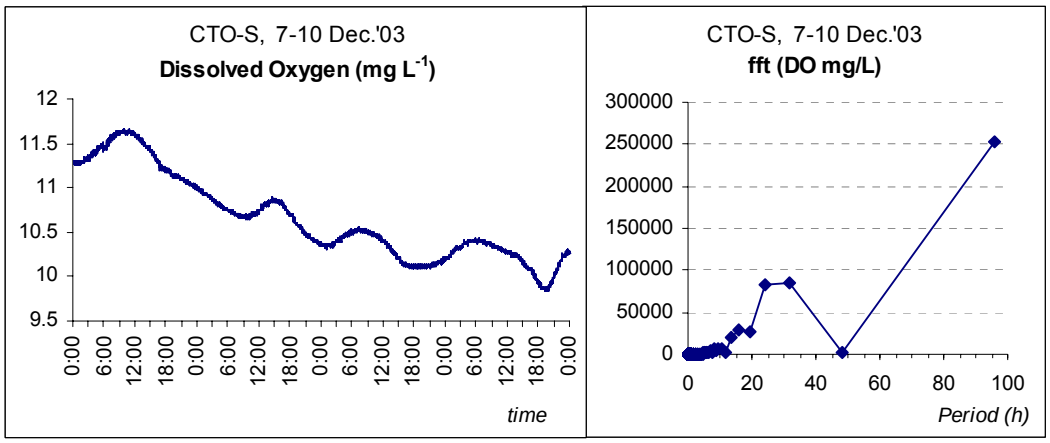

Figure WP2.3. Dissolved oxygen variation (left) and fast Fourier transform power spectrum (right) at station B surface level, for a 96h sampling period on December 2003.

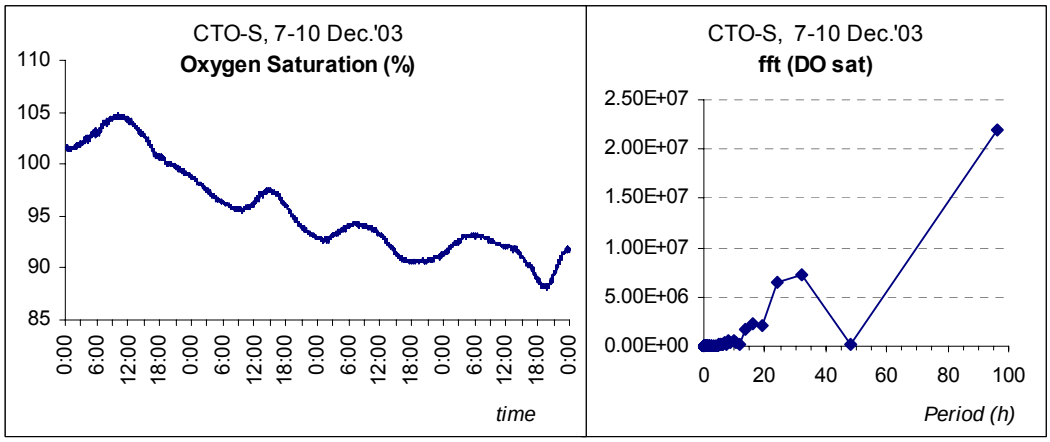

Figure 3.3. Oxygen saturation variation (left) and fast Fourier transform power spectrum (right) at station B surface level, for a 96h sampling period on December 2003.

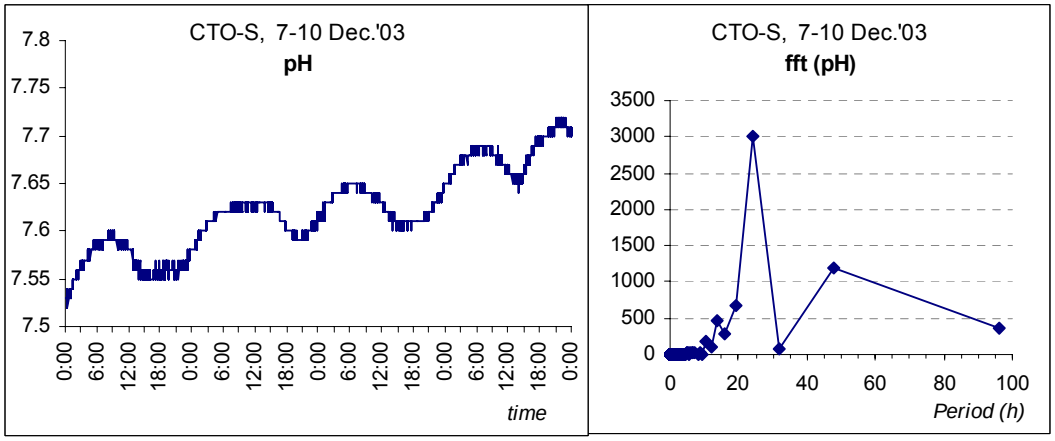

Figure 4.3.pH variation (left) and fast Fourier transform power spectrum (right) at station B surface level, for a 96h sampling period on December 2003.

February 2004 survey – surface

In February, circadian patterns were easily detectable by Fourier analysis, for oxygen and pH (Figs. WP7.3, 8.3 and 9.3). Dissolved oxygen and pH were highly correlated (r.c.c.= 0.73) for a 4 min lag, although the highest correlation among all parameters was between pH and conductivity (r.c.c. = 0.87 for a 2 min lag). The high correlation between pH and dissolved oxygen was consistent with the underwater photosynthetic process, where oxygen was the end product of a chemical pathway that comprised CO_2 consumption and a corresponding pH increase. The opposite was true during the night period, when community respiration leads to a pH reduction. Oxygen saturation was always above 100% (**Error! Reference source not found.**.3), as a result of a net predomination of photosynthetic activity over heterotrophic metabolism.

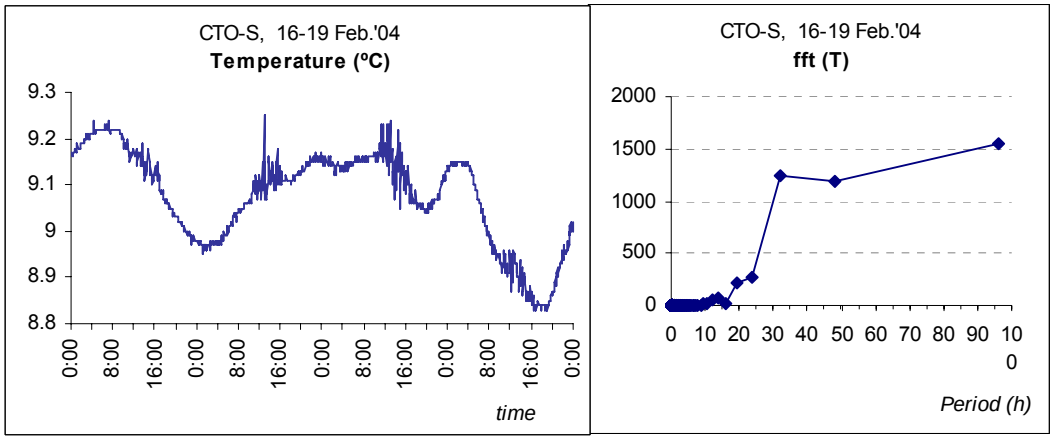

Figure WP5.3**.** Temperature variation (left) and fast Fourier transform power spectrum (right) at station B surface level, for a 96 h sampling period on February 2004.

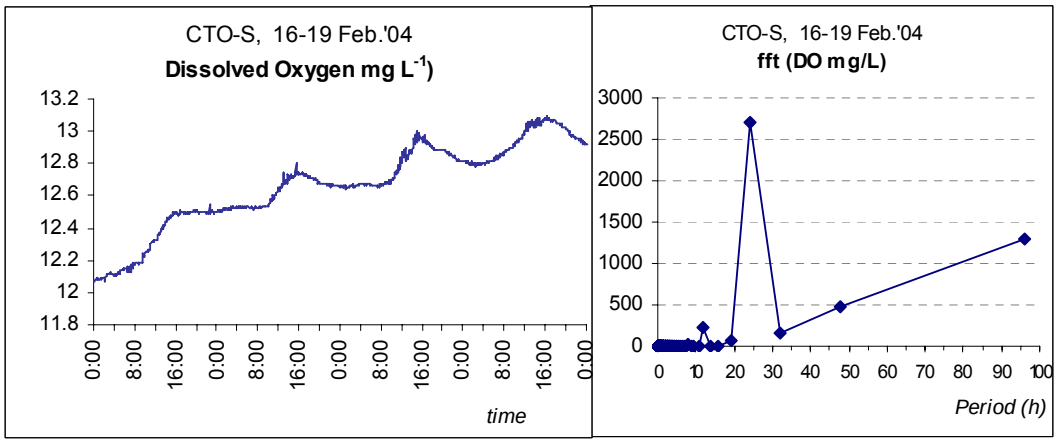

Figure WP6.3. Dissolved oxygen variation (left) and fast Fourier transform power spectrum (right) at station B surface level, for a 96h sampling period on February 2004.

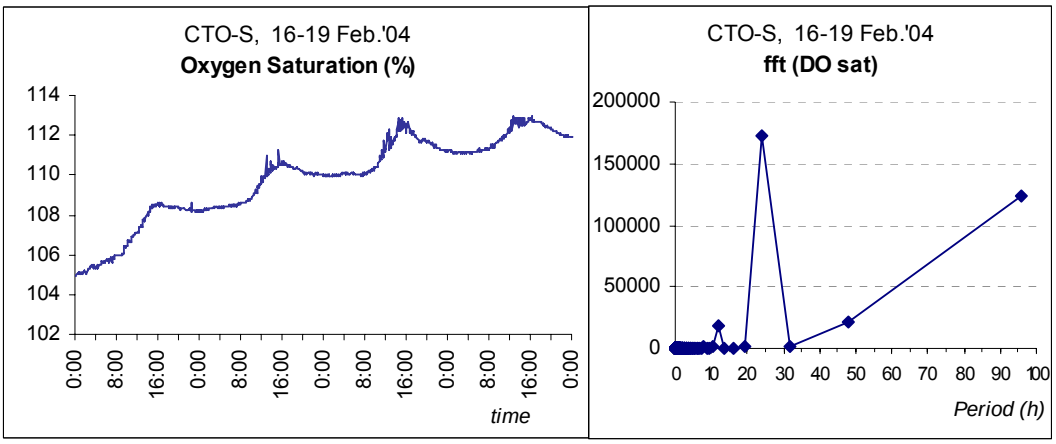

Figure WP7.3. Oxygen saturation variation (left) and fast Fourier transform power spectrum (right) at station B surface level, for a 96h sampling period on February 2004.

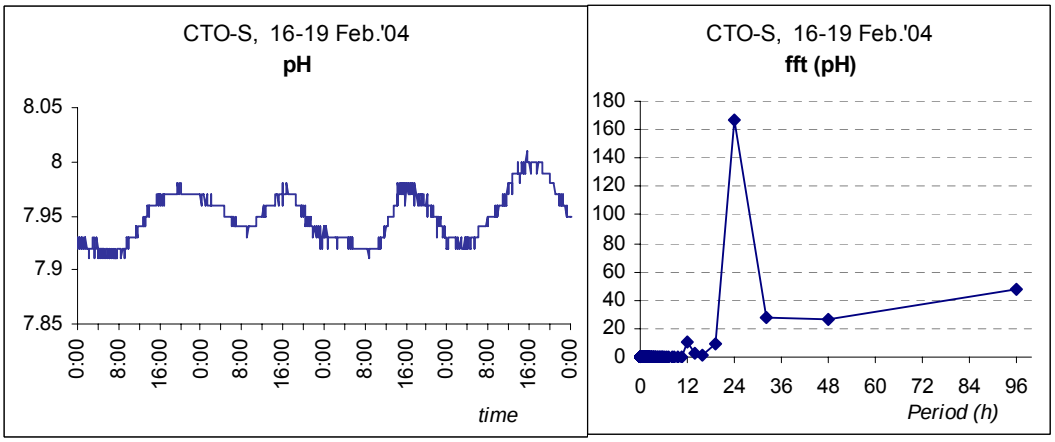

Figure 8.3. pH variation (left) and fast Fourier transform power spectrum (right) at station B surface level, for a 96h sampling period on February 2004.

May 2004 survey – surface

All variables showed considerable temporal variations, becoming quite difficult to visually identify cyclic events, contrasting with Fourier transform results where several periods were determined for each variable. It was possible to distinguish a 24h period only for temperature (**Error! Reference source not found.**.3). In general, temperature reached a maximum value in the morning (~9h) that was followed by a strong rapid decline, after

which a smooth decrease was observed until the first hours of the day. These patterns probably depended on water inputs at different temperatures from upstream. A high r.c.c. (0.91) was found between DO concentration (Fig.3) and pH (Figure WP13.3) and for a zero min lag, corroborating the close chemical relationship between those variables. Oxygen saturation was always above 100% suggesting autotrophy dominance (Fig.3). As for previous datasets, cyclic events in chlorophyll concentration variations were only detected by Fourier transform and were not identified in the time series, even after data interpolation.

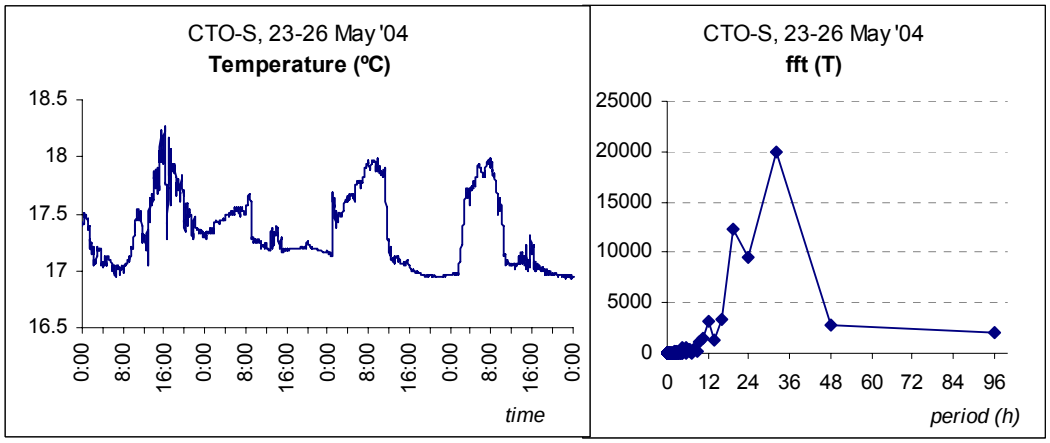

Figure WP9.3. Temperature variation (left) and fast Fourier transform power spectrum (right) at station B surface level, for a 96h sampling period on May 2004.

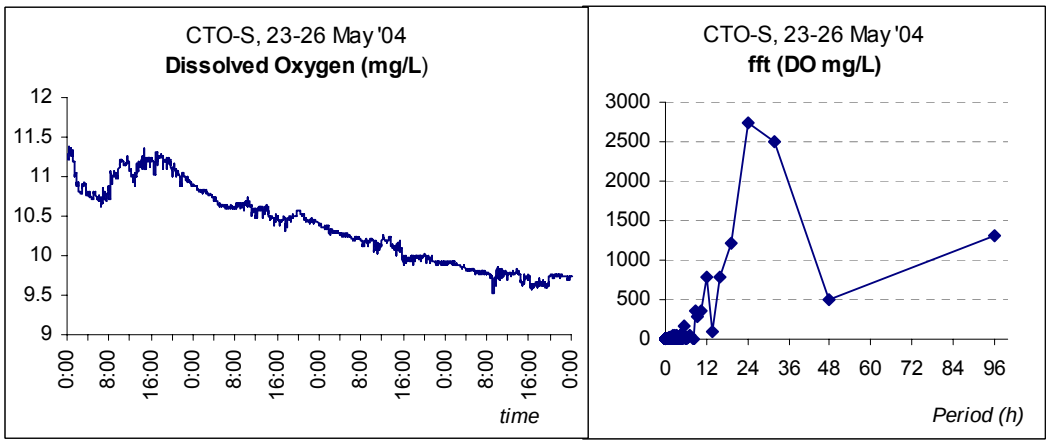

Figure WP10.3. Dissolved oxygen variation (left) and fast Fourier transform power spectrum (right) at station B surface level, for a 96h sampling period on May 2004.

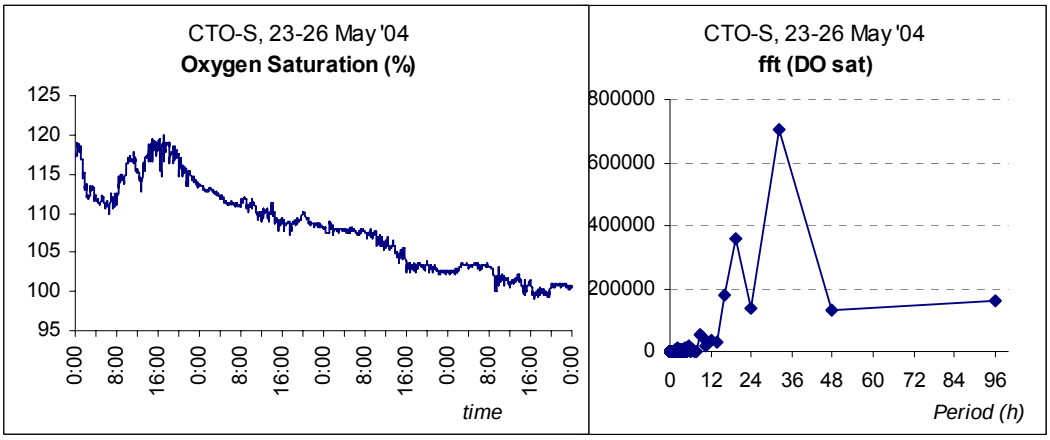

Figure WP11.3. Oxygen saturation variation (left) and fast Fourier transform power spectrum (right) at station B surface level, for a 96 h sampling period on May 2004.

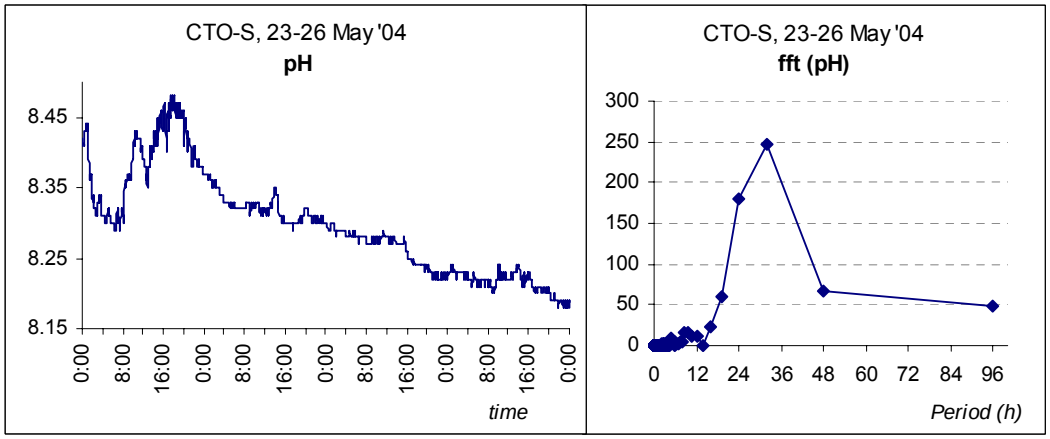

Figure WP12.3. pH variation (left) and fast Fourier transform power spectrum (right) at station B surface level, for a 96h sampling period on May 2004.

September 2004 *survey – surface*

Circadian patterns were detectable by Fourier analysis for oxygen and pH (Figs. WP15.3, 16.3, and 17.3). Cross-correlation results revealed low r.c.c. among all variables (below 0.57). Despite the distinct periods determined by Fourier transform for DO and pH, their temporal variation were rather consistent with the expected relationships between those variables. In contrast with preceding two surveys, DO saturation was always below 100% (Figure WP16.3) suggesting heterotrophic dominance.

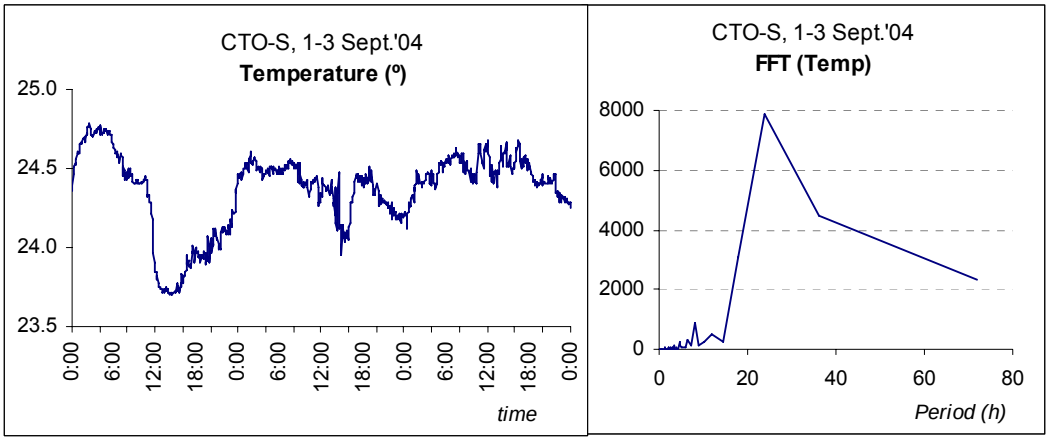

Figure WP13.3. Temperature variation (left) and fast Fourier transform power spectrum (right) at station B surface level, for a 96 h sampling period on September 2004.

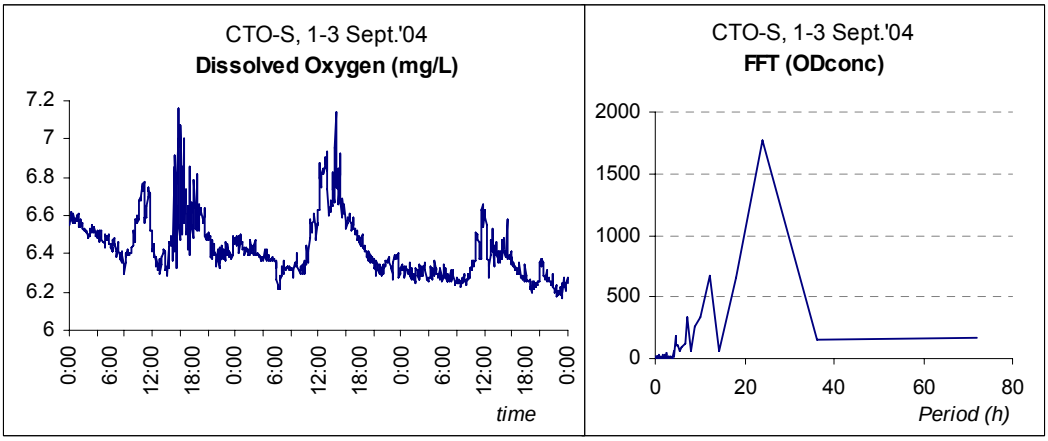

Figure WP14.3. Dissolved oxygen variation (left) and fast Fourier transform power spectrum (right) at station B surface level, for a 96 h sampling period on September 2004.

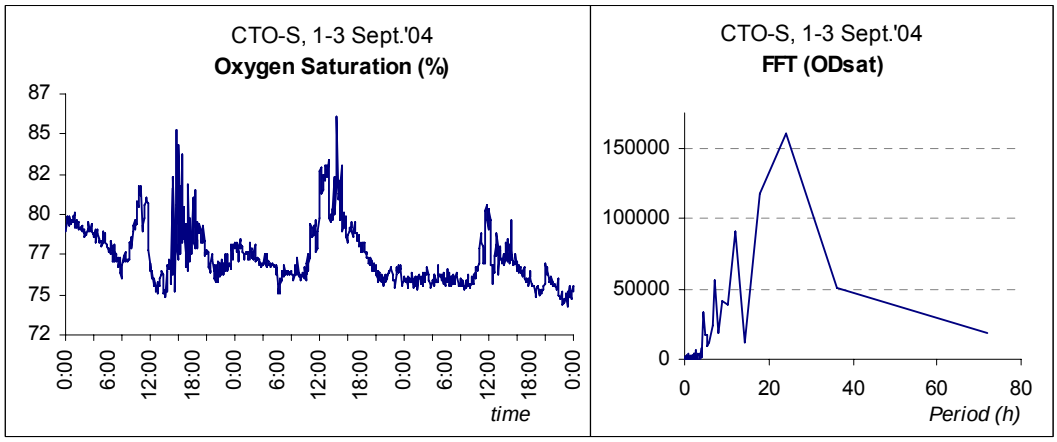

Figure WP15.3. Oxygen saturation variation (left) and fast Fourier transform power spectrum (right) at station B surface level, for a 96 h sampling period on September 2004

.

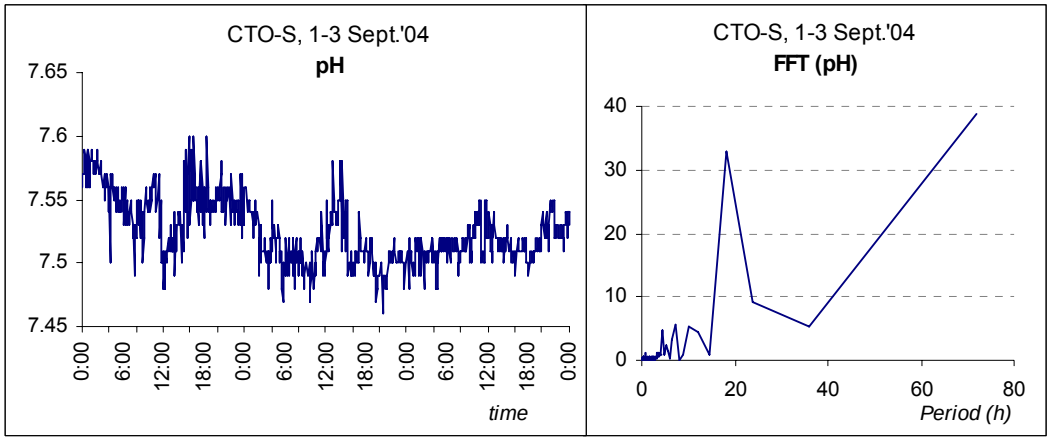

Figure WP16.3. pH variation (left) and fast Fourier transform power spectrum (right) at station B surface level, for a 96h sampling period on September 2004.

February 2004 survey – bottom (9 m)

DO (Figure WP19.3) and pH (Fig.3) showed the expected direct relationship, varying instantaneously in a direct way readily evident from graphical interpretation. Highest correlation was observed for a one minute time lag (r.c.c.=0.67). Oxygen saturation was always above 100% (**Error! Reference source not found.**.3), denoting a net autotrophic

metabolism of the system although measurements were carried out well below the light penetration zone (1% light saturation, or ~ 6 m). Oxygen was the only parameter with a well-defined variation pattern along the sampling period, where circadian cycles were easily identified.

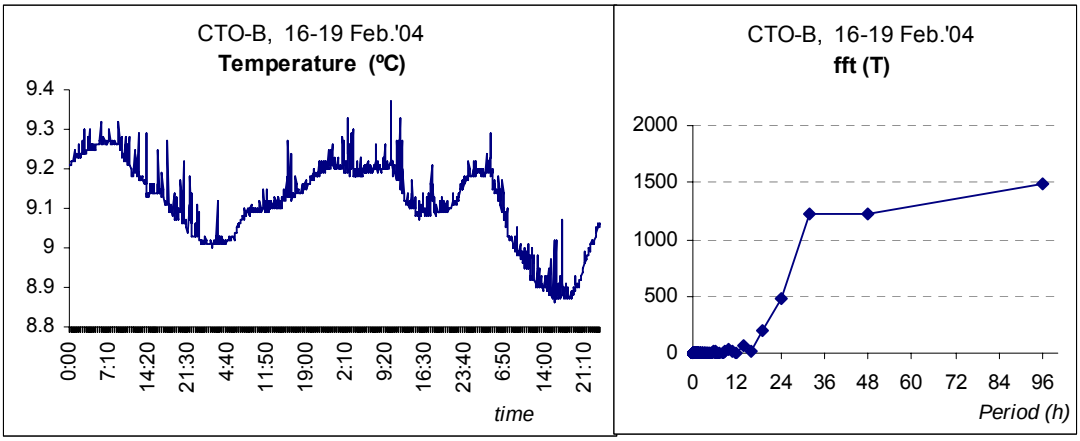

Figure WP17.3. Temperature variation (left) and fast Fourier transform power spectrum (right) at station B bottom level, for a 96h sampling period on February 2004.

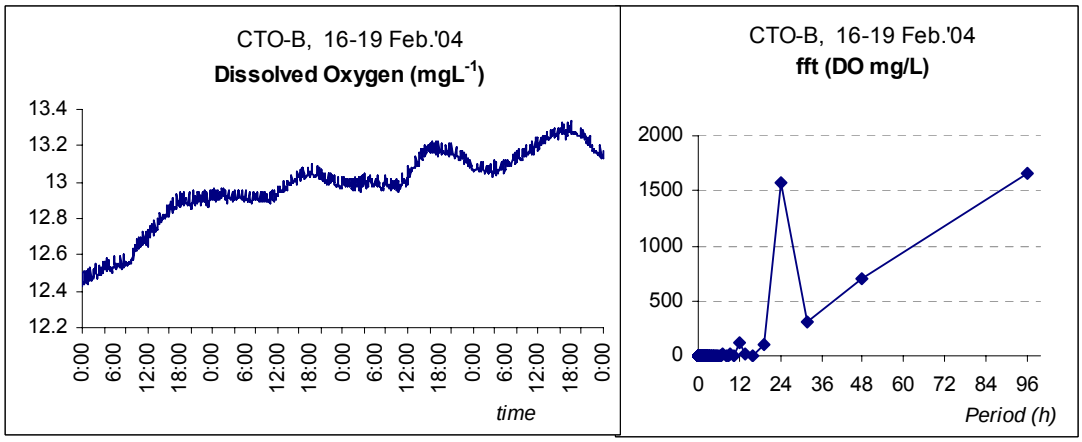

Figure WP18.3. Dissolved oxygen variation (left) and fast Fourier transform power spectrum (right) at station B bottom level, for a 96 h sampling period on February 2004.

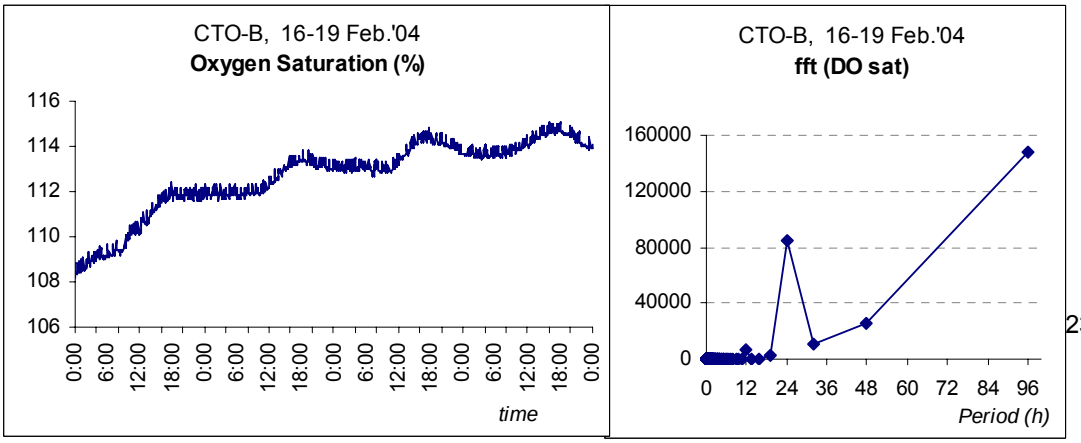

Figure WP19.3. Oxygen saturation variation (left) and fast Fourier transform power spectrum (right) at station B bottom level, for a 96 h sampling period on February 2004.

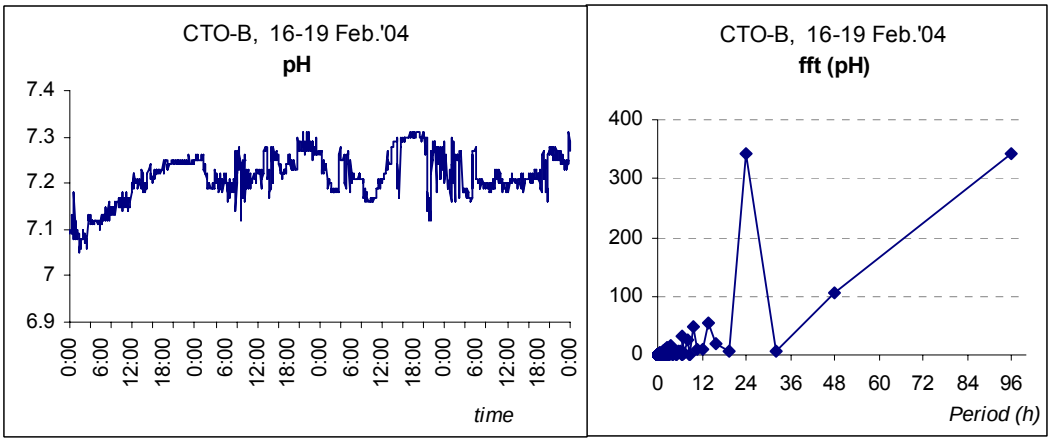

Figure WP 20.3. pH variation (left) and fast Fourier transform power spectrum (right) at station B bottom level, for a 96 h sampling period on February 2004.

May 2004 survey – bottom

DO concentration increased during the first hours of the day, but the daily DO maximum occurred at different times of the day. Consequently, it was very difficult to identify a regular pattern of variation (.3). Nevertheless, the pattern followed the temperature trend (**Error! Reference source not found.**.3). Fourier transform highlighted 32h and 48h periods, but were absent in temporal plots. Oxygen saturation was always above 100%, suggesting a net autotrophic metabolism (Figure WP23.3). In contrast with previous results, pH did not reveal any clear relationship with dissolved oxygen. In fact, the lowest r.c.c. found between them (0.45, for a 9 min lag) suggested the interference of external factors.

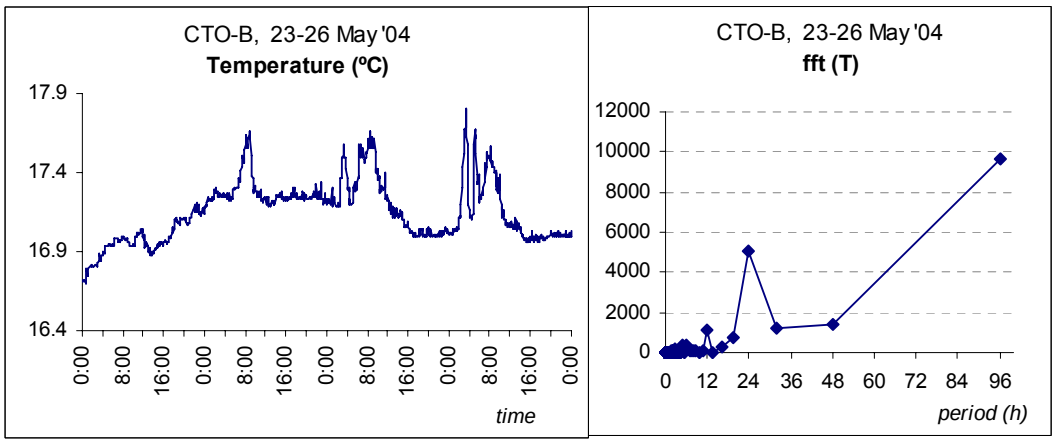

Figure WP21.3. Temperature variation (left) and fast Fourier transform power spectrum (right) at station B bottom level, for a 96h sampling period on May 2004.

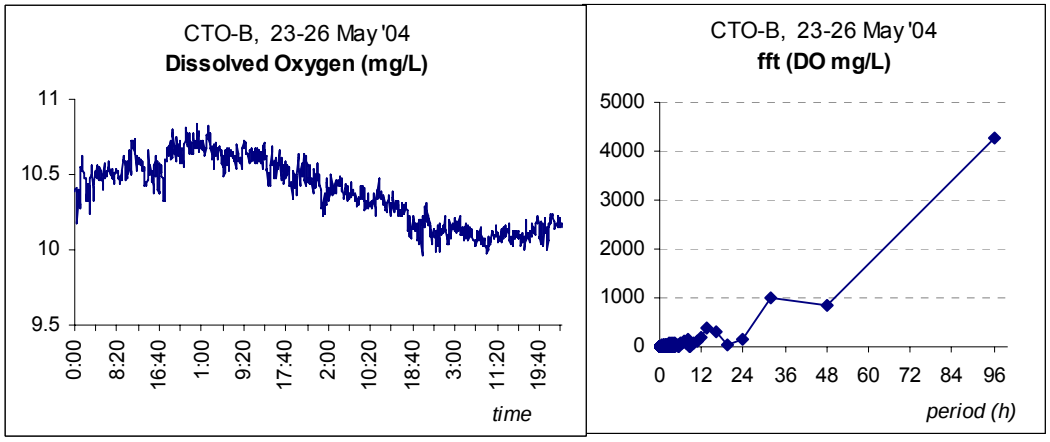

Figure WP22.3. Dissolved oxygen variation (left) and fast Fourier transform power spectrum (right) at station B bottom level, for a 96 h sampling period on May 2004.

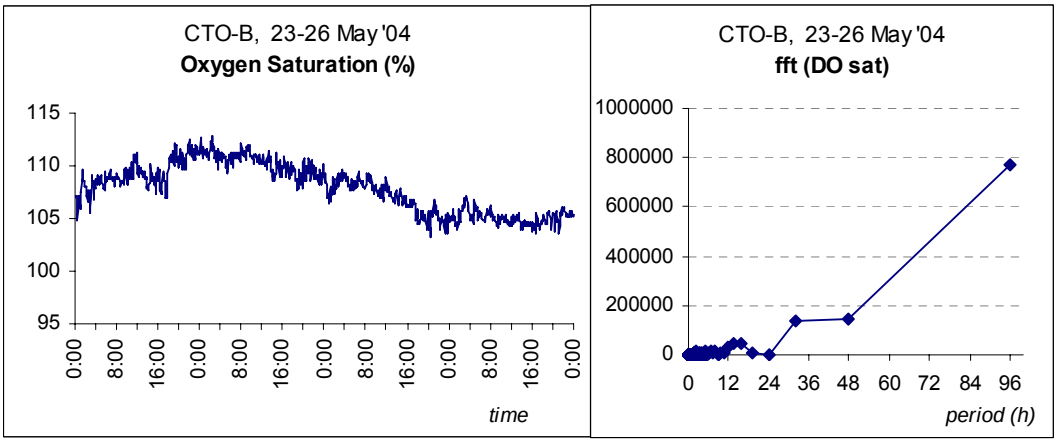

Figure WP23.3. Oxygen saturation variation (left) and fast Fourier transform power spectrum (right) at station B bottom level, for a 96 h sampling period on May 2004.

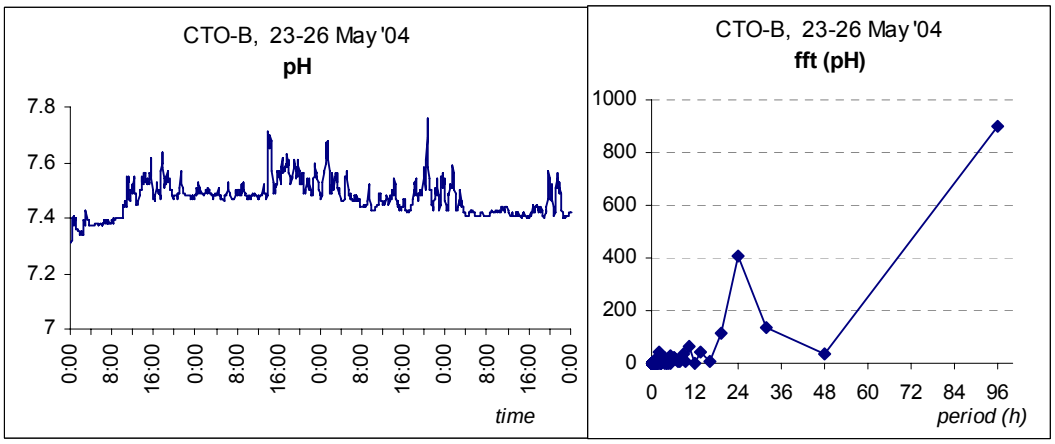

Figure WP24.3. pH variation (left) and fast Fourier transform power spectrum (right) at station B bottom level, for a 96 h sampling period on May 2004.

September 2004 survey – bottom

A 24h period was identified by Fourier transform for temperature (**Error! Reference source not found.**.3), oxygen concentration (Fig.3) and oxygen saturation (Figure WP27.3). Temperature was relatively high (always above 23.5ºC) as expected for this time of the year with minimum values consistently observed during the night. Oxygen saturation was always below 100%, indicating that respiratory metabolism prevailed over photosynthesis. On the other hand, Fourier transform of pH data revealed events with 20h and 30h periods, which were not visually identified in the time series data (**Error! Reference source not found.**.3). Moreover, the expected relationship between this variable and oxygen was not apparent.

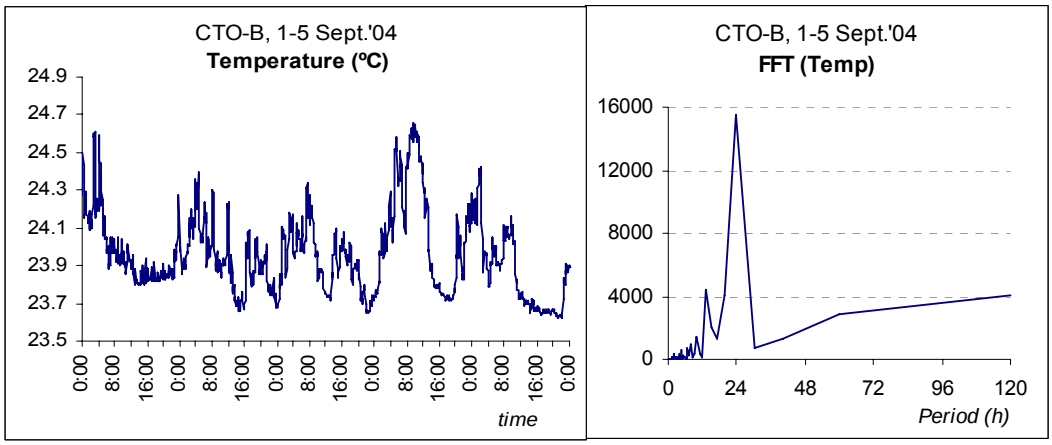

Figure WP25.3. Temperature variation (left) and fast Fourier transform power spectrum (right) at station B bottom level, for a 96h sampling period on September 2004.

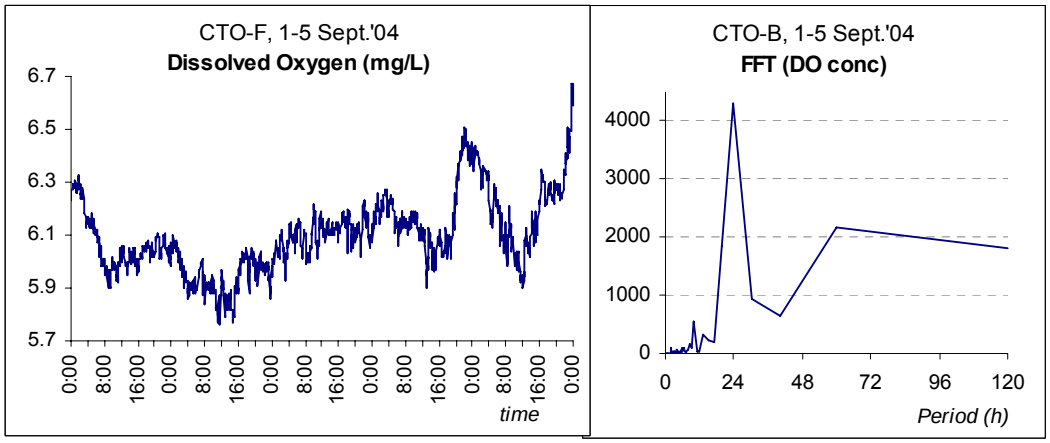

Figure WP26.3. Dissolved oxygen variation (left) and fast Fourier transform power spectrum (right) at station B bottom level, for a 96h sampling period on September 2004.

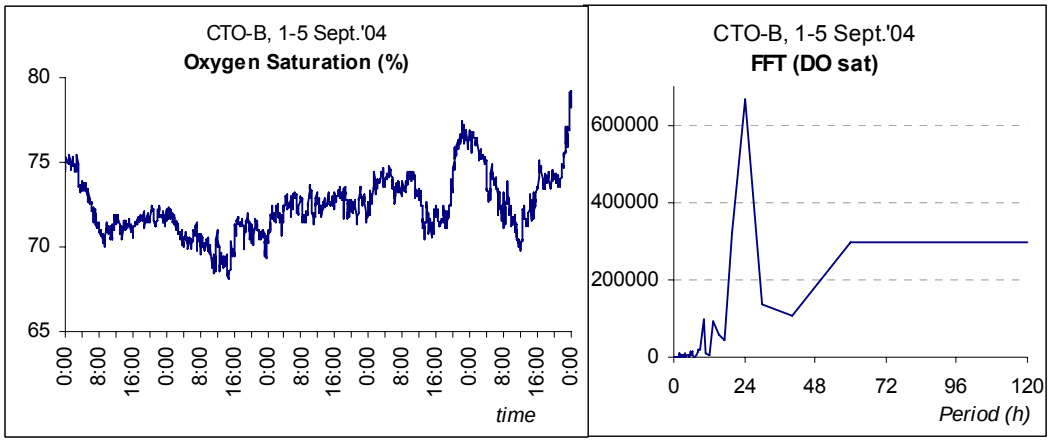

Figure WP27.3. Oxygen saturation variation (left) and fast Fourier transform power spectrum (right) at station B bottom level, for a 96h sampling period on September 2004.

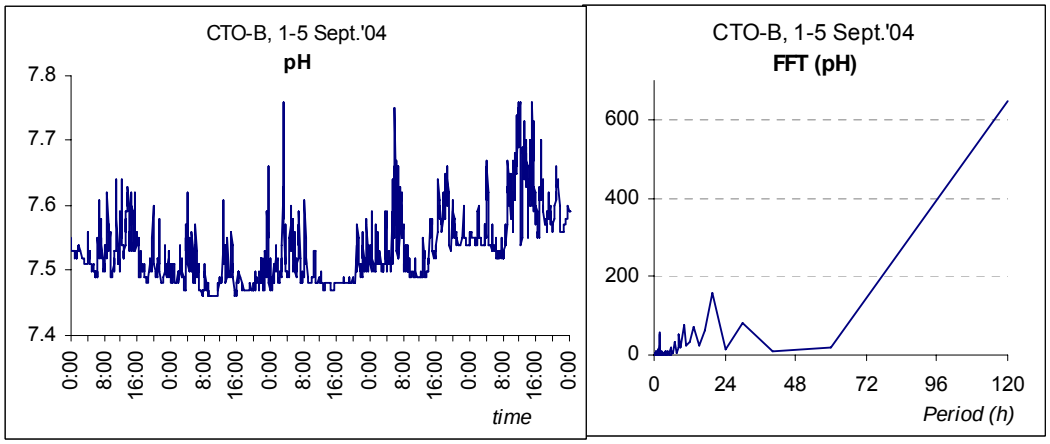

Figure WP28.3. pH variation (left) and fast Fourier transform power spectrum (right) at station B bottom level, for a 96h sampling period on September 2004.

Seasonal Analysis

The seasonal analysis was performed with the 96h datasets and was restricted to the upstream station CTO since at this station a complete surface-bottom data set was obtained throughout the study. At ETA station, the lack of a new multiprobe (never

purchased following the recommendations of the evaluation panel, and the malfunctioning of an existing old equipment (limited to temperature and conductivity) restricted the continuous gathering of data to the surface.

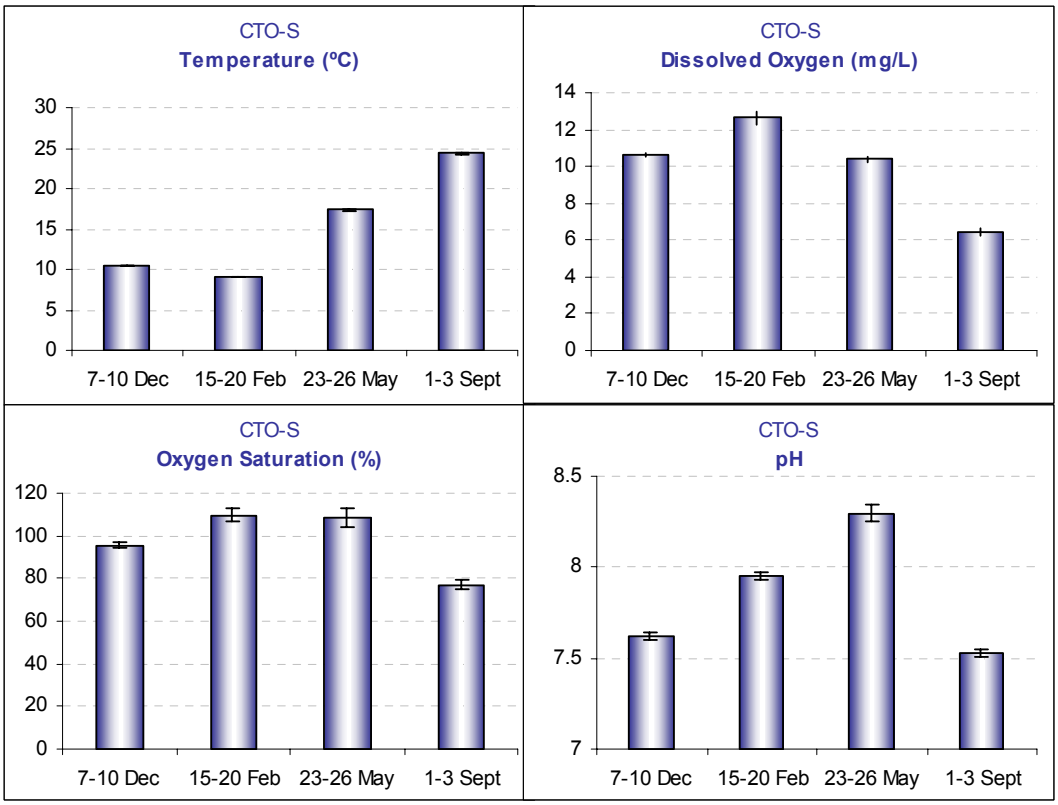

Figure WP29.3. Comparison among mean values of environmental variables, measured at sampling station B surface level (CTO-S), along the year.

Surface (Figure WP29.3)

Temperature and oxygen showed an inverse pattern of variation along the year. As temperature rose, dissolved oxygen decreased as well as oxygen saturation. Mean oxygen saturation was below 100% only in September. pH showed an identical seasonal pattern, increasing from February until May and then decreasing in September.

Bottom (Figure WP30.3)

Temperature increased from February to September as dissolved oxygen decreased to half values in the same period. An increase in pH was also observed along the year, but it was very slight (variation amplitude of only 0.3).

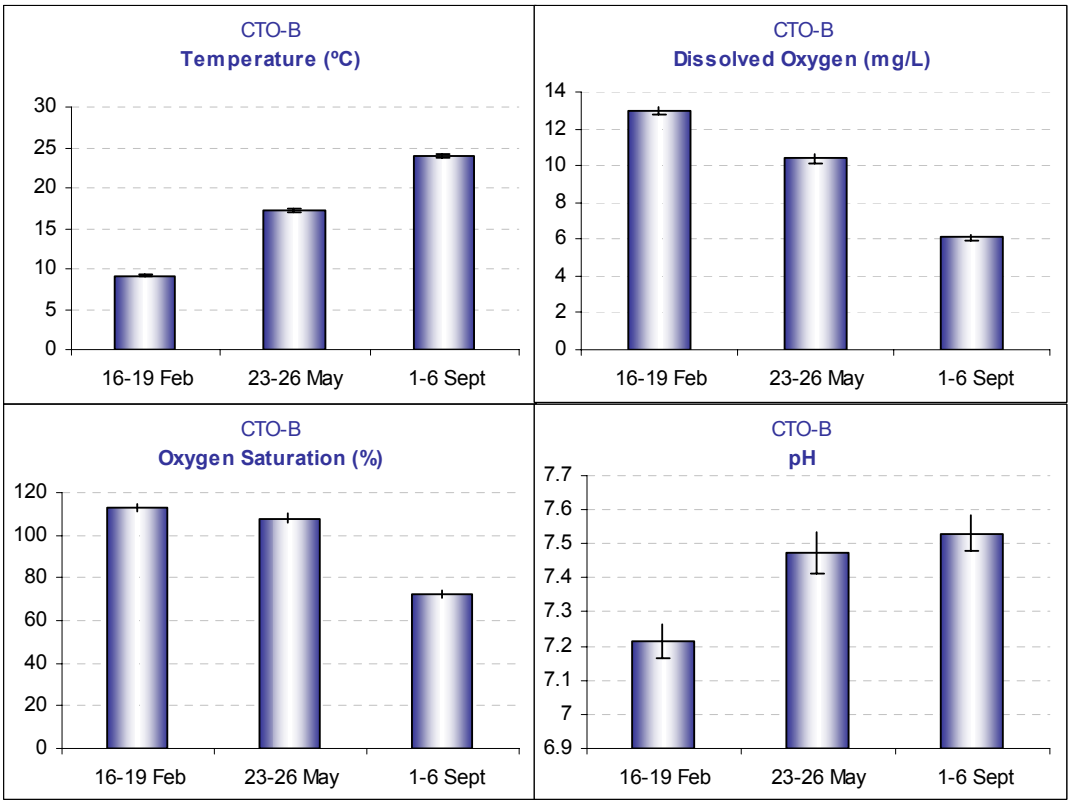

Figure WP30.3. Comparison among mean values of environmental variables, measured at sampling station B bottom level (CTO-B), along the year.

Overall comparison between surface and bottom data

The comparison between surface and bottom environment was only possible for the year 2004 (February, May and September), using the 96-h data set. Bottom and surface mean values of dissolved oxygen and oxygen saturation decreased from winter till summer. An overall heterotrophic metabolism was apparent in the hottest season (September) at both depth levels.

Station ETA

Mean values of all measured environmental variables were similar for surface and bottom data, except for dissolved oxygen, which was always higher at bottom (Figure WP 31.3). These higher levels of dissolved oxygen at lower depths suggest that heterotrophic metabolism was not consuming all the oxygen that was being produced at surface or the existence of DO transfers, either top-down or longitudinal.

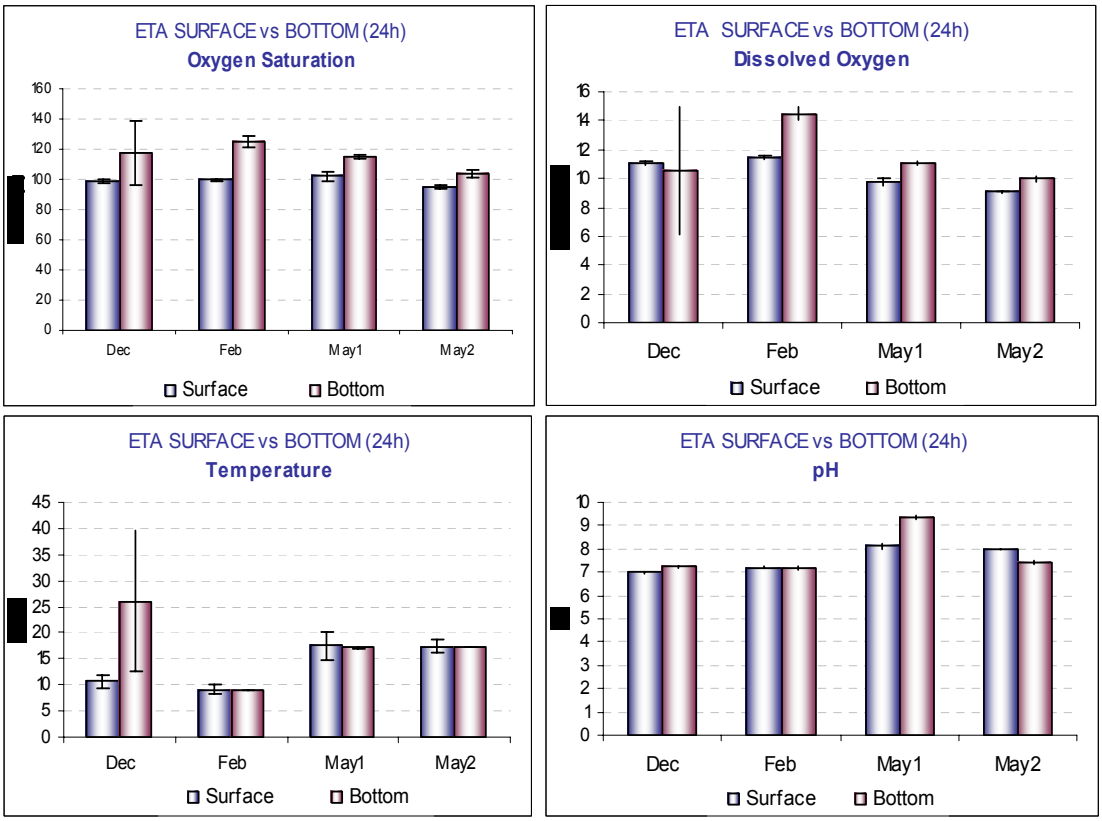

Figure WP31.3 Comparison between surface and bottom 24h data measured at ETA sampling station, for each season.

Station CTO

At CTO station large differences were not detected between surface and bottom data along the year, except for pH, that was relatively higher at surface in February and May (Figure WP32.3). As mean temperature increased along the year, mean dissolved oxygen decreased and, in Septembe,r this value was half of the February value. Mean oxygen saturation variation along the year was less pronounced and only in May it was below 100%.

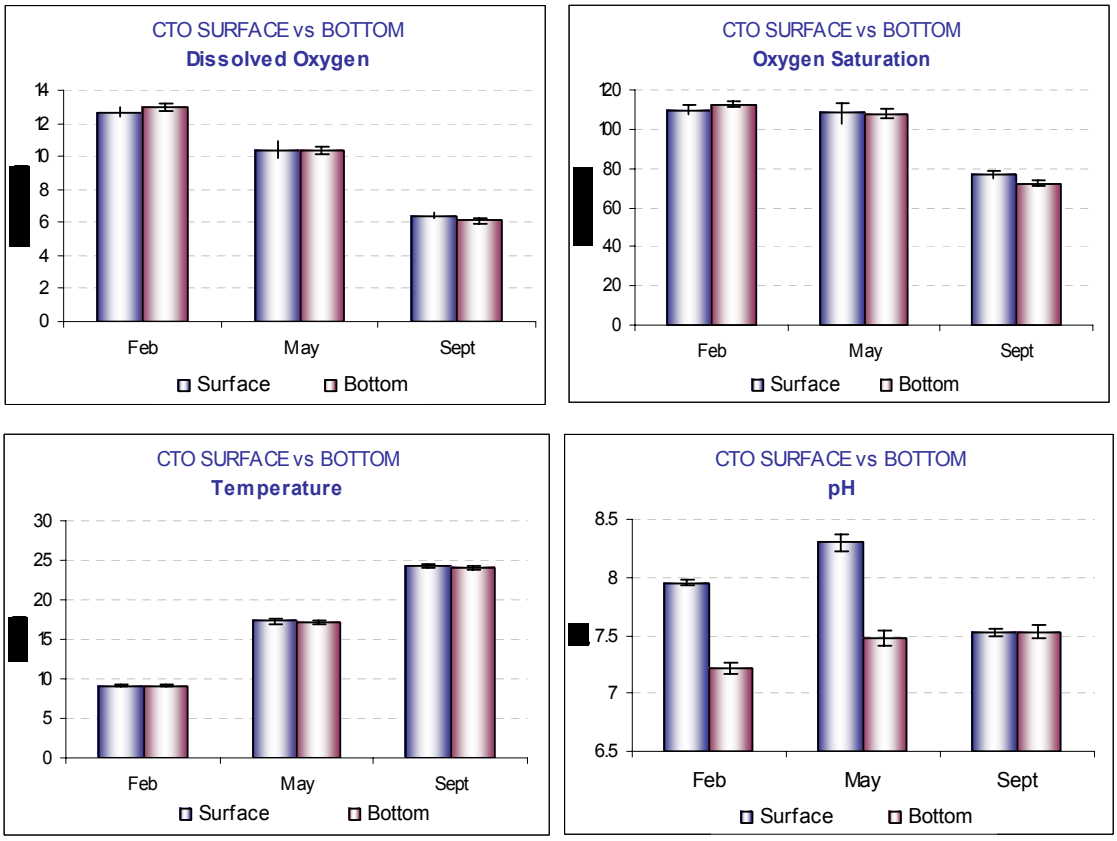

Figure WP32.3. Comparison between surface and bottom 96h data measured at CTO sampling station, for each season.

Analysis of 25-h datasets

DO, temperature and pH ranges observed at both stations over the sampling period are synthesized in Tables WP1.3-WP4.3. Diurnal variability of chlorophyll, nutrient concentrations and river flow are summarized in Figs. WP33.3 through WP40.3.

Correlation analysis did not reveal any clear influence of river flow on the remaining variables at short (25-h) time scales. The obtained results suggest that river flow may be strongly influence the behaviour of some variables in specific occasions, but without any consistent overall pattern. In fact, significant correlations ($p < 0.05$) between river flow and other variables were observed solely in three out of fifteen 25 h-datasets (station B X eight sampling occasion, plus station A X seven sampling occasions). However, these correlations were not consistent between the four mentioned datasets. For example, in two of them, photosynthetic pigments were significantly correlated with river flow, whereas in the third one only silicate exhibited a significant correlation with flow ($p< 0.05$).

Regarding long (seasonal) time scales, a significant negative correlation ($p < 0.05$) was observed between river flow and photosynthetic pigments. This may be explained by the fact that chlorophyll concentrations reached highest values in May, whereas river flow attained maximums in December and February i.e. during the coldest and the less light availability period of the year. Cluster analysis suggested a positive relationship between river flow and phosphate concentrations at seasonal time scales.

Table WP1.3. Range values measured for dissolved oxygen saturation (DOsat) and concentration (DOconc), temperature (T) and pH for sampling station A (ETA) at surface level.

	ETA surface			
	December	**February**	**May**	**September**
DO sat (%)	86.1 – 108.1	95.7 – 101.8	92.3 – 108.7	----------
DO conc (mg/L)	4.52 – 16.54	13.47 – 15.04	9.48 – 11.43	----------
T (ºC)	10.31 – 10.81	8.89 – 9.18	16.91 – 18.13	----------
pH	6.93 – 7.26	7.12 – 7.55	7.39 – 8.26	----------

Table WP2.3. Range values measured for dissolved oxygen saturation (DOsat) and concentration (DOconc), temperature (T) and pH for sampling station A (ETA)at bottom level.

	ETA bottom			
	December	**February**	**May**	**September**
DO sat (%)	83.8 – 148.1	117.2 – 130.6	98.6 – 119.3	----------
DO conc (mg/L)	4.52 – 16.54	13.47 – 15.04	9.48 – 11.43	----------
T (ºC)	10.34 -51.3	8.9 – 9.2	16.87 – 17.52	----------
pH	7.1 – 8.04	6.76 – 7.4	7.02 – 9.78	----------

Table WP3.3. Range values measured for dissolved oxygen saturation (DOsat) and concentration (DOconc), temperature (T) and pH for sampling station B (CTO) at surface level.

	CTO surface			
	December	**February**	**May**	**September**
DO sat (%)	87.9 – 104.9	104.9 - 113	99.1 – 119.9	73.7 – 85.6
DO conc (mg/L)	9.83 -11.67	12.07 – 13.1	9.52 – 11.38	6.17 – 7.16
T (ºC)	10.24 – 10.66	8.83 – 9.25	16.93 -18.27	23.7 -24.78
pH	7.52 – 7.72	7.91 – 8.01	8.18 – 8.48	7.46 – 7.6

Table WP4.3. Range values measured for dissolved oxygen saturation (DOsat) and concentration (DOconc), temperature (T) and pH for sampling station B (CTO) at bottom level.

	CTO bottom			
	December	**February**	**May**	**September**
DO sat (%)	----------	108.2 – 115.1	103.2 – 112.8	68.1 – 79.2
DO conc (mg/L)	----------	12.43 – 13.34	9.96 – 10.84	5.76 – 6.67
T (ºC)	----------	8.86 – 9.37	16.7 – 17.8	23.62 – 24.66
pH	----------	7.05 – 7.31	7.31 – 7.76	7.46 – 7.76

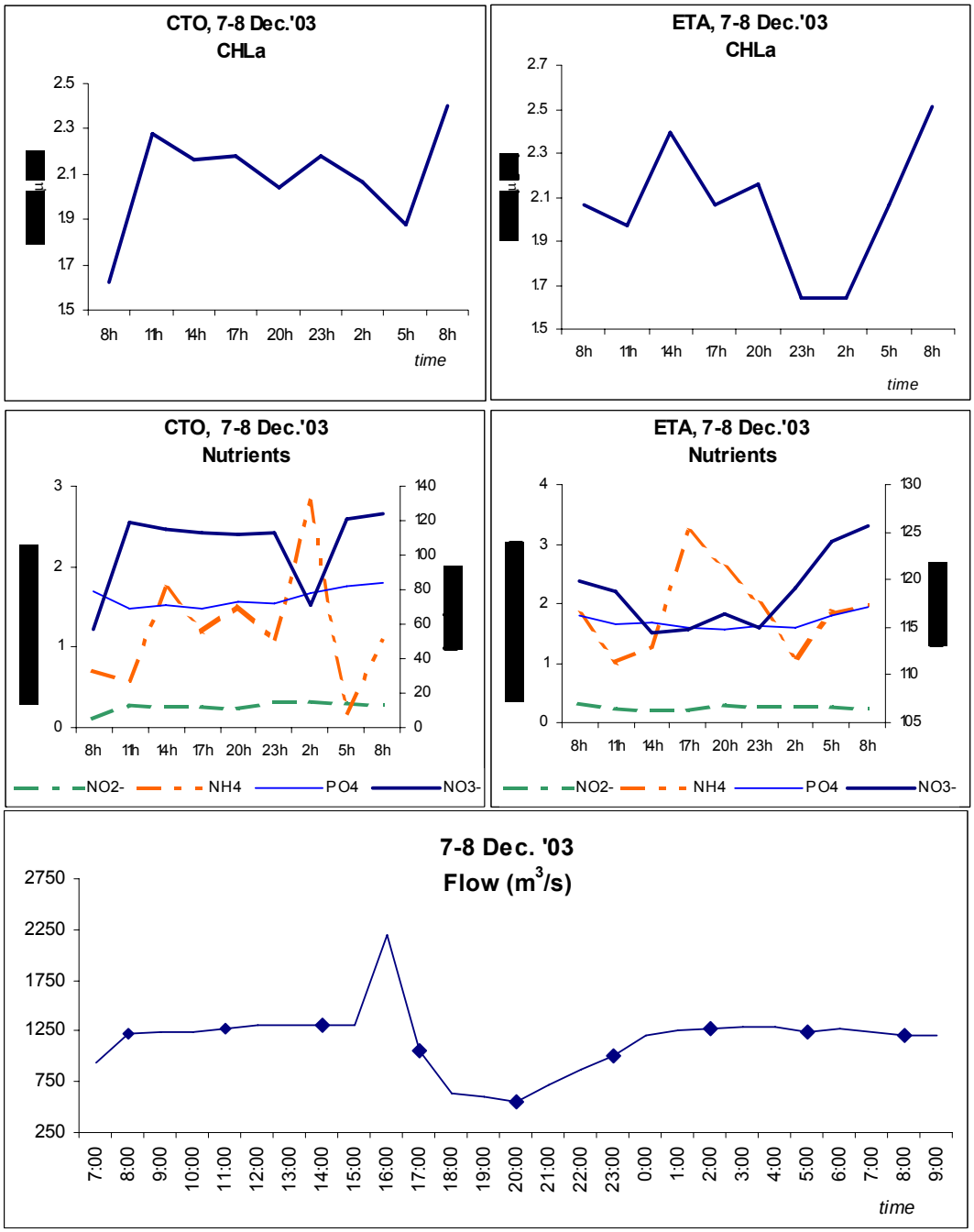

Figure WP33.3. Chlorophyll-a and nutrients data measured at both sampling stations (upper charts), corresponding to a 24h sampling period from 7 to 8 of December 2003. Bottom chart represents the flow regime and the dots the moments when chlorophyll-a and nutrients were sampled

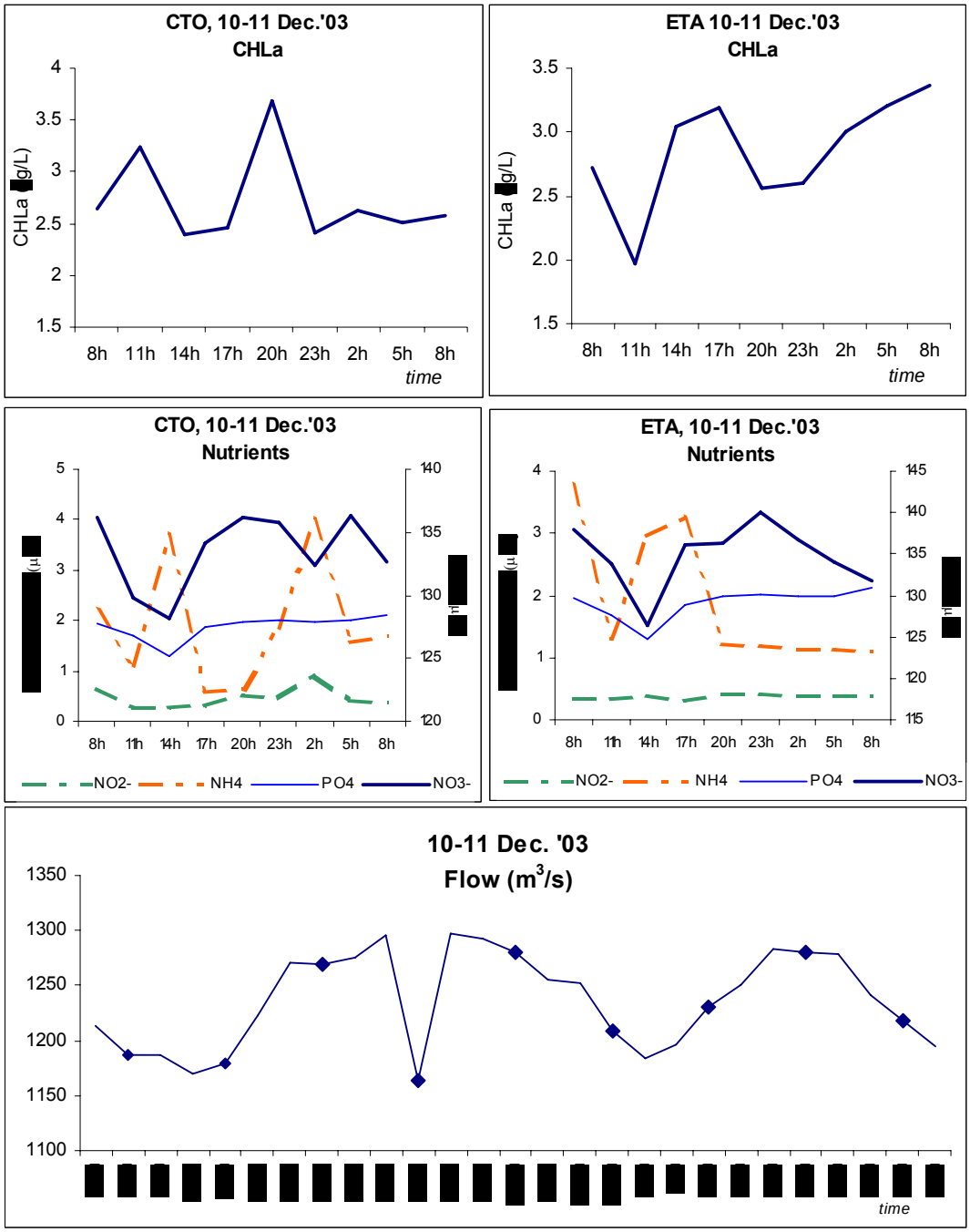

Figure WP34.3. Chlorophyll-a and nutrients data measured at both sampling stations (upper charts), corresponding to a 24h sampling period from 10 to 11 of December 2003. Bottom chart represents the flow regime and the dots the moments when chlorophyll-a and nutrients were sampled.

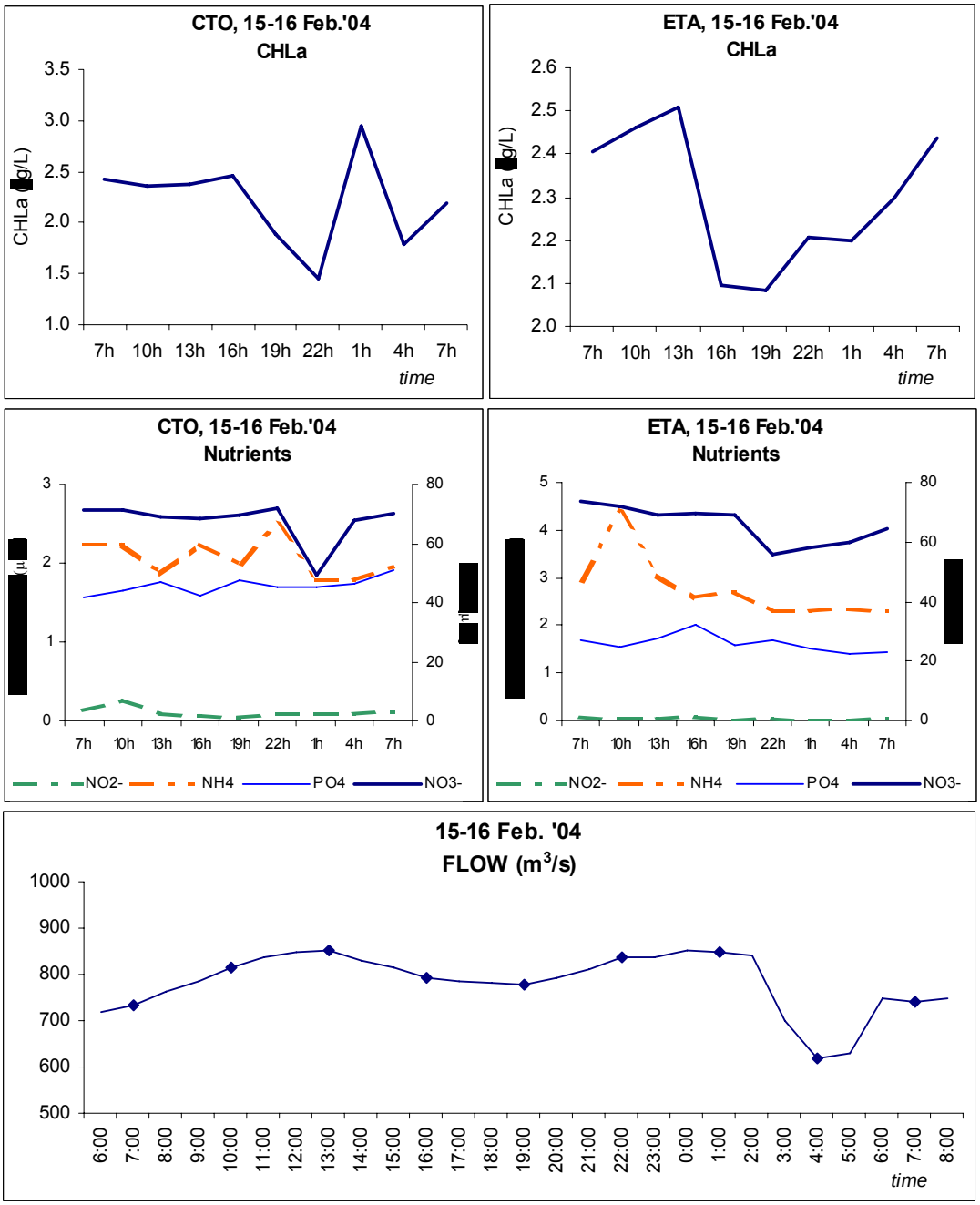

Figure WP35.3. Chlorophyll-a and nutrients data measured at both sampling stations (upper charts), corresponding to a 24h sampling period from 15 to 16 of February 2004. Bottom chart represents the flow regime and the dots the moments when chlorophyll-a and nutrients were sampled.

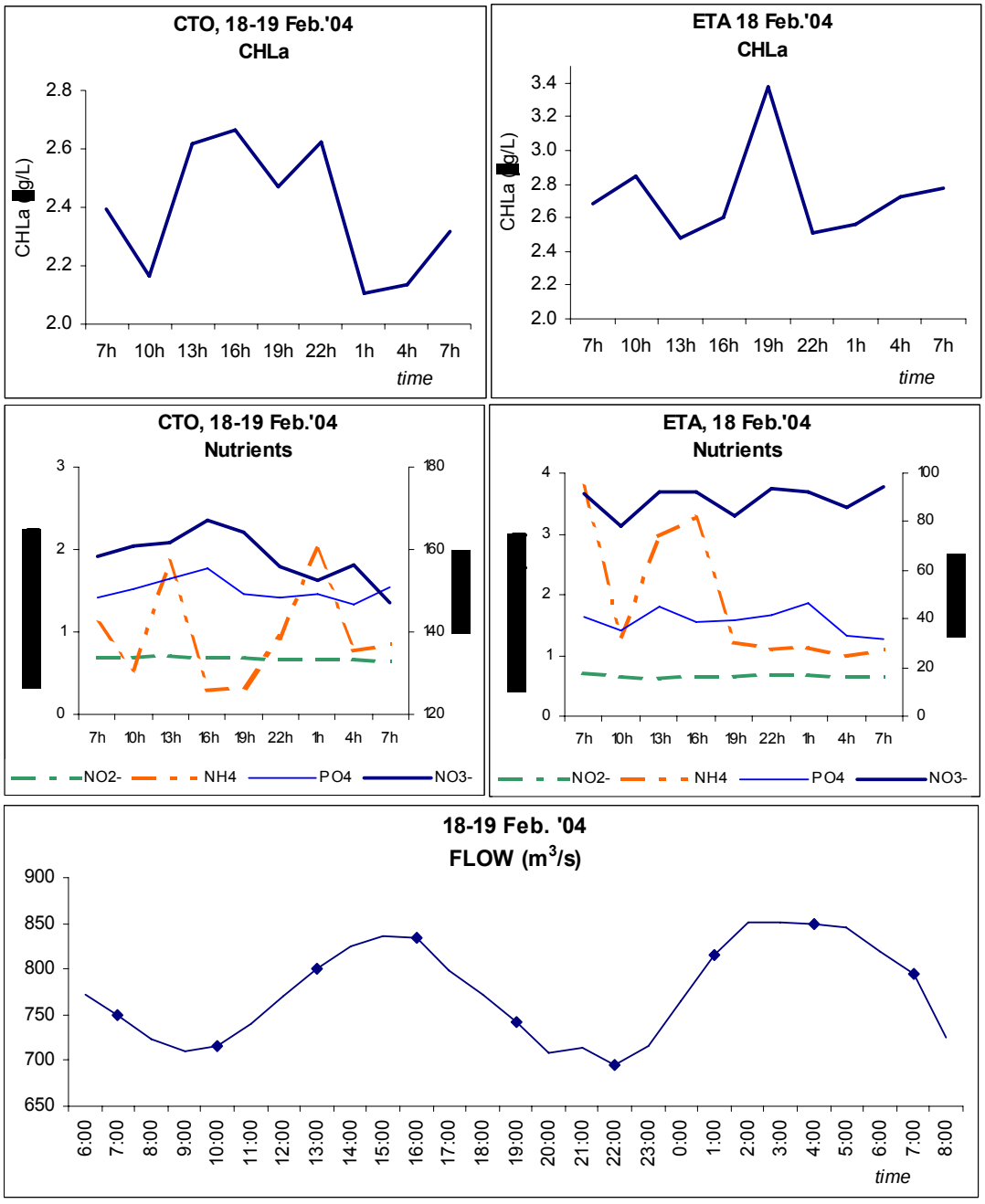

Figure WP36.3 Chlorophyll-a and nutrients data measured at both sampling stations (upper charts), corresponding to a 24h sampling period from 18 to 19 of February 2004. Bottom chart represents the flow regime and the dots the moments when chlorophyll-a and nutrients were sampled.

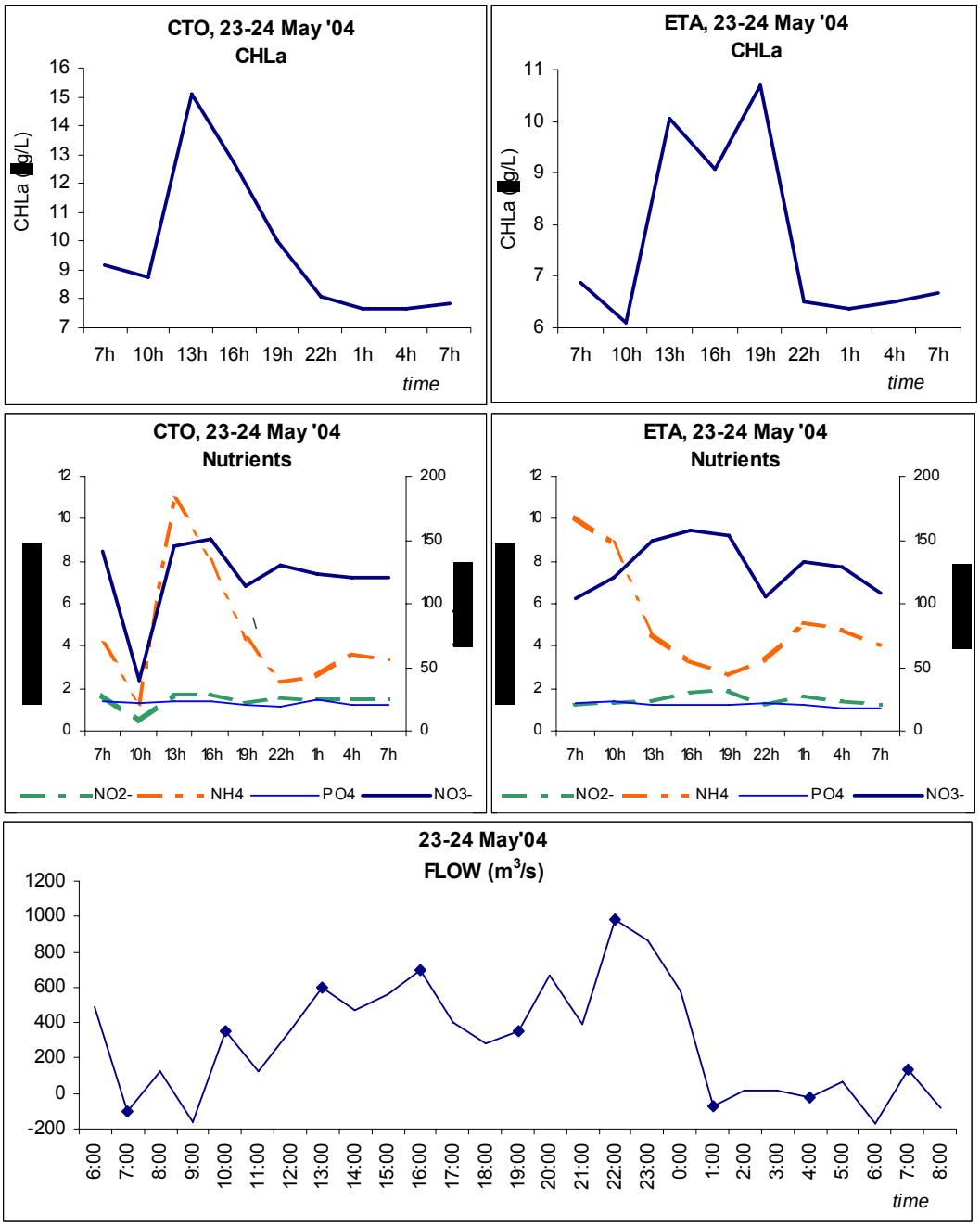

Figure 37.3. Chlorophyll-a and nutrients data measured at both sampling stations (upper charts), corresponding to a 24h sampling period from 23 to 24 of May 2004. Bottom chart represents the flow regime and the dots the moments when chlorophyll-a and nutrients were sampled.

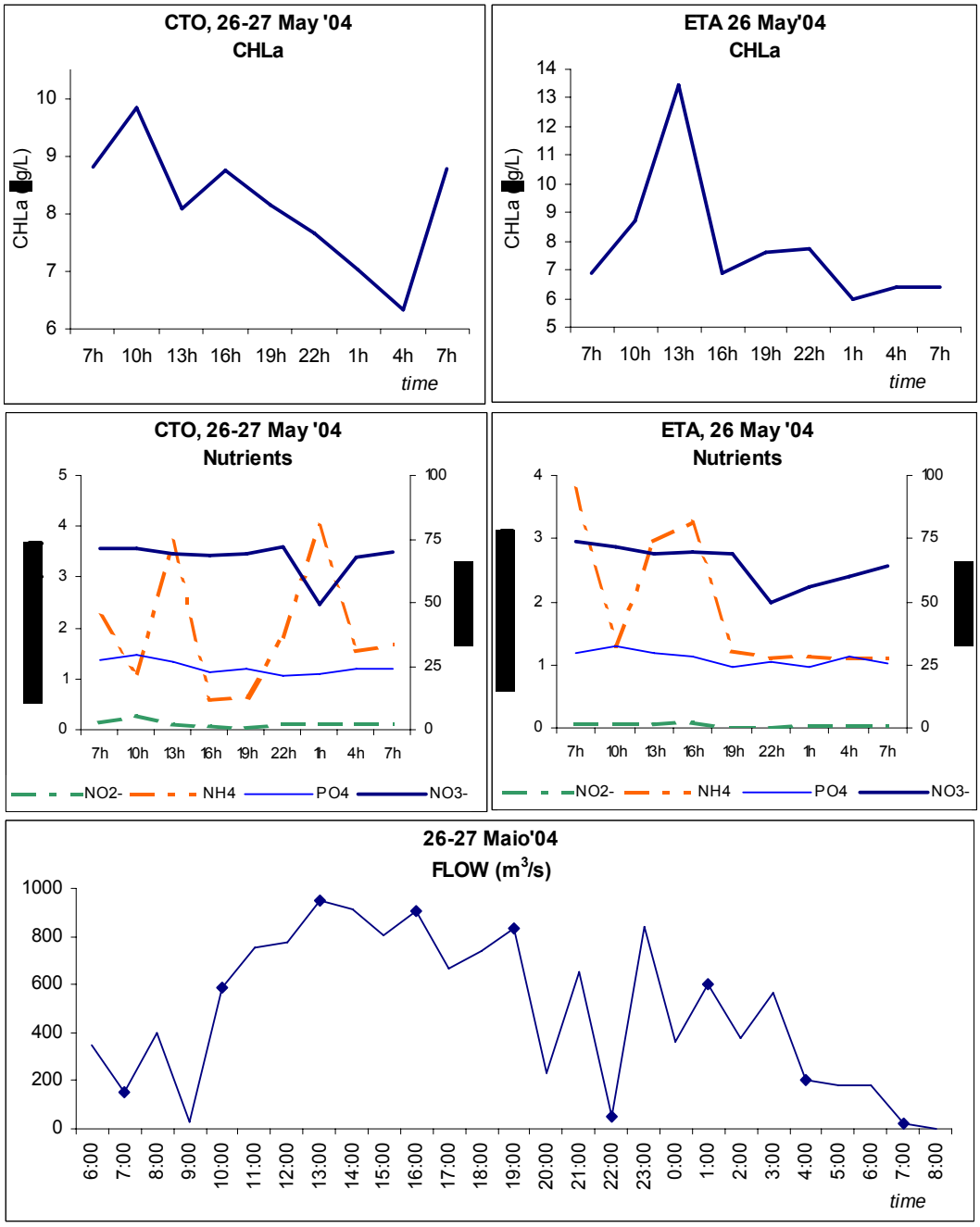

Figure 38.3. Chlorophyll-a and nutrients data measured at both sampling stations (upper charts), corresponding to a 24h sampling period from 26 to 27 of May 2004. Bottom chart represents the flow regime and the dots the moments when chlorophyll-a and nutrients were sampled.

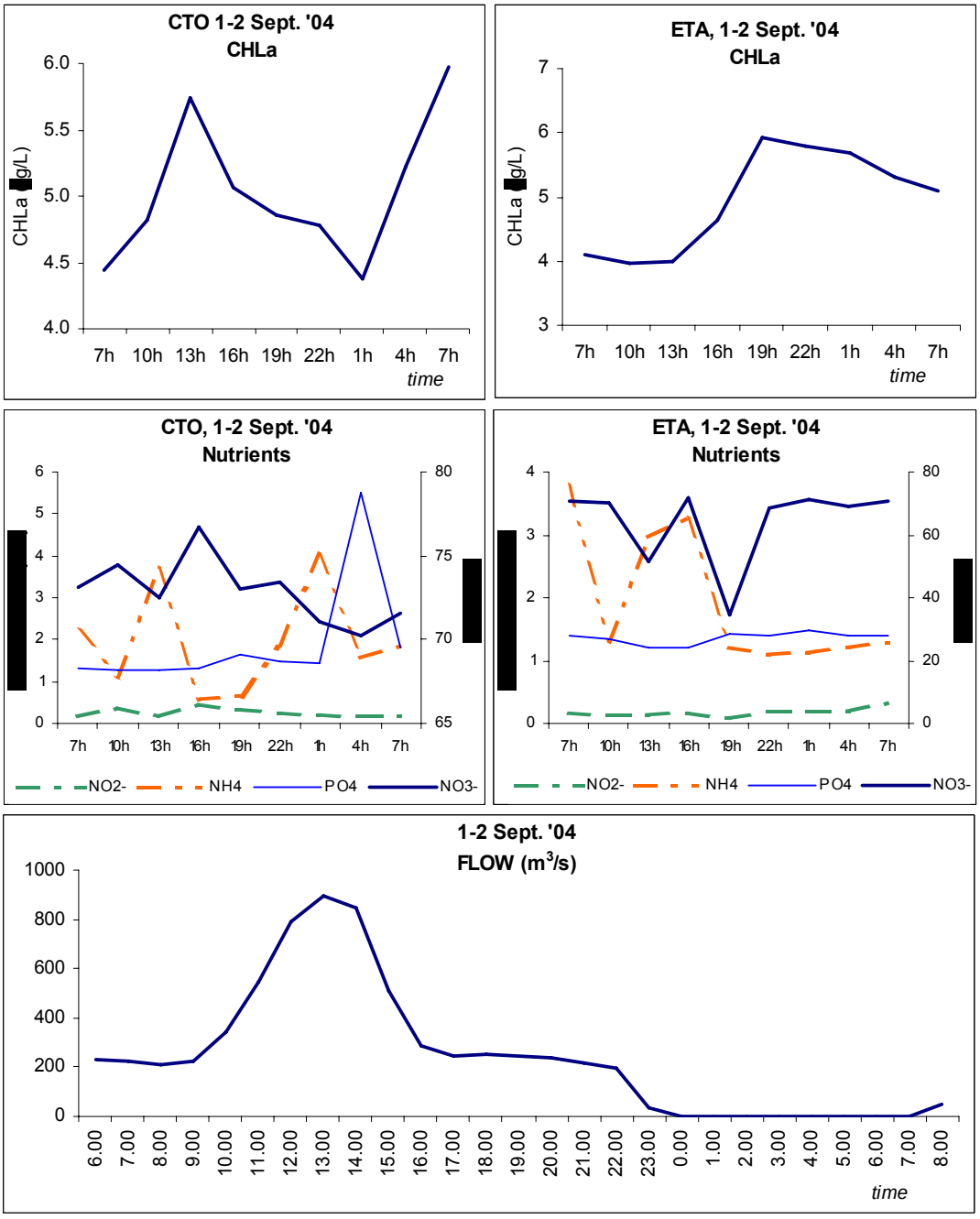

Figure 39.3. Chlorophyll-a and nutrients data measured at both sampling stations (upper charts), corresponding to a 24h sampling period from 1 to 2 of September 2004. Bottom chart represents the flow regime and the dots the moments when chlorophyll-a and nutrients were sampled.

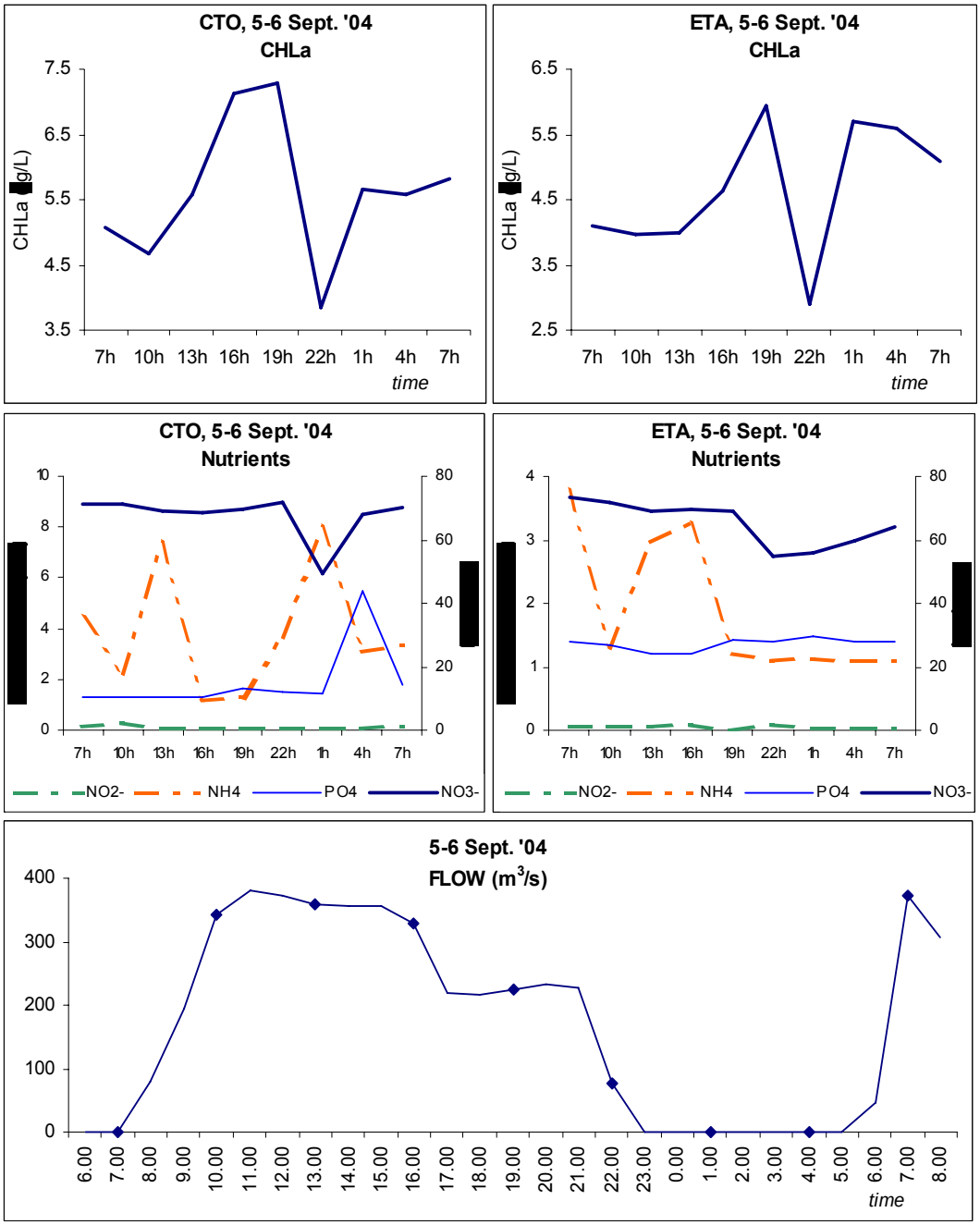

Figure 40.3. Chlorophyll-a and nutrients data measured at both sampling stations (upper charts), corresponding to a 24h sampling period from 5 to 6 of February 2004. Bottom chart represents the flow regime and the dots the moments when chlorophyll-a and nutrients were sampled.

Table WP5.3 summarizes the results obtained by fitting Steels' P/I equation (Steele, 1962) to production light data (cf. – Methodology – Data analysis). The analysis of these results suggests the following patterns:

1) Highest Pmax values were observed in May and September (up to five fold higher than in December and February);
2) □ was also generally higher in May and September. Therefore, phytoplankton was not only more productive but also more efficient in using available light;
3) □ decreased from morning to dawn, suggesting that in early morning phytoplankton cells were more efficient in using light – presumably, dark adapted;

Table WP5.3. Photosynthetic parameters *Pmax* (maximum photosynthetic rate), *Iopt* (optimal light intensity) and *Slope* (initial slope of the P-I relationship or quantum yield) estimated from the results of primary production measurements under various light intensities, conducted during the sampling campaigns. The second column indicates the incubation period in hours AM. The variance explained by all P-I curves obtained was significantly larger than the residual variance ($p < 0.05$), as tested by Analysis of Variance.

	Hours	**Pmax** (mgC mg Chla^{-1} h^{-1})	**Eopt** . mol quanta m^{-2} s^{-1})	(mgC mg Chla^{-1} h^{-1} mol quanta m^{2} s^{1})
Dec 7th	8 – 10	0.93	191.3	0.013
2003	12-12.33	1.25	238.2	0.014
	12-15	0.89	404.8	0.006
	15-17	0.57	347.5	0.004
Feb 15th	8 – 10	0.88	268.4	0.009
2004	11-13	1.16	492.5	0.006
	12-13.25	1.19	425.2	0.007
Feb 19th	8 – 10	0.86	219.6	0.011
2004	11-13	1.44	426.0	0.009
	14-16	1.01	579.5	0.005
May 22nd	7-8	2.01	436.6	0.013
2004	10-11	3.23	994.0	0.009
	13-14	2.58	999.4	0.007
	16-17	1.97	1015.3	0.005
May 26th	7-8	2.01	246.9	0.022
2004	10-11	3.69	523.3	0.019
	13-14	4.30	608.6	0.019
	16-17	5.33	762.2	0.019
Sep 1st	7 – 8	5.00	149.7	0.091
2004	12-13	5.83	414.2	0.038
	16-17	3.44	927.2	0.010
Sep 5th	7 – 8	2.86	28.27	0.275
2004	12-13	3.34	717.7	0.013
	16-17	1.61	666.5	0.007

WP4/WP5 – Implementation of a 2D vertically resolved model/ Model calibration and implementation

Introduction

This section describes the implementation of WP4 coupled with WP5. The model was implemented and tested after concluding its calibration and validation based upon the data gathered during WP2 and WP3 (Figure WP1.4).

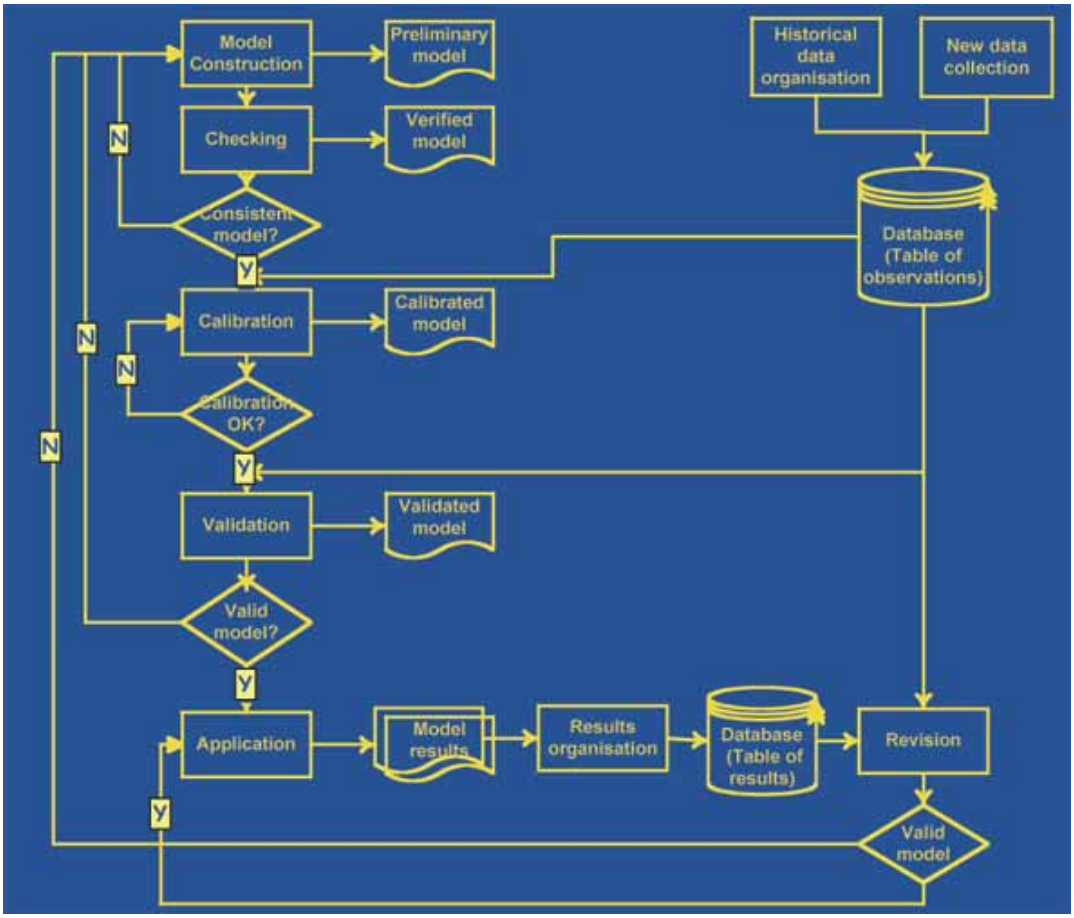

Figure WP1.4. Model flow chart.

Model conceptual and tools

The main processes and variables simulated by the model are summarized in Table WP1.4. There are feedbacks between most processes and variables. For example, water temperature depends on heat exchanges between the river, the atmosphere and other

water masses, but it also depends on the radiation budget. Phytoplankton production depends on light intensity, water temperature and nutrient concentrations. The concentration of any variable depends not only on its production and decay processes but also on transport (advection and diffusion) by river flow. Horizontal and vertical transport is calculated with a hydrodynamic 2D vertically resolved sub-model. This depends on river flow and horizontal pressure gradients due to differences in water level (barotropic pressure gradients) and density (baroclinic pressure gradients).

The model was implemented in EcoDyn – a shell for ecological modelling in windows environment (Duarte & Pereira, in prep) - following an object oriented programming methodology. Initially, it has been planned to use EcoWin (Ferreira, 1995). However, several technical difficulties in using EcoWin for coupled physical-biogeochemical modelling justified the development and implementation of EcoDyn, by the CEMAS research team. In Figure WP2.4 the model interface is shown together with some graphical outputs.

In EcoDyn, hydrodynamic transport, water temperature (Figure WP3.4), nutrients and phytoplankton are implemented though different sub-models, as classes (in object oriented programming language), written in C++ code. These classes may be plugged in or unplugged through the software interface (see the list box in Figure WP1.4. Each variable is described by a differential equation which is a mass balance including production, decay and transport processes (Table WP2.4). The variables are resolved simultaneously for each model compartment and layer and transported among them by the transport sub-model.

Table WP1.4. Main processes and variables simulated by the model. There are feedbacks between most of the processes and variables as in the real system (see text).

	Physical processes and variables			Biogeochemical processes and variables	
	Thermodynamic	Transport	Radiation balance	Nutrients	Phytoplankton
Processes	Heat exchanges between the water and the atmosphere and between different water masses	Advection and diffusion of water	Water reflection and emission and sun light absorption	Nutrient consumption and regeneration	Phytoplankton production and decay
Variables	Water temperature and density	Current velocity and flow	Light intensity as a function of depth and water turbidity	Nitrogen and phosphorus concentrations	Phytoplankton biomass

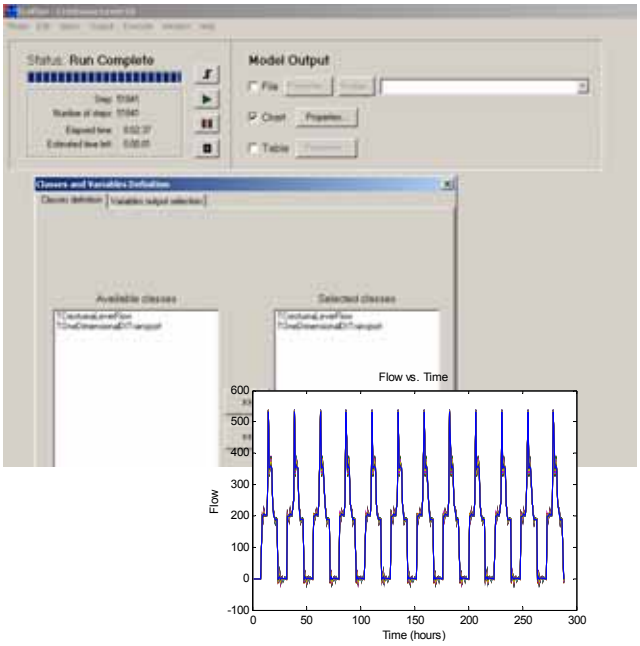

Figure WP2.4. Model interface of EcoDyn.

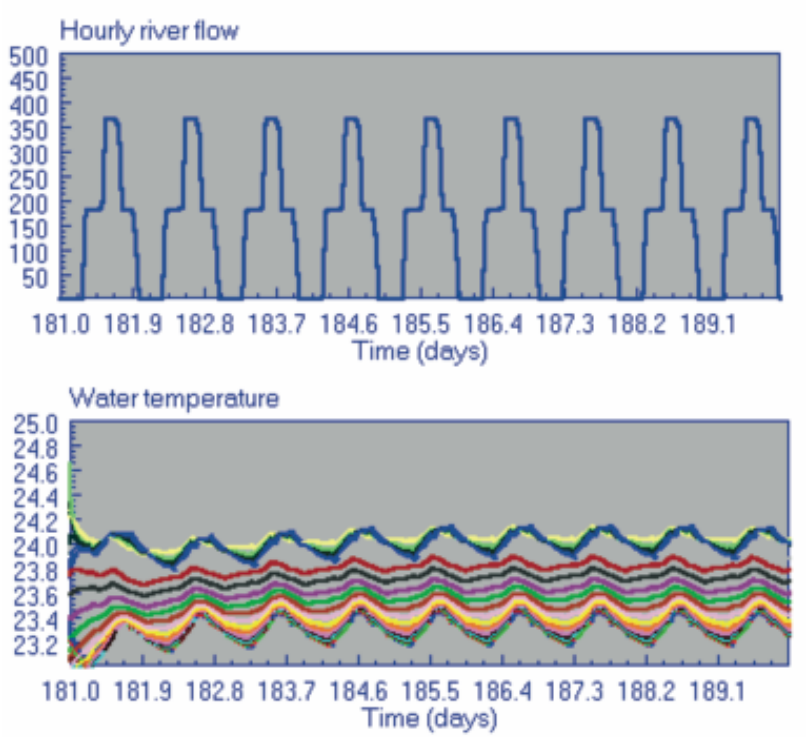

Figure WP3.4. Temporal simulations of flow and temperature for a summer situation.

The detailed equations for the 2D transport, the nutrient and the phytoplankton sub-model rate processes (the parcels of equations depicted in Table WP2.4) are presented together with the respective parameters in Annexes I and II.

Table WP2.4. Main model equations representing the changes in the state variables as a function of time. The equations are solved for all 22 model compartments and 7 layers. For details regarding current speed (transport model) refer to Annexes I and II. Note that the sinks for phytoplankton are sources for the dissolved nutrients and vice-versa. Fluxes are expressed in Carbon, Nitrogen and Phosphorus units (see text).

Current speed (m s^{-1})	
$\frac{du}{dt} = pressure\_gradient\_force \pm advection\_of\_momentum \pm diffusion\_of\_momentum \pm drag\_forces$	(WP4.1)
Water temperature changes (ºC d^{-1})	
$\frac{dT_{ij}}{dt} = solar\_radiation + atmospheric\_emission - water\_emission - latent\_heat \pm heat\_advection \pm heat\_diffusion$	(WP4.2)
Dissolved mineral nitrogen variation (μmol L^{-1} d^{-1})	
$\frac{dDIN_{ij}}{dt} = PHYRespN_{ij} + PHYExudN_{ij} + PHYMortN_{ij} + PHYSetN_{ij} + DINLoads_{ij} - PHYUptakeN_{ij} \pm Advection \pm Diffusion$ $DIN_{ij} = Nitrate_{ij} + Nitrite_{ij} + Ammonium_{ij}$	(WP4.3)
Dissolved mineral phosphorus variation (μmol L^{-1} d^{-1})	
$\frac{dP_{ij}}{dt} = PHYRespP_{ij} + PHYExudP_{ij} + PHYMortP_{ij} + PHYSetP_{ij} + PLoads_{ij} - PHYUptakeP_{ij} \pm Advection \pm Diffusion$	(WP4.4)
Phytoplankton carbon biomass changes (μg C L^{-1} d^{-1})	
$\frac{dPHYC_{ij}}{dt} = PHYC_{ij}\left(PHYGPP_{ij} - PHYExud_{ij} - PHYResp_{ij} - PHYMort_{ij} - PHYSet_{ij}\right) \pm Advection \pm Diffusion$ This is also expressed as μg Chl L^{-1} h^{-1} ($PHYChl_{ij}$) using a Carbon:Chlorophyll ratio of 50 Jørgensen & Jørgensen (1991)	(WP4.5)
Phytoplankton nitrogen biomass changes (μg N L^{-1} d^{-1})	
$\frac{dPHYN_{ij}}{dt} = PHYUptakeN_{ij} - PHYRespN_{ij} - PHYExudN_{ij} - PHYMortN_{ij} - PHYSetN_{ij} \pm Advection \pm Diffusion$	(WP4.6)
Phytoplankton phosphorus biomass changes (μg P L^{-1} d^{-1})	
$\frac{dPHYP_{ij}}{dt} = PHYUptakeP_{ij} - PHYRespP_{ij} - PHYExudP_{ij} - PHYMortP_{ij} - PHYSetP_{ij} \pm Advection \pm Diffusion$	(WP4.7)

$PHYGPP_{ij}$	Gross primary productivity	d^{-1}
$PHYExud_{ij}$	Exudation rate	
$PHYResp_{ij}$	Respiration rate	
$PHYMort_{ij}$	Mortality rate	
$PHYSet_{ij}$	Settling rate	
$PHYMortN_{ij}$	Phytoplankton mortality	$\mu mol\ N\ L^{-1}\ d^{-1}$ or $\mu g\ N\ L^{-1}\ d^{-1}$
$PHYExudN_{ij}$	Phytoplankton exudation	
$PHYRespN_{ij}$	Phytoplankton respiration	
$PHYUptakeN_{ij}$	Phytoplankton uptake	
$PHYSetN_{ij}$	Phytoplankton settling	
$PHYMortP_{ij}$	Phytoplankton mortality	$\mu mol\ P\ L^{-1}\ d^{-1}$ or $\mu g\ P\ L^{-1}\ d^{-1}$
$PHYExudP_{ij}$	Phytoplankton exudation	
$PHYRespP_{ij}$	Phytoplankton respiration	
$PHYUptakeP_{ij}$	Phytoplankton uptake	
$PHYSetP_{ij}$	Phytoplankton settling	

Note – All fluxes are referred to days except current speed, since its usual units are m s^{-1}

The Crestuma-Lever reservoir was divided in several compartments (boxes) (Figure WP4.4) each with 500 m length. In Table WP3.4, the areas, the depths and the volumes of each compartment are shown. In the model, each compartment is divided in 7 vertical layers (Figure WP5.4). The initial depth of each layer (but the bottom one) is 2.5 m, the average width and volume were estimated from frequency distributions of depths measured during a bathymetric survey. Recently, the results of this survey were loaded into a Geographical Information System (GIS), using ArcGIS 8.1, to obtain more accurate estimates of box and layer geometry (cf. - Implementation of a Geographical Information Ssytem (GIS) for accurate definition of model geometry). The 2D model represents the reservoir as a V-shaped channel divided in several compartments and layers.

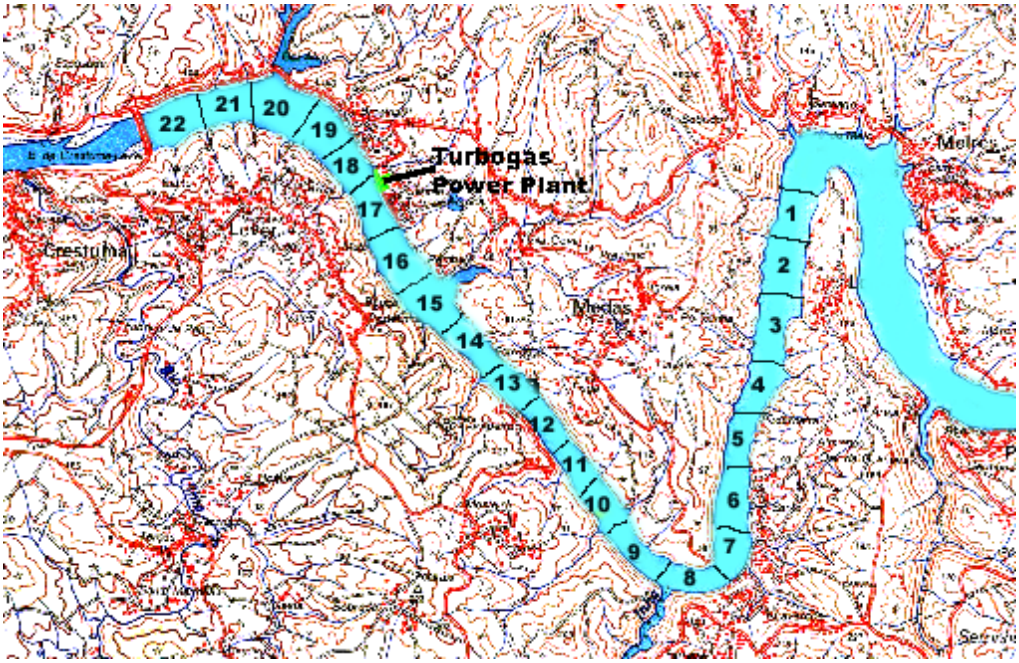

Figure WP4.4. The 22 model compartments, each with a length of 500 m (see text).

The model is forced by river flow, river temperature, nutrient and phytoplankton loads, light intensity, wind speed, cloud cover, air humidity and air temperature. There are forcing function objects in EcoDyn that read the appropriate values from files or calculate them for use by other objects. Surface light intensity and water temperature are calculated from standard formulations described in Brock (1981) and Portela & Neves (1994).

Phytoplankton light limited productivity was calculated with a depth integrated version of the Steele's equation (Steele, 1962). However, from experimental data collected during the first year of the project and experiments to describe the relationship between productivity and light intensity for the Crestuma reservoir, it is likely that other functional formulations canl also be used. Temperature limitation is considered using a standard exponential formulation. Nutrient limitation is calculated from internal cell nutrient quotas. All the involved equations, parameters and respective units are presented in Tables AII.1 and AII.2.

Table WP3.4. Model compartments and their morphology.

Compartment	Area (m^2)	Average depth (m)	Volume (m^3)
1	191423	14.3	2734375
2	233535	14.3	3335938
3	214393	14.3	3062500
4	164623	14.3	2351563
5	137824	14.3	1968750
6	156966	14.3	2242188
7	156966	14.3	2242188
8	130167	14.3	1859375
9	118682	14.3	1695313
10	130167	14.3	1859375
11	138426	14.6	2023438
12	131685	15.0	1968750
13	122567	15.6	1914063
14	111080	11.3	1257813
15	102948	11.5	1186979
16	131017	11.9	1559918
17	137664	12.5	1720806
18	133430	12.8	1707223
19	159353	13.0	2069271
20	173686	12.7	2201308
21	158579	12.7	2019643
22	142623	12.5	1789332

The analysis of previously collected data suggests that stratification is a phenomenon that can occur under particular conditions, especially during the summer low river flow discharge period. Rare situations can have very important consequences on natural ecosystems, and thus they must be carefully considered.

The model has been thoroughly tested. Herein, only an example simulation is presented, showing two flow fields along the reservoir predicted by the model forced by a river flow 0 and 350 m^3 s^{-1} (Figure WP5.4). During the day, longitudinal flows results from upstream forcing, with river water entering into the reservoir. There is a clear longitudinal flow profile, disturbed in some points by depth changes that forces upwelling of bottom water. During the night, in the absence of river flow, at it happens frequently in Spring through Fall, convective flow dominates, with surface cooled water sinking to the bottom and forcing the ascent of bottom water. Vertical flows may be larger than horizontal ones (Figure WP6.4), not because of their velocity, but because of the large surface area of

each model compartment. Therefore, even very small vertical velocities (in the order of a few mm s^{-1}) may produce large flows. These results were obtained with compartment geometry estimated from depth frequency distributions and not with the GIS (see above). The update of compartment geometry completed enabling the calibration of simulations.

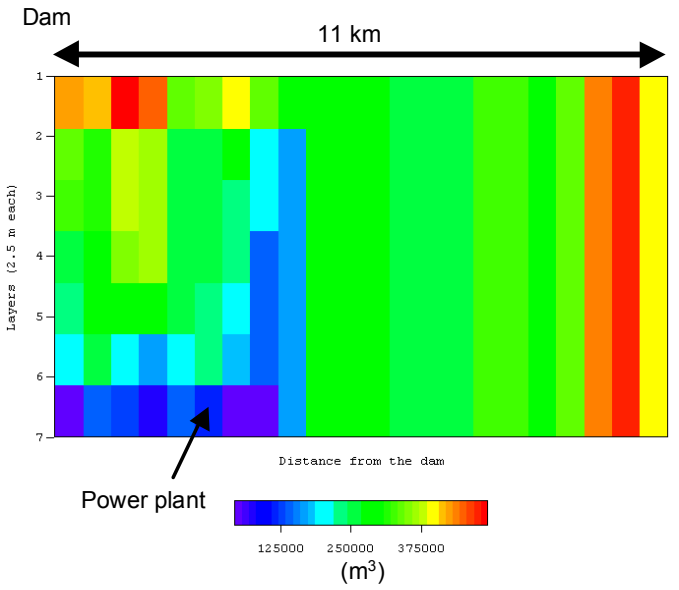

Figure WP5.4 - Bidimensional model setup. Longitudinal cross section of volumes, discretised in 7 layers and 22 columns over a horizontal distance of 11 km.
Vertical dimensions not to scale (see text).

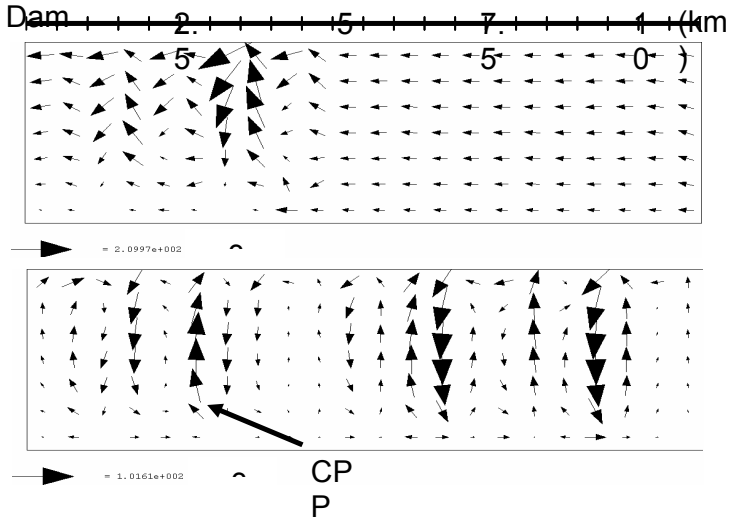

Figure WP6.4 - An example of flows predicted by the model during daytime (top), with river flow up to 350 m^3 s^{-1} and nigh time (bottom) with river flows down to zero m^3 s^{-1} (see text).

Implementation of a Geographical Information System (GIS) for accurate definition of model geometry

Introduction

The objective of this part of the work was to implement a Geographical Information System (GIS) to calculate areas and volumes of the model compartments and associate to the sampling points, bathymetric information as well as parameters of water quality. Since no geo-referred bathymetric data was available in the open literature for the Crestuma reservoir (the charts available are in Autocad and deal only with the 60-m wide navigational channel), an unscheduled bathymetric survey was carried out in a limited portion of the reservoir (see below Figure WP7.4). It should be noted that, initially, neither the bathymetric survey nor the GIS approach was stated in the initial proposal. However, the additional work (both field and data treatment) performed proved to be very useful for the project.

Procedure for the GIS elaboration

Digitalisation of the Military Chart

The first step was to acquire the Military Chart of the studied area - "Estuary of the Sousa (Gondomar)", sheet 134 of the Portugal Military Chart, series M 888, scale 1: 25000 - and proceed to its digitalization and input into the GIS as raster data.

Management of files in the ArcCatalog

With ArcCatalog it is possible to manage, create, organize and search geographic and alphanumeric data. It contains publishers to introduce metadata, a structure for the storage of these and sheets of properties to visualize the data. It also allows data conversions among different formats.

The file “carta_militar.jpg” and the file “Batimetria.dbf” of the X, Y, Z table that contains the coordinates (X, Y) of the points where the bathymetric data (Z) have been registered, were added to ArcCatalog.

In the properties of the file “carta_militar.jpg” the projected coordinate system was configured to “Lisboa Hayford Gauss IgeoE” (military coordinates).

From the table “Batimetria.dbf” a shapefile of points has been created - “Batimetria_ptos.shp”. The geographic coordinate system attributed to these points was WGS 1984 in accordance with the GPS readings.

Figure Wp4.5 represents the ArcCatalog window, where several types of introduced and/or created files can be seen.

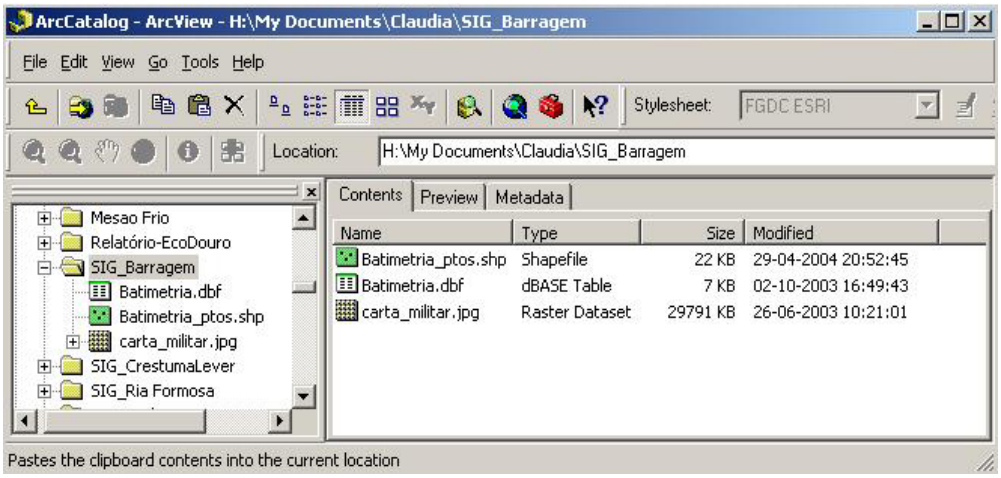

Figure WP7.4. Window of the application ArcCatalog.

Use of the ArcToolbox

The ArcToolbox is an application that contains GIS tools for geographic data processing. The shapefile of points created in the ArcCatalog, which represents the sites where bathymetric values were registered, was in the geographic coordinates system WGS 1984, but it was decided to represent all data using the military coordinate system and ArcToolbox was used to make the automatic transformation of the coordinates from one system to another.

Introduction of the data in the ArcMap

The ArcMap application is used for all tasks of creation and edition of maps as well as data analysis.

ArcMap allows to:

- Visualize geographic data;
- Identifying new standards and distributions of the geographic data;
- Create maps;
- Perform spatial analysis.

When introducing the file "carta_militar.jpg" into ArcMap, it was necessary to georeference the data, that is, to attribute known values of coordinates to points of the image. The chosen points have been the 4 edges of the map which geographic coordinates are defined in the military chart, but in the European Datum 50.

A transformation of coordinates from European Datum 50 to Military Coordinates had to be made (the transformation of coordinates was made in the website of the Instituto Geográfico do Exército: www.igeoe.pt).

Below is the correspondence between the two types of coordinates:

Table WP4.4. Correspondence between the values of the geographic coordinates of the European Datum 50 and the Military Coordinates.

	Geographic Coordinates – European Datum 50	**Millitary Coordinates**
X_1	8º30'45.''5	168001.75 m
Y_1	41º06'35.''0	459999.53 m
X_2	8º30'43.''6	168002.51 m
Y_2	41º01'10.''9	450001.00 m
X_3	8º19'19.''8	184001.38 m
Y_3	41º06'36.''7	459999.58 m
X_4	8º19'18.''8	184002.93 m
Y_4	41º01'12.''6	450001.22 m

The Georeferencing menu was used for georeferencing the military chart image. Figure WP8.4 shows, as example, the procedure made for georeferencing the upper left edge of the chart.

After georeferencing, the file “carta_militar.jpg” was added to the shapefile “Batimetria_ptos.shp”. In the ArcMap all added files (images, shapefiles, tables, etc) are added as layers.

Figure WP9.4 illustrates the general view of the ArcMap window where the layers added to the map are seen in the Table of Contents (on the left) and their graphical aspect in the Date Frame (on the right). The image of the military chart is already georeferenced and the lower part of the window shows the value of the coordinates where the cursor is going through. The points where the bathymetry was measured along the reservoir are also shown.

Figure WP8.4. Introduction of the coordinates for one of the control points.

Figure WP9.4. General view of the ArcMap window with the layers that compose the map.

Vectoring of the river margins

The next objective was vectoring the river margins, limiting the area where bathymetry has been surveyed. This area was divided in 500 m segments and 2 m layers as in the model (see above), the volumes and areas of each were estimated.

New shapefiles were created in ArcCatalog: “Eixo.shp” (line), “Pontos_divisorios.shp” (points) and “Segm01.shp”, “Segm02.shp”, “Segm03.shp”, “Segm04.shp”, “Segm05.shp”, etc. (polygons). The function of shapefiles “Eixo” and “Pontos_divisorios” was to assist in the creation of each segment.

In the ArcMap, after having added the file “Eixo.shp”, with the Editor menu and its function “Create New Feature”, a line was drawn along the centre of the riverbed in the image of the military map.

Then, the file “Pontos_divisorios.shp” was added and was selected the line drawn before. With the function “Divide” of the Editor menu was given indication to execute the task of

locating points every 500 m along the line. The result of these two operations is illustrated in Figure WP10.4.

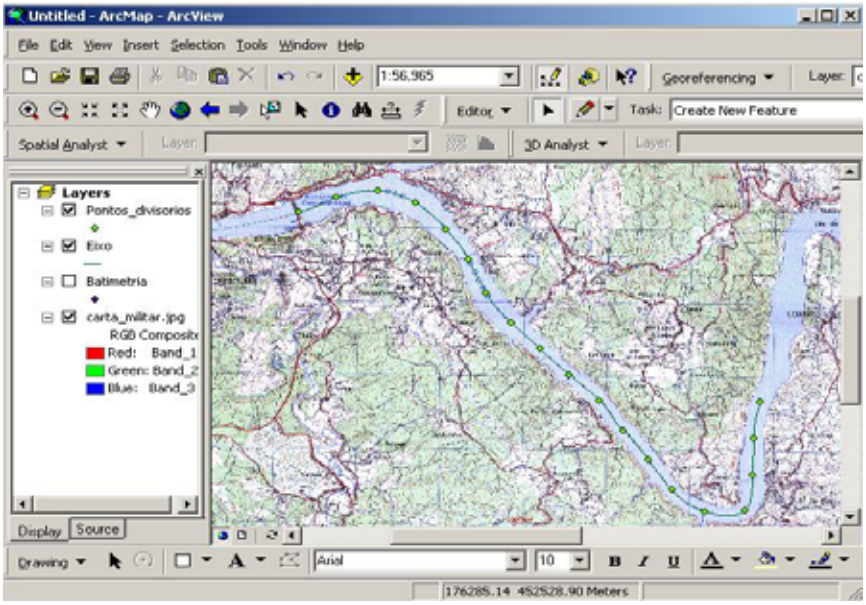

Figure WP10.4. Creation of 500 m segments along the reservoir – Line along the riverbed with points spaced 500 m from each other.

The next step was to add the file “Segm01.shp” and, once more, with the Editor menu and its function “Create New Feature” a polygon was drawn to limit the area comprised between the edges of the river and the two first dividing points of the axis-line. This procedure was repeated until the two last points, resulting in a total of 18 segments (Figure WP11.4).

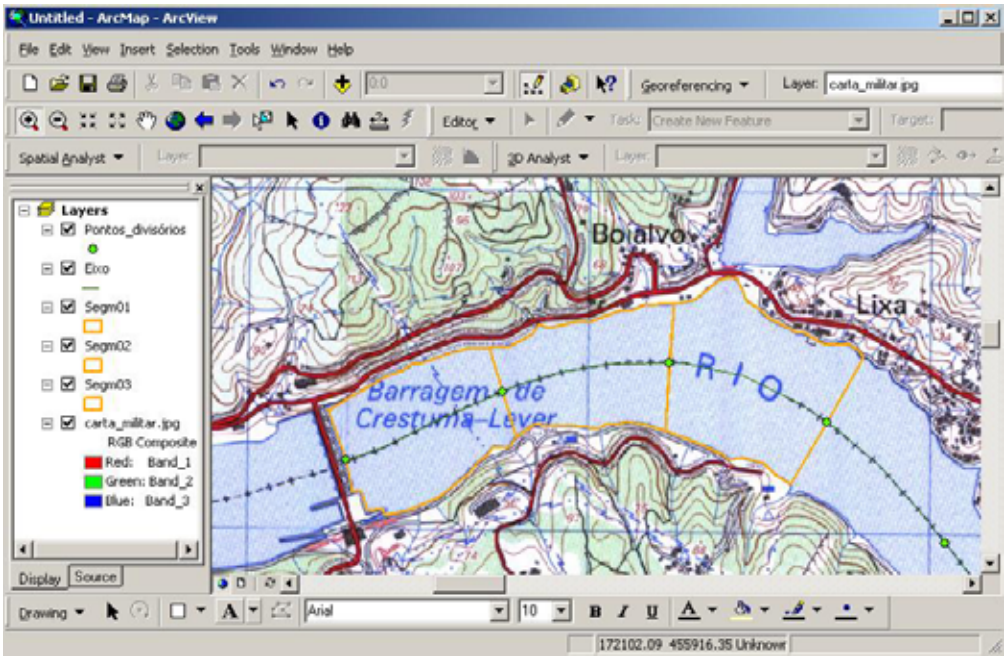

Figure WP11.4. Creation of 500 m segments along the reservoir – Example of the first three segments.

Use of the extension 3D Analyst

One of the extensions of ArcGis is 3D Analyst. Its main functions are: creation of surfaces from some several data types; interactive visualization of data in 3D; overlapping of 2D data and its visualization in 3D; etc. In the analysis component, 3D Analyst allows to create and analyse surfaces in format TIN or raster, including volumes and surface areas calculation.

Creation of surfaces in TIN format

The next step was to use the function “Create TIN” of the extension 3D Analyst to create TIN formatted surfaces in each segment. Figure WP12.4 demonstrates the surface creation for the first segment.

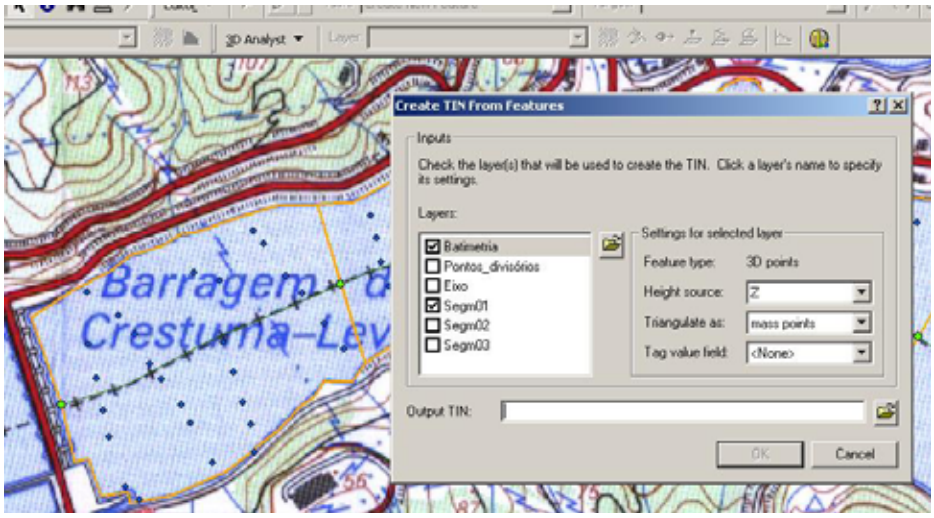

Figure WP12.4. Creation of a TIN formatted surface for the first model segment.

After having created all the surfaces in format TIN for all segments, a legend was produced. The final result is presented in Figure WP13.4.

Figure WP13.4. TIN formatted surfaces for the first three model segments and respective legend.

Creation of a scene in 3D – ArcScene

With ArcScene it is possible to create three dimension images of surfaces, with overlapped SIG information, scenes in which it is possible to navigate and interact with the data. The data overlapped in the surface can be extruded in order to simulate lines, walls and solids.

With ArcScene opened, all files TIN formatted surfaces for the model segments were added. The visualization of the data in 3D is illustrated in Figure WP14.4.

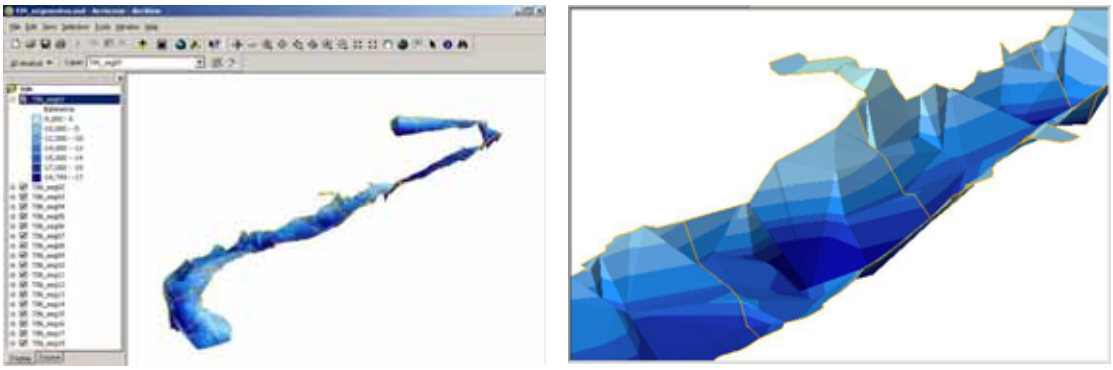

Figure WP14.4. 3D visualisation of the reservoir bathymetry and model segments. The upper figure represents a general view, whereas the lower figure represents a detailed view of some segments.

Calculation of areas and volumes

Table WP4.4 summarize the calculations done with the function Surface Analysis of the extension 3D Analyst, to estimate areas and volumes of all segments and respective 2 m layers.

Table WP4.4. Volumes and superficial areas for each 2 m depth layer of each longitudinal segment (see text).

		Segm01	Segm02	Segm03	Segm04	Segm05	Segm06	Segm07
0 – 2 (m)	**Volume (m^3)**	284320.93	303046.31	393759.71	373445.93	267085.52	287852.98	342307.63
	Sup. area (m^2)	142160.46	151523.16	196879.85	186722.97	133542.76	143926.49	171153.82
2 – 4 (m)	**Volume (m^3)**	284320.92	303046.32	393759.70	373445.93	267085.52	287852.98	342307.63
	Sup. area (m^2)	142160.46	151523.16	196879.85	186722.97	133542.76	143926.49	171153.82
4 – 6 (m)	**Volume (m^3)**	279139.89	303046.32	393759.71	373445.93	267085.52	287852.98	342307.63
	Sup. area (m^2)	142160.46	151523.16	196879.85	186722.97	133542.76	143926.49	171153.82
6 – 8 (m)	**Volume (m^3)**	241120.62	300602.66	393243.66	373445.93	265902.88	287852.98	336315.85
	Sup. area (m^2)	129450.25	151523.16	196879.85	186722.97	133542.76	143926.49	170924.72
8 – 10 (m)	**Volume (m^3)**	220691.57	287298.20	380369.86	372137.58	260628.38	284850.56	313520.43
	Sup. area (m^2)	115464.76	148378.31	196114.32	186722.97	131393.69	143926.49	163219.90
10 – 12 (m)	**Volume (m^3)**	195063.33	228246.29	251908.15	261553.84	252655.96	262225.85	281489.69
	Sup. area (m^2)	104844.96	135665.37	157768.78	173417.25	129215.21	138100.70	149707.46
12 – 14 (m)	**Volume (m^3)**	140474.42	178002.21	140989.72	130808.39	214345.69	206008.27	237507.78
	Sup. area (m^2)	86025.23	99277.38	91460.12	95651.58	119867.46	121330.36	130382.22
14 – 16 (m)	**Volume (m^3)**	58007.32	129210.66	58819.37	18426.75	155049.84	99381.86	136542.30
	Sup. area (m^2)	50351.50	77336.46	47319.44	26251.38	93376.16	79734.18	105469.16
16 – 18 (m)	**Volume (m^3)**	13485.57	73922.70	12275.87	1375.25(*)	79333.08	8420.42(*)	67088.58
	Sup. area (m^2)	13297.10	50512.83	14411.62	2746.33	59355.27	22769.90	45219.63
18 – 20 (m)	**Volume (m^3)**	544.52(*)	19792.45	358.39		13156.55(*)		32103.93
	Sup. area (m^2)	1784.70	22905.71	598.10		20459.58		23321.80
20 – 22 (m)	**Volume (m^3)**		740.67(*)	0.25(*)				11722.54
	Sup. area (m^2)		1839.98	3.80				10047.89
22 – 24 (m)	**Volume (m^3)**							1674.65
	Sup. area (m^2)							2511.97
Total volume (m^3)		1717169.09	2126954.79	2419244.39	2278085.55	2042328.95	2012298.88	2444778.36

Table WP4.4 - Continued.

		Segm08	Segm09	Segm13	Segm14	Segm15	Segm16	Segm18
0 – 2 (m)	**Volume (m^3)**	328445.08	221866.05	228088.57	201610.12	168176.92	195099.83	151648.41
	Sup. area (m^2)	164222.54	110933.02	114044.28	100805.06	84088.46	97549.91	75824,21
2 – 4 (m)	**Volume (m^3)**	323762.10	221866.05	228088.56	201610.12	168176.92	195099.83	151648.41
	Sup. area (m^2)	164222.54	110933.02	114044.28	100805.06	84088.46	97549.91	75824,21
4 – 6 (m)	**Volume (m^3)**	299363.89	221257.92	228071.32	201292.69	168176.92	195099.83	151529.29
	Sup. area (m^2)	155343.31	110933.02	114044.28	100805.06	84088.46	97549.91	75824,21
6 – 8 (m)	**Volume (m^3)**	271109.35	207870.65	226366.93	186905.03	164495.64	195099.83	144510.35
	Sup. area (m^2)	141815.14	109510.27	113934.94	99040.10	84088.46	97549.91	75432,39
8 – 10 (m)	**Volume (m^3)**	249161.83	158812.12	220375.40	16192560.81	148453.66	193581.93	128020.09
	Sup. area (m^2)	130959.12	94363.30	112030.12	87482.08	78573.16	97549.91	67962,31
10 – 12 (m)	**Volume (m^3)**	199665.18	83967.91	204378.92	132859.29	133256.81	172951.24	109958.12
	Sup. area (m^2)	115750.14	57488.60	107713.07	74120.05	69058.76	94307.46	59788,48
12 – 14 (m)	**Volume (m^3)**	122404.18	49820.56	173825.00	99667.26	113772.16	110372.20	88372.27
	Sup. area (m^2)	81283.06	31043.38	95770.30	58412.90	63699.16	76940.19	49874,33
14 – 16 (m)	**Volume (m^3)**	33155.30	32586.46	79473.83	64496.21	80032.76	48989.74	63553.90
	Sup. area (m^2)	39812.69	20037.03	73088.64	41117.34	48396.15	36399.33	38210,84
16 – 18 (m)	**Volume (m^3)**	924.09(*)	20653.64	7311.03	20552.52	49957.07	11429.22	39952.42
	Sup. area (m^2)	3358.09	12917.91	11969.17	23308.69	32105.51	13694.81	25480,80
18 – 20 (m)	**Volume (m^3)**		10226.45	59.12(*)	654.41	34847.87	906.66	19223.12
	Sup. area (m^2)		7937.09	274.50	930.35	19823.64	672.03	14869,34
20 – 22 (m)	**Volume (m^3)**		1888.66		16.39(*)	26850.85	540.25	4796.25
	Sup. area (m^2)		2603.85		56.82	15233.38	352.16	4754,00
22 – 24 (m)	**Volume (m^3)**		0.42(*)			20717.53	272.95	23.02(*)
	Sup. area (m^2)		4.25			11807.34	195.69	466,36

24 – 26 (m)	**Volume (m^3)**					15434.36	96.94	
	Sup. area (m^2)					8974.09	84.87	
26 – 28 (m)	**Volume (m^3)**					10917.83	12.18(*)	
	Sup. area (m^2)					6524.16	19.67	
28 – 30 (m)	**Volume (m^3)**					7183.69		
	Sup. area (m^2)					4457.56		
30 – 32 (m)	**Volume (m^3)**					4292.59		
	Sup. area (m^2)					2797.60		
32 – 34 (m)	**Volume (m^3)**					2259.07		
	Sup. area (m^2)					1566.45		
34 – 36 (m)	**Volume (m^3)**					1036.61		
	Sup. area (m^2)					764.09		
36 – 38 (m)	**Volume (m^3)**					331.47		
	Sup. area (m^2)					308.39		
38 – 40 (m)	**Volume (m^3)**					28.32(*)		
	Sup. area (m^2)					56.64		
Total volume (m^3)		1827991.00	1230816.89	1596038.68	1271589.85	1318399.05	1319552.63	1053235.65

Note: The volumes and areas for segments 10, 11, 12 and 17, have not been calculated, for not having points with bathymetric data inside their limits and therefore also the correspondent surfaces. The sign * that appears close to some volume values means that the layer depth is less than 2 m.

data frame

In ArcMap, a frame on the map that displays layers occupying the same geographic area. It can be one or more data frames on a map depending the data is to be organized. For instance, one data frame might highlight a study area and another might provide an overview of where the study area is located.

georeference

The process of defining how raster data is situated in map coordinates. Georeferencing raster data allows it to be viewed, queried and analysed with other geographic data.

layer

A collection of similar geographic features – such as rivers, lakes, cities, etc. – of a particular area or place for display on a map. A layer references geographic data stored in a data source and defines how to display it. Layers can be created and managed as any other type of data in a database.

raster

Represents any data source that uses a grid structure to store geographic information.

shapefile

A vector data storage format for storing the location, shape and attributes of geographic features.

TIN

Triangulated irregular network. A data structure that represents a continuous surface through a series of irregularly spaced points with values that describe the surface at that point (for example, an elevation). From these points, a network of linked triangles forms the surface.

WP6 – Data analysis and reporting

Several working meetings have been organized between the PI and the CEMAS coordinator team to evaluate and discuss the results.

According to the work plan, two interim progress reports were produced (May 2004 and December 2005). The present volume is the final report.

Up to now, one research paper was published in an international journal (BORDALO A. A, TEIXEIRA, R. & WIEBE, W.J. 2006. A water quality index applied to an international shared river basin: the case of the River Douro*. Environmental Management* 38 910–920) and one paper was published in a national scientific journal (AZEVEDO, B., DUARTE, P. & BORDALO, A.A. 2005. Análise e verificação de um modelo ecológico para a albufeira de Crestuma-Lever. *Revista da Faculdade de Ciência e Tecnologia da Universidade Fernando Pessoa*, 2: 8-25). Additionally, two BSc thesis were produced with data from ECODOURO (Azevedo, B.F.M., 2004. Análise e verificação de um modelo para a albufeira de Crestuma-Lever. Universidade Fernando Pessoa, 118pp. and Silva, R.M.B., 2005. Avaliação dos efeitos da magnitude e da variabilidade temporal dos caudais na qualidade da água da Albufeira de Crestuma-Lever. Universidade Fernando Pessoa, 73pp.)

WP7 – Web page

The ECODOURO web at http://ecodouro.icbas.up.pt is not yet full operational. It is expected to be completed during the Summer 07 in order to disseminate the information considered pertinent to the public.

References

Bordalo, A.A., Teixeira, R. & Wiebe, W.J. 2006. A water quality index applied to an international shared river basin: the case of the Douro River. *Environmental Management* 38 910–920.

Brock, T.D., 1981. Calculating solar radiation for ecological studies. *Ecological Modelling* 14 1 – 9.

Eilers, P.H.C. & J.C.H. Peeters. 1988. A model for the relationship between light intensity and the rate of photosynthesis in phytoplankton. *Ecological Modelling* 42 199-215.

Ferreira, J.G., 1995. EcoWin - an object-oriented ecological model for aquatic ecosystems. *Ecological Modelling* 79 21 - 34.

INAG. www.inag.pt

Legendre, P. & Legendre, L. (1998) Numerical ecology. Elsevier, Amsterdam

Portela, L.I. & Neves, R. (1994). Modelling temperature distribution in the shallow Tejo estuary. In: Tsakiris & Santos (ed.). Advances in Water Resources Technology and Management (pp. 457 – 463) Balkema.

Steele, J.H. 1962. Environmental control of photosynthesis in the sea. *Limnology Oceanography* 7 137-150.

Vieira, M.E.C. and Bordalo A. A. 2000. The Douro estuary (Portugal): A mesotidal salt wedge. *Oceanologica Acta* 23 585–594.

Annex I - Two dimensional vertically resolved transport Sub-model

The model is based on a 2D vertical finite differences grid (Figure AI.1). Current velocities and flows are calculated at the boundaries between the cells, whereas water properties are calculated at its centres. Surface elevation is calculated at the centre of each cell of the surface layer.

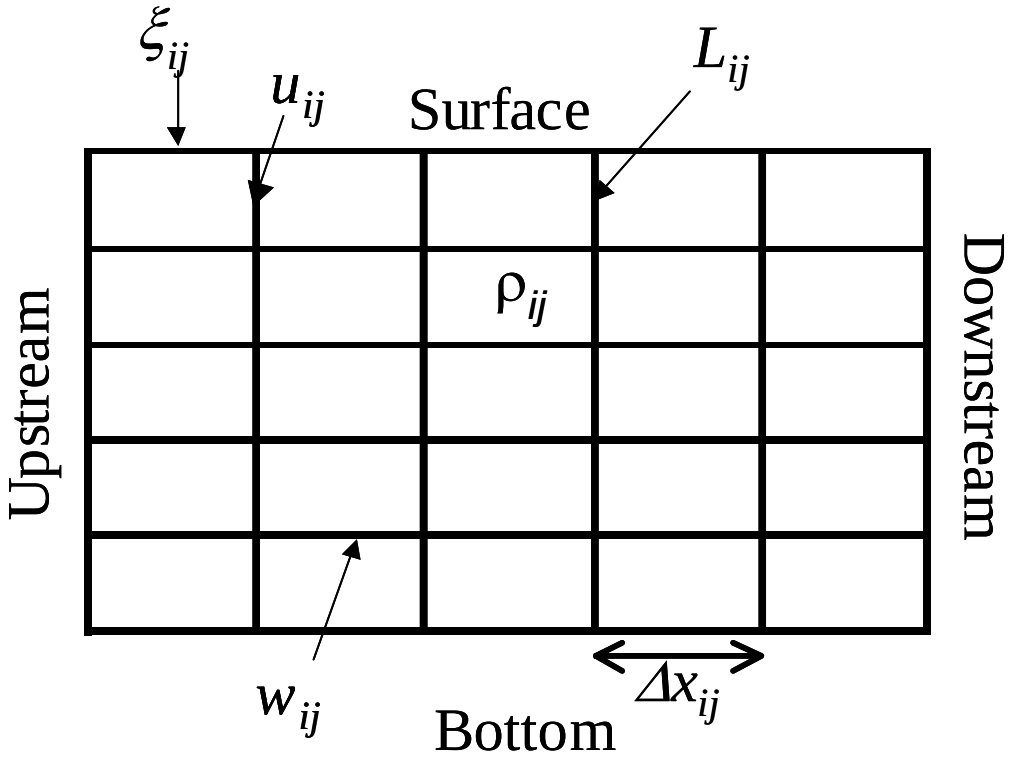

Figure AI.1 – Model grid. Horizontal (*u*) and vertical (*w*) velocities are calculated on the vertical and on the horizontal sides of the grid cells, respectively. Water elevation (ξ) is calculated at the surface of the top layer and water density (ρ) at the centre of each cell. ***i*** represents the layers and ***j*** the columns.

The basic model equations are the two dimensional versions of the equations of motion (AI.1) and continuity (AI.2) and (AI.3):

$$\frac{du_x}{dt}+\frac{\partial(uu)}{\partial x}+\frac{\partial(uw)}{\partial z}-\nu_x\frac{\partial^2 u}{\partial_x{}^2}-\nu_z\frac{\partial^2 w}{\partial_z{}^2}=-\frac{\partial P}{\rho\partial x}-\frac{Cf\,|u|u}{H}+\frac{\partial\tau_x}{\rho\partial z} \qquad \text{(AI.1)}$$

$$\frac{d\xi}{dt} = \frac{\partial u_X}{\partial x} + \frac{\partial w_Z}{\partial z} \qquad \text{(AI.2)}$$

$$\frac{\partial u_X}{\partial x} + \frac{\partial w_Z}{\partial z} = 0 \qquad \text{(AI.3)}$$

Where,

u and w – Horizontal (*x* direction) and vertical (*z* direction) current speeds (m s^{-1});
t – Time (s);
x and *z* – Horizontal and vertical distances (m);
ν_x and ν_z – Coefficients of horizontal and vertical turbulent diffusion (m^2 s^{-1});
P – Pressure (N m^{-2});
ρ – Density (kg m^{-3});
Cf – Drag coefficient;
H – Layer depth (m);
ξ – Surface elevation (m);
τ – Wind drag (N m^{-2}).

The first five terms of equation AI.1 represent the variation of flow rate over time, convection and turbulent diffusion in both directions. The right terms represent the pressure gradient, the bottom drag and the wind drag. The pressure term has two components (see below equation AI.4) – a barotropic and a baroclinic component. Equation AI.2 implies that any changes in flow rate over the river channel will produce correspondent changes in water height at the top layer, for volume conservation. These changes in water height generate the barotropic part of the pressure gradient represented in equation AI.1. The baroclinic parte results from pressure gradients caused by density variations. Equation AI.3 - a simplified form of equation AI.2 - is applied for all layers but the top one to calculate vertical velocities.

Both equations may be solved algebraically:

$$\frac{\Delta u_x}{dt}+\frac{\Delta(uuHL)}{HL\partial x}+\frac{\Delta(uwL)}{L\partial z}-\nu_x\frac{\Delta^2 u}{\Delta x^2}-\nu_z\frac{\Delta^2 w}{\Delta z^2}=-g\left(\frac{\Delta\xi}{\Delta x}+\frac{\int_{z=0}^{z}\rho_z\partial z}{\rho\Delta x}\right)-\frac{Cf\,|u|u}{H}+\frac{\Delta\tau_x}{\rho\Delta z}$$

(AI.4)

Where *L* represents cell width in m, measured at the boundaries between adjacent grid cells as velocity (see above and Figure A.1).

The convection terms include both *L* and *H* to account for the effect of geometry variability in the solution. The pressure gradient term has been decomposed in the barotropic (elevation over distance) and baroclinic (density gradient) components.

The stability analysis described in Santos (1995) and Martins (1999) suggests that all terms of equation (AI.4) may be solved explicitly, except the barotropic pressure, the vertical diffusion and the bottom drag terms (hereafter terms in *t+1*) that should be solved implicitly (equations AI.5, AI.6). The numerical solution of AI.4 varies according to whether ***i*** is a surface, intermediate or bottom layer.

(i) Intermediate layers:

$$\frac{u_{ij}^{t+1}-u_{ij}^{t}}{\Delta t}+\frac{1}{L_{ij}\left(H_{ij}^{t}+H_{ij-1}^{t}\right)}\left[\begin{array}{l}\dfrac{L_{ij+1/2}H_{ij}^{t}\left(u_{ij+1/2}^{t}+\left|u_{ij+1/2}^{t}\right|\right)u_{ij}^{t}-L_{ij-1/2}H_{ij-1}^{t}\left(u_{ij-1/2}^{t}+\left|u_{ij-1/2}^{t}\right|\right)u_{ij-1}^{t}}{\Delta x_{ij-1/2}}+\\ \dfrac{L_{ij+1/2}H_{ij}^{t}\left(u_{ij+1/2}^{t}-\left|u_{ij+1/2}^{t}\right|\right)u_{ij+1}^{t}-L_{ij-1/2}H_{ij-1}^{t}\left(u_{ij-1/2}^{t}-\left|u_{ij-1/2}^{t}\right|\right)u_{ij}^{t}}{\Delta x_{ij-1/2}}\end{array}\right]$$

$$+\frac{1}{\left(L_{i+1/2\,j}+L_{i-1/2\,j}\right)}\left[\begin{array}{l}\dfrac{L_{i+1/2\,j}\left(w_{i+1\,j-1/2}^{\,t-1/2}+\left|w_{i+1\,j-1/2}^{\,t-1/2}\right|\right)u_{ij}^{t}-L_{i-1/2\,j}\left(w_{ij-1/2}^{\,t-1/2}+\left|w_{ij-1/2}^{\,t-1/2}\right|\right)u_{i-1\,j}^{t}}{\Delta z_{ij}}+\\ \dfrac{L_{i+1/2\,j}\left(w_{i+1\,j-1/2}^{\,t-1/2}-\left|w_{i+1\,j-1/2}^{\,t-1/2}\right|\right)u_{i+1\,j}^{t}-L_{i-1/2\,j}\left(w_{ij-1/2}^{\,t-1/2}-\left|w_{ij-1/2}^{\,t-1/2}\right|\right)u_{ij}^{t}}{\Delta z_{ij}}\end{array}\right]=$$

$$-g\left(\frac{\xi_{ij}^{\,t+1/2}-\xi_{ij-1}^{\,t+1/2}}{\Delta x_{ij-1/2}}+\frac{\sum_{k=0}^{k=surflayer}\left(\rho_{kj}-\rho_{kj-1}\right)\left(H_{kj}^{t}+H_{kj-1}^{t}\right)/2}{\left(\rho_{ij}+\rho_{ij-1}\right)/2\,\Delta x_{ij-1/2}}\right)$$

$$+\frac{\nu_x}{\Delta x_{ij}^{2}}\left(u_{ij+1}^{t}-u_{ij}^{t}\right)-\frac{\nu_x}{\Delta x_{ij-1}^{2}}\left(u_{ij}^{t}-u_{ij-1}^{t}\right)+\frac{\nu_{i+1\,j}}{\Delta z_{ij+1/2}^{2}}\left(u_{i+1\,j}^{t+1}-u_{ij}^{t+1}\right)-\frac{\nu_{ij}}{\Delta z_{i-1\,j+1/2}^{2}}\left(u_{ij}^{t+1}-u_{i-1\,j}^{t+1}\right)$$

(AI.5)

Equation (AI.5) may be rearranged in order to obtain a tridiagonal system with coefficients *a*, *b*, *c* and *r*, that may be solved for *u* in *t+1* (AI.6 and AI.7). The system is represented in (AI.8). It may be solved by matrix inversion and multiplication using very efficient algorithms, like Tridag (Press et al., 1992).

$$-\frac{\Delta t\nu_{ij}}{\Delta z^2_{i-1\,j+1/2}}u^{t+1}_{i-1\,j}+u^{t+1}_{ij}+\frac{\Delta t\nu_{ij}}{\Delta z^2_{i-1\,j+1/2}}u^{t+1}_{ij}+\frac{\Delta t\nu_{i+1\,j}}{\Delta z^2_{ij+1/2}}u^{t+1}_{ij}-\frac{\Delta t\nu_{i+1\,j}}{\Delta z^2_{ij+1/2}}u^{t+1}_{i+1\,j}=u^{t}_{ij}$$

$$-\frac{\Delta t}{L_{ij}\left(H^t_{ij}+H^t_{ij-1}\right)}\left[\begin{array}{l}\dfrac{L_{ij+1/2}H^t_{ij}\left(u^t_{ij+1/2}+\left|u^t_{ij+1/2}\right|\right)u^t_{ij}-L_{ij-1/2}H^t_{ij-1}\left(u^t_{ij-1/2}+\left|u^t_{ij-1/2}\right|\right)u^t_{ij-1}}{\Delta x_{ij-1/2}}+\\ \dfrac{L_{ij+1/2}H^t_{ij}\left(u^t_{ij+1/2}-\left|u^t_{ij+1/2}\right|\right)u^t_{ij+1}-L_{ij-1/2}H^t_{ij-1}\left(u^t_{ij-1/2}-\left|u^t_{ij-1/2}\right|\right)u^t_{ij}}{\Delta x_{ij-1/2}}\end{array}\right]$$

$$-\frac{\Delta t}{\left(L_{i+1/2\,j}+L_{i-1/2\,j}\right)}\left[\begin{array}{l}\dfrac{L_{i+1/2\,j}\left(w^{t-1/2}_{i+1\,j-1/2}+\left|w^{t-1/2}_{i+1\,j-1/2}\right|\right)u^t_{ij}-L_{i-1/2\,j}\left(w^{t-1/2}_{ij-1/2}+\left|w^{t-1/2}_{ij-1/2}\right|\right)u^t_{i-1\,j}}{\Delta z_{ij}}+\\ \dfrac{L_{i+1/2\,j}\left(w^{t-1/2}_{i+1\,j-1/2}-\left|w^{t-1/2}_{i+1\,j-1/2}\right|\right)u^t_{i+1\,j}-L_{i-1/2\,j}\left(w^{t-1/2}_{ij-1/2}-\left|w^{t-1/2}_{ij-1/2}\right|\right)u^t_{ij}}{\Delta z_{ij}}\end{array}\right]$$

$$-g\Delta t\left(\frac{\xi^{t+1/2}_{ij}-\xi^{t+1/2}_{ij-1}}{\Delta x_{ij-1/2}}+\frac{\sum_{k=0}^{k=surflayer}\left(\rho_{kj}-\rho_{kj-1}\right)\left(H^t_{kj}+H^t_{kj-1}\right)/2}{\left(\rho_{ij}+\rho_{ij-1}\right)/2\,\Delta x_{ij-1/2}}\right)$$

$$+\frac{\nu_x}{\Delta x^2_{ij}}\left(u^t_{ij+1}-u^t_{ij}\right)-\frac{\nu_x}{\Delta x^2_{ij-1}}\left(u^t_{ij}-u^t_{ij-1}\right)$$

(AI.6)

$$a_{ij}u^{t+1}_{i-1\,j}+b_{ij}u^{t+1}_{ij}+c_{ij}u^{t+1}_{i+1\,j}=r_{ij}$$

$$a_{ij}=-\frac{\Delta t\nu_{ij}}{\Delta z^2_{i-1\,j+1/2}}$$

$$b_{ij}=1+\frac{\Delta t\nu_{ij}}{\Delta z^2_{i-1\,j+1/2}}+\frac{\Delta t\nu_{i+1\,j}}{\Delta z^2_{ij+1/2}}\qquad\text{(AI.7)}$$

$$c_{ij}=-\frac{\Delta t\nu_{i+1\,j}}{\Delta z^2_{ij+1/2}}$$

$$\begin{vmatrix}b_{ij} & c_{ij} & \cdots & \cdots\\ a_{ij} & b_{ij} & c_{ij} & \cdots\\ \cdots & \cdots & \cdots & \cdots\\ \cdots & \cdots & a_{ij} & b_{ij}\end{vmatrix}\begin{vmatrix}u^{t+1}_{ij}\\ \cdots\\ \cdots\\ \cdots\end{vmatrix}=\begin{vmatrix}r_{ij}\\ \cdots\\ \cdots\\ \cdots\end{vmatrix}\qquad\text{(AI.8)}$$

(ii) Bottom layer:

At the bottom layer it is necessary to consider bottom drag (last term on the right side of AI.9.

$$\frac{u_{ij}^{t+1}-u_{ij}^{t}}{\Delta t}+\frac{1}{L_{ij}\left(H_{ij}^{t}+H_{ij-1}^{t}\right)}\left[\begin{array}{l}\dfrac{L_{ij+1/2}H_{ij}^{t}\left(u_{ij+1/2}^{t}+\left|u_{ij+1/2}^{t}\right|\right)u_{ij}^{t}-L_{ij-1/2}H_{ij-1}^{t}\left(u_{ij-1/2}^{t}+\left|u_{ij-1/2}^{t}\right|\right)u_{ij-1}^{t}}{\Delta x_{ij-1/2}}+\\ \dfrac{L_{ij+1/2}H_{ij}^{t}\left(u_{ij+1/2}^{t}-\left|u_{ij+1/2}^{t}\right|\right)u_{ij+1}^{t}-L_{ij-1/2}H_{ij-1}^{t}\left(u_{ij-1/2}^{t}-\left|u_{ij-1/2}^{t}\right|\right)u_{ij}^{t}}{\Delta x_{ij-1/2}}\end{array}\right]$$

$$+\frac{1}{\left(L_{i+1/2\,j}+L_{i-1/2\,j}\right)}\left[\begin{array}{l}\dfrac{L_{i+1/2\,j}\left(w_{i+1\,j-1/2}^{t-1/2}+\left|w_{i+1\,j-1/2}^{t-1/2}\right|\right)u_{ij}^{t}-L_{i-1/2\,j}\left(w_{ij-1/2}^{t-1/2}+\left|w_{ij-1/2}^{t-1/2}\right|\right)u_{i-1\,j}^{t}}{\Delta z_{ij}}+\\ \dfrac{L_{i+1/2\,j}\left(w_{i+1\,j-1/2}^{t-1/2}-\left|w_{i+1\,j-1/2}^{t-1/2}\right|\right)u_{i+1\,j}^{t}-L_{i-1/2\,j}\left(w_{ij-1/2}^{t-1/2}-\left|w_{ij-1/2}^{t-1/2}\right|\right)u_{ij}^{t}}{\Delta z_{ij}}\end{array}\right]=$$

$$-g\left(\frac{\xi_{ij}^{t+1/2}-\xi_{ij-1}^{t+1/2}}{\Delta x_{ij-1/2}}+\frac{\sum_{k=0}^{k=surflayer}\left(\rho_{kj}-\rho_{kj-1}\right)\left(H_{kj}^{t}+H_{kj-1}^{t}\right)/2}{\left(\rho_{ij}+\rho_{ij-1}\right)/2\,\Delta x_{ij-1/2}}\right)$$

$$+\frac{\nu_x}{\Delta x_{ij}^{2}}\left(u_{ij+1}^{t}-u_{ij}^{t}\right)-\frac{\nu_x}{\Delta x_{ij-1}^{2}}\left(u_{ij}^{t}-u_{ij-1}^{t}\right)+\frac{\nu_{i+1\,j}}{\Delta z_{ij+1/2}^{2}}\left(u_{i+1\,j}^{t+1}-u_{ij}^{t+1}\right)$$

$$-\frac{1}{H_{ij}^{t}+H_{ij-1}^{t}}\left(Cf_{ij}+Cf_{ij-1}\right)\left|u_{ij}^{t}\right|u_{ij}^{t+1}$$

(AI.9)

Again, this equation is rearranged in order to obtain a tridiagonal system (AI.10 and AI.11). However, due to stability criteria (see above) the bottom drag term is solved implicitly, reason why it is on the left side of AI.10.

$$u_{ij}^{t+1}\left(1+\frac{\Delta t}{H_{ij}^{t}+H_{ij-1}^{t}}\left(Cf_{ij}+Cf_{ij-1}\right)\left|u_{ij}^{t}\right|\right)+u_{ij}^{t+1}\frac{\Delta t\nu_{i+1j}}{\Delta z_{ij+1/2}^{2}}-u_{i+1j}^{t+1}\frac{\Delta t\nu_{i+1j}}{\Delta z_{ij+1/2}^{2}}=$$

$$u_{ij}^{t}-\frac{\Delta t}{L_{ij}\left(H_{ij}^{t}+H_{ij-1}^{t}\right)}\left[\begin{array}{l}\dfrac{L_{ij+1/2}H_{ij}^{t}\left(u_{ij+1/2}^{t}+\left|u_{ij+1/2}^{t}\right|\right)u_{ij}^{t}-L_{ij-1/2}H_{ij-1}^{t}\left(u_{ij-1/2}^{t}+\left|u_{ij-1/2}^{t}\right|\right)u_{ij-1}^{t}}{\Delta x_{ij-1/2}}+\\ \dfrac{L_{ij+1/2}H_{ij}^{t}\left(u_{ij+1/2}^{t}-\left|u_{ij+1/2}^{t}\right|\right)u_{ij+1}^{t}-L_{ij-1/2}H_{ij-1}^{t}\left(u_{ij-1/2}^{t}-\left|u_{ij-1/2}^{t}\right|\right)u_{ij}^{t}}{\Delta x_{ij-1/2}}\end{array}\right]$$

$$-\frac{\Delta t}{\left(L_{i+1/2j}+L_{i-1/2j}\right)}\left[\begin{array}{l}\dfrac{L_{i+1/2j}\left(w_{i+1j-1/2}^{t-1/2}+\left|w_{i+1j-1/2}^{t-1/2}\right|\right)u_{ij}^{t}-L_{i-1/2j}\left(w_{ij-1/2}^{t-1/2}+\left|w_{ij-1/2}^{t-1/2}\right|\right)u_{i-1j}^{t}}{\Delta z_{ij}}+\\ \dfrac{L_{i+1/2j}\left(w_{i+1j-1/2}^{t-1/2}-\left|w_{i+1j-1/2}^{t-1/2}\right|\right)u_{i+1j}^{t}-L_{i-1/2j}\left(w_{ij-1/2}^{t-1/2}-\left|w_{ij-1/2}^{t-1/2}\right|\right)u_{ij}^{t}}{\Delta z_{ij}}\end{array}\right]-$$

$$-g\Delta t\left(\frac{\xi_{ij}^{t+1/2}-\xi_{ij-1}^{t+1/2}}{\Delta x_{ij-1/2}}+\frac{\sum_{k=0}^{k=surflayer}\left(\rho_{kj}-\rho_{kj-1}\right)\left(H_{kj}^{t}+H_{kj-1}^{t}\right)/2}{\left(\rho_{ij}+\rho_{ij-1}\right)/2\,\Delta x_{ij-1/2}}\right)+\frac{\nu_x}{\Delta x_{ij}^{2}}\left(u_{ij+1}^{t}-u_{ij}^{t}\right)-\frac{\nu_x}{\Delta x_{ij-1}^{2}}\left(u_{ij}^{t}-u_{ij-1}^{t}\right)$$

(AI.10)

$$a_{ij}u_{i-1j}^{t+1}+b_{ij}u_{ij}^{t+1}+c_{ij}u_{i+1j}^{t+1}=r_{ij}$$

$$a_{ij}=0$$

$$b_{ij}=\left(1+\frac{\Delta t}{H_{ij}^{t}+H_{ij-1}^{t}}\left(Cf_{ij}+Cf_{ij-1}\right)\left|u_{ij}^{t}\right|\right)+\frac{\Delta t\nu_{i+1j}}{\Delta z_{ij+1/2}^{2}}\qquad\text{(AI.11)}$$

$$c_{ij}=-\frac{\Delta t\nu_{i+1j}}{\Delta z_{ij+1/2}^{2}}$$

(iii) Upper layer:

At the upper layer it is necessary to consider the wind drag (last term on the right side of AI.12.

$$\frac{u_{ij}^{t+1}-u_{ij}^{t}}{\Delta t}+\frac{1}{L_{ij}\left(H_{ij}^{t}+H_{ij-1}^{t}\right)}\left[\begin{array}{l}\dfrac{L_{ij+1/2}H_{ij}^{t}\left(u_{ij+1/2}^{t}+\left|u_{ij+1/2}^{t}\right|\right)u_{ij}^{t}-L_{ij-1/2}H_{ij-1}^{t}\left(u_{ij-1/2}^{t}+\left|u_{ij-1/2}^{t}\right|\right)u_{ij-1}^{t}}{\Delta x_{ij-1/2}}+\\ \dfrac{L_{ij+1/2}H_{ij}^{t}\left(u_{ij+1/2}^{t}-\left|u_{ij+1/2}^{t}\right|\right)u_{ij+1}^{t}-L_{ij-1/2}H_{ij-1}^{t}\left(u_{ij-1/2}^{t}-\left|u_{ij-1/2}^{t}\right|\right)u_{ij}^{t}}{\Delta x_{ij-1/2}}\end{array}\right]$$

$$+\frac{1}{\left(L_{i+1/2\,j}+L_{i-1/2\,j}\right)}\left[\begin{array}{l}\dfrac{L_{i+1/2\,j}\left(w_{i+1\,j-1/2}^{t-1/2}+\left|w_{i+1\,j-1/2}^{t-1/2}\right|\right)u_{ij}^{t}-L_{i-1/2\,j}\left(w_{ij-1/2}^{t-1/2}+\left|w_{ij-1/2}^{t-1/2}\right|\right)u_{i-1\,j}^{t}}{\Delta z_{ij}}+\\ \dfrac{L_{i+1/2\,j}\left(w_{i+1\,j-1/2}^{t-1/2}-\left|w_{i+1\,j-1/2}^{t-1/2}\right|\right)u_{i+1\,j}^{t}-L_{i-1/2\,j}\left(w_{ij-1/2}^{t-1/2}-\left|w_{ij-1/2}^{t-1/2}\right|\right)u_{ij}^{t}}{\Delta z_{ij}}\end{array}\right]=$$

$$-g\left(\frac{\xi_{ij}^{t+1/2}-\xi_{ij-1}^{t+1/2}}{\Delta x_{ij-1/2}}+\frac{\sum_{k=0}^{k=surflayer}\left(\rho_{kj}-\rho_{kj-1}\right)\left(H_{kj}^{t}+H_{kj-1}^{t}\right)/2}{\left(\rho_{ij}+\rho_{ij-1}\right)/2\,\Delta x_{ij-1/2}}\right)$$

$$+\frac{\nu_x}{\Delta x_{ij}^{2}}\left(u_{ij+1}^{t}-u_{ij}^{t}\right)-\frac{\nu_x}{\Delta x_{ij-1}^{2}}\left(u_{ij}^{t}-u_{ij-1}^{t}\right)-\frac{\nu_{ij}}{\Delta z_{i-1\,j+1/2}^{2}}\left(u_{ij}^{t+1}-u_{i-1\,j}^{t+1}\right)+\frac{\tau_{j}^{vento}}{\rho\Delta z_{ij}}$$

(AI.12)

$$u_{ij}^{t+1}+\frac{\Delta t\nu_{ij}}{\Delta z_{i-1\,j+1/2}^{2}}\left(u_{ij}^{t+1}-u_{i-1\,j}^{t+1}\right)=$$

$$u_{ij}^{t}-\frac{\Delta t}{L_{ij}\left(H_{ij}^{t}+H_{ij-1}^{t}\right)}\left[\begin{array}{l}\dfrac{L_{ij+1/2}H_{ij}^{t}\left(u_{ij+1/2}^{t}+\left|u_{ij+1/2}^{t}\right|\right)u_{ij}^{t}-L_{ij-1/2}H_{ij-1}^{t}\left(u_{ij-1/2}^{t}+\left|u_{ij-1/2}^{t}\right|\right)u_{ij-1}^{t}}{\Delta x_{ij-1/2}}+\\ \dfrac{L_{ij+1/2}H_{ij}^{t}\left(u_{ij+1/2}^{t}-\left|u_{ij+1/2}^{t}\right|\right)u_{ij+1}^{t}-L_{ij-1/2}H_{ij-1}^{t}\left(u_{ij-1/2}^{t}-\left|u_{ij-1/2}^{t}\right|\right)u_{ij}^{t}}{\Delta x_{ij-1/2}}\end{array}\right]$$

$$-\frac{\Delta t}{\left(L_{i+1/2\,j}+L_{i-1/2\,j}\right)}\left[\begin{array}{l}\dfrac{L_{i+1/2\,j}\left(w_{i+1\,j-1/2}^{t-1/2}+\left|w_{i+1\,j-1/2}^{t-1/2}\right|\right)u_{ij}^{t}-L_{i-1/2\,j}\left(w_{ij-1/2}^{t-1/2}+\left|w_{ij-1/2}^{t-1/2}\right|\right)u_{i-1\,j}^{t}}{\Delta z_{ij}}+\\ \dfrac{L_{i+1/2\,j}\left(w_{i+1\,j-1/2}^{t-1/2}-\left|w_{i+1\,j-1/2}^{t-1/2}\right|\right)u_{i+1\,j}^{t}-L_{i-1/2\,j}\left(w_{ij-1/2}^{t-1/2}-\left|w_{ij-1/2}^{t-1/2}\right|\right)u_{ij}^{t}}{\Delta z}\end{array}\right]$$

$$-g\Delta t\left(\frac{\xi_{ij}^{t+1/2}-\xi_{ij-1}^{t+1/2}}{\Delta x_{ij-1/2}}+\frac{\sum_{k=0}^{k=surflayer}\left(\rho_{kj}-\rho_{kj-1}\right)\left(H_{kj}^{t}+H_{kj-1}^{t}\right)/2}{\left(\rho_{ij}+\rho_{ij-1}\right)/2\,\Delta x_{ij-1/2}}\right)$$

$$+\frac{\nu_x}{\Delta x_{ij}^{2}}\left(u_{ij+1}^{t}-u_{ij}^{t}\right)-\frac{\nu_x}{\Delta x_{ij-1}^{2}}\left(u_{ij}^{t}-u_{ij-1}^{t}\right)+\frac{\Delta t\tau_{j}^{vento}}{\rho\Delta z_{ij}}$$

(AI.13)

$$a_{ij}u_{i-1\,j}^{t+1} + b_{ij}u_{ij}^{t+1} + c_{ij}u_{i+1\,j}^{t+1} = r_{ij}$$

$$a_{ij} = -\frac{\Delta t \nu_{ij}}{\Delta z_{i-1\,j+1/2}^{2}}$$

$$b_{ij} = 1 + \frac{\Delta t \nu_{ij}}{\Delta z_{i-1\,j+1/2}^{2}} \qquad \text{(AI.14)}$$

$$c_{ij} = 0$$

Again, this equation is rearranged in order to obtain a tridiagonal system (AI.12 and AI.13). The three different solutions of the terms *a*, *b*, *c* and *r* (equations AI.7, AI.11 and AI.14) are applied according to the type of layers.

The numerical version of the equation of continuity (AI.2) is presented in (AI.15). The elevation is calculated from the difference between the total inflows and the total outflows of each grid column, making unnecessary to know the values of vertical velocities at this point. The terms "*FlowInput*" and "*FlowOutput*" are included to account for any water discharges and uptakes.

$$\xi_{ij}^{t+1/2} = \xi_{ij}^{t} + \Delta t \sum_{i=ibottom}^{surface} \left(\begin{array}{c} \frac{u_{ij}^{t+1}\left(H_{ij}^{t} + H_{ij-1}^{t}\right)L_{ij} + u_{ij}^{t}\left(H_{ij}^{t} + H_{ij-1}^{t}\right)L_{ij}}{4\Delta x_{j} L_{j+1/2}} - \\ \frac{u_{ij+1}^{t+1}\left(H_{ij}^{t} + H_{ij+1}^{t}\right)L_{ij+1} + u_{ij+1}^{t}\left(H_{ij}^{t} + H_{ij+1}^{t}\right)L_{ij+1}}{4\Delta x_{j} L_{j+1/2}} \end{array} \right)$$

$$+\Delta t \sum_{i=ibottom}^{surface} \left(\frac{FlowInput_{ij} - FlowOutput_{ij}}{\Delta x_{j} L_{j+1/2}} \right) =$$

$$+\frac{\Delta t}{4\Delta x_{j} L_{j+1/2}} \left[\sum_{i=ibottom}^{surface} \left(u_{ij}^{t+1}\left(H_{ij}^{t} + H_{ij-1}^{t}\right)L_{ij} \right) + \sum_{i=ibottom}^{surface} \left(u_{ij}^{t}\left(H_{ij}^{t} + H_{ij-1}^{t}\right)L_{ij} \right) \right]$$

$$-\frac{\Delta t}{4\Delta x_{j} L_{j+1/2}} \left[\sum_{i=ibottom}^{surface} \left(u_{ij+1}^{t+1}\left(H_{ij}^{t} + H_{ij+1}^{t}\right)L_{ij+1} \right) - \sum_{i=ibottom}^{surface} \left(u_{ij+1}^{t}\left(H_{ij}^{t} + H_{ij+1}^{t}\right)L_{ij+1} \right) \right]$$

$$+\Delta t \sum_{i=ibottom}^{surface} \left(\frac{FlowInput_{ij} - FlowOutput_{ij}}{\Delta x_{j} L_{j+1/2}} \right)$$

(AI.15)

The velocity terms in *t+1* may be obtained by solving equations AI.5, AI.9 and AI.12 for u_{ij}^{t+1} and summing them over each column obtaining (AI.16). The vertical diffusion terms cancel each others and it is possible to obtain an equation for u^{t+1} to use in (AI.15).

$$\sum_{i=ibottom}^{isurface}\left[u_{ij}^{t+1}L_{ij}\left(H_{ij}^{t}+H_{ij-1}^{t}\right)\right]=\sum_{i=ibottom}^{isurface}\left[u_{ij}^{t}L_{ij}\left(H_{ij}^{t}+H_{ij-1}^{t}\right)\right]$$

$$+\Delta t\left[\begin{array}{l}\dfrac{L_{ij+1/2}H_{ij}^{t}\left(u_{ij+1/2}^{t}+\left|u_{ij+1/2}^{t}\right|\right)u_{ij}^{t}-L_{ij-1/2}H_{ij-1}^{t}\left(u_{ij-1/2}^{t}+\left|u_{ij-1/2}^{t}\right|\right)u_{ij-1}^{t}}{\Delta x_{ij-1/2}}+\\ \dfrac{L_{ij+1/2}H_{ij}^{t}\left(u_{ij+1/2}^{t}-\left|u_{ij+1/2}^{t}\right|\right)u_{ij+1}^{t}-L_{ij-1/2}H_{ij-1}^{t}\left(u_{ij-1/2}^{t}-\left|u_{ij-1/2}^{t}\right|\right)u_{ij}^{t}}{\Delta x_{ij-1/2}}\end{array}\right]$$

$$-\sum_{i=ibottom}^{isurface}\left[\begin{array}{l}-\dfrac{\Delta t L_{ij}\left(H_{ij}^{t}+H_{ij-1}^{t}\right)}{\left(L_{i+1/2\,j}+L_{i-1/2\,j}\right)}\\ \left[\begin{array}{l}\dfrac{L_{i+1/2\,j}\left(w_{i+1\,j-1/2}^{t-1/2}+\left|w_{i+1\,j-1/2}^{t-1/2}\right|\right)u_{ij}^{t}-L_{i-1/2\,j}\left(w_{ij-1/2}^{t-1/2}+\left|w_{ij-1/2}^{t-1/2}\right|\right)u_{i-1\,j}^{t}}{\Delta z_{ij}}+\\ \dfrac{L_{i+1/2\,j}\left(w_{i+1\,j-1/2}^{t-1/2}-\left|w_{i+1\,j-1/2}^{t-1/2}\right|\right)u_{i+1\,j}^{t}-L_{i-1/2\,j}\left(w_{ij-1/2}^{t-1/2}-\left|w_{ij-1/2}^{t-1/2}\right|\right)u_{ij}^{t}}{\Delta z_{ij}}\end{array}\right]\end{array}\right]$$

$$-g\Delta t\sum_{i=ibottom}^{isurface}\left(\begin{array}{l}L_{ij}\left(H_{ij}^{t}+H_{ij-1}^{t}\right)\dfrac{\xi_{ij}^{t+1/2}-\xi_{ij-1}^{t+1/2}}{\Delta x_{ij-1/2}}\\ +L_{ij}\left(H_{ij}^{t}+H_{ij-1}^{t}\right)\dfrac{\sum_{k=0}^{k=surflayer}\left(\rho_{kj}-\rho_{kj-1}\right)\left(H_{kj}^{t}+H_{kj-1}^{t}\right)/2}{\left(\rho_{ij}+\rho_{ij-1}\right)/2\,\Delta x_{ij-1/2}}\end{array}\right)$$

$$+\sum_{i=ibottom}^{isurface}\left[L_{ij}\left(H_{ij}^{t}+H_{ij-1}^{t}\right)\Delta t\left(\frac{\nu_x}{\Delta x_{ij}^{2}}\left(u_{ij+1}^{t}-u_{ij}^{t}\right)-\frac{\nu_x}{\Delta x_{ij-1}^{2}}\left(u_{ij}^{t}-u_{ij-1}^{t}\right)\right)\right]$$

$$+\frac{L_{ij}\left(H_{ij}^{t}+H_{ij-1}^{t}\right)\Delta t\tau_j^{vento}}{\rho\Delta z_{ij}}-L_{bottomj}\Delta t\left(Cf_{\,bottomj}+Cf_{\,bottomj-1}\right)\left|u_{bottomj}^{t}\right|u_{bottomj}^{t+1}$$

(AI.16)

However, there is still a velocity in *t+1* on the right side of AI.16, in the bottom drag term. This term may be replaced by solving AI.9 for u_{ij}^{t+1} as shown in AI.17 and AI.18.

$$u_{ij}^{t+1}\left(1+\frac{\Delta t}{H_{ij}^{t}+H_{ij-1}^{t}}\left(Cf_{ij}+Cf_{ij-1}\right)\left|u_{ij}^{t}\right|\right)=u_{ij}^{t}$$

$$-\frac{\Delta t}{L_{ij}\left(H_{ij}^{t}+H_{ij-1}^{t}\right)}\left[\begin{array}{l}\dfrac{L_{ij+1/2}H_{ij}^{t}\left(u_{ij+1/2}^{t}+\left|u_{ij+1/2}^{t}\right|\right)u_{ij}^{t}-L_{ij-1/2}H_{ij-1}^{t}\left(u_{ij-1/2}^{t}+\left|u_{ij-1/2}^{t}\right|\right)u_{ij-1}^{t}}{\Delta x_{ij-1/2}}+\\ \dfrac{L_{ij+1/2}H_{ij}^{t}\left(u_{ij+1/2}^{t}-\left|u_{ij+1/2}^{t}\right|\right)u_{ij+1}^{t}-L_{ij-1/2}H_{ij-1}^{t}\left(u_{ij-1/2}^{t}-\left|u_{ij-1/2}^{t}\right|\right)u_{ij}^{t}}{\Delta x_{ij-1/2}}\end{array}\right]$$

$$-\frac{\Delta t}{\left(L_{i+1/2\,j}+L_{i-1/2\,j}\right)}\left[\begin{array}{l}\dfrac{L_{i+1/2\,j}\left(w_{i+1\,j-1/2}^{t-1/2}+\left|w_{i+1\,j-1/2}^{t-1/2}\right|\right)u_{ij}^{t}-L_{i-1/2\,j}\left(w_{ij-1/2}^{t-1/2}+\left|w_{ij-1/2}^{t-1/2}\right|\right)u_{i-1\,j}^{t}}{\Delta z_{ij}}+\\ \dfrac{L_{i+1/2\,j}\left(w_{i+1\,j-1/2}^{t-1/2}-\left|w_{i+1\,j-1/2}^{t-1/2}\right|\right)u_{i+1\,j}^{t}-L_{i-1/2\,j}\left(w_{ij-1/2}^{t-1/2}-\left|w_{ij-1/2}^{t-1/2}\right|\right)u_{ij}^{t}}{\Delta z_{ij}}\end{array}\right]$$

$$-g\Delta t\left(\frac{\xi_{ij}^{t+1/2}-\xi_{ij-1}^{t+1/2}}{\Delta x_{ij-1/2}}+\frac{\sum_{k=0}^{k=surflayer}\left(\rho_{kj}-\rho_{kj-1}\right)\left(H_{kj}^{t}+H_{kj-1}^{t}\right)/2}{\left(\rho_{ij}+\rho_{ij-1}\right)/2\,\Delta x_{ij-1/2}}\right)$$

$$+\frac{\nu_{x}}{\Delta x_{ij}^{2}}\left(u_{ij+1}^{t}-u_{ij}^{t}\right)-\frac{\nu_{x}}{\Delta x_{ij-1}^{2}}\left(u_{ij}^{t}-u_{ij-1}^{t}\right)+\frac{\nu_{i+1\,j}}{\Delta z_{ij+1/2}^{2}}\left(u_{i+1\,j}^{t+1}-u_{ij}^{t+1}\right)$$

(AI.17)

By inserting AI.18 in AI.16, AI.19 is obtained. At this stage the sums in AI.15 may be replaced using AI.19 and obtaining AI.20, AI.21 and AI.22, between boundaries, at the upstream and the downstream boundaries, respectively.

$$
u_{ij}^{t+1}=\frac{\left[\begin{array}{l}
u_{ij}^{t}-\dfrac{\Delta t}{L_{ij}\left(H_{ij}^{t}+H_{ij-1}^{t}\right)}\left[\begin{array}{l}
\dfrac{L_{ij+1/2}H_{ij}^{t}\left(u_{ij+1/2}^{t}+\left|u_{ij+1/2}^{t}\right|\right)u_{ij}^{t}-L_{ij-1/2}H_{ij-1}^{t}\left(u_{ij-1/2}^{t}+\left|u_{ij-1/2}^{t}\right|\right)u_{ij-1}^{t}}{\Delta x_{ij-1/2}}+\\
\dfrac{L_{ij+1/2}H_{ij}^{t}\left(u_{ij+1/2}^{t}-\left|u_{ij+1/2}^{t}\right|\right)u_{ij+1}^{t}-L_{ij-1/2}H_{ij-1}^{t}\left(u_{ij-1/2}^{t}-\left|u_{ij-1/2}^{t}\right|\right)u_{ij}^{t}}{\Delta x_{ij-1/2}}
\end{array}\right]\\
-\dfrac{\Delta t}{\left(L_{i+1/2\,j}+L_{i-1/2\,j}\right)}\left[\begin{array}{l}
\dfrac{L_{i+1/2\,j}\left(w_{i+1\,j-1/2}^{t-1/2}+\left|w_{i+1\,j-1/2}^{t-1/2}\right|\right)u_{ij}^{t}-L_{i-1/2\,j}\left(w_{ij-1/2}^{t-1/2}+\left|w_{ij-1/2}^{t-1/2}\right|\right)u_{i-1\,j}^{t}}{\Delta z_{ij}}+\\
\dfrac{L_{i+1/2\,j}\left(w_{i+1\,j-1/2}^{t-1/2}-\left|w_{i+1\,j-1/2}^{t-1/2}\right|\right)u_{i+1\,j}^{t}-L_{i-1/2\,j}\left(w_{ij-1/2}^{t-1/2}-\left|w_{ij-1/2}^{t-1/2}\right|\right)u_{ij}^{t}}{\Delta z_{ij}}
\end{array}\right]\\
-g\Delta t\left(\dfrac{\xi_{ij}^{t+1/2}-\xi_{ij-1}^{t+1/2}}{\Delta x_{ij-1/2}}+\dfrac{\sum_{k=0}^{k=surflayer}\left(\rho_{kj}-\rho_{kj-1}\right)\left(H_{kj}^{t}+H_{kj-1}^{t}\right)/2}{\left(\rho_{ij}+\rho_{ij-1}\right)/2\,\Delta x_{ij-1/2}}\right)\\
+\dfrac{\nu_x}{\Delta x_{ij}^{2}}\left(u_{ij+1}^{t}-u_{ij}^{t}\right)-\dfrac{\nu_x}{\Delta x_{ij-1}^{2}}\left(u_{ij}^{t}-u_{ij-1}^{t}\right)+\dfrac{\nu_{i+1\,j}}{\Delta z_{ij+1/2}^{2}}\left(u_{i+1\,j}^{t+1}-u_{ij}^{t+1}\right)
\end{array}\right]}{\left(1+\dfrac{\Delta t}{H_{ij}^{t}+H_{ij-1}^{t}}\left(Cf_{\,ij}+Cf_{\,ij-1}\right)\left|u_{ij}^{t}\right|\right)}
$$

(AI.18)

$$\sum_{i=ibottom}^{isurface}\left[u_{ij}^{t+1}L_{ij}\left(H_{ij}^{t}+H_{ij-1}^{t}\right)\right]=\sum_{i=ibottom}^{isurface}\left[u_{ij}^{t}L_{ij}\left(H_{ij}^{t}+H_{ij-1}^{t}\right)\right]$$

$$-\sum_{i=ibottom}^{isurface}\left[\begin{array}{l}\Delta t\left[\begin{array}{l}\dfrac{L_{ij+1/2}H_{ij}^{t}\left(u_{ij+1/2}^{t}+\left|u_{ij+1/2}^{t}\right|\right)u_{ij}^{t}-L_{ij-1/2}H_{ij-1}^{t}\left(u_{ij-1/2}^{t}+\left|u_{ij-1/2}^{t}\right|\right)u_{ij-1}^{t}}{\Delta x_{ij-1/2}}+\\ \dfrac{L_{ij+1/2}H_{ij}^{t}\left(u_{ij+1/2}^{t}-\left|u_{ij+1/2}^{t}\right|\right)u_{ij+1}^{t}-L_{ij-1/2}H_{ij-1}^{t}\left(u_{ij-1/2}^{t}-\left|u_{ij-1/2}^{t}\right|\right)u_{ij}^{t}}{\Delta x_{ij-1/2}}\end{array}\right]\\ -\dfrac{\Delta t L_{ij}\left(H_{ij}^{t}+H_{ij-1}^{t}\right)}{\left(L_{i+1/2j}+L_{i-1/2j}\right)}\left[\begin{array}{l}\dfrac{L_{i+1/2j}\left(w_{i+1j-1/2}^{t-1/2}+\left|w_{i+1j-1/2}^{t-1/2}\right|\right)u_{ij}^{t}-L_{i-1/2j}\left(w_{ij-1/2}^{t-1/2}+\left|w_{ij-1/2}^{t-1/2}\right|\right)u_{i-1j}^{t}}{\Delta z_{ij}}+\\ \dfrac{L_{i+1/2j}\left(w_{i+1j-1/2}^{t-1/2}-\left|w_{i+1j-1/2}^{t-1/2}\right|\right)u_{i+1j}^{t}-L_{i-1/2j}\left(w_{ij-1/2}^{t-1/2}-\left|w_{ij-1/2}^{t-1/2}\right|\right)u_{ij}^{t}}{\Delta z_{ij}}\end{array}\right]\end{array}\right]$$

$$-g\Delta t\sum_{i=ibottom}^{isurface}\left(L_{ij}\left(H_{ij}^{t}+H_{ij-1}^{t}\right)\frac{\xi_{ij}^{t+1/2}-\xi_{ij-1}^{t+1/2}}{\Delta x_{ij-1/2}}+L_{ij}\left(H_{ij}^{t}+H_{ij-1}^{t}\right)\frac{\sum_{k=0}^{k=surflayer}\left(\rho_{kj}-\rho_{kj-1}\right)\left(H_{kj}^{t}+H_{kj-1}^{t}\right)/2}{\left(\rho_{ij}+\rho_{ij-1}\right)/2\,\Delta x_{ij-1/2}}\right)$$

$$+\sum_{i=ibottom}^{isurface}\left[L_{ij}\left(H_{ij}^{t}+H_{ij-1}^{t}\right)\Delta t\left(\frac{\nu_x}{\Delta x_{ij}^{2}}\left(u_{ij+1}^{t}-u_{ij}^{t}\right)-\frac{\nu_x}{\Delta x_{ij-1}^{2}}\left(u_{ij}^{t}-u_{ij-1}^{t}\right)\right)\right]+\frac{L_{surfj}\left(H_{ij}^{t}+H_{ij-1}^{t}\right)\Delta t\tau_{j}^{vento}}{\rho\Delta z_{ij}}$$

$$-L_{bottomj}\Delta t\left(Cf_{\,bottomj}+Cf_{\,bottomj-1}\right)\left|u_{bottomj}^{t}\right|$$

$$\left[\begin{array}{l}u_{bottomj}^{t}-\dfrac{\Delta t}{L_{bottomj}\left(H_{ij}^{t}+H_{ij-1}^{t}\right)}\left[\begin{array}{l}\dfrac{L_{bottomj+1/2}H_{ij}^{t}\left(u_{bottomj+1/2}^{t}+\left|u_{bottomj+1/2}^{t}\right|\right)u_{bottomj}^{t}-}{\Delta x_{ij-1/2}}+\\ \dfrac{L_{bottomj-1/2}H_{ij-1}^{t}\left(u_{bottomj-1/2}^{t}+\left|u_{bottomj-1/2}^{t}\right|\right)u_{bottomj-1}^{t}}{\Delta x_{ij-1/2}}+\\ \dfrac{L_{bottomj+1/2}H_{ij}^{t}\left(u_{bottomj+1/2}^{t}-\left|u_{bottomj+1/2}^{t}\right|\right)u_{bottomj+1}^{t}-}{\Delta x_{ij-1/2}}\\ \dfrac{L_{bottomj-1/2}H_{ij-1}^{t}\left(u_{bottomj-1/2}^{t}-\left|u_{bottomj-1/2}^{t}\right|\right)u_{bottomj}^{t}}{\Delta x_{ij-1/2}}\end{array}\right]\\ -\dfrac{\Delta t}{\left(L_{bottom+1/2j}+L_{bottom-1/2j}\right)}\left[\begin{array}{l}\dfrac{L_{bottom+1/2j}\left(w_{bottom+1j-1/2}^{t-1/2}+\left|w_{bottom+1j-1/2}^{t-1/2}\right|\right)u_{bottomj}^{t}-}{\Delta z_{ij}}+\\ \dfrac{L_{bottom-1/2j}\left(w_{bottomj-1/2}^{t-1/2}+\left|w_{bottomj-1/2}^{t-1/2}\right|\right)u_{bottom-1j}^{t}}{\Delta z_{ij}}+\\ \dfrac{L_{bottom+1/2j}\left(w_{bottom+1j-1/2}^{t-1/2}-\left|w_{bottom+1j-1/2}^{t-1/2}\right|\right)u_{bottom+1j}^{t}-}{\Delta z_{ij}}\\ \dfrac{L_{bottom-1/2j}\left(w_{bottomj-1/2}^{t-1/2}-\left|w_{bottomj-1/2}^{t-1/2}\right|\right)u_{bottomj}^{t}}{\Delta z_{ij}}\end{array}\right]\\ -g\Delta t\left(\dfrac{\xi_{ij}^{t+1/2}-\xi_{ij-1}^{t+1/2}}{\Delta x_{ij-1/2}}+\dfrac{\sum_{k=0}^{k=surflayer}\left(\rho_{kj}-\rho_{kj-1}\right)\left(H_{kj}^{t}+H_{kj-1}^{t}\right)/2}{\left(\rho_{bottomj}+\rho_{bottomj-1}\right)/2\,\Delta x_{ij-1/2}}\right)\\ +\dfrac{\nu_x}{\Delta x_{bottomj}^{2}}\left(u_{bottomj+1}^{t}-u_{bottomj}^{t}\right)-\dfrac{\nu_x}{\Delta x_{bottomj-1}^{2}}\left(u_{bottomj}^{t}-u_{bottomj-1}^{t}\right)+\dfrac{\Delta t\nu_{bottom+1j}}{\Delta z_{bottomj+1/2}^{2}}\left(u_{bottom+1j}^{t+1}-u_{bottomj}^{t+1}\right)\end{array}\right]}{\left(1+\dfrac{\Delta t}{H_{ij}^{t}+H_{ij-1}^{t}}\left(Cf_{\,bottomj}+Cf_{\,bottomj-1}\right)\left|u_{bottomj}^{t}\right|\right)}$$

(AIAI.19

)

$$\xi_{ij}^{t+1/2}+\Delta t g\Delta t\sum_{i=ibottom}^{isurface}\left(L_{ij}\left(H_{ij}^{t}+H_{ij-1}^{t}\right)\frac{\xi_{ij}^{t+1/2}-\xi_{ij-1}^{t+1/2}}{\Delta x_j}\Big/\left(4\Delta x_j L_{j+1/2}\right)\right)$$

$$-\Delta t g\Delta t\sum_{i=ibottom}^{isurface}\left(L_{ij+1}\left(H_{ij+1}^{t}+H_{ij}^{t}\right)\frac{\xi_{ij+1}^{t+1/2}-\xi_{ij}^{t+1/2}}{\Delta x_j}\Big/\left(4\Delta x_j L_{j+1/2}\right)\right)=\xi_{ij}^{t}+\Delta t\sum_{i=ibottom}^{isurface}\left[u_{ij}^{t}L_{ij}\left(H_{ij}^{t}+H_{ij-1}^{t}\right)\Big/4\Delta x_j L_{j+1/2}\right]$$

$$-\Delta t\sum_{i=ibottom}^{isurface}\left[\begin{array}{l}\Delta t\left[\begin{array}{l}\dfrac{L_{ij+1/2}H_{ij}^{t}\left(u_{ij+1/2}^{t}+\left|u_{ij+1/2}^{t}\right|\right)u_{ij}^{t}-L_{ij-1/2}H_{ij-1}^{t}\left(u_{ij-1/2}^{t}+\left|u_{ij-1/2}^{t}\right|\right)u_{ij-1}^{t}}{\Delta x_{ij-1/2}}+\\ \dfrac{L_{ij+1/2}H_{ij}^{t}\left(u_{ij+1/2}^{t}-\left|u_{ij+1/2}^{t}\right|\right)u_{ij+1}^{t}-L_{ij-1/2}H_{ij-1}^{t}\left(u_{ij-1/2}^{t}-\left|u_{ij-1/2}^{t}\right|\right)u_{ij}^{t}}{\Delta x_{ij-1/2}}\end{array}\right]\Big/\left(4\Delta x_j L_{j+1/2}\right)\\ -\dfrac{\Delta t L_{ij}\left(H_{ij}^{t}+H_{ij-1}^{t}\right)}{\left(L_{i+1/2j}+L_{i-1/2j}\right)}\left[\begin{array}{l}\dfrac{L_{i+1/2j}\left(w_{i+1j-1/2}^{t-1/2}+\left|w_{i+1j-1/2}^{t-1/2}\right|\right)u_{ij}^{t}-L_{i-1/2j}\left(w_{ij-1/2}^{t-1/2}+\left|w_{ij-1/2}^{t-1/2}\right|\right)u_{i-1j}^{t}}{\Delta z_{ij}}+\\ \dfrac{L_{i+1/2j}\left(w_{i+1j-1/2}^{t-1/2}-\left|w_{i+1j-1/2}^{t-1/2}\right|\right)u_{i+1j}^{t}-L_{i-1/2j}\left(w_{ij-1/2}^{t-1/2}-\left|w_{ij-1/2}^{t-1/2}\right|\right)u_{ij}^{t}}{\Delta z_{ij}}\end{array}\right]\Big/\left(4\Delta x_j L_{j+1/2}\right)\end{array}\right]$$

$$-\Delta t g\Delta t\sum_{i=ibottom}^{isurface}\left(L_{ij}\left(H_{ij}^{t}+H_{ij-1}^{t}\right)\frac{\sum_{k=i}^{k=surflayer}\left(\rho_{kj}-\rho_{kj-1}\right)\left(H_{kj}^{t}+H_{kj-1}^{t}\right)/2}{\left(\rho_{ij}+\rho_{ij-1}\right)/2\,\Delta x_{ij-1/2}}\Big/\left(4\Delta x_j L_{j+1/2}\right)\right)$$

$$+\Delta t\sum_{i=ibottom}^{isurface}\left[L_{ij}\left(H_{ij}^{t}+H_{ij-1}^{t}\right)\Delta t\left(\frac{\nu_x}{\Delta x_{ij}^{2}}\left(u_{ij+1}^{t}-u_{ij}^{t}\right)-\frac{\nu_x}{\Delta x_{ij-1}^{2}}\left(u_{ij}^{t}-u_{ij-1}^{t}\right)\right)\Big/\left(4\Delta x_j L_{j+1/2}\right)\right]$$

$$-\Delta t L_{ij}\Delta t\left(Cf_{ij}+Cf_{ij-1}\right)\left|u_{ij}^{t}\right|u_{ij}^{t+1}\Big/\left(4\Delta x_j L_{j+1/2}\right)+\Delta t\frac{L_{ij}\left(H_{ij}^{t}+H_{ij-1}^{t}\right)\Delta t\tau_{j}^{vento}}{\rho\Delta z_{ij}}\Big/\left(4\Delta x_j L_{j+1/2}\right)$$

$$+\Delta t\sum_{i=ibottom}^{surface}\left(\frac{u_{ij}^{t}\left(H_{ij}^{t}+H_{ij-1}^{t}\right)L_{ij}}{4\Delta x_j L_{j+1/2}}\right)-\Delta t\sum_{i=ibottom}^{isurface}\left[u_{ij+1}^{t}L_{ij+1}\left(H_{ij+1}^{t}+H_{ij}^{t}\right)\Big/\left(4\Delta x_j L_{j+1/2}\right)\right]$$

$$+\Delta t\sum_{i=ibottom}^{isurface}\left[\begin{array}{l}\Delta t\left[\begin{array}{l}\dfrac{L_{ij+3/2}H_{ij+1}^{t}\left(u_{ij+3/2}^{t}+\left|u_{ij+3/2}^{t}\right|\right)u_{ij+1}^{t}-L_{ij+1/2}H_{ij}^{t}\left(u_{ij+1/2}^{t}+\left|u_{ij+1/2}^{t}\right|\right)u_{ij}^{t}}{\Delta x_{ij+1/2}}+\\ \dfrac{L_{ij+3/2}H_{ij+1}^{t}\left(u_{ij+3/2}^{t}-\left|u_{ij+3/2}^{t}\right|\right)u_{ij+2}^{t}-L_{ij+1/2}H_{ij}^{t}\left(u_{ij+1/2}^{t}-\left|u_{ij+1/2}^{t}\right|\right)u_{ij+1}^{t}}{\Delta x_{ij+1/2}}\end{array}\right]\Big/\left(4\Delta x_j L_{j+1/2}\right)\\ -\dfrac{\Delta t L_{ij+1}\left(H_{ij+1}^{t}+H_{ij}^{t}\right)}{\left(L_{i+1/2j+1}+L_{i+1/2j}\right)}\left[\begin{array}{l}\dfrac{L_{i+1/2j+1}\left(w_{i+1j+1/2}^{t-1/2}+\left|w_{i+1j+1/2}^{t-1/2}\right|\right)u_{ij+1}^{t}-L_{i+1/2j}\left(w_{ij+1/2}^{t-1/2}+\left|w_{ij+1/2}^{t-1/2}\right|\right)u_{i-1j+1}^{t}}{\Delta z_{ij+1}}+\\ \dfrac{L_{i+1/2j+1}\left(w_{i+1j+1/2}^{t-1/2}-\left|w_{i+1j+1/2}^{t-1/2}\right|\right)u_{i+1j+1}^{t}-L_{i+1/2j}\left(w_{ij+1/2}^{t-1/2}-\left|w_{ij+1/2}^{t-1/2}\right|\right)u_{ij+1}^{t}}{\Delta z_{ij+1}}\end{array}\right]\Big/\left(4\Delta x_j L_{j+1/2}\right)\end{array}\right]$$

$$+\Delta t g\Delta t\sum_{i=ibottom}^{isurface}\left(L_{ij+1}\left(H_{ij+1}^{t}+H_{ij}^{t}\right)\frac{\sum_{k=i}^{k=surflayer}\left(\rho_{ij+1}-\rho_{ij}\right)\left(H_{ij+1}^{t}+H_{ij}^{t}\right)/2}{\left(\rho_{ij+1}+\rho_{ij}\right)/2\,\Delta x_{ij+1/2}}\Big/\left(4\Delta x_j L_{j+1/2}\right)\right)$$

$$-\Delta t\sum_{i=ibottom}^{isurface}\left[L_{ij+1}\left(H_{ij+1}^{t}+H_{ij}^{t}\right)\Delta t_x\left(\frac{\nu_x}{\Delta x_{ij}^{2}}\left(u_{ij+2}^{t}-u_{ij+1}^{t}\right)-\frac{\nu_x}{\Delta x_{ij-1}^{2}}\left(u_{ij+1}^{t}-u_{ij}^{t}\right)\right)\Big/\left(4\Delta x_j L_{j+1/2}\right)\right]$$

$$+\Delta t L_{ij+1}\Delta t\left(Cf_{ij+1}+Cf_{ij}\right)\left|u_{ij+1}^{t}\right|u_{ij+1}^{t+1}\Big/\left(4\Delta x_j L_{j+1/2}\right)-\Delta t\frac{L_{ij+1}\left(H_{ij+1}^{t}+H_{ij}^{t}\right)\Delta t\tau_{j+1}^{vento}}{\rho\Delta z_{ij+1}}\Big/\left(4\Delta x_j L_{j+1/2}\right)$$

$$-\Delta t\sum_{i=ibottom}^{surface}\left(\frac{u_{ij+1}^{t}\left(H_{ij}^{t}+H_{ij+1}^{t}\right)L_{ij+1}}{4\Delta x_j L_{j+1/2}}\right)+\Delta t\sum_{i=ibottom}^{surface}\left(\frac{FlowInput_{ij}-FlowOutput_{ij}}{\Delta x_j L_{j+1/2}}\right)$$

(AI.20)

At the upstream boundary:

$$\xi_{ij}^{t+1/2} - \Delta t g \Delta t \sum_{i=ibottom}^{isurface} \left(L_{ij+1}\left(H_{ij+1}^{t} + H_{ij}^{t}\right) \frac{\xi_{ij+1}^{t+1/2} - \xi_{ij}^{t+1/2}}{\Delta x_j} \Big/ \left(4 \Delta x L_{j+1/2}\right) \right) = \xi_{ij}^{t} + \Delta t \sum_{i=ibottom}^{surface} \left(\frac{u_{iriver}^{t+1} H_{ij}^{t} L_{iriver}}{2 \Delta x_j L_{j+1/2}} \right)$$

$$+\Delta t \sum_{i=ibottom}^{surface} \left(\frac{u_{iriver}^{t} H_{ij}^{t} L_{iriver}}{2 \Delta x_j L_{j+1/2}} \right) - \Delta t \sum_{i=ibottom}^{isurface} \left[u_{ij+1}^{t} L_{ij+1} \left(H_{ij+1}^{t} + H_{ij}^{t}\right) \Big/ \left(4 \Delta x_j L_{j+1/2}\right) \right]$$

$$+\Delta t \sum_{i=ibottom}^{isurface} \left[\Delta t \left[\begin{array}{l} \dfrac{L_{ij+3/2} H_{ij+1}^{t} \left(u_{ij+3/2}^{t} + \left| u_{ij+3/2}^{t} \right| \right) u_{ij+1}^{t} - L_{ij+1/2} H_{ij}^{t} \left(u_{ij+1/2}^{t} + \left| u_{ij+1/2}^{t} \right| \right) u_{ij}^{t}}{\Delta x_{ij+1/2}} + \\ \dfrac{L_{ij+3/2} H_{ij+1}^{t} \left(u_{ij+3/2}^{t} - \left| u_{ij+3/2}^{t} \right| \right) u_{ij+2}^{t} - L_{ij+1/2} H_{ij}^{t} \left(u_{ij+1/2}^{t} - \left| u_{ij+1/2}^{t} \right| \right) u_{ij+1}^{t}}{\Delta x_{ij+1/2}} \end{array} \right] \Big/ \left(4 \Delta x_j L_{j+1/2}\right) \right.$$

$$\left. - \frac{\Delta t L_{ij+1} \left(H_{ij+1}^{t} + H_{ij}^{t}\right)}{\left(L_{i+1/2 j+1} + L_{i+1/2 j}\right)} \left[\begin{array}{l} \dfrac{L_{i+1/2 j+1} \left(w_{i+1 j+1/2}^{t-1/2} + \left| w_{i+1 j+1/2}^{t-1/2} \right| \right) u_{ij+1}^{t} - L_{i+1/2 j} \left(w_{ij+1/2}^{t-1/2} + \left| w_{ij+1/2}^{t-1/2} \right| \right) u_{i-1 j+1}^{t}}{\Delta z_{ij}} + \\ \dfrac{L_{i+1/2 j+1} \left(w_{i+1 j+1/2}^{t-1/2} - \left| w_{i+1 j+1/2}^{t-1/2} \right| \right) u_{i+1 j+1}^{t} - L_{i+1/2 j} \left(w_{ij+1/2}^{t-1/2} - \left| w_{ij+1/2}^{t-1/2} \right| \right) u_{ij+1}^{t}}{\Delta z_{ij}} \end{array} \right] \Big/ \left(4 \Delta x_j L_{j+1/2}\right) \right]$$

$$+\Delta t g \Delta t \sum_{i=ibottom}^{isurface} \left(L_{ij+1} \left(H_{ij+1}^{t} + H_{ij}^{t}\right) \frac{\sum_{k=i}^{k=surflayer} \left(\rho_{ij+1} - \rho_{ij}\right) \left(H_{ij+1}^{t} + H_{ij}^{t}\right) / 2}{\left(\rho_{ij+1} + \rho_{ij}\right) / 2 \, \Delta x_{ij+1/2}} \Big/ \left(4 \Delta x_j L_{j+1/2}\right) \right)$$

$$-\Delta t \sum_{i=ibottom}^{isurface} \left[L_{ij} \left(H_{ij}^{t} + H_{ij-1}^{t}\right) \Delta t \left(\frac{\nu_x}{\Delta x_{ij}^{2}} \left(u_{ij+1}^{t} - u_{ij}^{t}\right) - \frac{\nu_x}{\Delta x_{ij-1}^{2}} \left(u_{ij}^{t} - u_{ij-1}^{t}\right) \right) \Big/ \left(4 \Delta x_j L_{j+1/2}\right) \right]$$

$$+\Delta t L_{ij+1} \Delta t \left(Cf_{ij+1} + Cf_{ij}\right) \left| u_{ij+1}^{t} \right| u_{ij+1}^{t+1} \Big/ \left(4 \Delta x_j L_{j+1/2}\right) - \Delta t \frac{L_{ij+1} \left(H_{ij+1}^{t} + H_{ij}^{t}\right) \Delta t \tau_j^{vento}}{\rho \Delta z_{ij+1}} \Big/ \left(4 \Delta x_j L_{j+1/2}\right)$$

$$-\Delta t \sum_{i=ibottom}^{surface} \left(\frac{u_{ij+1}^{t} \left(H_{ij}^{t-1} + H_{ij+1}^{t-1}\right) L_{ij+1}}{4 \Delta x_j L_{j+1/2}} \right) + \Delta t \sum_{i=ibottom}^{surface} \left(\frac{FlowInput_{ij} - FlowOutput_{ij}}{\Delta x_j L_{j+1/2}} \right)$$

(AI.21)

At the downstream boundary

$$
\begin{aligned}
&\xi_{ij}^{t+1/2} + \Delta t g \Delta t \sum_{i=ibottom}^{isurface} \left(L_{ij}\left(H_{ij}^{t} + H_{ij-1}^{t}\right) \frac{\xi_{ij}^{t+1/2} - \xi_{ij-1}^{t+1/2}}{\Delta x_j} \Big/ \left(4 \Delta x_j L_{j+1/2}\right) \right) \\
&= \xi_{ij}^{t} + \Delta t \sum_{i=ibottom}^{isurface} \left[u_{ij}^{t} L_{ij} \left(H_{ij}^{t} + H_{ij-1}^{t}\right) \Big/ 4 \Delta x_j L_{j+1/2} \right] \\
&- \Delta t \sum_{i=ibottom}^{isurface} \left[\begin{array}{l} \Delta t \left[\begin{array}{l} \dfrac{L_{ij+1/2} H_{ij}^{t} \left(u_{ij+1/2}^{t} + \left|u_{ij+1/2}^{t}\right|\right) u_{ij}^{t} - L_{ij-1/2} H_{ij-1}^{t} \left(u_{ij-1/2}^{t} + \left|u_{ij-1/2}^{t}\right|\right) u_{ij-1}^{t}}{\Delta x_{ij-1/2}} + \\ \dfrac{L_{ij+1/2} H_{ij}^{t} \left(u_{ij+1/2}^{t} - \left|u_{ij+1/2}^{t}\right|\right) u_{ij+1}^{t} - L_{ij-1/2} H_{ij-1}^{t} \left(u_{ij-1/2}^{t} - \left|u_{ij-1/2}^{t}\right|\right) u_{ij}^{t}}{\Delta x_{ij-1/2}} \end{array} \right] \Big/ \left(4 \Delta x_j L_{j+1/2}\right) \\ - \dfrac{\Delta t L_{ij} \left(H_{ij}^{t} + H_{ij-1}^{t}\right)}{\left(L_{i+1/2\,j} + L_{i-1/2\,j}\right)} \left[\begin{array}{l} \dfrac{L_{i+1/2\,j} \left(w_{i+1\,j-1/2}^{t-1/2} + \left|w_{i+1\,j-1/2}^{t-1/2}\right|\right) u_{ij}^{t} - L_{i-1/2\,j} \left(w_{ij-1/2}^{t-1/2} + \left|w_{ij-1/2}^{t-1/2}\right|\right) u_{i-1\,j}^{t}}{\Delta z_{ij}} + \\ \dfrac{L_{i+1/2\,j} \left(w_{i+1\,j-1/2}^{t-1/2} - \left|w_{i+1\,j-1/2}^{t-1/2}\right|\right) u_{i+1\,j}^{t} - L_{i-1/2\,j} \left(w_{ij-1/2}^{t-1/2} - \left|w_{ij-1/2}^{t-1/2}\right|\right) u_{ij}^{t}}{\Delta z_{ij}} \end{array} \right] \Big/ \left(4 \Delta x_j L_{j+1/2}\right) \end{array} \right] \\
&- \Delta t g \Delta t \sum_{i=ibottom}^{isurface} \left(L_{ij}\left(H_{ij}^{t} + H_{ij-1}^{t}\right) \frac{\sum_{k=i}^{k=surflayer} \left(\rho_{kj} - \rho_{kj-1}\right)\left(H_{kj}^{t} + H_{kj-1}^{t}\right)/2}{\left(\rho_{ij} + \rho_{ij-1}\right)/2\, \Delta x_{ij-1/2}} \Big/ \left(4 \Delta x_j L_{j+1/2}\right) \right) \\
&+ \Delta t \sum_{i=ibottom}^{isurface} \left[L_{ij}\left(H_{ij}^{t} + H_{ij-1}^{t}\right) \Delta t \left(\frac{\nu_x}{\Delta x_{ij}^{2}} \left(u_{ij+1}^{t} - u_{ij}^{t}\right) - \frac{\nu_x}{\Delta x_{ij-1}^{2}} \left(u_{ij}^{t} - u_{ij-1}^{t}\right) \right) \Big/ \left(4 \Delta x_j L_{j+1/2}\right) \right] \\
&- \Delta t L_{ij} \Delta t \left(Cf_{ij} + Cf_{ij-1}\right) \left|u_{ij}^{t}\right| u_{ij}^{t+1} \Big/ \left(4 \Delta x_j L_{j+1/2}\right) + \Delta t \frac{L_{ij}\left(H_{ij}^{t} + H_{ij-1}^{t}\right) \Delta t \Delta \tau_x}{\rho \Delta z} \Big/ \left(4 \Delta x_j L_{j+1/2}\right) \\
&+ \Delta t \sum_{i=ibottom}^{surface} \left(\frac{u_{ij}^{t}\left(H_{ij}^{t-1} + H_{ij-1}^{t-1}\right) L_{ij}}{4 \Delta x_j L_{j+1/2}} \right) \\
&- \Delta t \sum_{i=ibottom}^{surface} \left(\frac{u_{idam}^{t+1} H_{ij}^{t} L_{idam}}{2 \Delta x_j L_{j+1/2}} \right) - \Delta t \sum_{i=ibottom}^{surface} \left(\frac{u_{idam}^{t} H_{ij}^{t} L_{idam}}{2 \Delta x_j L_{j+1/2}} \right) + \Delta t \sum_{i=ibottom}^{surface} \left(\frac{FlowInput_{ij} - FlowOutput_{ij}}{\Delta x_j L_{j+1/2}} \right)
\end{aligned}
$$

(AI.22)

Equations AI.20, AI.21 and AI.22 are rearranged with elevations in *t+1/2* on the left in order to obtain a tridiagonal system (AI.23), that is solved implicitly for the elevations. The *r* term for this tridiagonal system is the right side of equations AI.20, AI21 or AI.22.

$$a_{ij}\xi_{ij-1}^{t+1/2} = -\xi_{ij-1}^{t+1/2}\frac{g\Delta t^2}{\Delta x}\sum_{i=ibottom}^{isurface}\left(\frac{L_{ij}\left(H_{ij}^{t}+H_{ij-1}^{t}\right)}{4\Delta x L_{j+1/2}}\right)$$

$$b_{ij}\xi_{ij}^{t+1/2} = \xi_{ij}^{t+1/2}\left[1+\frac{g\Delta t^2}{\Delta x}\left(\sum_{i=ibottom}^{isurface}\left(\frac{L_{ij}\left(H_{ij}^{t}+H_{ij-1}^{t}\right)}{4\Delta x L_{j+1/2}}\right)+\sum_{i=ibottom}^{isurface}\left(\frac{L_{ij+1}\left(H_{ij+1}^{t}+H_{ij}^{t}\right)}{4\Delta x L_{j+1/2}}\right)\right)\right]$$

$$c_{ij}\xi_{ij+1}^{t+1/2} = -\xi_{ij+1}^{t+1/2}\frac{g\Delta t^2}{\Delta x}\sum_{i=ibottom}^{isurface}\left(\frac{L_{ij+1}\left(H_{ij+1}^{t}+H_{ij}^{t}\right)}{4\Delta x L_{j+1/2}}\right)$$

(AI.23)

The elevations calculated at *t+1/2* are used to compute the *u* velocities at *t+1* and the *w* velocities at *t+1/2*. Vertical velocities are calculated assuming volume conservation. Knowing the horizontal inflows, *w* may be calculated by difference, starting at the bottom layer (numerical solution of AI.3):

$$w_{i+1j}^{t+1/2} = \frac{w_{ij}^{t}L_{i-1/2j+1/2}}{L_{i+1/2j+1/2}} - \frac{\left(u_{ij+1}^{t}+u_{ij+1}^{t+1}\right)\left(H_{ij}^{t}+H_{ij+1}^{t}\right)L_{ij+1}-\left(u_{ij}^{t}+u_{ij}^{t+1}\right)\left(H_{ij-1}^{t}+H_{ij}^{t}\right)L_{ij}}{4L_{i+1/2j+1/2}\Delta x_{ij}}$$
$$+\left(\frac{FlowInput_{ij}-FlowOutput_{ij}}{\Delta x_{ij}L_{ij+1/2}}\right) \qquad \text{(AI.24)}$$

Volume changes at surface grid cells may be calculated from flow divergence (equation AI.25) and its numerical solution (AI.26):

$$\frac{dV_{ij}}{dt} = \left(\frac{\partial u}{\partial x}+\frac{\partial w}{\partial z}\right)\Delta z\Delta x L \qquad \text{(AI.25)}$$

$$V_{Surfj}^{t+1} = V_{ij}^{t} - \frac{\left(u_{ij+1}^{t}+u_{ij+1}^{t+1}\right)\left(H_{ij}^{t}+H_{ij+1}^{t}\right)L_{ij+1}-\left(u_{ij}^{t}+u_{ij}^{t+1}\right)\left(H_{ij-1}^{t}+H_{ij}^{t}\right)L_{ij}\Delta t}{4}$$
$$+w_{ij}^{t}\Delta x_{ij}L_{i-1/2j+1/2}\Delta t \qquad \text{(AI.26)}$$
$$+\left(FlowInput_{ij}-FlowOutput_{ij}\right)\Delta t$$

An updated estimate of elevation is then obtained from cell volume, width and length.

The generic algorithm is:

$$\xi_{ij}^{t+1/2} \rightarrow u_{ij}^{t+1} \rightarrow w_{ij}^{t+1/2} \rightarrow V_{ij}^{t+1} and\, \xi_{ij}^{t+1} \rightarrow S_{ij}^{t+1}$$

Finally, the concentration of any property (ϕ) may be calculated with the transport equation (AI.27) using its numerical solution (AI.28):

$$\frac{dS}{dt}+\frac{\partial(uS)}{\partial x}+\frac{\partial(wS)}{\partial z}=\frac{\partial\left(A_x\frac{\partial S}{\partial x}\right)}{\partial x}+\frac{\partial\left(A_z\frac{\partial S}{\partial z}\right)}{\partial z} \qquad \text{(AI.27)}$$

Where *S* is the concentration of any property and the terms *Ax and Az* stand for horizontal and vertical diffusivity, respectively. In the present model, horizontal diffusivity of momentum or any other property are assumed to be constant. Vertical diffusivity of momentum are calculated from a mixing length model as described in Santos (1995). Vertical diffusivity of mass and heat is calculated from Leendertse and Liu (1978) fide Santos (1995).

$$\begin{aligned}
&\frac{S_{ij}^{t+1}H_{ij}^{t+1}\Delta x_{ij}L_{ij+\frac{1}{2}}-S_{ij}^{t}H_{ij}^{t}\Delta x_{ij}L_{ij+\frac{1}{2}}}{\Delta t}=\\
&\frac{u_{ij}^{t+1}\left(H_{ij}^{t}+H_{ij-1}^{t}\right)L_{ij}+u_{ij}^{t}\left(H_{ij}^{t}+H_{ij-1}^{t}\right)L_{ij}}{4}S_{ij-1}^{t}-\\
&\frac{u_{ij+1}^{t+1}\left(H_{ij}^{t}+H_{ij+1}^{t}\right)L_{ij+1}+u_{ij+1}^{t}\left(H_{ij}^{t}+H_{ij+1}^{t}\right)L_{ij+1}}{4}S_{ij}^{t}+\\
&\frac{w_{ij}^{t+1}\left(L_{i-1j+\frac{1}{2}}+L_{ij+\frac{1}{2}}\right)+w_{ij}^{t}\left(L_{i-1j+\frac{1}{2}}+L_{ij+\frac{1}{2}}\right)}{4}S_{i-1j}^{t}\Delta x_{ij}-\\
&\frac{w_{i+1j}^{t+1}\left(L_{ij+\frac{1}{2}}+L_{i+1j+\frac{1}{2}}\right)+w_{i+1j}^{t}\left(L_{ij+\frac{1}{2}}+L_{i+1j+\frac{1}{2}}\right)}{4}S_{ij}^{t}\Delta x_{ij}-\\
&A_{xij}\frac{\left(S_{ij}^{t}-S_{ij-1}^{t}\right)\left(H_{ij}^{t}+H_{ij-1}^{t}\right)L_{ij}}{2\Delta x_{ij}}+A_{xij+1}\frac{\left(S_{ij+1}^{t}-S_{ij}^{t}\right)\left(H_{ij+1}^{t}+H_{ij}^{t}\right)L_{ij+1}}{2\Delta x_{ij}}-\\
&A_{zij}\frac{\left(S_{ij}^{t+1}-S_{i-1j}^{t+1}\right)\left(L_{i-1j+\frac{1}{2}}+L_{ij+\frac{1}{2}}\right)}{2\Delta z_{i-\frac{1}{2}}}\Delta x_{ij}+\\
&A_{zi+1j}\frac{\left(S_{i+1j}^{t+1}-S_{ij}^{t+1}\right)\left(L_{ij+\frac{1}{2}}+L_{i+1j+\frac{1}{2}}\right)}{2\Delta z_{i+\frac{1}{2}}}\Delta x_{ij}
\end{aligned} \qquad \text{(AI.28)}$$

By rearranging AI.28 with *t+1* terms on the left (equation AI.29), another implicit solution based on a tridiagonal system may be obtained (AI.30 and AI.31) (in this equation, loads and uptakes were also included).

$$
\begin{aligned}
&S_{ij}^{t+1}H_{ij}^{t+1}+\\
&A_{zij}\frac{\left(S_{ij}^{t+1}-S_{i-1j}^{t+1}\right)\left(L_{i-1j+\frac{1}{2}}+L_{ij+\frac{1}{2}}\right)}{2\Delta z_{i-\frac{1}{2}}L_{ij+\frac{1}{2}}}\Delta t-\\
&A_{zi+1j}\frac{\left(S_{i+1j}^{t+1}-S_{ij}^{t+1}\right)\left(L_{ij+\frac{1}{2}}+L_{i+1j+\frac{1}{2}}\right)}{2\Delta z_{i+\frac{1}{2}}L_{ij+\frac{1}{2}}}\Delta t=\\
&S_{ij}^{t}H_{ij}^{t}+\frac{u_{ij}^{t+1}\left(H_{ij}^{t}+H_{ij-1}^{t}\right)L_{ij}+u_{ij}^{t}\left(H_{ij}^{t}+H_{ij-1}^{t}\right)L_{ij}}{4\Delta x_{ij}L_{ij+\frac{1}{2}}}S_{ij-1}^{t}\Delta t-\\
&\frac{u_{ij+1}^{t+1}\left(H_{ij}^{t}+H_{ij+1}^{t}\right)L_{ij+1}+u_{ij+1}^{t}\left(H_{ij}^{t}+H_{ij+1}^{t}\right)L_{ij+1}}{4\Delta x_{ij}L_{ij+\frac{1}{2}}}S_{ij}^{t}\Delta t+\\
&\frac{w_{ij}^{t+1}\left(L_{i-1j+\frac{1}{2}}+L_{ij+\frac{1}{2}}\right)+w_{ij}^{t}\left(L_{i-1j+\frac{1}{2}}+L_{ij+\frac{1}{2}}\right)}{4L_{ij+\frac{1}{2}}}S_{i-1j}^{t}\Delta t-\\
&\frac{w_{i+1j}^{t+1}\left(L_{ij+\frac{1}{2}}+L_{i+1j+\frac{1}{2}}\right)+w_{i+1j}^{t}\left(L_{ij+\frac{1}{2}}+L_{i+1j+\frac{1}{2}}\right)}{4L_{ij+\frac{1}{2}}}S_{ij}^{t}\Delta t-\\
&A_{xij}\frac{\left(S_{ij}^{t}-S_{ij-1}^{t}\right)\left(H_{ij}^{t}+H_{ij-1}^{t}\right)L_{ij}}{2\Delta x_{ij}^{2}L_{ij+\frac{1}{2}}}\Delta t+A_{xij+1}\frac{\left(S_{ij+1}^{t}-S_{ij}^{t}\right)\left(H_{ij+1}^{t}+H_{ij}^{t}\right)L_{ij+1}}{2\Delta x_{ij}^{2}L_{ij+\frac{1}{2}}}\Delta t\\
&+Loads_{ij}-Uptakes_{ij}
\end{aligned}
\qquad \textbf{(AI.29)}
$$

$$
\begin{aligned}
&-A_{zij}\frac{\left(L_{i-1j+\frac{1}{2}}+L_{ij+\frac{1}{2}}\right)}{2\Delta z_{i-\frac{1}{2}}L_{ij+\frac{1}{2}}}\Delta t S_{i-1j}^{t+1}+\\
&\left[\begin{array}{l}
H_{ij}^{t+1}+A_{zij}\dfrac{\left(L_{i-1j+\frac{1}{2}}+L_{ij+\frac{1}{2}}\right)}{2\Delta z_{i-\frac{1}{2}}L_{ij+\frac{1}{2}}}\Delta t+\\
A_{zij}\dfrac{\left(L_{ij+\frac{1}{2}}+L_{i+1j+\frac{1}{2}}\right)}{2\Delta z_{i+\frac{1}{2}}L_{ij+\frac{1}{2}}}\Delta t
\end{array}\right]S_{ij}^{t+1}-\\
&A_{zij}\frac{\left(L_{ij+\frac{1}{2}}+L_{i+1j+\frac{1}{2}}\right)}{2\Delta z_{i+\frac{1}{2}}L_{ij+\frac{1}{2}}}\Delta t S_{i+1j}^{t+1}=X^{t}
\end{aligned}
\qquad \textbf{(AI.30)}
$$

Where X^t represents all the explicit terms on the right of AI.29.

$$a_{ij}S_{i-1j}^{t+1} + b_{ij}S_{ij}^{t+1} + c_{ij}S_{i+1j}^{t+1} = X^{t}$$

$$a_{ij} = -A_{zij}\frac{\left(L_{i-1j+1/2} + L_{ij+1/2}\right)}{2\Delta z_{i-1/2}L_{ij+1/2}}\Delta t$$

$$b_{ij} = H_{ij}^{t+1} + A_{zij}\frac{\left(L_{i-1j+1/2} + L_{ij+1/2}\right)}{2\Delta z_{i-1/2}L_{ij+1/2}}\Delta t +$$

$$A_{zij}\frac{\left(L_{ij+1/2} + L_{i+1j+1/2}\right)}{2\Delta z_{i+1/2}L_{ij+1/2}}\Delta t$$

$$c_{ij} = -A_{zij}\frac{\left(L_{ij+1/2} + L_{i+1j+1/2}\right)}{2\Delta z_{i+1/2}L_{ij+1/2}}\Delta t \qquad \text{(AI.31)}$$

Annex II – Rate equations for the biogeochemical processes and general model parameters

General differential model equations are shown in Table III.1. Rate equations are listed in Table AII.1. Model parameters are listed in Table AII.2. Equation AII.1 is a simplified version of the momentum equations (AI.1 and AI.1)). Equation AII.2 represents the heat budget of the water mass. The calculations of the fluxes represented on the right side of AII.2 is based on standard formulations described in Brock (1981) and Portela & Neves (1994). Equations AII.3 and AII.4 represent the mass balance for dissolved inorganic nitrogen and phosphorus, respectively. In fact, the model computes the concentrations of three nitrogen forms – ammonia, nitrite and nitrate. The fluxes represented in these equations correspond to gain and loss processes dependent on nutrient uptake by phytoplankton, nutrient regeneration and nutrient loads. Loads are considered to account for river input and thermal discharges from the power plant. Equations AII.5, AII.6 and AII.7 describe phytoplankton mass balance in carbon, nitrogen and phosphorus units.

Phytoplankton productivity is described as a function of light intensity (depth integration Steele's equation (Steele, 1969), temperature and a limiting nutrient – nitrogen or phosphorus (Table AII.1, equations AII.8 and AII.11). In this model, phytoplankton is represented through a chlorophyll, a carbon, a nitrogen and a phosphorus pool. This allows the necessary bookkeeping calculations on cell quotas. Traditional approaches with models based solely on nitrogen or phosphorus do not allow these computations. Internal cell quotas are then used to limit carbon fixation through photosynthesis. A nutrient limiting factor in the range 0 – 1 is calculated both for internal nitrogen and phosphorus. The lowest obtained value is then multiplied by light and temperature limited photosynthesis following Liebig's law of minimum.

Nutrient uptake and limitation is described as a three-stage process (Table AII.1, equations AII.14 - AII.19):

(i) The uptake of nitrogen and phosphorus is dependent on their concentration in the water, on their cell quotas and on their cellular ratios;
(ii) After uptake, nutrients accumulate in the cells;
(iii) The internal nutrient concentration is used to limit phytoplankton productivity.

A Michaelis-Menten equation is used to relate nutrient uptake with their concentration in the water, following several authors (e.g. Parsons et. al., 1984; Ducobu et al., 1998; Jørgensen & Bendoriccchio, 2001). The parameters of this equation are the half-saturation constant and the maximum uptake rate. These were taken from the literature, within the range of measured values (Cochlan and Harrison, 1991; Jørgensen & Jørgensen, 1991). The Michaelis-Menten equation is not the only regulating mechanism of nutrient uptake, which is also constrained by current cell quotas to avoid values outside ranges reported in the literature. Further, when N:P ratios are outside limits currently measured, N or P uptake is constrained. Nitrogen uptake rate is calculated first for ammonium nitrogen and then for nitrite + nitrate, reducing their uptake proportionally to ammonium uptake (AII.17). This is based on the usual assumption that ammonium is the preferred nitrogen source for phytoplankton (Parsons et al., 1984).

Phytoplankton respiration is based on the model of Langdon (1993) (Table AII.1, equations AII.23 and AII.24).

Table AII. 1 – Equations for the rate processes. Each rate is multiplied by corresponding carbon, nitrogen or phosphorus stocks to obtain fluxes (see text).

Processes	Equations	Units
Vertically integrated light limited productivity	$$P\,g(I) = P\,max\,\frac{\exp}{k\,z}\left(exp\left(-\frac{I\,z}{I\,opt} \right) - exp\left(-\frac{I\,0}{I\,opt} \right) \right)$$ (AII.8) where, *Pmax* – Maximum rate of photosynthesis; I_{opt} – Optimal light intensity for photosynthesis; I_z – Light intensity at depth z;	d^{-1}
Light intensity at box depth	$$I_z = I_0 \exp(-kz)$$	μ E m^{-2} s^{-1}
Light extinction coefficient	$$k = k_0 + 0.04 + 0.0088 \cdot PHYCHl_{ij} + 0.054\,.\,PHYCHl_{ij}^{2/3}$$ (AII.9) where, K_0 – Reference light extinction coefficient (m^{-1});	m^{-1}
Light and temperature limited productivity	$$P\,g(I,T) = P\,g(I).Tlimit$$ (AII.10) where, *Tlimit* – Temperature limitation factor	d^{-1}
Light, temperature and nutrient limited productivity	$$PHYGPP_{ij} = P\,g(I,T,Nut) = P\,g(I,T)\min\left(\frac{Ncell_{ij}}{k_{Ncell} + Ncell_{ij}}, \frac{Pcell_{ij}}{k_{Pcell} + Pcell_{ij}} \right)$$ (AII.11) where, K_{Ncell} – Half saturation constant for growth limited by nitrogen cell quota; K_{Pcell} – Half saturation constant for growth limited by phosphorus cell quota.	d^{-1}
Nitrogen cell quota	$$Ncell_{ij} = \frac{PHYN_{ij}}{PHYC_{ij}}$$ (AII.12)	mg N mg C^{-1}
Phosphorus cell quota	$$Pcell_{ij} = \frac{PHYP_{ij}}{PHYC_{ij}}$$ (AII.13)	mg P mg C^{-1}
Nitrogen uptake	$$PHYUptakeN_{ij} = V_N . PHYN_{ij}$$ (AII.14)	μg N L^{-1} d^{-1}
Phosphorus uptake	$$PHYUptakeP_{ij} = V_P . PHYP_{ij}$$ (AII.15)	μg P L^{-1} d^{-1}
	If $Nmin < PHYN_{ij} < Nmax$ and $PHYN_{ij} / PHYP_{ij} < maxN/P_{ij}$	

Nitrogen uptake rate (V_N)	$$V\,Ammonium = V\max N \frac{Ammonium_{ij}}{k_{Ammonium} + Ammonium_{ij}} \quad \text{(AII.16)}$$ $$V\,Nitrate + Nitrite = \max\left(0, V\max_N - V\,Ammonium\right) \cdot \frac{\left(Nitrate + Nitrite\right)_{ij}}{k_{Nitrate+Nitrite} + \left(Nitrate + Nitrite\right)_{ij}} \quad \text{(AII.17)}$$ $$V_N = V\,Ammonium + V\,Nitrate + Nitrite$$ else V_N = 0, (AII.18)where *Nmin* – minimal nitrogen cell quota (mg N mg C^{-1}) ; *Nmax* - maximal nitrogen cell quota (mg N mg C^{-1}) ; $K_{Ammonium}$ – half saturation constant for ammonium-nitrogen uptake (μmol N L^{-1}); $maxN/P_{ij}$ – Maximal cellular nitrogen:phosphorus ratio; V_{maxN}– Maximal uptake rate (d^{-1}); $K_{Nitrate+Nitrite}$ – half saturation constant for Nitrate + Nitrite -nitrogen uptake (μmol N L^{-1});	d^{-1}
Phosphorus uptake rate (V_P)	If $PHOSmin < PHYP_{ij} < PHOSmax$ and $PHYN_{ij} / PHYP_{ij} > minN/P_{ij}$ $$V_P = V\max P \frac{P_{ij}}{k_P + P_{ij}}$$ (AII.19) else V_P = 0, where *PHOSmin* – minimal phosphous cell quota (mg P mg C^{-1}) ; *PHOSmax* - maximal phosphous cell quota (mg P mg C^{-1}) ; K_p – half saturation constant for phosphous uptake (μmol P L^{-1}); $minN/P_{ij}$ – Minimal cellular nitrogen:phosphorus ratio; V_{maxP}– Maximal uptake rate (d^{-1}); V_{max} – Maximal uptake rate (d^{-1}) (the same value for nitrogen uptake)	d^{-1}
Phytoplankton exudation rate of Carbon	$$PHYExud_{ij} = Exud.PHYGPP_{ij}$$, where (AII.20) *Exud* – Fraction exudated;	d^{-1}
Phytoplankton exudation of Nitrogen	$$PHYExudN_{ij} = PHYExud_{ij} \cdot PHYC_{ij}.Ncell_{ij}$$ (AII.21)	μg N $L^{-1}d^{-1}$
Phytoplankton exudation of Phosphorus	$$PHYExudP_{ij} = PHYExud_{ij}.PHYC_{ij}.Pcell_{ij}$$ (AII.22)	μg P $L^{-1}d^{-1}$
Phytoplankton respiration rate	$$PHYResp_{ij} = \left(R_0 + R_{dark}.Tlimit.DailyMean\overline{GPP_{ij}}\right). \frac{CarbonToOxygen}{ChlorophyllToCarbon}.OxygenMolecularWeight.24$$ (AII.23) during the night $$PHYResp_{ij} = \left(R_0 + R_{dark}.Tlimit.DLratio.DailyMean\overline{GPP_{ij}}\right) \frac{CarbonToOxygen}{ChlorophyllToCarbon}.OxygenMolecularWeight.24$$ (AII.24)	d^{-1}

	during the day, where R_0 – Maintenance respiration (mmol O_2 mg Chl^{-1} h^{-1}); R_{dark}– Linear coefficient of increase in biomass-specific dark respiration with gross photosynthesis (dimensionless); DLratio – Ratio between respiration in the light and respiration in the dark (adimensional); $DailyMean\overline{GPP_{ij}}$ - Daily integrated gross productivity (mmol O_2 mg Chl^{-1} h^{-1}); CarbonToOxygen – Conversion factor between oxygen consumed and carbon produced in respiration (mg C mg O_2^{-1}); ChlorophyllToCarbon – Conversion factor from chlorophyll to carbon (mg C mg Chl^{-1})	
Temperature limitation factor	$Tlimit = \exp\left(\text{TempAugRate}\left(T_{ij} - T_0\right)\right)$ (AII.25) where, TempAugRate – Temperature augmentation rate; T_0 – Reference temperature.	dimensionless
Nitrogen respiration loss	$PHYRespN_{ij} = PHYResp_{ij}.PHYC_{ij}.Ncell_{ij}$ (AII.26)	$\mu g\ N\ l^{-1}d^{-1}$
Phosphorus respiration loss	$PHYRespP_{ij} = PHYResp_{ij}.PHYC_{ij}.Pcell_{ij}$ (AII.27)	$\mu g\ P\ l^{-1}d^{-1}$
Nitrogen mortality loss	$PHYMortN_{ij} = PHYMort_{ij}.PHYC_{ij}.Ncell_{ij}$ (AII.28)	$\mu g\ N\ l^{-1}d^{-1}$
Phosphorus mortality loss	$PHYMortP_{ij} = PHYMort_{ij}.PHYC_{ij}.Pcell_{ij}$ (AII.29)	$\mu g\ P\ l^{-1}d^{-1}$
Carbon settling loss rate	$PHYSet_{ij} = \frac{SettlingSpeed}{Depth_{ij}}$, (AII.30) where, *SettlingSpeed* – Fall velocity of phytoplankton cells (m d^{-1}); $Depth_{ij}$ – Depth of layer j in column i (m)	d^{-1}
Nitrogen settling loss	$PHYSetN_{ij} = SettlingSpeed.\frac{PHYN_{ij}}{Depth_{ij}}$ (AII.31)	$\mu g\ N\ l^{-1}d^{-1}$
Phosphorus settling loss	$PHYSetP_{ij} = SettlingSpeed.\frac{PHYP_{ij}}{Depth_{ij}}$ (AII.32)	$\mu g\ P\ l^{-1}d^{-1}$

Table AII.2 – Model parameters and respective values. Most values were calibrated from ranges reported by quoted authors.

Object	Parameter	Value	Reference
Hydrodynamic 2D object	Manning coefficient	0.025 s $m^{-1/3}$	Grant and Bacher (2001)
	Eddy diffusivity	100 m^2 s^{-1}	Neves (1985)
Phytoplankton object	*Nmin*	0.1 mg N mg C^{-1}	Jørgensen & Jørgensen (1991)
	Nmax	0.53 mg N mg C^{-1}	Jørgensen & Jørgensen (1991)
	$K_{Ammonium}$	2.94 μmol N l^{-1}	Jørgensen & Jørgensen (1991)
	$maxN/P_{ij}$	291	Jørgensen & Jørgensen (1991)
	V_{maxP} *and* V_{maxN}	1.08 d^{-1}	Cochlan & Harrison (1991)
	$K_{Nitrate+Nitrite}$	30 μmol N l^{-1}	Jørgensen & Jørgensen (1991)
	PHOSmin	0.002 mg P mg C^{-1}	Jørgensen & Jørgensen (1991)
	PHOSmax	0.08 mg P mg C^{-1}	Jørgensen & Jørgensen (1991)
	$minN/P_{ij}$	4	Jørgensen & Jørgensen (1991)
	K_p	2 μmol P l^{-1}	Jørgensen & Jørgensen (1991)
	P_{max}	1.2 d^{-1}	Jørgensen & Jørgensen (1991)
	I_{opt}	300 μE m^{-2} s^{-1}	Jørgensen & Jørgensen (1991)
	K_0	0.6 – 2.0 m^{-1}	Measured
	K_{Ncell}	0.028 mg N mg C^{-1}	Calibrated
	K_{Pcell}	0.004 mg P mg C^{-1}	Calibrated
	Exud	0.1	Jørgensen & Jørgensen (1991)
	R_0	0.02 mmol O_2 mg Chl^{-1} h^{-1}	Langdon (1993)
	R_{dark}	0.11	Langdon (1993)
	DLratio	2	Langdon (1993)
	CarbonToOxygen	0.3125 mg C mg O_2^{-1}	Vollenweider (1974)
	ChlorophyllToCarbon	50 mg C mg Chl^{-1}	Jørgensen & Jørgensen (1991)
	TempAugRate	0.069 $ºC^{-1}$	Estimated
	T_0	0ºC for photosynthesis and 25ºC for respiration	Calibrated
	SettlingSpeed	1 m d^{-1}	Mann & Lazier (1996)
	$PHYMort_{ij}$	0.1 day^{-1}	Jørgensen & Jørgensen (1991)

ANNEX III

Variability of water quality parameters at different time scales in a Portuguese reservoir (Crestuma, River Douro)

Historical data

The raw long-term environmental data were obtained from the INAG web site (INAG 2003) and refer to water column surface samples collected on a monthly basis from January 1992 to December 2001. A total of 345 data sets were available.

Sampling

Sampling was based on four seasonal eulerian sampling campaigns at December 2003, February, May and July 2004, providing short-term data sets. At each campaign three datasets were obtained – two datasets based on 25-hours surveys carried out on Sundays-Mondays and Wednesdays-Thursdays, taking place simultaneously at points A and B (Figure 1) – and one dataset based on a 5-days sampling survey at point B, starting on Saturdays and ending on Thursday mornings. The former datasets were supposed to contrast situations of reduced flow at the weekend, due to lower needs in hydroelectric power, and increased flow during the working days. These datasets consist of several physical, chemical and biological variables and processes, sampled with different frequency according to whether sensors or laboratory methods were used (Table 1). Sensor measurements were carried out with CTDs, with 1 minute frequency at surface and 5 m depth at point B and only at surface at point A (Figure 1), according to available equipment. Samples were processed immediately in a field laboratory installed on location, equipped with all required hardware. Wastes (especially toxic and/or radioactive liquid effluents) were disposed according to good laboratory practice.

Chemical analyses

Samples for chorophyll-a (Chla) and phaeopigments (Phae) were filtered through 0.45 μm membrane filters. Pigments were extracted in 90% acetone and analysed

spectrophotometrically by the method of (insert citation). Chlorophyll was used as a surrogate for phytoplankton biomass. Inorganic nutrient analyses (nitrate, nitrite, ammonia and phosphate) were performed according to the methods described in A.P.H.A. (1992) and Parsons *et al*. (1984). Total available inorganic carbon was determined in the water samples prior to incubation from pH (pH Meter ESD model 69) and alkalinity measurements according to Parsons *et al.* (1984).

Incubation procedures

Samples were incubated in the field laboratory. Light was provided by 1500 W tungsten halogen lamps, for productivity measurements. Light intensity (0 to 950 μE m^{-2} s^{-1}) was measured with a LICOR spherical quantum sensor (LI–193SA). Attenuation was achieved with grey PVC nets. All productivity and respiration experiments were performed using 2 and 24 hours incubation periods, respectively, under a controlled temperature, similar to that measured during sampling.

Primary production determination

Primary production was measured using standard ^{14}C techniques (Steemann Nielsen 1952) and following the ICES CM 19967L:3 recommendations. Water samples were placed in 60 ml Winkler bottles and inoculated with 1 ml of $NaH^{14}CO_3$ with 10 μCi (Carbon 14 Centralen). A dark bottle was used for the blank determination. After incubation, samples were filtered onto 25 mm membrane filters (0.45 μm) using gentle vacuum, and filters were acidified with HCl to eliminate inorganic ^{14}C. Filters were placed in 20 ml scintillation vials to which 10 ml of scintillation fluid (Insta-Gel Plus, Packard) was added. Sample's scintillation was then counted in a liquid scintillation analyser (Tri-Carb Model 1600CA). Liquid scintillation counts were corrected for quenching by external standard. Primary production (mg C m^{-3} h^{-1}) was calculated following ICES CM 1996/L:3 and then divided by the phytoplankton biomass to calculate the primary production rate (mg C mgChl a^{-1} h^{-1}).

Community respiration

Respiration was measured with the oxygen method (Vollenweider, 1974).

Data analysis

According to the main objective of this work, historical data were time integrated in order to allow the analysis of inter-annual variability, variability and diurnal variability (cf. – *Historical data*). Regarding inter-annual variability, annual averages for several water quality variables were used. Concerning monthly variability, monthly data were integrated over a period of up to 15 years. Time series graphs were made and, for inter-annual variability, regression analysis on the time dependence of the studied variables was performed. Furthermore, correlation and cluster analysis were also carried out in order to study the relationships between different variables. In what regards diurnal variability, data from sampling surveys were used (cf. – *Sampling*).

According to Bordalo (pers. comm.), the Asiatic clam *Corbicula sp*, a bivalve suspension-feeder, invaded the Douro during the eighties. The same author estimated densities of this invasive species at the Crestuma reservoir, in 1999, of c.a. 1000 ind./m^2, within the limits reported for *C. fluminea* (Karatayev et al., 2003). Therefore, an attempt was made to evaluate the potential role of this invasive species – a bivalve suspension feeder. The methodology used was to compare the time needed for bivalves to filter all the water in the reservoir (clearance time – CT), with the water residence time (RT) and the time it takes for phytoplankton to renew its biomass (biomass: production or B/P ratio), following Dame & Prins (1998).

Analysis of variance (ANOVA) was used to relate variance of each studied variable at different time scales. The null hypothesis about no significant differences between the same season over the years, was tested using as surrogates for replicates, values obtained at each season of each year, from 1990 till 2005. These are not true replicates, because they correspond to results obtained at previously chosen moments – three samples per season (one every month). Therefore, they may be not representative of intra-seasonal variability. A similar approach was used to compare results obtained in different seasons (during the 25-hour surveys), using as “pseudo-replicates” values measured in each campaign.

Light intensity and phytoplankton primary production data were fitted to different Producton-Light (P-E) curves, using non-linear regression (Quasi Newton method with Statistica 6.0 software). Several trials were carried out with each data set, using different P-E models (see Duarte (2005) for a review), according to whether or not photoinhibition was present and also to the quality of the fit obtained. From light

intensity and water transparency data, obtained during the 25-hour surveys, and integrating the P-E functions over depth and time, using Eiler's method, daily production was estimated. This was then combined with community respiration data to obtain net primary production (NPP). In converting oxygen to carbon a photosynthetic ratio of one was assumed, between molecules of oxygen produced/consumed and carbon consumed/produced in photosynthesis/respiration.

Results and Discussion

The first part of this section will deal with time-series analysis of 16-years datasets for each variable under study. Here, the focus will be on inter-annual variability. The second part will deal with monthly variability and the third part will focus on daily variability.

Inter-annual variability

Ammonia showed a regular pattern throughout the 16 years, except in 1999, reaching a maximum near 0.9 mg/l (Figure 2). Nitrate + nitrite and phosphate exhibited significant increasing trends over the years, as shown by regression analysis (Figure 2). A similar significant trend was observed for the N:P ratio (not shown), that ranged between near 40 and over 100, suggesting that phytoplankton is phosphorus limited. The same applies to temperature, with a minimum annual average of 14.7 ºC and a maximum of 17.5 ºC. In spite of the mentioned nutrient, N:P ratios and temperature increasing trends, chlorophyll showed a significant decreasing tendency over the past 16 years, from an annual average of 18 mg/L, in 1990, till 4 mg/l, in 2005 (Figure 2). Total suspended solids (TSS) did not exhibit any specific trend over the period under analysis. However, it is noteworthy that concentration variability increased after 1995. This is probably related to intensive dredging operations that took place in the reservoir since that period. The average dissolved oxygen saturation concentration is 91 %, suggesting that heterotrophy dominates in this ecosystem.

In Figure 3, a tree clustering, obtained from the Pearson correlation coefficient (Statistica 6.0 software), displays two main groups of variables. Chlorophyll and dissolved oxygen are separated from the remaining variables. In fact, the significant correlation ($p < 0.05$) between those two variables suggests that phytoplankton

variability explains a significant part of dissolved oxygen variability. The significant correlation between TSS and river flow is an expected result, with high suspended matter loads occurring during flood events. The absence of clusters joining chlorophyll and nutrients suggests that the latter do not explain much of phytoplankton variability at large time scales.

Inter-annual variability of different seasons

Figure 4 depicts long-term chlorophyll trends for each season, exhibiting a decreasing tendency over the studied period, especially in Summer and Autumn, from values of c.a. 25 mg/L, in 1990, to near 2 mg/L, in 2005 (Figure 4). Phosphate showed significant increasing trends for winter and spring (over a three fold increase during the studied period) (Figure 5). Regarding summer and autumn, significant trends were not apparent, in spite of the large increase from 2004 to 2005, with a maximum near 1.6 mg/L. Nitrate + nitrite exhibited increasing trends for spring and summer, with a c.a. three and two-fold concentration increase, respectively (Figure 6). Temperature increased in summer over the years, from 22.3ºC, in1990, to 24.3ºC, in 2005 (Figure 7). This suggests that the long-term temperature trends mentioned before are mostly explained by the summer increase.

The results of the ANOVA described previously (cf. – Methodology – Data analysis), to test the differences between years for each season, regarding several water quality variables are summarised in Table 2. The null hypothesis of no significant differences was rejected for chlorophyll, phosphate (except summer data), and spring nitrate. This suggests that inter-annual variability for these variables/seasons is significantly larger than intra-annual variability, pointing out to long-term trends, as suggested before. However, these results contradict the previously mentioned long term temperature trends, suggested by regression analysis.

Significant correlations between chlorophyll and nutrients were not obtained in this long –term analysis for each season. However, when only the period 2000-2005 is considered, there is a significant correlation ($p < 0.05$) between phytoplankton and nitrate in autumn (Figure 8). This result suggests that there was a shift from phosphorus towards nitrate limitation in the last autumns. In fact, the N:P molar ratio (Figure 9) was minimum in autumn, with an average of 38.6, significantly lower than values observed for the other seasons.

From the results presented so far, it is tempting to try to explain the long-term nitrate + nitrite and phosphorus increase as a result of the decreasing phytoplankton trends. In fact, if the annual average phytoplankton decrease, over the period 1990-2005, is expressed in nitrogen and phosphorus, according to the Redfield ratio, the values obtained are well within the corresponding increases in nitrate and phosphorus. One of the larger uncertainties in this calculation, results from the conversion of chlorophyll to carbon, before converting phytoplankton to nitrogen or phosphorus units. In any case, if a value of 50 is assumed for the carbon: chlorophyll ratio (Jørgensen & Jørgensen, 1991), the corresponding theoretical phytoplankton nitrogen and phosphorus decrease would roughly explain half of the nitrate and phosphate increase. Therefore, considering the mentioned uncertainties and the fact that average values integrated over several years are being used in the calculations, it seems that, at least, an important part of nutrient long-term increase may be explained by the phytoplankton decrease. The question that remains to be answered is "Why is phytoplankton decreasing?".

One possible answer to the question posed above could be the filtering activities of the invasive Asiatic clams. Considering a CR of c.a. 22 mL/h/g of total fresh weight, assuming an average clam with 9 g (Karatayev et al., 2003) and considering the total area of the reservoir – 12.98 km^2 – a total clearance rate of c.a 77 X 10^6 m^3/day may be expected. Knowing that the volume of the reservoir is 110 X 10^6 m^3 and dividing this volume by the total clearance rate, it appears that clams may clear this volume in less than two days – well within values reported for *C. fluminea* in other ecosystems (Karatayev et al., 2003). This time is shorter than the RT of almost three days, under average flow – c.a. 455 m^3s^{-1}. It is also lower than the phytoplankton B/P in the reservoir, according to previous modelling studies conducted by the authors (unpublished). Therefore, it is tempting to explain the decreasing phytoplankton long-term trends mentioned before, with the filtration activities of the Asiatic clam, according to results obtained for other ecosystems after invasion by bivalve suspension-feeders (Cohen et al., 1984; Beaver et al., 1991). However, the above calculations may grossly overestimate the role of the clams, due to the large uncertainties about their density and average weight and, due to the fact that being a bottom species they do not have access to most of the overflowing water. Furthermore, if their impact is as large as predicted by the above calculations, it would be expectable to see some decreasing long-term trend in TSS, which was not the observed. In any case, this hypothesis needs further clarification.

Monthly variability

The analysis of Figure 10 suggests that differences between months were, in most cases, non-significant, considering the magnitude of the error bars, resulting from inter-annual variability of monthly data. Ammonia showed two maximum values near 0.4 mg/L in July and October, but the confidence interval is very large. Lower values are around 0.1 mg/L. Nitrate + nitrite exhibited higher values in Winter and Spring – up to near 20 mg/L. Minimum values were above 2 mg/L. Phosphate showed less variability, with minimum values close to 0.1 mg/L and a maximum of 0.4 mg/L in August. TSS were higher in Winter and Autumn, ranging between c.a. 5 and 20 mg/L. Phytoplankton showed the two "classic" peaks – one in June and another in October, with a range between 4 and 12 mg/L. Temperature ranged between c.a. 10 and 25 ºC. Monthly average dissolved oxygen concentration is always below saturation, with values close to 90% (not shown).

In Figure 11, a tree clustering, obtained from the Pearson correlation coefficient (Statistica 6.0 software), displays two main groups of variables. It is noteworthy that at the monthly time scale, the correlation between chlorophyll and dissolved oxygen is not significant ($p > 0.05$), in opposition to what was observed at the inter-annual time scale. Dissolved oxygen is in the same cluster with river flow (significantly correlated), exhibiting a significant negative correlation with temperature. This suggests that at monthly time scales, oxygen depends mostly on seasonal physical phenomena rather than biological forcing. Lower temperatures increase oxygen solubility and high river flows "dilute" biological processes. Although chlorophyll is in the same cluster of ammonia and phosphate, the correlation between the former and the latter ones is not significant. A significant correlation was obtained between TSS and river flow, as before.

Diurnal variability

Figures 12 – 15 summarise results for dissolved oxygen saturation, water temperature and pH time series, obtained during the five-day surveys conducted in December 2003, February, May and September 2004. It is apparent that dissolved oxygen concentration is below saturation in several occasions. Temperature ranged between 8.86 and 24.78 ºC and pH between 6.93 and 9.78. Surface and bottom temperatures are very similar, because water column is generally well mixed (Figs.

13 – 15). Time series of February and September surveys exhibit a “normal” behaviour, with dissolved oxygen and pH peaks coinciding and occurring at midday or during the afternoon, when photosynthesis is expected to be at its maximum. These patterns are less clear for bottom data. The analysis of the remaining time-series does not reveal the same patterns. In fact, both for December and May surveys, water temperature, dissolved oxygen and pH peaks do not always coincide with what is expected from the solar cycle. The reason for this behaviour may be related to flow variability and horizontal displacement of water masses with different properties. In fact, at this reservoir, flow rates may shift from near zero to over 1000 m^3s^{-1} in just a few hours.

Figure 16 summarizes chlorophyll and nutrient data obtained during the 25-hour data sets, averaged for points A and B (Figure 1). It is apparent that chlorophyll reached higher concentrations in May and September, whereas the opposite was found for nitrate and phosphate. However, ammonium behaviour was comparable to that of chlorophyll, suggesting that mineralization during the warmer period may increase ammonium concentrations in the reservoir. The ANOVA used to test differences between campaigns (December 2003, February, May and September 2004), using values measured at each campaign as surrogates for replicates (cf. – methodology – Data analysis), led to the rejection of the null hypothesis for all water quality variables, suggesting that inter-seasonal variability is significantly larger than intra-seasonal variability.

Correlation analysis did not reveal any clear influence of river flow over the remaining variables at short (25 hours) time scales. The obtained results suggest that river flow may be strongly related with some variables in some occasions, but without any consistent pattern between occasions. In fact, significant correlations ($p < 0.05$) between river flow and other variables were observed solely in three out of fifteen 25h-datasets (station B X eight sampling occasion, plus station A X seven sampling occasions). However, these correlations were not consistent between the mentioned datasets.

Table 3 summarizes the results obtained by fitting different production-light (P-E) models to phytoplankton photosynthesis data obtained during the 25-hour surveys. (cf. – Methodology – Sampling surveys). The analysis of these results suggests the following patterns:

4) Highest Pmax values were observed in May and September (up to five fold higher than in December and February);
5) a was also generally higher in May and September. Therefore, phytoplankton was not only more productive but also more efficient in using light intensity;
6) a decreased from morning to dawn, suggesting that in early morning phytoplankton cells were more efficient in using light – presumably, dark adapted.

Table 4 summarizes gross and net primary production (GPP and NPP, respectively) estimates for the 25-hour sampling surveys. Results obtained confirm the previous statement about the heterotrophic character of the Crestuma reservoir (cf. Inter-annual variability), with the production: respiration ratio being below 0.5.

Conclusions

From the results presented and discussed, it seems reasonable to conclude that the Crestuma reservoir has undergone some important changes over the period 1999-2005, with significant increases in nitrogen and phosphorus and a decrease in the nitrogen: phosphorus ratio. One possible change, arising from the shifts in the nitrogen: phosphorus ratio, is the apparent autumn shift towards nitrate-nitrogen limitation of phytoplankton. The long term nutrient increasing trends may partly be explained by a reduction on chlorophyll concentration that may be a result of the feeding activities of the invasive *Corbicula sp*. Another possible explanation to the chlorophyll decrease may be the increase in the usage of pesticides along the Douro drainage basin. The Crestuma reservoir appears to be a predominantly heterotrophic ecosystem. The long term changes mentioned above may have impacts on the Douro estuary, by alleviating nutrient limitation and stimulating primary production. It is important to clarify the true reason for the phytoplankton reduction and nutrient increase by conducting properly designed surveys, since these may be important signs of ecosystem change.

Bibliography

1. Beaver, J.R., Criman, T.L. & R.J. Brock, 1991. Grazing effects of an exotic bivalve (*Corbicula fluminea*) on hypereutrophic lake water. Lakes Reserve: Res Manage 7: 45 – 51.

2. Cohen, R.R.H., Dresler, P.V., Phillips, E.J.P. & R.L. Cory, 1984. The effect of the Asiatic clam, *Corbicula fluminea*, on phytoplankton of the Potomac river, Maryland. Limnology and Oceanography 29: 170 – 180.

3. Dame, R.F. & T.C. Prins, 1998. Bivalve carrying capacity in coastal ecosystems. Aquatic Ecology, 31: 409 – 421.

4. Duarte, P., 2005. Photosynthesis-Irradiance Relationships in Marine Microalgae. Chapter 17: pp 639-670, Vol 2. In: Algal Cultures Analogues of Blooms and Applications. (Editor) D.V. Subba Rao. Science Publishers Enfield (NH), USA, Plymouth,UK.

5. Eilers, P.H.C. & J.C.H. Peeters. 1988. A model for the relationship between light intensity and the rate of photosynthesis in phytoplankton. Ecol. Model. 42:199-215.

6. INAG. 2003. http://snirh.inag.pt.

7. Jørgensen, S.E., Nielsen, S., Jørgensen, L., 1991. Handbook of Ecological Parameters and Ecotoxicology. Elsevier, Amsterdam, 1263 pp.

8. Karatayev, A.Y., Burlakova, L.E. & D.K. Padilla, 2003. Constrasting ditribution and impacts of two freshwater exotic suspension feeders, *Dreissena polymorpha* and *Corbicula fluminea*. In: Dame, R. and Olenin, S. (Eds.), The comparative role of suspension feeders in aquatic systems (NATO ARW in Nida, Lithuania, 3-9 October, 2003): 239 - 262. Kluwer Scientific Publishers, Dordrecht, The Netherlands.

9. Steele, J.H. 1962. Environmental control of photosynthesis in the sea. Limnol. Oceanogr. 7: 137-150.

10. Vieira, M. E. C., and Bordalo A. A. 2000. The Douro estuary (Portugal): A mesotidal salt wedge. Oceanologica Acta 23: 585–594.

11. WFD. 2000. Water framework directive. Official Journal of the European Community 22.12.2000, L327:1–73.

Tables

Table 1 – Sampling variables, processes and corresponding frequency at the different surveys.

Variables and processes	25-hours surveys	5-days surveys
Water temperature	1 - 5 minutes	1 - 5 minutes
Current velocity	1 minute	1 minute
Fluorimetry	1 minute	1 minute
Light intensity (surface and underwater)	15 minutes	
Turbidity	1 minute	1 minute
pH	1 minute	1 minute
Dissolved oxygen	1 minute	1 minute
BOD_5	3 hours	-
Nutrient concentrations (Ammonia, nitrate, nitrite and phosphate)	3 hours	-
Bacterial counts	3 hours	-
Chlorophyll concentration	3 hours	-
Water column respiration	3 hours	-
Water column primary productivity	3 hours	-

Table 2 –ANOVA results to test the null hypothesis about the absence of significant differences among years for each season (cf. – Methodology – Data analysis).

Variables	*p*
Chlorophyll Winter	< 0.001
Chlorophyll Spring	< 0.05
Chlorophyll Summer	< 0.01
Chlorophyll Autumn	< 0.01
Phosphate Winter	< 0.05
Phosphate Spring	< 0.001
Phosphate Summer	N.S.
Phosphate Autumn	< 0.01
Nitrate Winter	N.S.
Nitrate Spring	< 0.01
Nitrate Summer	N.S.
Nitrate Autumn	N.S.
Temperature Winter	N.S.
Temperature Spring	N.S.
Temperature Summer	N.S.
Temperature Autumn	N.S.

Table 3 – Photosynthetic parameters *Pmax* (maximum photosynthetic rate), *Eopt* (optimal light intensity) and *Slope* (initial slope of the P-E relationship or quantum yield) estimated from the results of primary production measurements under various light intensities, conducted during the sampling campaigns. The second column indicates the incubation period in hours AM.

	Hours	Pmax (mgC mg $Chla^{-1}$ h^{-1})	Eopt . mmol quanta m^{-2} s^{-1})	a (mgC mg $Chla^{-1}$ h^{-1} mmol quanta m^2 s^1)	R^2	P-E Formulation
Dec 7th 2003	8 – 10	1.08	18.13	0.036	0.92	Eilers & Peeters (1988)
	12-12.33	1.25	271.1	0.013	0.61	Steele (1962)
	12-14	0.92	306.0	0.004	0.87	Eilers & Peeters (1988)
	15-17	0.98	-	0.005	0.72	Michaelis-Menten
Feb 15th 2004	8 – 10	0.88	268.4	0.009	0.77	
	11-13	1.16	492.5	0.006	0.38	
	12-13.25	1.19	425.16	0.007	0.49	
Feb 19th 2004	8 – 10	0.86	219.6	0.011	0.58	
	11-13	1.44	426.0	0.009	0.71	Steele (1962)
	14-16	1.01	579.5	0.005	0.62	
May 22nd 2004	7-8	2.01	436.6	0.013	0.23	
	10-11	3.23	994.0	0.009	0.53	
	13-14	2.58	999.4	0.007	0.06	
	16-17	1.97	1015.3	0.005	0.5	
May 26th 2004	7-8	2.01	246.9	0.022	0.56	
	10-11	3.69	523.3	0.019	0.80	
	13-14	4.30	608.6	0.019	0.08	
	16-17	5.33	762.2	0.019	0.20	
Sep 1st 2004	7 – 8	5.00	149.7	0.091	0.82	
	12-13	5.83	414.2	0.038	0.67	
	16-17	3.44	927.2	0.010	0.50	

Sep 5th 2004	7 – 8	2.86	28.27	0.275	0.45	
	12-13	3.34	717.7	0.013	0.32	
	16-17	1.61	666.5	0.007	0.50	

Table 4 – Gross Primary Production (GPP), Community Respiration (CR) and Net Primary Production (NPP) estimates for each of the 25-hours sampling surveys. Also shown the production: respiration ratio.

	PPB mg C / m2 / d	CR mg C / m2 / d	PPL mg C / m2 / d	P/R
Dec 7th 2003	21.8	584.6	-562.8	0.04
Feb 15th 2004	60.9	2682.2	-2621.3	0.02
Feb 19th 2004	74.0	556.2	-482.3	0.13
May 22nd 2004	591.2	2642.7	-2051.5	0.22
May 26th 2004	952.4	3620.7	-2668.3	0.26
Sep 1st 2004	837.0	2388.3	-1551.4	0.35
Sep 5th 2004	455.1	1416.7	-961.6	0.32

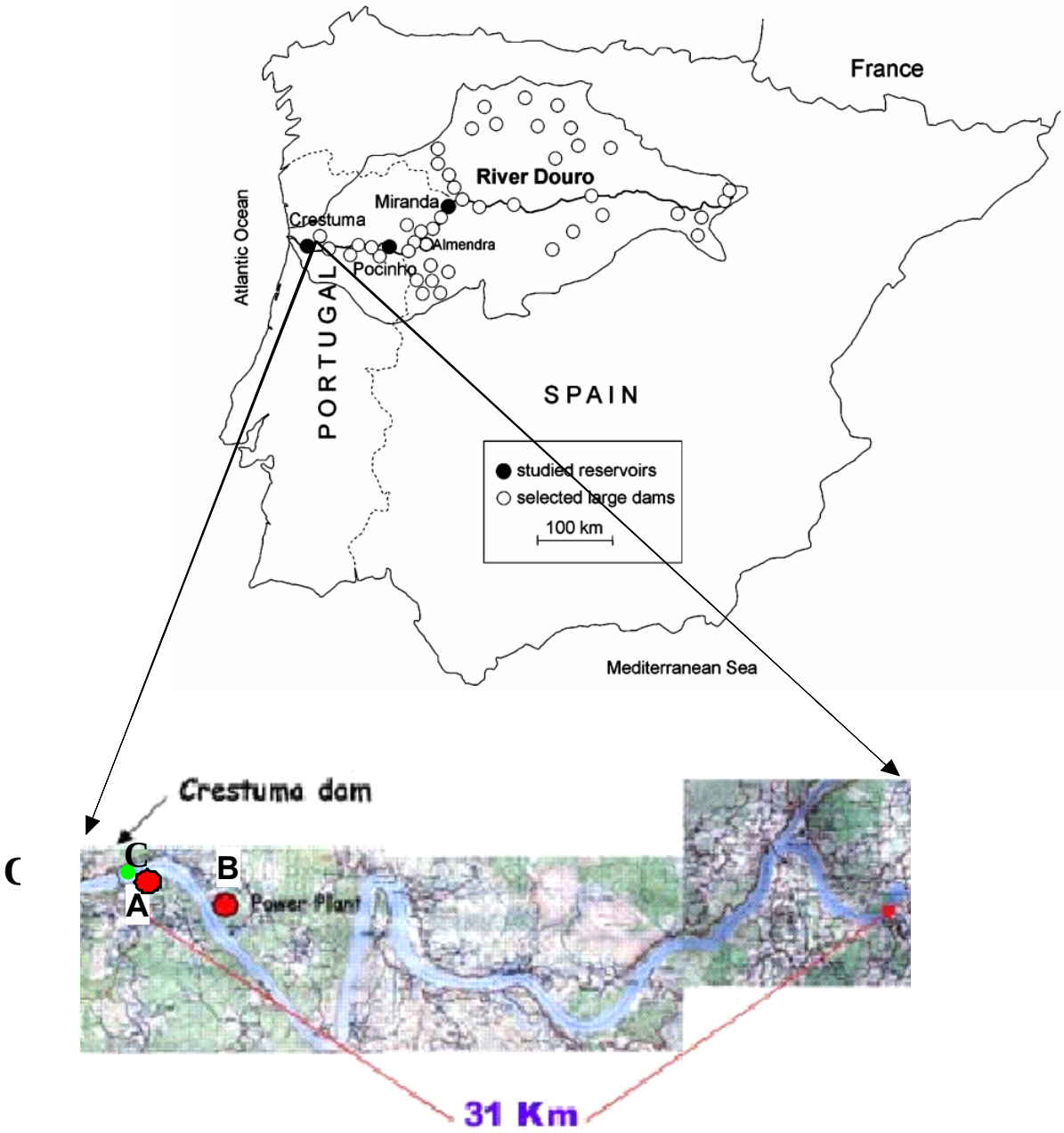

Figure 1 –Crestuma-Lever reservoir with the location of the station where long-term data was obtained (C) by the Portuguese Water Institute (INAG 2003) (cf. Methodology – Data gathering). Also shown the two sampling stations (A and B), used to obtain hourly water quality time-series data between December 2003 and September 2004 (cf. – Methodology – Sampling). Station A located at 500 m from the dam and station B at 2.5 km nearby a Power Plant.

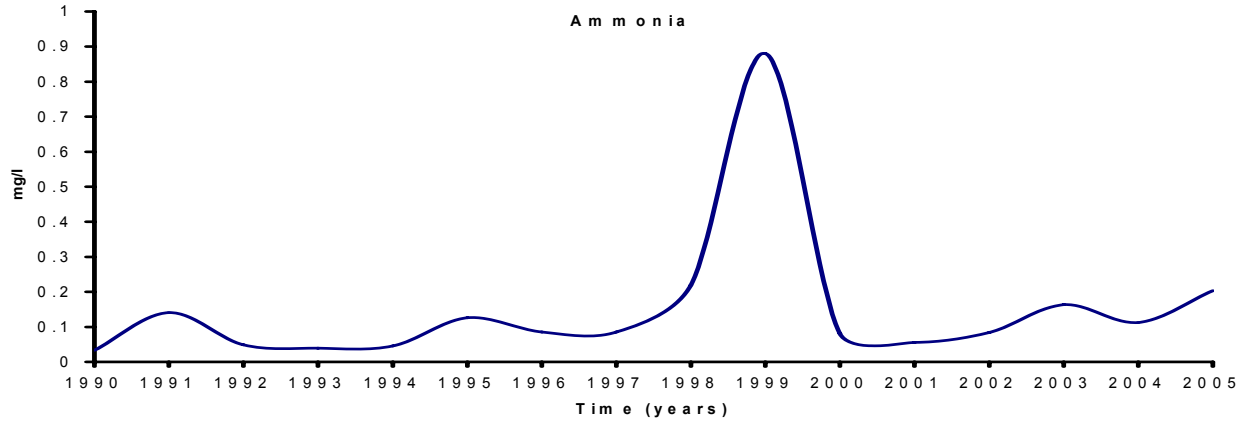
Ammonia
mg/l
1
0.9
0.8
0.7
0.6
0.5
0.4
0.3
0.2
0.1
0
1990 1991 1992 1993 1994 1995 1996 1997 1998 1999 2000 2001 2002 2003 2004 2005
Time (years)

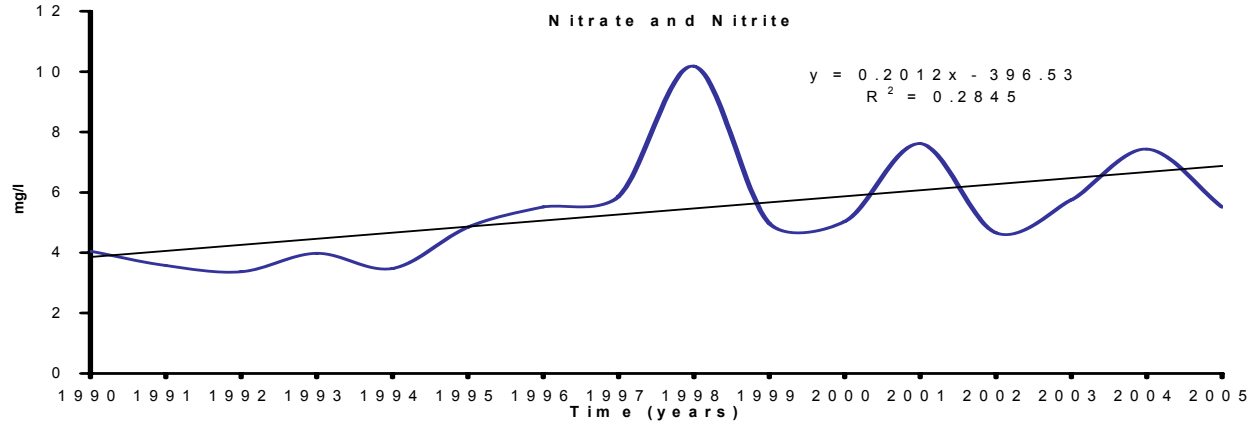
Nitrate and Nitrite
y = 0.2012x - 396.53
R 2 = 0.2845
mg/l
12
10
8
6
4
2
0
1990 1991 1992 1993 1994 1995 1996 1997 1998 1999 2000 2001 2002 2003 2004 2005
Time (years)

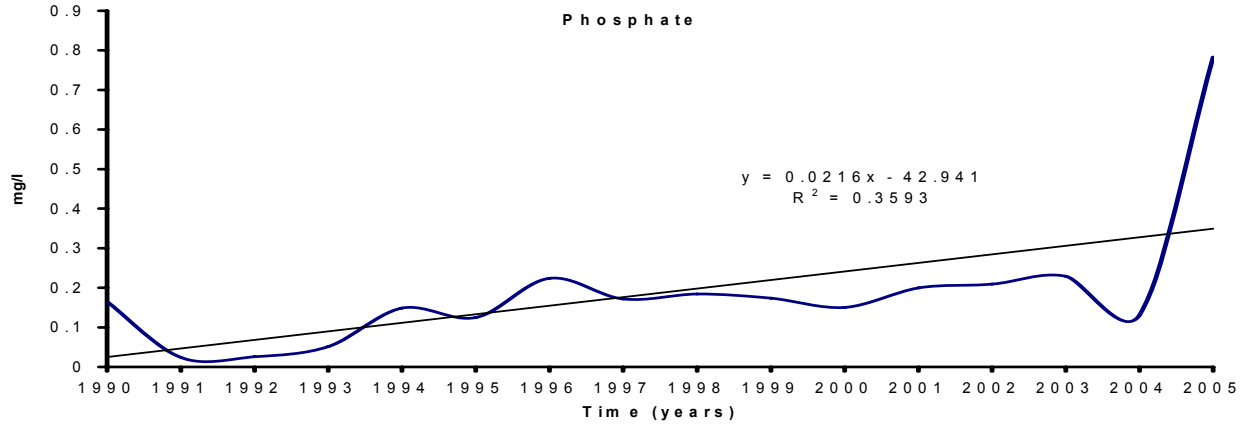
Phosphate
y = 0.0216x - 42.941
R 2 = 0.3593
mg/l
0.9
0.8
0.7
0.6
0.5
0.4
0.3
0.2
0.1
0
1990 1991 1992 1993 1994 1995 1996 1997 1998 1999 2000 2001 2002 2003 2004 2005
Time (years)

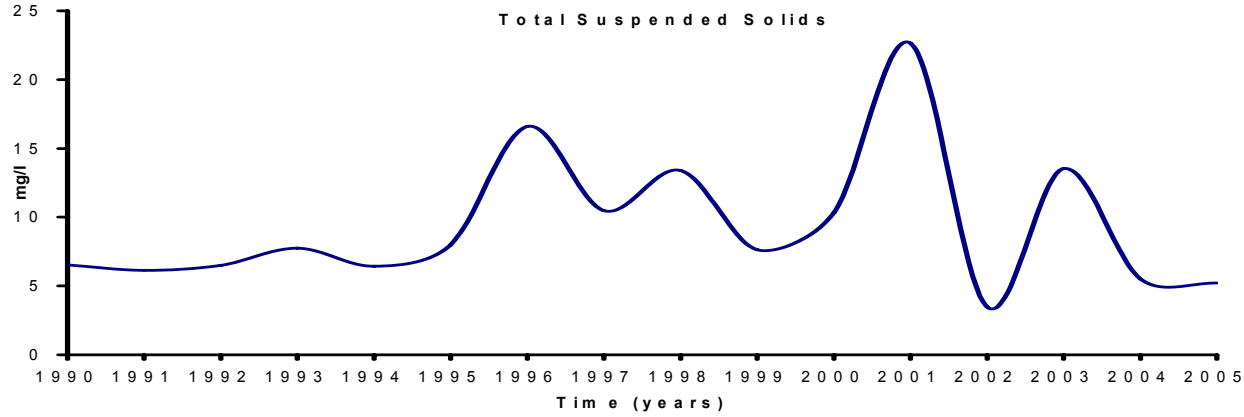
Total Suspended Solids
mg/l
25
20
15
10
5
0
1990 1991 1992 1993 1994 1995 1996 1997 1998 1999 2000 2001 2002 2003 2004 2005
Time (years)

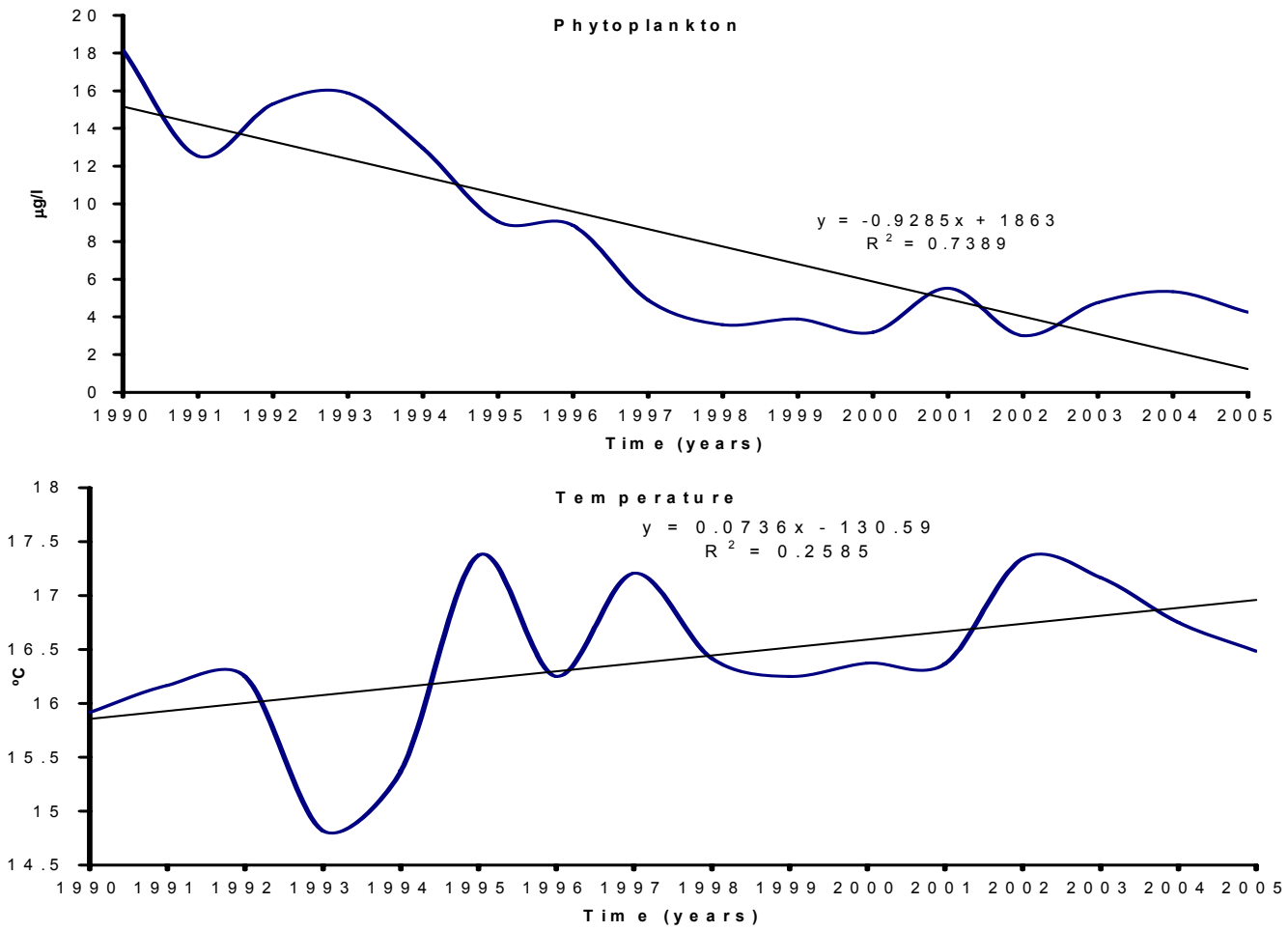

Figure 2 – Yearly variation of several water quality variables from 1990 till 2005. Trend lines are shown where regression slopes between variables and time were significantly different from zero ($p < 0.05$).

Figure 3 – Cluster analysis using the Pearson correlation coefficient and the weighted pair-group average amalgamation scheme, between annual averages for the listed variables, over the period 1990 – 2004 (see text).

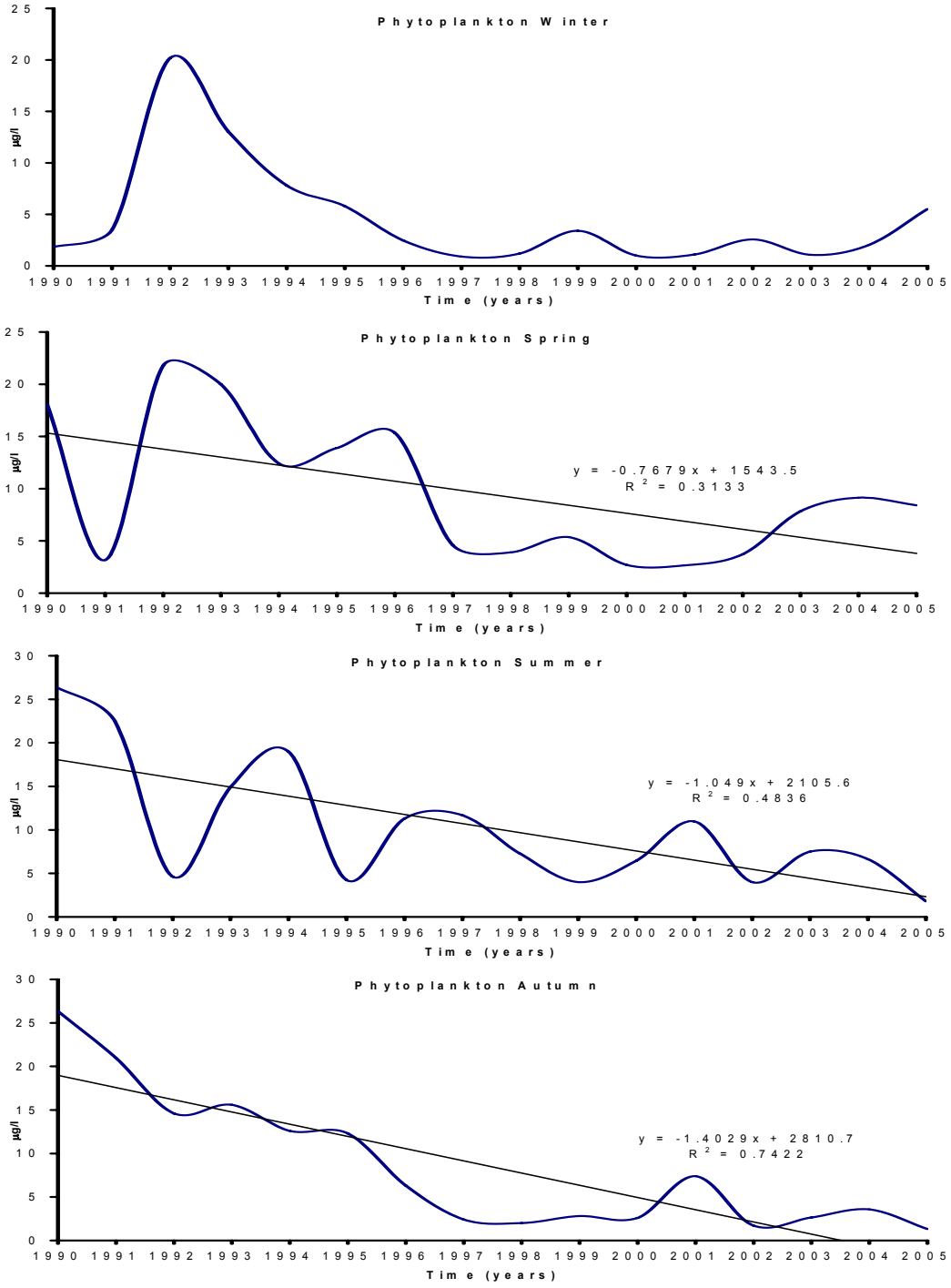

Figure 4 – Inter-annual phytoplankton variation for each season. Trend lines are shown where regression slopes between variables and time were significantly different from zero ($p < 0.05$).

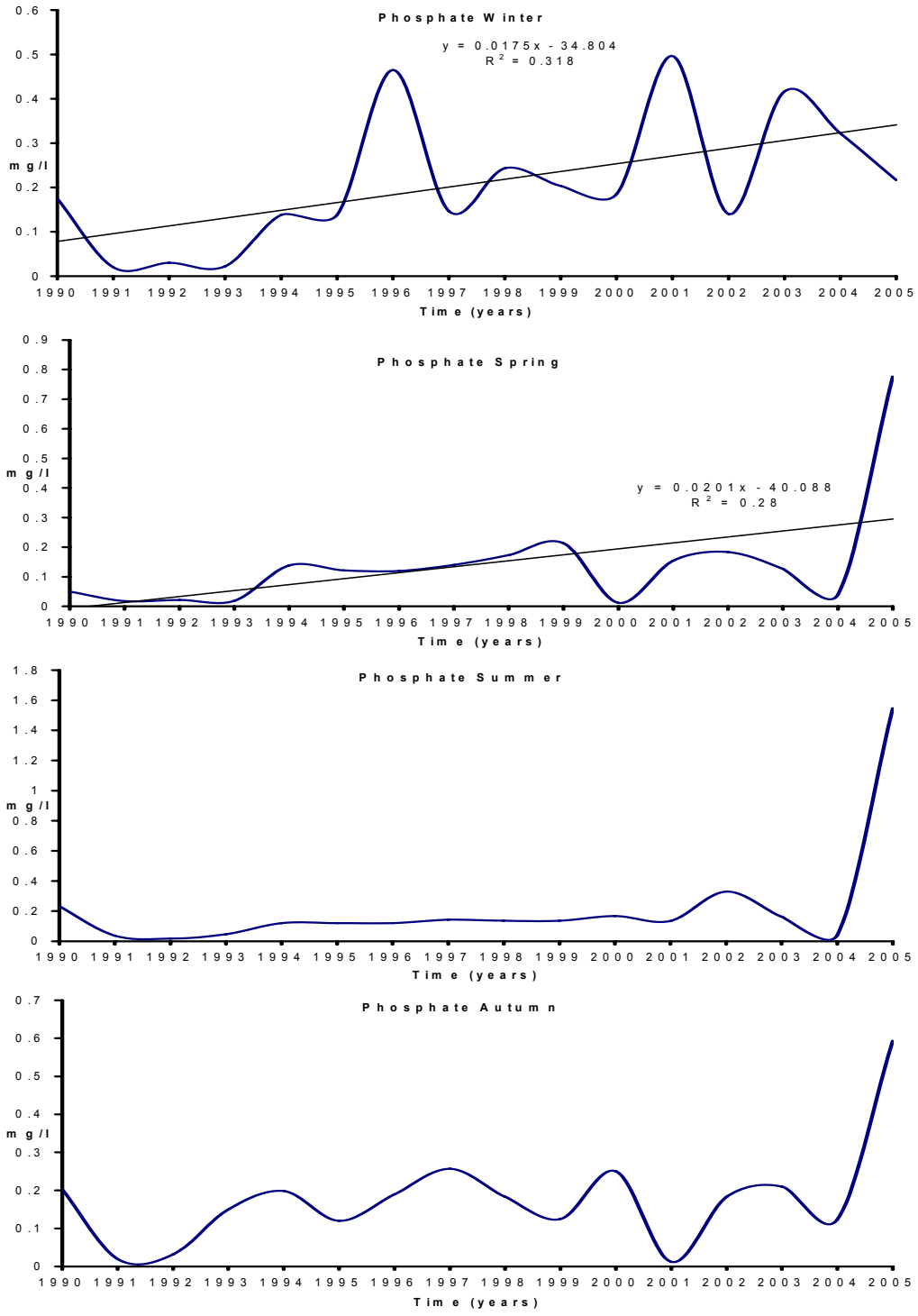

Figure 5 – Inter-annual phosphate variation for each season. Trend lines are shown where regression slopes between variables and time were significantly different from zero ($p < 0.05$).

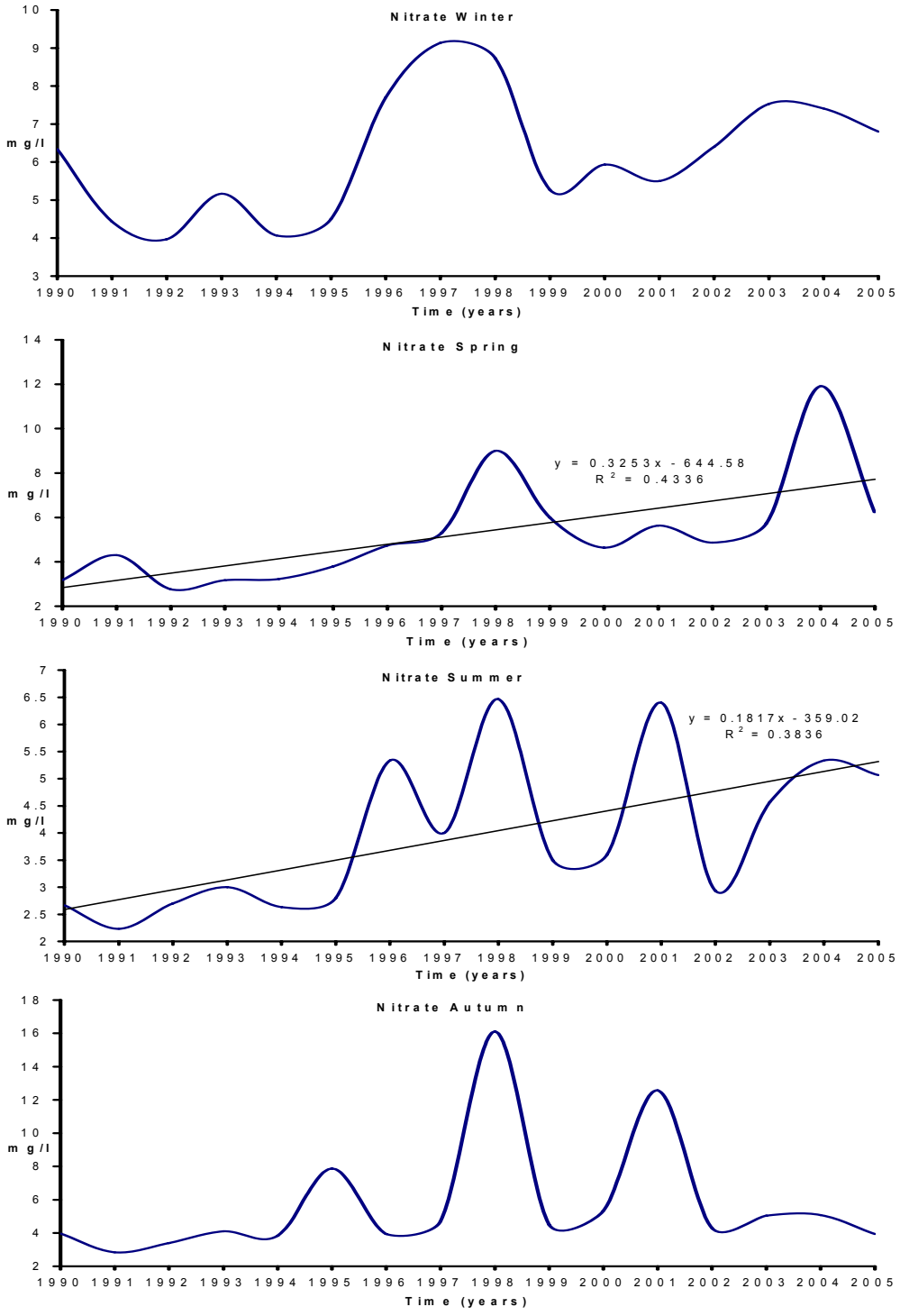

Figure 6 – Inter-annual nitrate variation for each season Trend lines are shown where regression slopes between variables and time were significantly different from zero ($p < 0.05$).

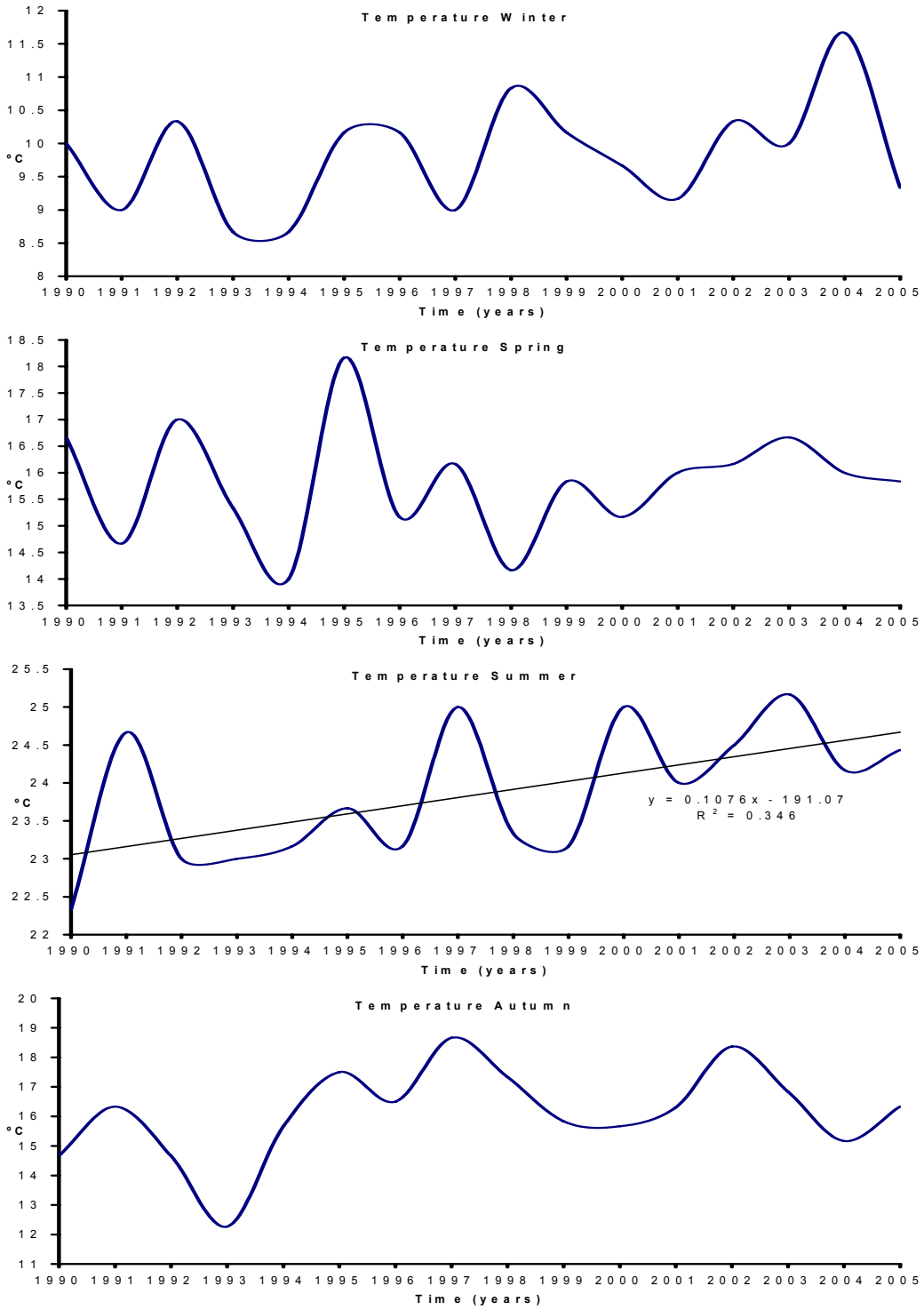

Figure 7 – Inter-annual temperature variation for each. Trend lines are shown where regression slopes between variables and time were significantly different from zero ($p < 0.05$).

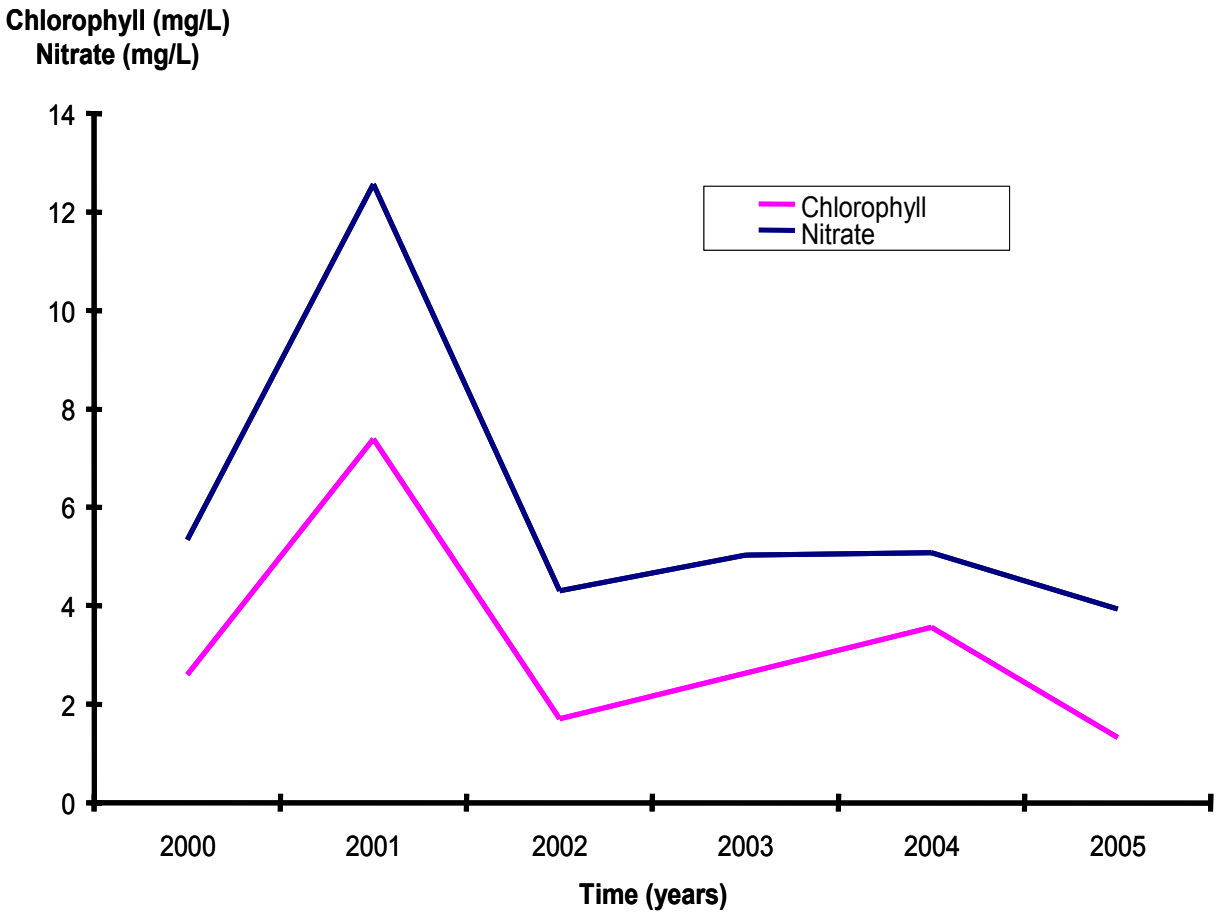

Figure 8 – Comparison between autumn average nitrate and Phytoplankton in Autumn for years 2000 - 2005.

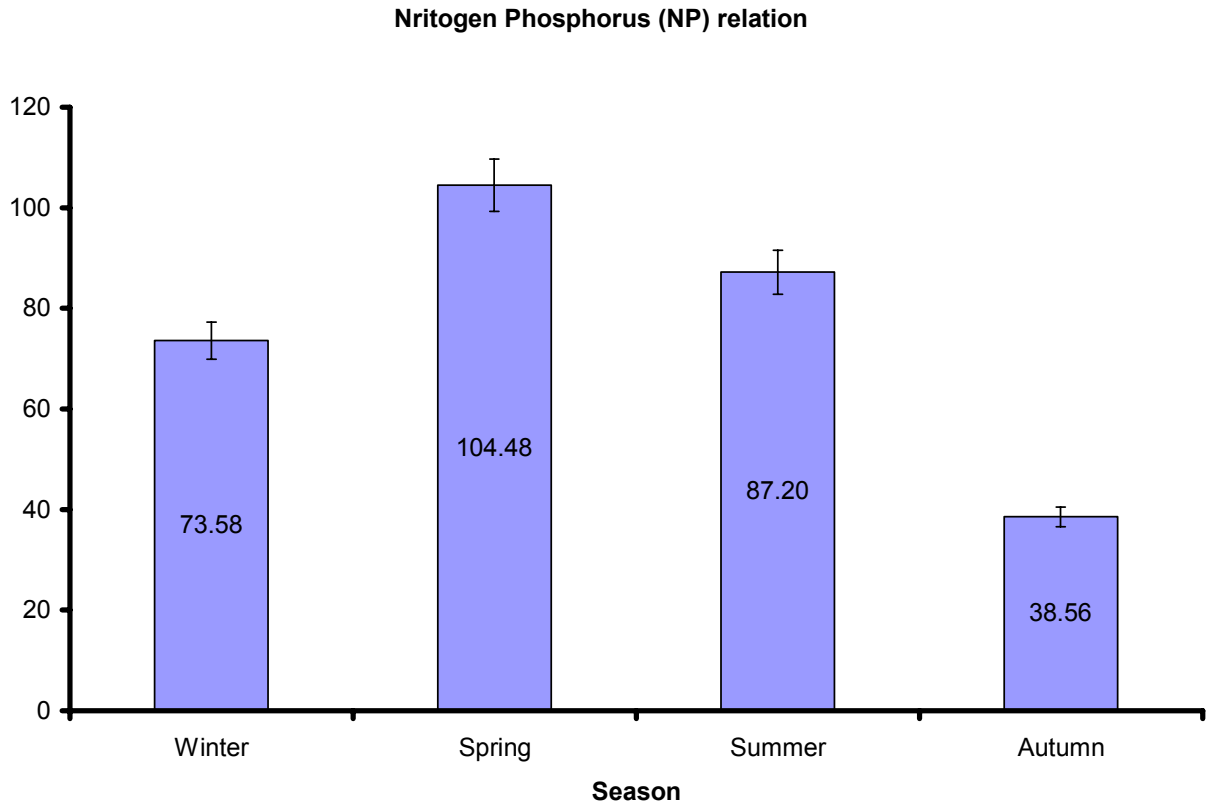

Figure 9 – Average N:P seasonal molar ratios and 95% error bars. Values were integrated for the period 2000 - 2005.

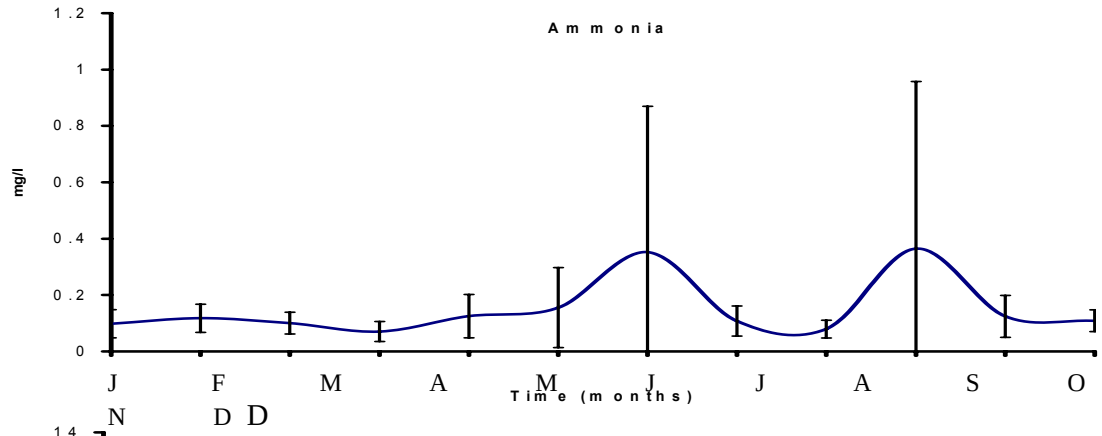
Ammonia
mg/l
1.2
1
0.8
0.6
0.4
0.2
0
J F M A M J J A S O N D D
Time (months)

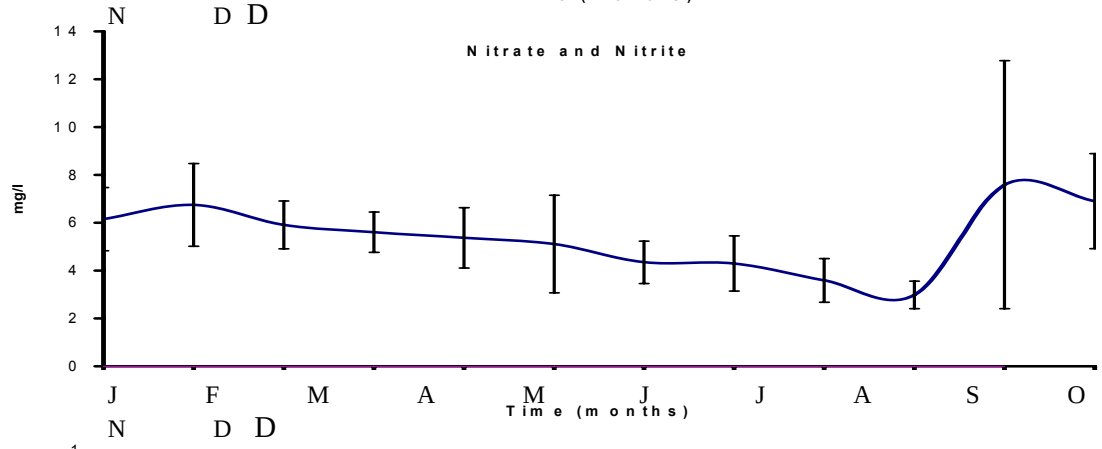
Nitrate and Nitrite
mg/l
14
12
10
8
6
4
2
0
J F M A M J J A S O N D D
Time (months)

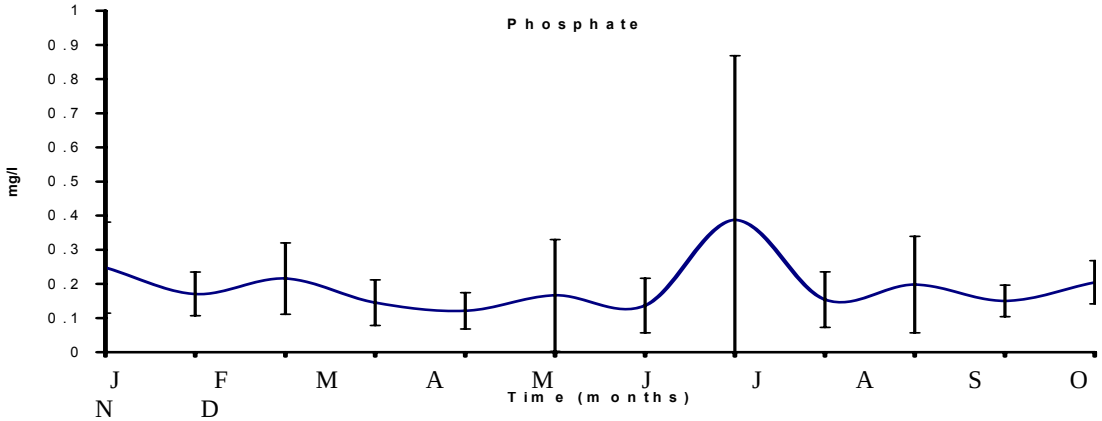
Phosphate
mg/l
1
0.9
0.8
0.7
0.6
0.5
0.4
0.3
0.2
0.1
0
J F M A M J J A S O N D
Time (months)

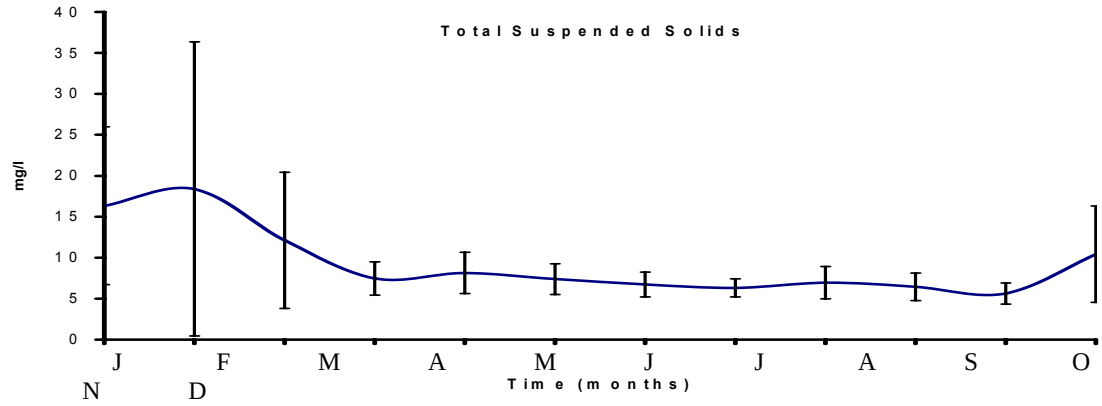
Total Suspended Solids
mg/l
40
35
30
25
20
15
10
5
0
J F M A M J J A S O N D
Time (months)

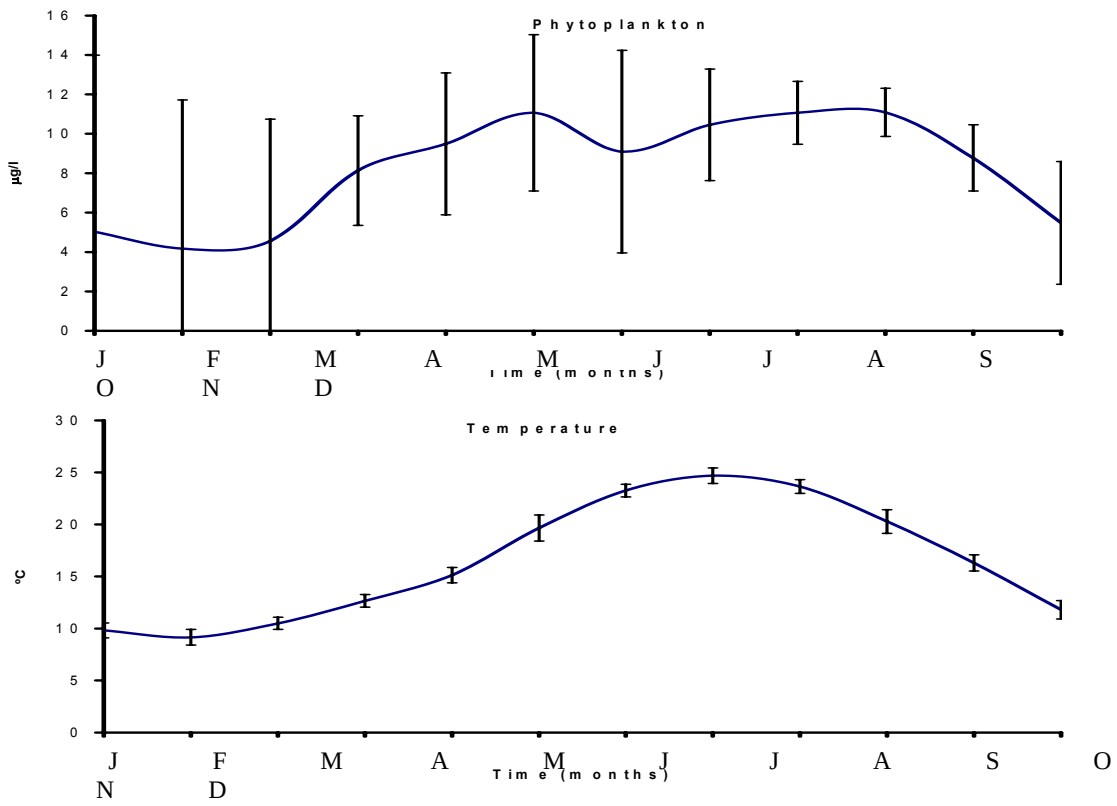

Figure 10 – Monthly variation of several water quality variables. Monthly values were integrated from 1990 till 2005. Error bars were obtained for the 95% confidence level (see text).

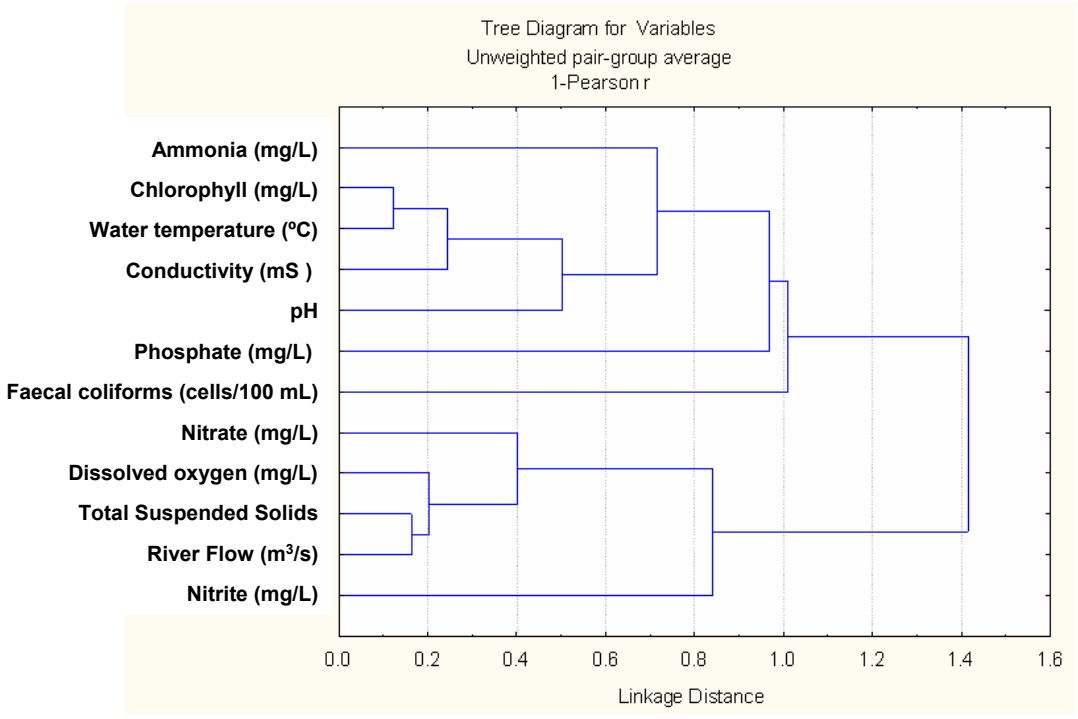

Figure 11 - Cluster analysis using the Pearson correlation coefficient and the weighted pair-group average amalgamation scheme, between monthly averages for the listed variables, integrated for the period 1990 – 2004 (see text).

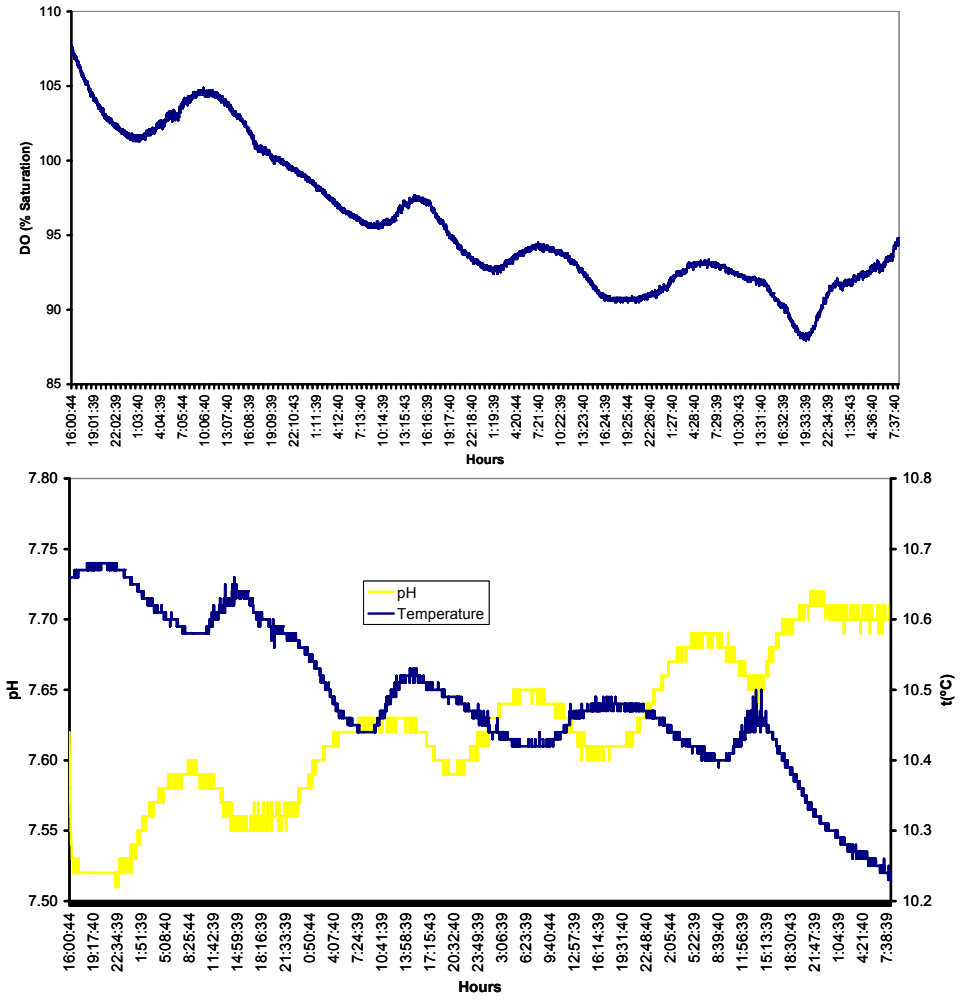

Figure 12 – December 2003: Surface dissolved oxygen saturation, pH and temperature measured at point B (Figure 1), during a five day survey (cf. Table 1).

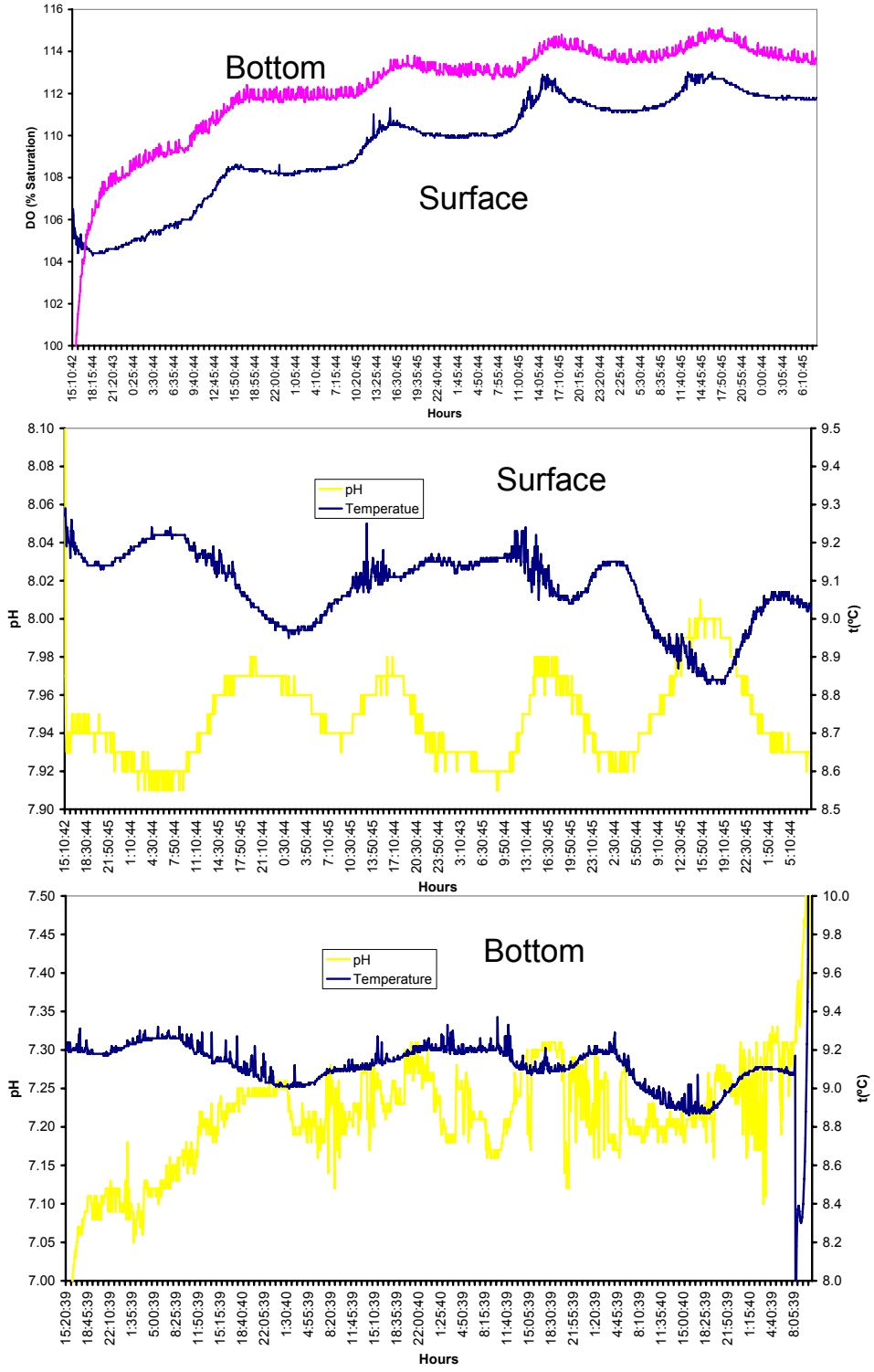

Figure 13 – February 2004: Surface dissolved oxygen saturation, pH and temperature measured at point B (Figure 1), during a five day survey (cf. Table 1).

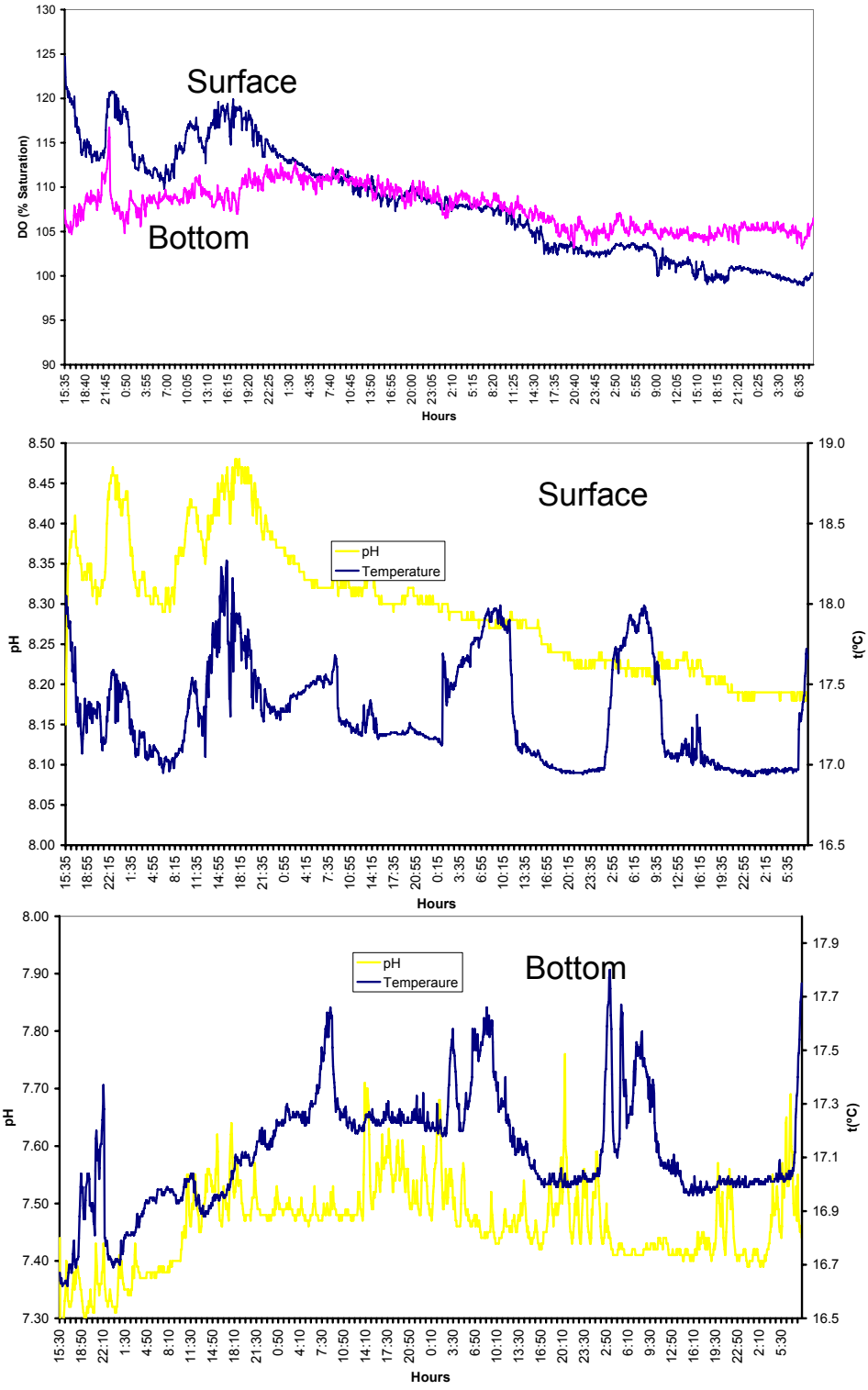

Figure 14 – May 2004: Surface dissolved oxygen saturation, pH and temperature measured at point B (Figure 1), during a five day survey (cf. Table 1).

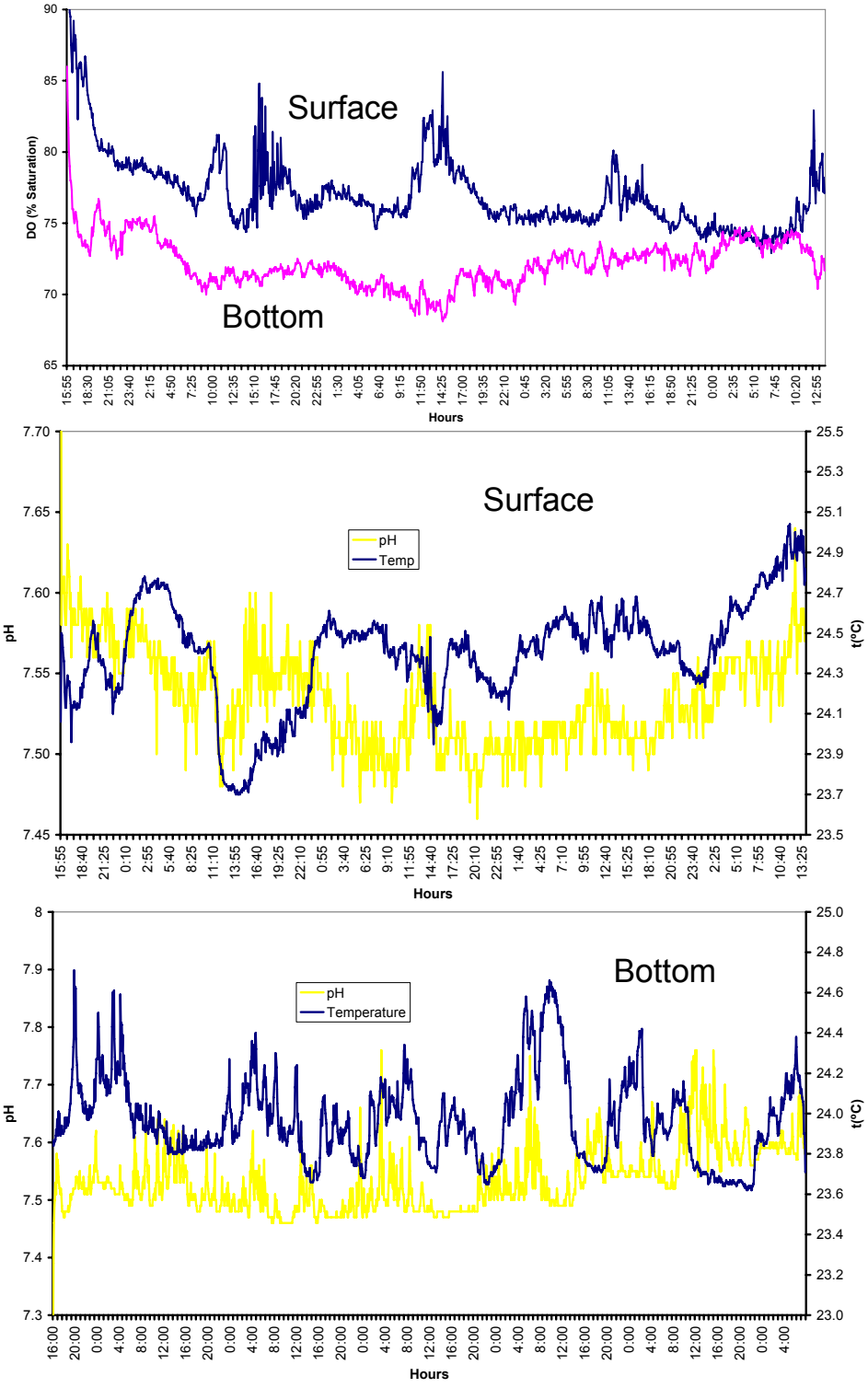

Figure 15 – September 2004: Surface dissolved oxygen saturation, pH and temperature measured at point B (Figure 1), during a five day survey (cf. Table 1).

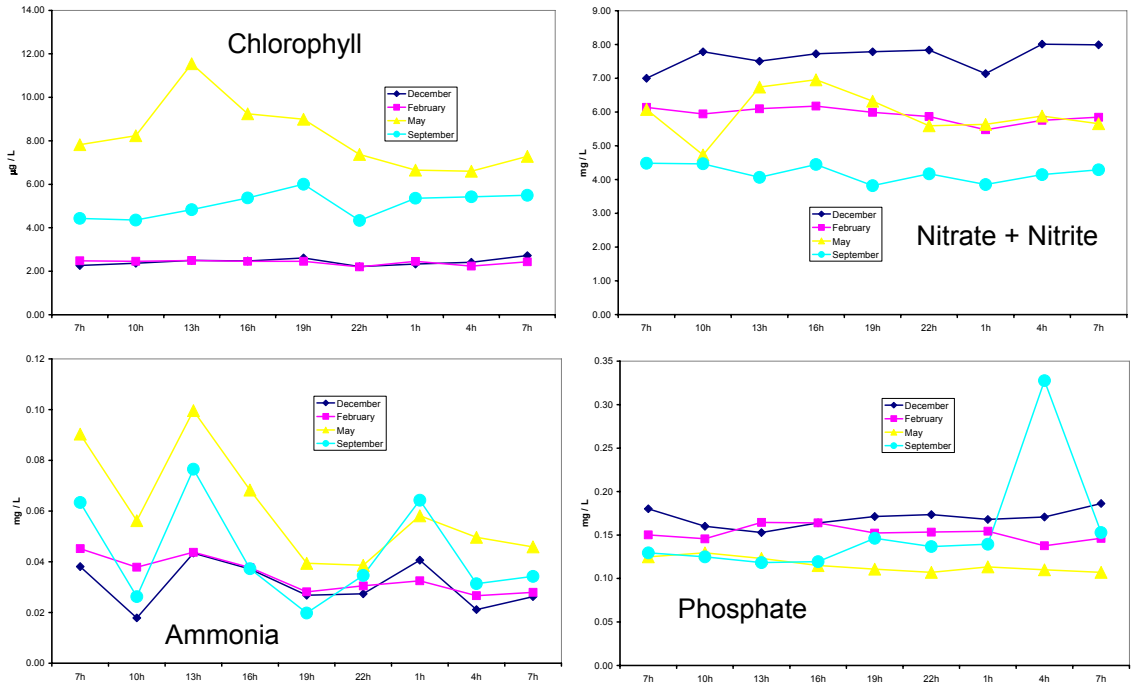

Figure 16 – Surface chlorophyll and nutrient concentrations measured during the 25h campaigns (cf. Table 1). Values were averaged for points A and B depicted in Figure 1.

ANNEX IV

Flow induced variability in ecosystem functioning of Crestuma-Lever reservoir (North of Portugal)

Sampling

Two anchor stations were established. One located 2.5 km upstream the dam crest (station B), and another located at the surface water treatment plant of Águas do Douro e Paiva (ETA), about 500 m from the dam crest (station A) (Fig. 1). Sampling was based on four seasonal eulerian sampling campaigns at December 2003, February, May and July 2004. Data from these campaigns was used to validate the model. Methods used and details on results obtained during these campaigns were discussed elsewhere (Duarte et al., in prep.). Available data consist of several physical, chemical and biological variables and processes such as ammonia, nitrate+nitrite, chlorophyll and dissolved oxygen concentrations and water temperature.

Model conceptuals and tools

The main processes and variables simulated by the model are summarized in Table 2. There are feedbacks between most of them. For example, water temperature depends on heat exchanges between the river, the atmosphere and other water masses, but it also depends on the radiation budget. Phytoplankton production depends on light intensity, water temperature and nutrient concentrations. The concentration of any variable depends not only on its production and decay processes but also on transport (advection and diffusion) by river flow. Horizontal and vertical transport is calculated with a hydrodynamic 2D vertically resolved sub-model, similar to CE-QUAL-W2 (Cole and Wells, 2002). This depends on river flow and horizontal pressure gradients due to differences in water level (barotropic pressure gradients) and density (baroclinic pressure gradients).

The model was implemented in EcoDynamo – a shell for ecological modelling in windows environment (Duarte & Pereira, 2005) - following an object oriented programming methodology. In EcoDynamo, hydrodynamic transport, water temperature, nutrients and phytoplankton are implemented though different sub-

models, as classes (in object oriented programming language), written in C++ code. These classes may be plugged in or unplugged through the software interface.

The basic model equations are the two dimensional versions of the equations of motion (1), continuity (2 for the top layer), (3 for the remaining layers) and the transport equation (4) (Knauss, 1997):

$$\frac{du_X}{dt}+\frac{\partial(uu)}{\partial x}+\frac{\partial(uw)}{\partial z}-\nu_X\frac{\partial^2 u}{\partial_X{}^2}-\nu_Z\frac{\partial^2 w}{\partial_Z{}^2}=-\frac{\partial P}{\rho\partial x}-\frac{Cf\,|u|u}{H}+\frac{\partial\tau_X}{\rho\partial z} \qquad (1)$$

$$\frac{d\xi}{dt}=\frac{\partial u_X}{\partial x}+\frac{\partial w_Z}{\partial z} \qquad (2)$$

$$\frac{\partial u_X}{\partial x}+\frac{\partial w_Z}{\partial z}=0 \qquad (3)$$

$$\frac{dS}{dt}+\frac{\partial(uS)}{\partial x}+\frac{\partial(wS)}{\partial z}=\frac{\partial\left(A_X\frac{\partial S}{\partial x}\right)}{\partial x}+\frac{\partial\left(A_Z\frac{\partial S}{\partial z}\right)}{\partial z} \qquad (4)$$

Where,

u and w – Horizontal (*x* direction) and vertical (*z* direction) current speeds (m s^{-1});
t – Time (s);
x and *z* – Horizontal and vertical distances (m);
n_x and $\tilde{\eta}_z$Coefficients of horizontal and vertical momentum diffusion (m^2 s^{-1});
P – Pressure (N m^{-2});
r – Density (kg m^{-3});
Cf – Drag coefficient;
H – Layer depth (m);
x – Surface elevation (m);
t – Wind drag (N m^{-2});
S – Concentration of any property;
A_x and $\tilde{A}_z$Coefficients of horizontal and vertical mass diffusion (m^2 s^{-1}).

A finite differences grid was used to implement the above equations. Crestuma-Lever reservoir was divided in several compartments (boxes) (Fig. 2) each with 500 m length. Each compartment is divided in 20 vertical layers. The initial depth of each

layer (but the bottom one) is 2 m. The average width and volume were estimated from data obtained with a bathymetric survey, using a GIS under ArcGIS 8.1. The 2D model represents the reservoir as a V-shaped channel divided in several compartments and layers. Current velocities and flows are calculated at the boundaries between the cells, whereas water properties are calculated at its centres. Surface elevation is calculated at the centre of each cell of the surface layer (Fig. 3).

The first five terms of equation 1 represent the variation of flow rate over time, convection and turbulent diffusion in both directions. The right terms represent the pressure gradient, the bottom drag and the wind drag. The pressure term has two components – a barotropic and a baroclinic component. Equation 2 implies that any changes in flow rate over the river channel will produce correspondent changes in water height at the top layer, for volume conservation. These changes in water height generate the barotropic part of the pressure gradient represented in equation 1. The baroclinic part results from pressure gradients caused by density variations. Equation 3 - a simplified form of equation 2 - is applied for all layers but the top one to calculate vertical velocities.

The above equations are solved algebraically, similarly to what has been described in Martins (1999). The stability analysis described in Santos (1995) and Martins (1999) suggests that all terms of equation (1) may be solved explicitly, except the barotropic pressure, the vertical diffusion and the bottom drag terms that should be solved implicitly.

Each variable is described by a differential equation which is a mass balance including production, decay and transport processes (Table 3). The variables are resolved simultaneously for each model compartment and layer and transported among them by the transport sub-model using the numerical solution of equation 4. Equation 5 represents the heat budget of the water mass. The calculations of the fluxes represented on the right side of 5 is based on standard formulations described in Brock (1981) and Portela & Neves (1994). Equations 6 and 7 represent the mass balance for dissolved inorganic nitrogen and phosphorus, respectively. In fact, the model computes the concentrations of three nitrogen forms – ammonia, nitrite and nitrate. The fluxes represented in these equations correspond to gain and loss processes dependent on nutrient uptake by phytoplankton, nutrient regeneration and nutrient loads. Equations 8 – 10 describe phytoplankton mass balance in carbon, nitrogen and phosphorus units.

The model is forced by river flow, river temperature, nutrient and phytoplankton loads, light intensity, wind speed, cloud cover, air humidity and air temperature. There are forcing function objects in EcoDynamo that read the appropriate values from files or calculate them for use by other objects. Surface light intensity is calculated from standard formulations described in Brock (1981) and Portela & Neves (1994).

Phytoplankton productivity is described as a function of light intensity (depth integration Steele's equation (Steele, 1969), temperature and a limiting nutrient – nitrogen or phosphorus (Table 4, equations 11 and 15). In this model, phytoplankton is represented through a chlorophyll, a carbon, a nitrogen and a phosphorus pool. This allows the necessary bookkeeping calculations on cell quotas. Traditional approaches with models based solely on nitrogen or phosphorus do not allow these computations. Internal cell quotas are then used to limit carbon fixation through photosynthesis. A nutrient limiting factor in the range 0 – 1 is calculated both for internal nitrogen and phosphorus. The lowest obtained value is then multiplied by light and temperature limited photosynthesis following Liebig's law of minimum.

Nutrient uptake and limitation is described as a three-stage process (Table 4, equations 18 - 23):

(i) The uptake of nitrogen and phosphorus is dependent on their concentration in the water, on their cell quotas and on their cellular ratios;

(ii) After uptake, nutrients accumulate in the cells;

(iii) The internal nutrient concentration is used to limit phytoplankton productivity.

A Michaelis-Menten equation is used to relate nutrient uptake with their concentration in the water, following several authors (e.g. Parsons et. al., 1984; Ducobu et al., 1998; Jørgensen & Bendoriccchio, 2001). The parameters of this equation are the half-saturation constant and the maximum uptake rate. These were taken from the literature, within the range of measured values (Cochlan and Harrison, 1991; Jørgensen & Jørgensen, 1991). The Michaelis-Menten equation is not the only regulating mechanism of nutrient uptake, which is also constrained by current cell quotas to avoid values outside ranges reported in the literature. Further, when N:P ratios are outside limits currently measured, N or P uptake is constrained. Nitrogen uptake rate is calculated first for ammonium nitrogen and then for nitrite + nitrate, reducing their uptake proportionally to ammonium uptake (21). This is based on the

usual assumption that ammonium is the preferred nitrogen source for phytoplankton (Parsons et al., 1984). Phytoplankton respiration is based on the model of Langdon (1993) (Table 4, equations 27 and 28). Table 5 synthesizes parameter values used in the model.

Model simulations

Four simulations were carried out with the same average flow magnitude and forcing conditions, in terms of water temperature, nutrients and chlorophyll concentrations, but different flow frequencies and amplitudes. Forcing conditions were based on data from INAG web site (http://cnpgb.inag.pt/) (Fig. 4), averaged over the period 1990-2005 and collected upstream the model domain (Fig. 2). Regarding river flows, hourly values were used, provided by EDP for the year 2003. A first simulation (hereafter referred as simulation 1) was carried out to compare model data with observations made during 2003/2004 at sampling points A and B, depicted in Fig. 1 (cf. – *Sampling*). Since hourly flow data was not made available for the same period when field data was obtained, it was not possible to properly validate the model. In any case, a comparison was made between model and observations to see whether predictions remained within normal ranges. The hourly flow rate was then integrated to obtain a time series of daily flow rates to produce simulation 2. Simulation 3 was carried out with monthly integrated flow data. Finally, simulation 4 was based on yearly integrated flow data (i.e. a constant flow rate). Therefore, from simulation 1 till 4, time variability in flow rates was reduced. All simulations covered a period of one year and their results compared at several time scales: yearly, monthly and daily (Fig. 5). Model time step is two seconds.

Results and Discussion

Figs. 6 - 9 show daily integrated model results for a period of one year, against daily integrated nutrient, chlorophyll and water temperatures, for the sampling campaigns described above (cf. – Methodology – *Sampling*). As mentioned before (cf. – Methodology – *Model simulations*), comparisons between observations and model results are limited by the fact that the model was forced with average water quality data for the period 1990 – 2005 and river flows for the year 2003, whereas sampling was carried out in December 2003, February, May and September 2004. This lack of agreement between different sources of information is explained by the fact that it was not possible to get hourly flow data for 2004. Therefore, it was assumed that

using forcing function nutrient, chlorophyll and water temperature data, integrated over a large time span, would be more representative then using values for years 2003/2004, when river flows were not available for the same period.

The analysis of Figs. 6 - 9, suggests that model results are comparable with observations. The model tends to overestimate chlorophyll concentrations mainly in the second half of the year. This may be explained by the forcing data problems mentioned above and/or by not taking into account the rope of the invasive species *Corbicula sp*.- the Asiatic clam – present in the Douro since the eighties. This suspension feeder may have a significant impact on phytoplankton (Duarte et al., in prep), specially considering the large densities that were observed in areas of Crestuma-Lever reservoir - 1000 ind. m^{-2} (Bordalo e Sá, unpublished). When different forcing data was used (e.g. water temperature, nutrient and chlorophyll concentrations for 2003) model results showed the same type of agreement with observations, suggesting that the model is reasonably realistic for the purposes of this work (not shown).

A sensitivity analysis was carried out by running several simulations and changing one parameter at each time. Changes consisted in a 10% increase or decrease. The average results for several variables were compared with those of a standard simulation (parameter values as in Table 5). Results obtained show that the 10% changes in model parameters produced less than 5% changes in variables depicted in Table 6, except for *Pmax*, the phytoplankton respiration parameters and the horizontal diffusion coefficient over Net Primary Production (NPP) and the B/P ratio (chlorophyll / NPP). In these cases, changes were larger than 5 % in response to changes in the respiration parameters and over 10 % in response to changes in the diffusion coefficient. These are therefore the parameters that may be more influential in future improvements on model performance.

Table 7 synthesizes yearly averages, minimum and maximum values for simulations 1, 2, 3 and 4. It is apparent that differences between simulations are rather small, except for ammonium. Obtained results suggest that at the annual time scale flow variability does not seem to have a very strong effect on water temperature, nutrient concentrations (except ammonia), phytoplankton biomass and production.

Figs 10 and 11 compare seasonally averaged model results for the four simulations mentioned above. It is apparent that simulation 4 is the one that exhibits the larger

differences by comparison with all the others, especially concerning ammonium, chlorophyll and NPP in summer. The higher NPP per unit of biomass may result from the lower phytoplankton biomass and higher ammonium concentration. A similar comparison is made in Figs 12 and 13, but with monthly averaged results. Here again simulation 4 is clearly different from the remaining ones, with respect to ammonia and NPP, exhibiting higher values. These differences result from synergies between forcing from upstream and internal processes within the reservoir. In simulation 4, flow rates remain relatively high in summer probably diluting phytoplankton growth and releasing cells from nutrient limitation, leading to high NPP.

Figs 14 and 15 show surface plots for the whole model domain, for water temperature and chlorophyll, obtained from simulation 1, for a day in July, at 0, 12 and 17H, under low river flow – around 100 $m^3 s^{-1}$. In Fig. 14 a thermocline develops during daytime. It is also clear the temperature signal at the area where a power plant discharges its warm effluent. This effect was included in the model as a constant outflow of 10 $m^3 s^{-1}$ over the whole water column, at the grid points corresponding to the proximate location of the power plant, following Bordalo e Sá et al. (2003). The thermocline holds phytoplankton near the surface during the day (Fig. 16).

Conclusions

The results obtained in this work suggest that flow variability may not have a large effect on water temperature, nutrient and chlorophyll concentration and NPP at annual time scales. However, when the time scale under analysis is reduced to seasonal and monthly, effects of flow variability become apparent, especially in summer and when the flow is hold constant. Under this situation of “extreme” flow regulation, it appears that the synergies between river forcing and reservoir processes tend to reduce nutrient limitation, increasing NPP. This may result from larger summer flow rates diluting phytoplankton biomass within the reservoir. Therefore, from a management point of view, it is apparent that stabilizing the flow may prevent the development of phytoplankton blooms. Surprisingly were the insignificant differences between simulations 1, 2 and 3, suggesting that rapid flow changes, as those in simulation 1, do not produce results differing much from those resulting from a smoothed flow, as in simulations 2 and 3.

References

Bordalo e Sá, A., Duarte, P., Teixeira, R., Azevedo, I. & W. J. Wiebe, 2003. Possible effects of cooling water discharge on the water quality of the Crestuma reservoir. Instituto de Ciências Biomédicas Abel Salazar.

Brock, T.D., 1981. Calculating solar radiation for ecological studies. Ecol. Modelling 14: 1 – 9.

Busch DE, Smith SD. 1995. Mechanisms associated with decline of woody species in riparian ecosystems of the Southwestern US. Ecological Monographs 65: 347–370. Castleberry DT, et al. 1996. Uncertainty and instream flow standards. Fisheries 21: 20–21.

Cochlan, W. P. & P.J. Harrison, 1991. Uptake of nitrate, ammonium, and urea by nitrogens-starved cultures of Micromonas pusilla (Prasinophyceae): transient esponses. J. Phycol.: 673-679.

Cole, T. Wells, M., 2002. CE-QUAL-W2: A two-dimensional, laterally averaged, Hydrodinamic and Water Quality Model, Version 3.1, Instructions Report EL-2002-1, US Army Engineering and Research Development Center, Vicksburg, MS.

Cushman RM. 1985. Review of ecological effects of rapidly varying flows downstream from hydroelectric facilities. North American Journal of Fisheries Management 5: 330–339.

Ducobu, H., Huisman, J., Richard, Jonker, R. & L.R. Mur, 1998. Competition between a Prochlorophyte and a Cyanobacterium under various phosphorus regimes: comparison with the droop model. Journal of Phycology: 467-476.

Duncan RP. 1993. Flood disturbance and the coexistence of species in a lowland podocarp forest, south Westland, New Zealand. Journal of Ecology 81: 403–416.

Grant, J., & C. Bacher, 2001. A numerical model of flow modification induced by suspended aquaculture in a Chinese Bay. Can. J. Fish. Aquat. Sci. 58: 1 - 9.

European Commission, 2000. Directive 2000/60/CE of the European Parliament and of the Council of 23 October 2003 establishing a framework Different modelling tools of aquatic ecosystems 33 for Community actin in the field of water policy. Off. J. Eur. Communi. L327, 22.12.2000, p.1.

Fausch KD, Bestgen KR. 1997. Ecology of fishes indigenous to the central and south- western Great Plains. Pages 131–166 in Knopf FL, Samson FB, eds. Ecology and conservation of Great Plains vertebrates. New York: Springer-Verlag.

Gehrke PC, Brown P, Schiller CB, Moffatt DB, Bruce AM. 1995. River regulation and fish communities in the Murray-Darling river system, Australia. Regulated Rivers: Research & Management 11: 363–375.

Jørgensen, S.E. & G. Bendoricchio, 2001. Fundamentals of ecological modelling. Developments in Ecological Modelling 21. Elsevier, Amsterdam, 530 pp.

Jørgensen, S.E., Nielsen, S. & L. Jørgensen, 1991. Handbook of Ecological Parameters and Ecotoxicology. Elsevier, Amsterdam, 1263 pp.

Kingsolving AD, Bain MB. 1993. Fish assemblage recovery along a riverine disturbance gradient. Ecological Applications 3: 531–544.

Knauss, J.A. 1997. Introduction to physical oceanography. Prentice-Hall.

Kupferberg SK. 1996. Hydrologic and geomor- phic factors affecting conservation of a river- breeding frog (Rana boylii). Ecological Applications 6: 1332–1344.

Langdon, C., 1993. The significance of respiration in production measurements based on oxygen. ICES mar. Sci. Symp. 197, 69-78.

Mann, K.H. & J.R.M. Lazier, 1996. Dynamics of marine ecosystems. Blackwell Science.

Martins, F.A.B.C., 1999. Modelação matemática tridimensional de escoamentos costeiros e estuarinos usando uma abordagem de coordenada vertical genérica. PhD, Instituto Superior Técnico, Universidade Técnica de Lisboa.

Meffe GK. 1984. Effects of abiotic disturbance on coexistence of predator and prey fish species. Ecology 65: 1525–1534.

Montgomery WL, McCormick SD, Naiman RJ, Whoriskey FG, Black GA. 1983. Spring migratory synchrony of salmonid, catostomid, and cyprinid fishes in Rivière á la Truite, Québec. Canadian Journal of Zool- ogy 61: 2495–2502.

Moyle PB, Light T. 1996. Fish invasions in California: do abiotic factors determine success? Ecology 77: 1666–1669.

Neves, R.J.J., 1985. Étude expérimentale et modélisation mathématique des circulations transitoire et rédiduelle dans l'estuaire du Sado. Ph.D. Thesis, Université de Liège.

Nilsson C. 1982. Effects of stream regulation on riparian vegetation. Pages 93–106 in Lillehammer A, Saltveit SJ, eds. Regulated rivers. New York: Columbia University Press.

Parsons, T.R., Takahashi, M., & B. Hargrave, 1984. Biological oceanographic processes. 3rd. Edition. Pergamon Press.

Pereira, A. and Duarte, P., 2005. EcoDynamo: Ecological Dynamics Model Application. DITTY report. Available at http://www.dittyproject.org/Reports.asp.

Petts GE. 1984. Impounded rivers: perspectives for ecological management. New York: John Wiley & Sons.

Poff NL, Ward JV. 1989. Implications of streamflow variability and predictability for lotic community structure: a regional analysis of streamflow patterns. Canadian Jour- nal of Fisheries and Aquatic Sciences 46: 1805–1818.

Portela, L.I. & Neves, R. (1994). Modelling temperature distribution in the shallow Tejo estuary. In: Tsakiris & Santos (ed.). Advances in Water Resources Technology and Management (pp. 457 – 463) Balkema.

Power ME. 1992. Hydrologic and trophic controls of seasonal algal blooms in northern California rivers. Archiv für Hydrobiologie 125: 385–410.

Richter BD, Baumgartner JV, Powell J, Braun DP. 1996. A method for assessing hydro- logic alteration within ecosystems. Conservation Biology 10: 1163–1174.

Santos, A.J.P., 1995. Modelo hidrodinâmico tridimensional de circulação oceânica e estuarina. PhD, Instituto Superior Técnico, Universidade Técnica de Lisboa.

Shankman D, Drake DL. 1990. Channel migration and regeneration of bald cypress in western Tennessee. Physical Geography 11: 343–352.

Sparks, R.E., Bayley, P.B., Kohler, S.L. and Osborne, L.L., 1990. Disturbance and recovery of large floodplain rivers. Environ. Mgmt, 14, 699-709.

Stanford JA. 1994. Instream flows to assist the recovery of endangered fishes of the Upper Colorado River Basin. Washington (DC): US Department of the Interior, National Biological Survey. Biological Report nr 24. Stanford JA, Ward JV, Liss WJ, Frissell CA, Williams RN, Lichatowich JA, Coutant CC.

Steele, J.H., 1962. Environmental control of photosynthesis in the sea. Limnol. Oceanogr., 7: 137-150.

Taylor DW. 1982. Eastern Sierra riparian vegetation: ecological effects of stream diversion. Mono Basin Research Group Contribution nr 6, Report to Inyo National Forest.

Travnichek VH, Bain MB, Maceina MJ. 1995. Recovery of a warm water fish assemblage after the initiation of a minimum-flow re- lease downstream from a hydroelectric dam. Transactions of the American Fisheries Society 124: 836–844.

Valentin S, Wasson JG, Philippe M. 1995. Effects of hydropower peaking on epilithon and invertebrate community trophic structure. Regulated Rivers: Research & Management 10: 105-119.

Vieira, M. E. C., and Bordalo A. A. 2000. The Douro estuary (Portugal): A mesotidal salt wedge. Oceanologica Acta 23: 585–594.

Walker KF, Sheldon F, Puckridge JT. 1995. A perspective on dryland river ecosystems. Regulated Rivers: Research & Management 11: 85–104.

Ward JV, Stanford JA. 1979. The ecology of regulated streams. New York: Plenum Press.

WFD. 2000. Water framework directive. Official Journal of the European Community 22.12.2000, L327:1–73.

Tables

Table 1 – Average value for several water quality variables over the period 1990-2005, according to data from INAG web site (http://cnpgb.inag.pt/).

Variables	Mean values
Ammonia	0.15 mg L^{-1}
Chlorophyll	8.20 mg L^{-1}
Conductivity	210.4mS
Faecal coliforms	5314 per 100 mL
Nitrate + nitrite	5.37 mg L^{-1}
Oxygen saturation	91.0 %
pH	7.50
Phosphate	0.19 mg L^{-1}

Table 2 - Main processes and variables simulated by the model. There are feedbacks between most of the processes and variables as in the real system (see text).

	Physical processes and variables			Biogeochemical processes and variables	
	Thermodynamic	Transport	Radiation balance	Nutrients	Phytoplankton
Processes	Heat exchanges between the water and the atmosphere and between different water masses	Advection and diffusion of water	Water reflection and emission and sun light absorption	Nutrient consumption and regeneration	Phytoplankton production and decay
Variables	Water temperature and density	Current velocity and flow	Light intensity as a function of depth and water turbidity	Nitrogen and phosphorus concentrations	Phytoplankton biomass

Table 3 - Main model equations representing the changes in the state variables as a function of time. The equations are solved for all 22 model compartments and 7 layers. Fluxes are expressed in Carbon, Nitrogen and Phosphorus units (see text).

Water temperature changes (ºC d^{-1})

$$\frac{dT_{ij}}{dt} = solar\_radiation + atmospheric\_emission - water\_emission - latent\_heat \pm heat\_advection \pm heat\_diffusion \quad (5)$$

Dissolved mineral nitrogen variation (μmol L^{-1} d^{-1})

$$\frac{dDIN_{ij}}{dt} = PHYRespN_{ij} + PHYExudN_{ij} + PHYMortN_{ij} + PHYSetN_{ij} + DINLoads_{ij} - PHYUptakeN_{ij} \pm Advection \pm Diffusion \quad (6)$$

$$DIN_{ij} = Nitrate_{ij} + Nitrite_{ij} + Ammonium_{ij}$$

Dissolved mineral phosphorus variation (μmol L^{-1} d^{-1})

$$\frac{dP_{ij}}{dt} = PHYRespP_{ij} + PHYExudP_{ij} + PHYMortP_{ij} + PHYSetP_{ij} + PLoads_{ij} - PHYUptakeP_{ij} \pm Advection \pm Diffusion \quad (7)$$

Phytoplankton carbon biomass changes (μg C L^{-1} d^{-1})

$$\frac{dPHYC_{ij}}{dt} = PHYC_{ij}\left(\begin{array}{l} PHYGPP_{ij} - PHYExud_{ij} - \\ PHYResp_{ij} - PHYMort_{ij} - PHYSet_{ij} \end{array}\right) \pm Advection \pm Diffusion \quad (8)$$

This is also expressed as μg Chl L^{-1} h^{-1} ($PHYChl_{ij}$) using a Carbon:Chlorophyll ratio of 50 Jørgensen & Jørgensen (1991)

Phytoplankton nitrogen biomass changes (μg N L^{-1} d^{-1})

$$\frac{dPHYN_{ij}}{dt} = PHYUptakeN_{ij} - PHYRespN_{ij} - PHYExudN_{ij} - PHYMortN_{ij} - PHYSetN_{ij} \pm Advection \pm Diffusion \quad (9)$$

Phytoplankton phosphorus biomass changes (μg P L^{-1} d^{-1})

$$\frac{dPHYP_{ij}}{dt} = PHYUptakeP_{ij} - PHYRespP_{ij} - PHYExudP_{ij} - PHYMortP_{ij} - PHYSetP_{ij} \pm Advection \pm Diffusion \quad (10)$$

$PHYGPP_{ij}$	Gross primary productivity	d^{-1}
$PHYExud_{ij}$	Exudation rate	
$PHYResp_{ij}$	Respiration rate	
$PHYMort_{ij}$	Mortality rate	
$PHYSet_{ij}$	Settling rate	
$PHYMortN_{ij}$	Phytoplankton mortality	mmol N L^{-1} d^{-1} or
$PHYExudN_{ij}$	Phytoplankton exudation	

$PHYRespN_{ij}$	Phytoplankton respiration	mg N L^{-1} d^{-1}
$PHYUptakeN_{ij}$	Phytoplankton uptake	
$PHYSetN_{ij}$	Phytoplankton settling	
$PHYMortP_{ij}$	Phytoplankton mortality	mmol P L^{-1} d^{-1} or mg P L^{-1} d^{-1}
$PHYExudP_{ij}$	Phytoplankton exudation	
$PHYRespP_{ij}$	Phytoplankton respiration	
$PHYUptakeP_{ij}$	Phytoplankton uptake	
$PHYSetP_{ij}$	Phytoplankton settling	

Note – All fluxes are referred to days except current speed, since its usual units are m s^{-1}

Table 4 – Equations for the rate processes. Each rate is multiplied by corresponding carbon, nitrogen or phosphorus stocks to obtain fluxes (see text).

Processes	Equations	Units
Vertically integrated light limited productivity	$$P_{g(I)} = P_{max} \frac{\exp}{k_z} \left(exp\left(-\frac{I_z}{I_{opt}} \right) - exp\left(-\frac{I_0}{I_{opt}} \right) \right) \quad (11)$$ where, *Pmax* – Maximum rate of photosynthesis; I_{opt} – Optimal light intensity for photosynthesis; I_z – Light intensity at depth z;	d^{-1}
Light intensity at box depth	$$I_z = I_0 \exp(-kz) \quad (12)$$	m E m^{-2} s^{-1}
Light extinction coefficient	$$k = k_0 + 0.04 + 0.0088 \cdot PHYCHl_{ij} + 0.054 \cdot PHYCHl_{ij}^{2/3} \quad (13)$$ where, K_0 – Reference light extinction coefficient (m^{-1});	m^{-1}
Light and temperature limited productivity	$$P_{g(I,T)} = P_{g(I)} . Tlimit \quad (14)$$ where, *Tlimit* – Temperature limitation factor	d^{-1}
Light, temperature and nutrient limited productivity	$$PHYGPP_{ij} = P_{g(I,T,Nut)} = P_{g(I,T)} \min\left(\frac{Ncell_{ij}}{k_{Ncell} + Ncell_{ij}}, \frac{Pcell_{ij}}{k_{Pcell} + Pcell_{ij}} \right) \quad (15)$$ where, K_{Ncell} – Half saturation constant for growth limited by nitrogen cell quota; K_{Pcell} – Half saturation constant for growth limited by phosphorus cell quota.	d^{-1}
Nitrogen cell quota	$$Ncell_{ij} = \frac{PHYN_{ij}}{PHYC_{ij}} \quad (16)$$	mg N mg C^{-1}
Phosphorus cell quota	$$Pcell_{ij} = \frac{PHYP_{ij}}{PHYC_{ij}} \quad (17)$$	mg P mg C^{-1}

Nitrogen uptake	$PHYUptakeN_{ij} = V_N \cdot PHYN_{ij}$ (18)	mg N L^{-1} d^{-1}
Phosphorus uptake	$PHYUptakeP_{ij} = V_P \cdot PHYP_{ij}$ (19)	mg P L^{-1} d^{-1}
Nitrogen uptake rate (V_N)	If $Nmin < PHYN_{ij} < Nmax$ and $PHYN_{ij} / PHYP_{ij} < maxN/P_{ij}$ $V\,Ammonium = V\max N \frac{Ammonium_{ij}}{k_{Ammonium} + Ammonium_{ij}}$ (20) $V\,Nitrate + Nitrite = \max\left(0, V\max_N - V\,Ammonium\right) \cdot \frac{\left(Nitrate + Nitrite\right)_{ij}}{k_{Nitrate+Nitrite} + \left(Nitrate + Nitrite\right)_{ij}}$ (21) $V_N = V\,Ammonium + V\,Nitrate + Nitrite$ else V_N = 0, (22)where *Nmin* – minimal nitrogen cell quota (mg N mg C^{-1}) ; *Nmax* - maximal nitrogen cell quota (mg N mg C^{-1}) ; $K_{Ammonium}$ – half saturation constant for ammonium-nitrogen uptake (mmol N L^{-1}); $maxN/P_{ij}$ – Maximal cellular nitrogen:phosphorus ratio; V_{maxN}– Maximal uptake rate (d^{-1}); $K_{Nitrate+Nitrite}$ – half saturation constant for Nitrate + Nitrite - nitrogen uptake (mmol N L^{-1});	d^{-1}
Phosphorus uptake rate (V_P)	If $PHOSmin < PHYP_{ij} < PHOSmax$ and $PHYN_{ij} / PHYP_{ij} > minN/P_{ij}$ $V_P = V\max P \frac{P_{ij}}{k_P + P_{ij}}$ (23) else V_P = 0, where *PHOSmin* – minimal phosphous cell quota (mg P mg C^{-1}) ; *PHOSmax* - maximal phosphous cell quota (mg P mg C^{-1}) ; K_p – half saturation constant for phosphous uptake (□mol P L^{-1}); $minN/P_{ij}$ – Minimal cellular nitrogen:phosphorus ratio; V_{maxP}– Maximal uptake rate (d^{-1}); V_{max} – Maximal uptake rate (d^{-1}) (the same value for nitrogen uptake)	d^{-1}

Phytoplankton exudation rate of Carbon	$PHYExud_{ij} = Exud.PHYGPP_{ij}$, where (24) *Exud* – Fraction exudated;	d^{-1}
Phytoplankton exudation of Nitrogen	$PHYExudN_{ij} = PHYExud_{ij}.PHYC_{ij}.Ncell_{ij}$ (25)	□g N $L^{-1}d^{-1}$
Phytoplankton exudation of Phosphorus	$PHYExudP_{ij} = PHYExud_{ij}.PHYC_{ij}.Pcell_{ij}$ (AII.26)	□g P $L^{-1}d^{-1}$
Phytoplankton respiration rate	$PHYResp_{ij} = \left(R_0 + R_{dark}.Tlimit.DailyMean\overline{GPP_{ij}}\right).\frac{CarbonToOxygen}{ChlorophyllToCarbon}.OxygenMolecularWeight.24$ (27) during the night $PHYResp_{ij} = \left(R_0 + R_{dark}.Tlimit.DLratio.DailyMean\overline{GPP_{ij}}\right)\frac{CarbonToOxygen}{ChlorophyllToCarbon}.OxygenMolecularWeight.24$ (28) during the day, where R_0 – Maintenance respiration (mmol O_2 mg Chl^{-1} h^{-1}); R_{dark}– Linear coefficient of increase in biomass-specific dark respiration with gross photosynthesis (dimensionless); DLratio – Ratio between respiration in the light and respiration in the dark (adimensional); $DailyMean\overline{GPP_{ij}}$ - Daily integrated gross productivity (mmol O_2 mg Chl^{-1} h^{-1}); CarbonToOxygen – Conversion factor between oxygen consumed and carbon produced in respiration (mg C mg O_2^{-1}); ChlorophyllToCarbon – Conversion factor from chlorophyll to carbon (mg C mg Chl^{-1})	d^{-1}
Temperature limitation factor	$Tlimit = \exp\left(\text{TempAugRate}\left(T_{ij} - T_0\right)\right)$ (29) where, TempAugRate – Temperature augmentation rate;	dimensionless

	T_0 – Reference temperature.	
Nitrogen respiration loss	$PHYRespN_{ij} = PHYResp_{ij} \cdot PHYC_{ij} \cdot Ncell_{ij}$ (30)	□g N l-1d-1
Phosphorus respiration loss	$PHYRespP_{ij} = PHYResp_{ij} \cdot PHYC_{ij} \cdot Pcell_{ij}$ (31)	□g P l-1d-1
Nitrogen mortality loss	$PHYMortN_{ij} = PHYMort_{ij} \cdot PHYC_{ij} \cdot Ncell_{ij}$ (32)	□g N l-1d-1
Phosphorus mortality loss	$PHYMortP_{ij} = PHYMort_{ij} \cdot PHYC_{ij} \cdot Pcell_{ij}$ (33)	□g P l-1d-1
Carbon settling loss rate	$PHYSet_{ij} = \frac{SettlingSpeed}{Depth_{ij}}$, (34) where, *SettlingSpeed* – Fall velocity of phytoplankton cells (m d-1); $Depth_{ij}$ – Depth of layer j in column i (m)	d-1
Nitrogen settling loss	$PHYSetN_{ij} = SettlingSpeed \cdot \frac{PHYN_{ij}}{Depth_{ij}}$ (35)	□g N l-1d-1
Phosphorus settling loss	$PHYSetP_{ij} = SettlingSpeed \cdot \frac{PHYP_{ij}}{Depth_{ij}}$ (36)	□g P l-1d-1

Table 5 – Model parameters and respective values. Most values were calibrated from ranges reported by quoted authors.

Object	Parameter	Value	Reference
Hydrodynamic 2D object	Manning coefficient	0.025 s $m^{-1/3}$	Grant and Bacher (2001)
	Eddy diffusivity	100 m^2 s^{-1}	Neves (1985)
Phytoplankton object	*Nmin*	0.1 mg N mg C^{-1}	Jørgensen & Jørgensen (1991)
	Nmax	0.53 mg N mg C^{-1}	Jørgensen & Jørgensen (1991)
	$K_{Ammonium}$	2.94 □mol N l^{-1}	Jørgensen & Jørgensen (1991)
	$maxN/P_{ij}$	291	Jørgensen & Jørgensen (1991)
	V_{maxP} *and* V_{maxN}	1.08 d^{-1}	Cochlan & Harrison (1991)
	$K_{Nitrate+Nitrite}$	30 □mol N l^{-1}	Jørgensen & Jørgensen (1991)
	PHOSmin	0.002 mg P mg C^{-1}	Jørgensen & Jørgensen (1991)
	PHOSmax	0.08 mg P mg C^{-1}	Jørgensen & Jørgensen (1991)
	$minN/P_{ij}$	4	Jørgensen & Jørgensen (1991)
	K_p	2 □mol P l^{-1}	Jørgensen & Jørgensen (1991)
	P_{max}	1.2 d^{-1}	Jørgensen & Jørgensen (1991)
	I_{opt}	300 □E m^{-2} s^{-1}	Jørgensen & Jørgensen (1991)
	K_0	0.6 – 2.0 m^{-1}	Measured
	K_{Ncell}	0.028 mg N mg C^{-1}	Calibrated
	K_{Pcell}	0.004 mg P mg C^{-1}	Calibrated
	Exud	0.1	Jørgensen & Jørgensen (1991)
	R_0	0.02 mmol O_2 mg Chl^{-1} h^{-1}	Langdon (1993)
	R_{dark}	0.11	Langdon (1993)
	DLratio	2	Langdon (1993)
	CarbonToOxygen	0.3125 mg C mg O_2^{-1}	Vollenweider (1974)
	ChlorophyllToCarbon	50 mg C mg	Jørgensen &

		Chl^{-1}	Jørgensen (1991)
	TempAugRate	$0.069\ ^{o}C^{-1}$	Estimated
	T_0	0ºC for photosynthesis and 25ºC for respiration	Calibrated
	SettlingSpeed	$1\ m\ d^{-1}$	Mann & Lazier (1996)
	$PHYMort_{ij}$	$0.1\ day^{-1}$	Jørgensen & Jørgensen (1991)

Table 6 – Sensitivity analysis of model parameters. Average results obtained with the model after simulating a period of a few days, compared with results obtained with similar simulations, except for the parameter values. Each simulation differed from the others in the value of one parameter that was increased or decreased by 10 %. Parameter names and default values as in Table 5. NPP stands for Net Primary Production and B/P stands for the chlorophyll / production ratio (see text).

Standard Simulation			Chlorophyll (mg L^{-1})	% var.	NPP (h^{-1})	% var.	B/P(days)	% var.	Temp. (°C)	% var.
			11.9704		0.0028		14.7485		23.2675	
Nmin	+10%	0.11	11.8662	-0.87	0.0029	1.46	14.5362	-1.44	23.2673	0.00
	-10%	0.09	12.0640	0.78	0.0029	4.02	14.1778	-3.87	23.2676	0.00
Nmax	+10%	0.583	11.9706	0.00	0.0028	0.12	14.7313	-0.12	23.2675	0.00
	-10%	0.477	11.9698	-0.01	0.0028	0.29	14.7053	-0.29	23.2675	0.00
KAmmonium	+10%	3.234	11.9656	-0.04	0.0028	-0.18	14.7746	0.18	23.2674	0.00
	-10%	2.646	11.9756	0.04	0.0029	1.77	14.4925	-1.74	23.2675	0.00
maxN/Pij	+10%	320.1	11.9704	0.00	0.0028	0.00	14.7485	0.00	23.2675	0.00
	-10%	261.9	11.9704	0.00	0.0028	0.00	14.7485	0.00	23.2675	0.00
VmaxP	+10%	0.0495	12.0584	0.73	0.0029	3.48	14.2521	-3.37	23.2675	0.00
	-10%	0.0405	11.8729	-0.81	0.0027	-2.86	15.1822	2.94	23.2673	0.00
VmaxN	+10%	0.0495	12.0584	0.73	0.0029	3.48	14.2521	-3.37	23.2675	0.00
	-10%	0.0405	11.8729	-0.81	0.0027	-2.86	15.1822	2.94	23.2673	0.00
KNitrate+Nitrite	+10%	33	11.9596	-0.09	0.0028	0.49	14.6768	-0.49	23.2674	0.00
	-10%	27	11.9818	0.09	0.0029	1.10	14.5875	-1.09	23.2675	0.00
PHOSmin	+10%	0.0022	11.9704	0.00	0.0028	0.00	14.7485	0.00	23.2675	0.00
	-10%	0.0018	11.9704	0.00	0.0028	0.00	14.7485	0.00	23.2675	0.00
PHOSmax	+10%	0.088	11.9704	0.00	0.0028	0.00	14.7485	0.00	23.2675	0.00
	-10%	0.072	11.9704	0.00	0.0028	0.00	14.7485	0.00	23.2675	0.00
minN/Pij	+10%	4.4	11.9704	0.00	0.0028	0.00	14.7485	0.00	23.2675	0.00
	-10%	3.6	11.9704	0.00	0.0028	0.00	14.7485	0.00	23.2675	0.00

Kp	+10%	2.2	11.9605	-0.08	0.0029	0.99	14.6042	-0.98	23.2674	0.00
	-10%	1.8	11.9812	0.09	0.0029	2.51	14.3878	-2.45	23.2675	0.00
Pmax	+10%	0.055	12.1209	1.26	0.0029	3.10	14.3052	-3.01	23.2674	0.00
	-10%	0.045	11.7855	-1.55	0.0027	-4.77	15.4872	**5.01**	23.2674	0.00
Iopt	+10%	330	11.9044	-0.55	0.0028	-2.39	15.1102	2.45	23.2674	0.00
	-10%	270	12.0362	0.55	0.0029	4.03	14.1775	-3.87	23.2674	0.00
K0	+10%	0.66	11.9094	-0.51	0.0028	-0.86	14.8765	0.87	23.2671	0.00
	-10%	0.54	11.9701	0.00	0.0028	0.25	14.7114	-0.25	23.2676	0.00
KNcell	+10%	0.0308	11.9700	0.00	0.0028	0.32	14.7015	-0.32	23.2675	0.00
	-10%	0.0252	11.9704	0.00	0.0028	0.00	14.7485	0.00	23.2675	0.00
KPcell	+10%	0.0044	11.9365	-0.28	0.0029	0.89	14.6188	-0.88	23.2674	0.00
	-10%	0.0036	12.0054	0.29	0.0029	2.98	14.3210	-2.90	23.2675	0.00
Exud	+10%	0.11	11.9232	-0.39	0.0028	-0.92	14.8854	0.93	23.2674	0.00
	-10%	0.09	12.0184	0.40	0.0029	2.86	14.3390	-2.78	23.2675	0.00
R0	+10%	0.022	11.8858	-0.71	0.0027	**-5.20**	15.5571	**5.48**	23.2674	0.00
	-10%	0.018	12.0567	0.72	0.0030	**7.84**	13.6763	**-7.27**	23.2675	0.00
Rdark	+10%	0.121	11.8738	-0.81	0.0027	-3.32	15.2541	3.43	23.2674	0.00
	-10%	0.099	12.0676	0.81	0.0031	**8.05**	13.6500	**-7.45**	23.2675	0.00
DLratio	+10%	2.2	11.8964	-0.62	0.0028	-1.67	14.9985	1.70	23.2674	0.00
	-10%	1.8	12.0451	0.62	0.0029	4.01	14.1802	-3.85	23.2675	0.00
TempAugRate	+10%	0.0759	12.2357	2.22	0.0031	**8.77**	13.5595	**-8.06**	23.2674	0.00
	-10%	0.0621	11.6737	-2.48	0.0026	**-7.56**	15.9543	**8.18**	23.2673	0.00
SettlingSpeed	+10%	1.1	11.9180	-0.44	0.0029	1.81	14.4858	-1.78	23.2674	0.00
	-10%	0.9	12.0244	0.45	0.0029	0.97	14.6069	-0.96	23.2675	0.00
PHYMortij	+10%	0.11	11.8823	-0.74	0.0029	4.00	14.1814	-3.84	23.2674	0.00
	-10%	0.09	12.0603	0.75	0.0028	0.20	14.7184	-0.20	23.2675	0.00
Horizontal diffusion	50 $m^2 s^{-1}$		11.6094	-3.02	0.0024	**-13.92**	17.1338	**16.17**	23.3124	0.19

Table 7 – Comparison between annual averages results for simulations 1, 2, 3 and 4 (cf. – Methodology – *Model simulations*).

Simulations	1	2	3	4
Ammonia	□M			
Average	6.66	6.66	6.20	7.82
Max	18.05	18.05	13.99	19.03
Min	1.76	1.76	2.05	3.55
Nitrate	□M			
Average	85.21	85.21	85.18	86.21
Max	121.89	121.89	121.96	121.95
Min	38.82	38.82	46.74	48.07
Nitrite	□M			
Average	2.03	2.03	2.06	1.93
Max	3.58	3.58	3.05	3.06
Min	1.27	1.27	1.28	1.26
Phosphate	□M			
Average	1.31	1.31	1.31	1.33
Max	2.59	2.59	2.52	2.69
Min	0.85	0.85	0.85	0.85
Phytoplankton biomass	mg L^{-1}			
Average	8.43	8.43	8.36	8.17
Max	17.08	17.08	12.38	11.22
Min	4.08	4.08	4.08	3.76
Water temperature	ºC			
Average	16.59	16.59	16.61	16.55
Max	24.85	24.85	24.86	24.71
Min	8.19	8.19	8.19	8.02
Phytop. GPP	mg C m^{-3} d^{-1}			
Average	90.58	90.58	87.90	79.46
Max	327.08	327.08	273.01	226.60
Min	4.50	4.50	4.48	4.28
Phytop. NPP	mg C m^{-3} d^{-1}			
Average	23.53	23.53	21.44	24.18
Max	145.67	145.67	117.34	124.61
Min	-20.02	-20.02	-20.02	-19.94

Figures

Fig. 1 – Crestuma-Lever reservoir with the location of the two sampling stations. Station A located at 500 m from the dam and station B at 2.5 km nearby a Power Plant.

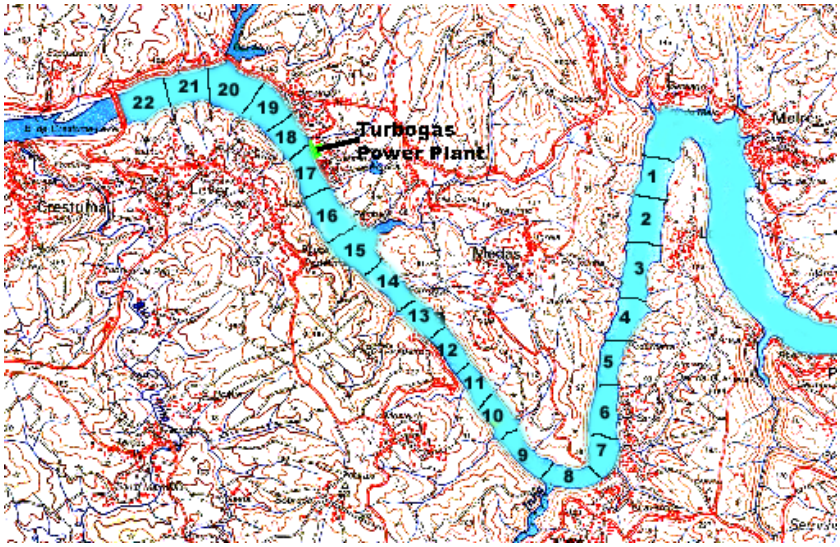

Fig. 2 - The 22 model compartments, each with a length of 500 m (see text).

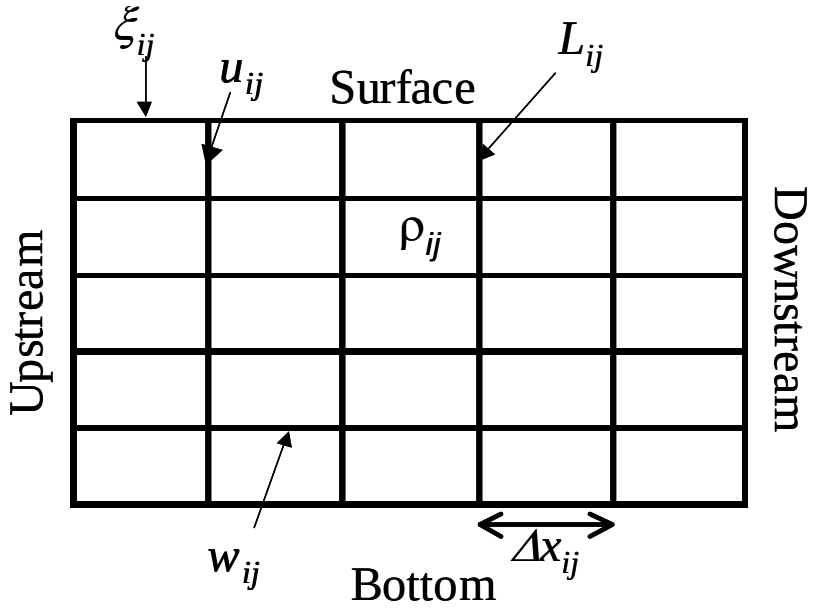

Fig. 3 – Model grid. Horizontal (*u*) and vertical (*w*) velocities are calculated on the vertical and on the horizontal sides of the grid cells, respectively. Water elevation (□) is calculated at the surface of the top layer and water density (□) at the centre of each cell. *i* represents the layers and *j* the columns.

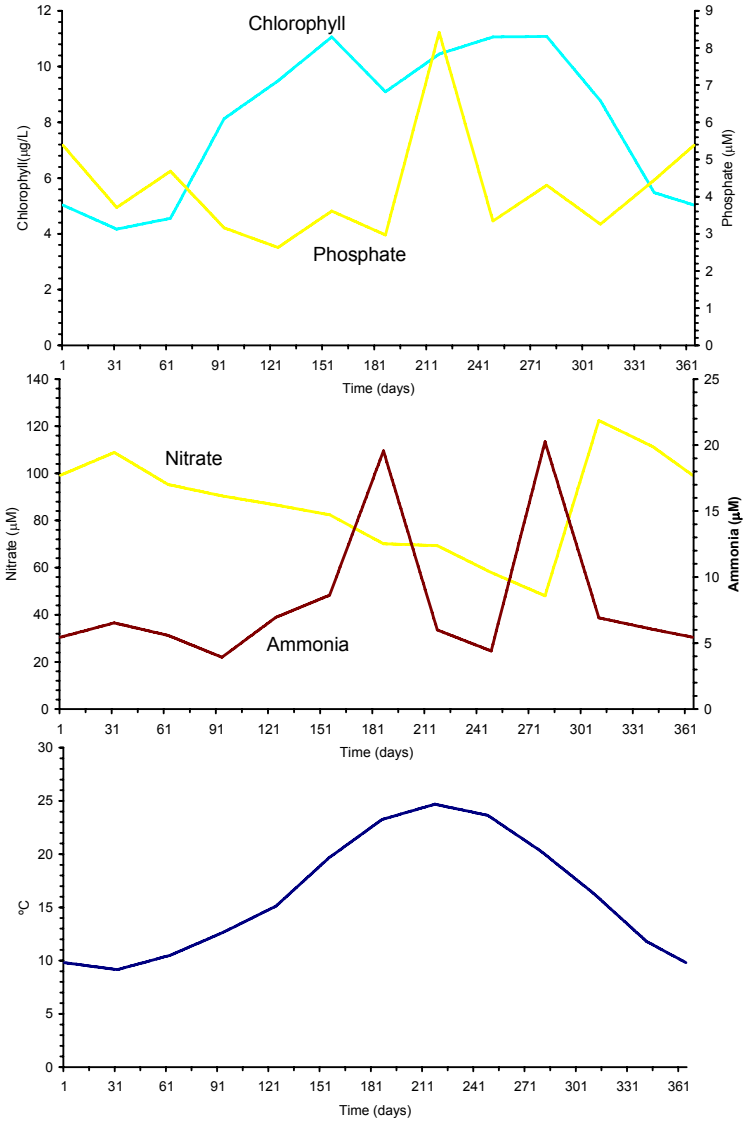

Fig. 4 – Nutrient and chlorophyll concentrations and water temperature used to force the model (see text).

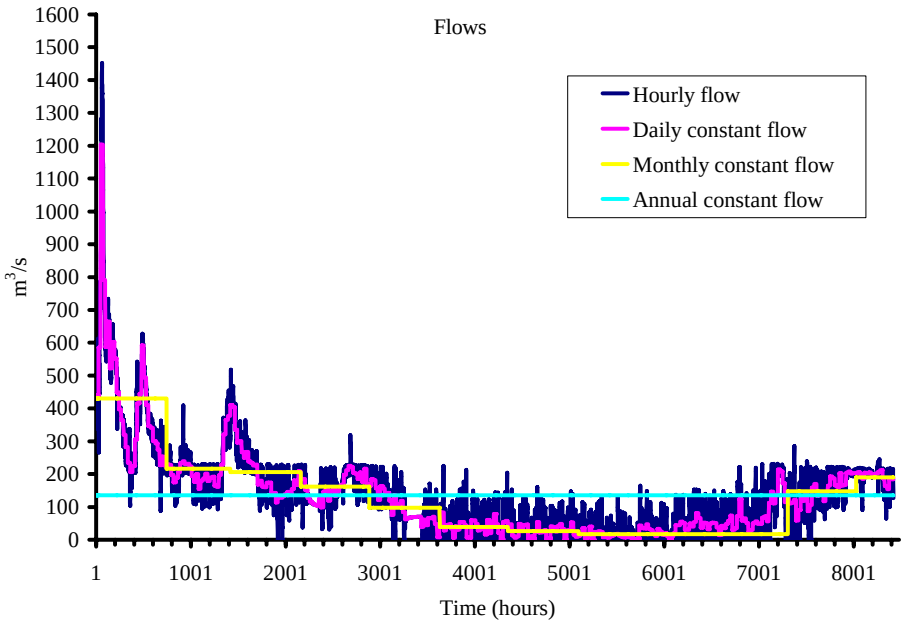

Fig. 5 – Flows used to force simulations 1, 2, 3 and 4 (see text).

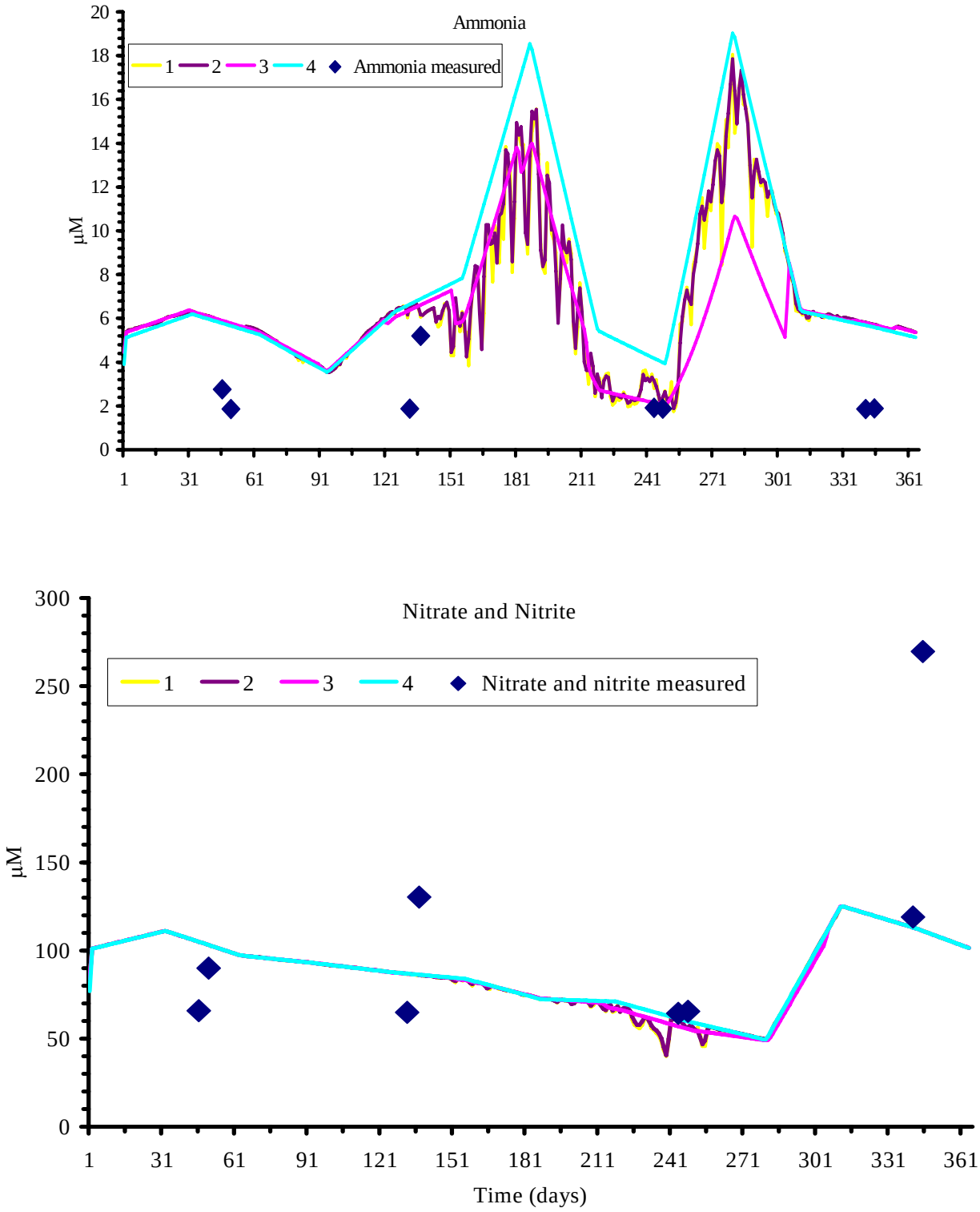

Fig. 6 – Predicted and measured ammonia and nitrate + nitrite at station A shown in Fig. 1 (see text).

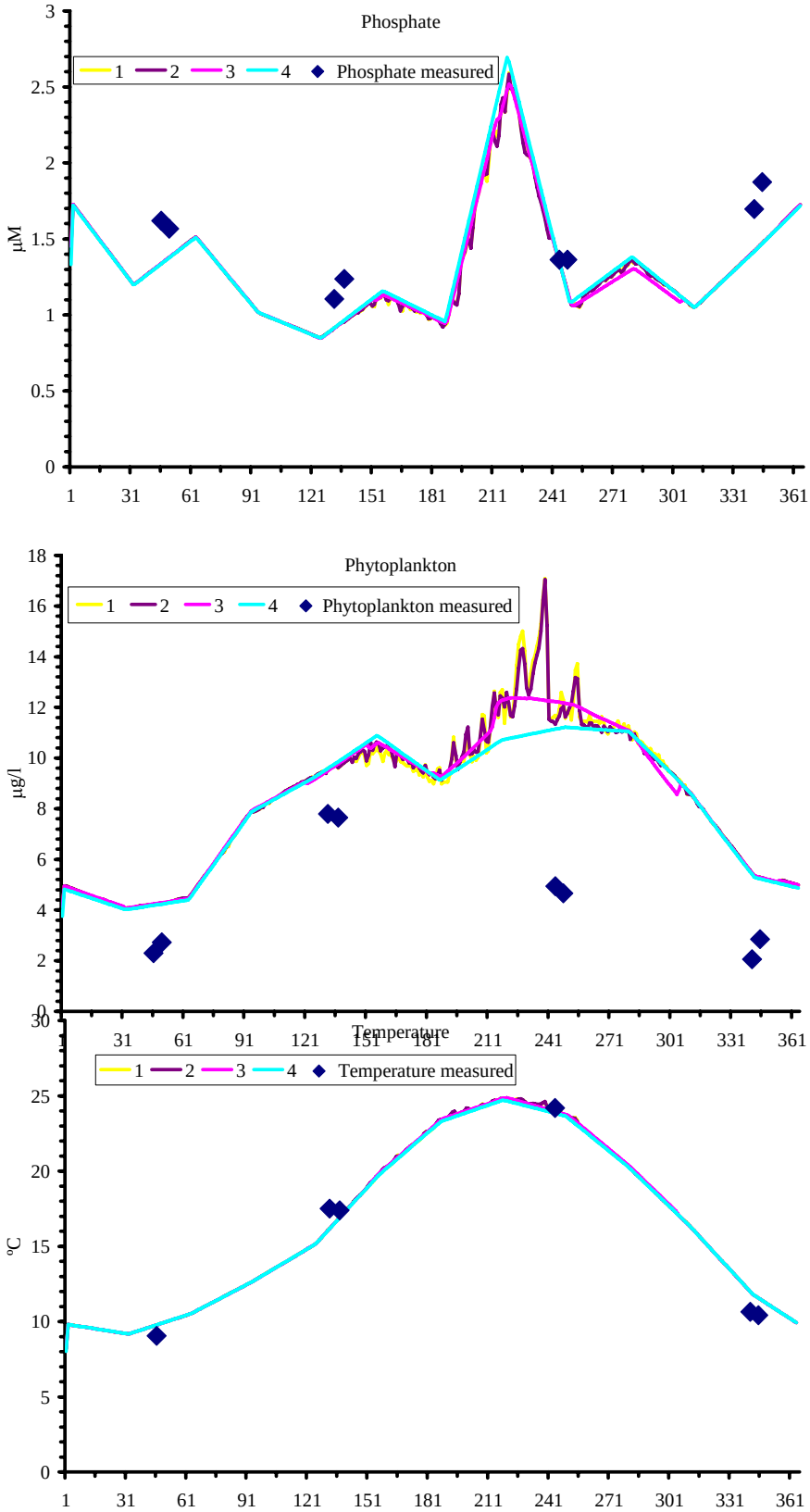

Fig. 7 – Predicted and measured phosphate, chlorophyll and water temperature at station A shown in Fig. 1 (see text).

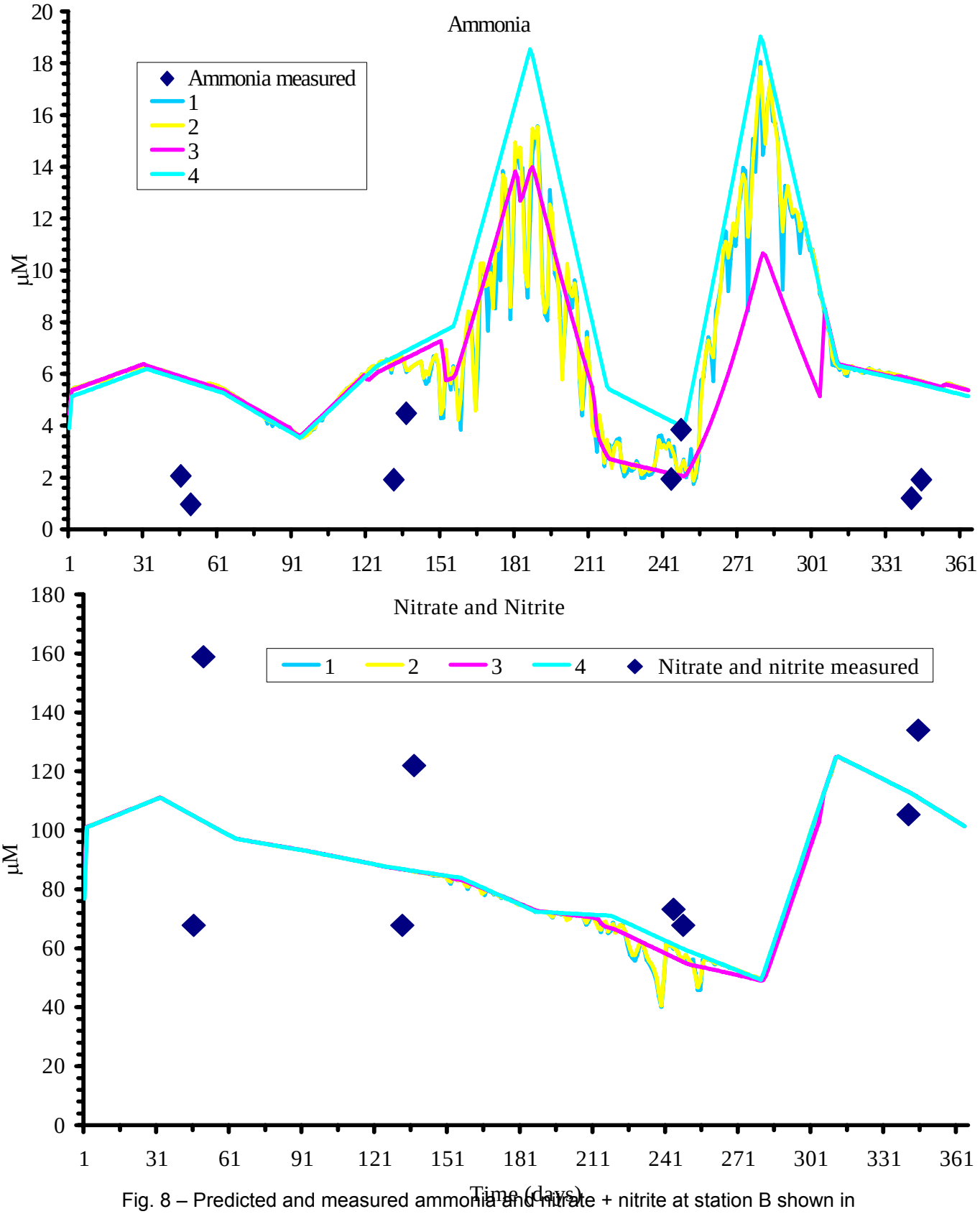

Fig. 8 – Predicted and measured ammonia and nitrate + nitrite at station B shown in Fig. 1 (see text).

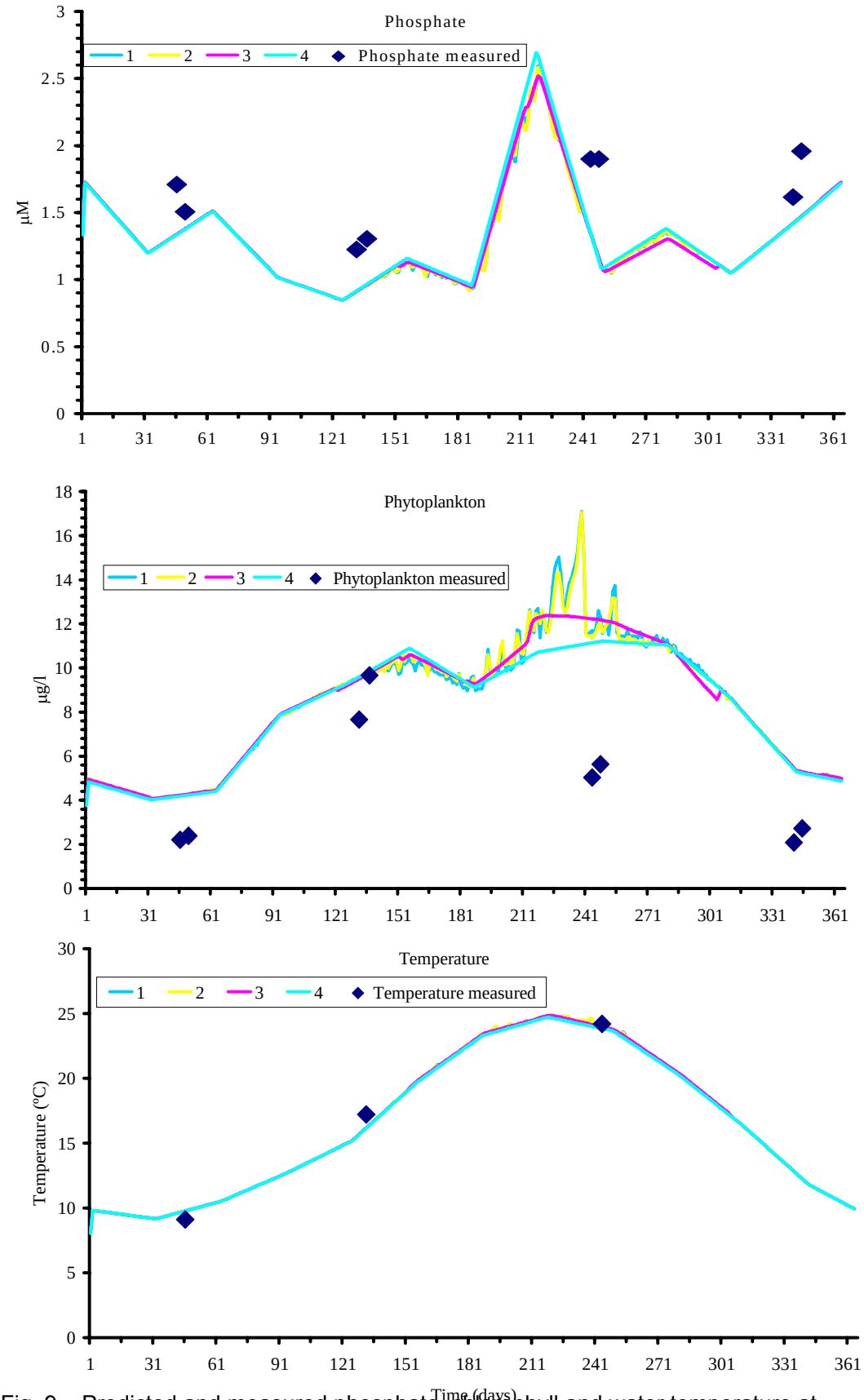

Fig. 9 – Predicted and measured phosphate, chlorophyll and water temperature at station B shown in Fig. 1 (see text).

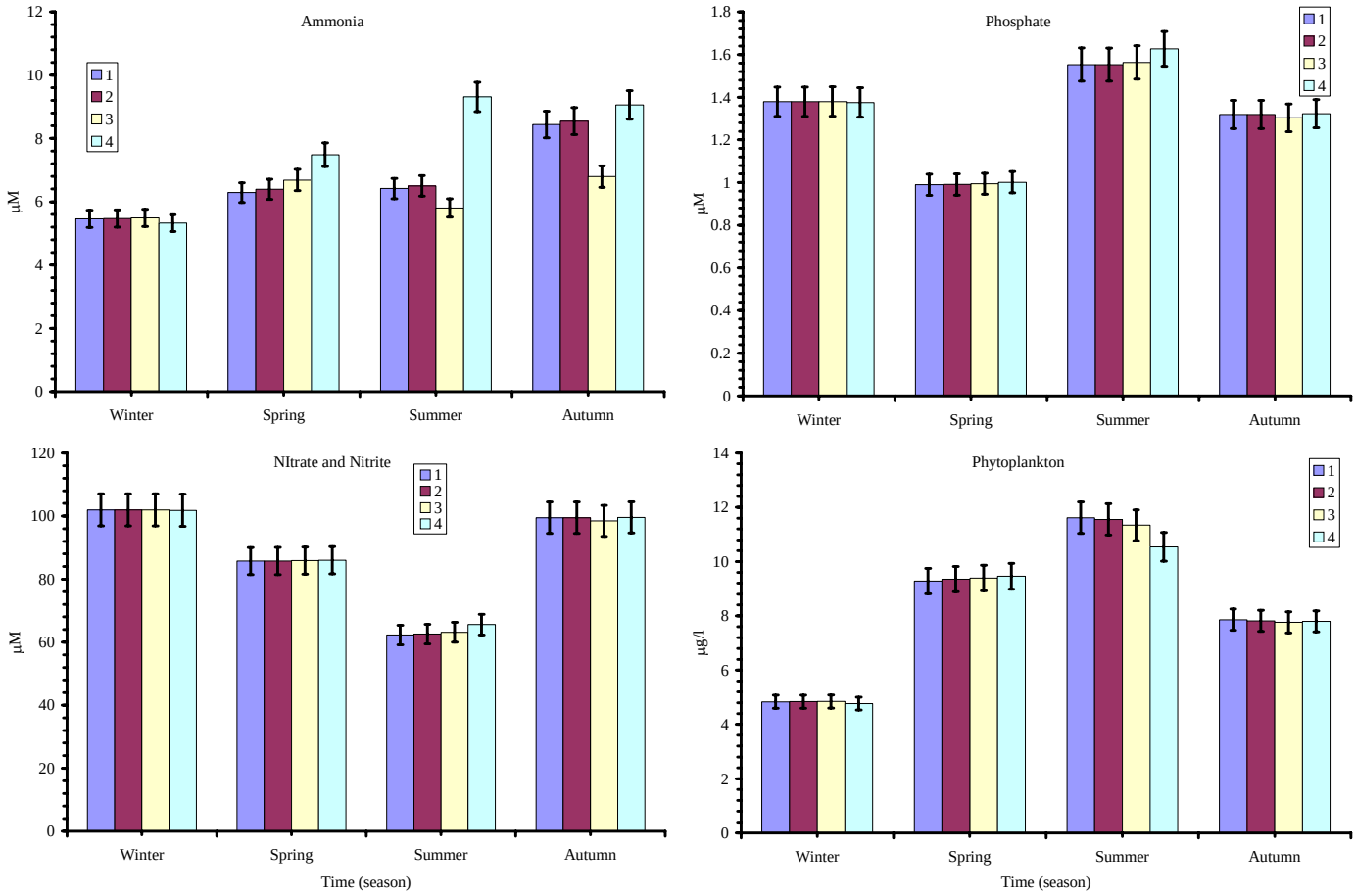

Figure 10 – Seasonal average ammonium, nitrate+nitrite, phosphate and chlorophyll for the simulations. Also shown and 5% error bars (see text).

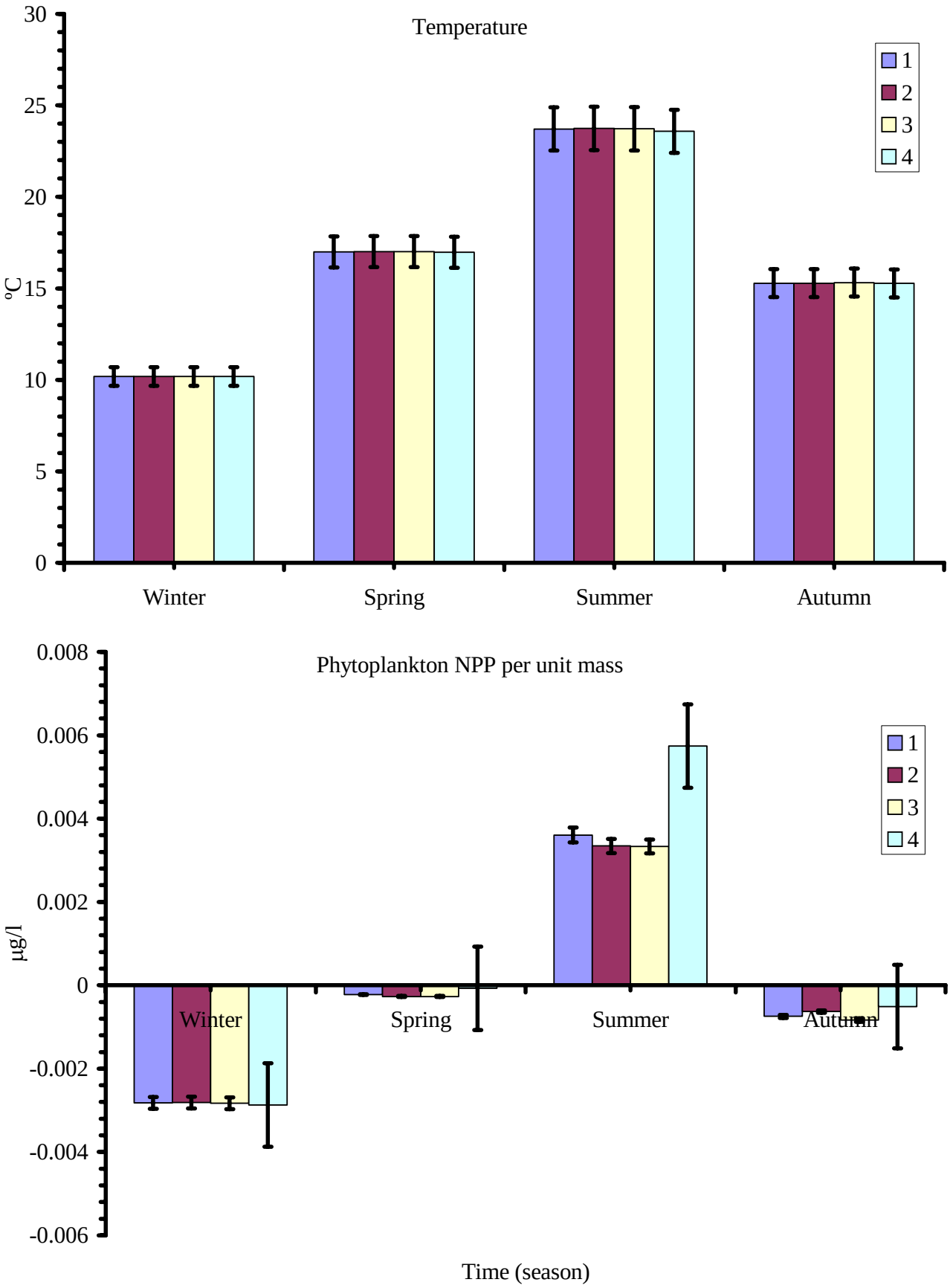

Figure 11 – Seasonal average water temperature and NPP for the simulations. Also shown and 5% error bars (see text).

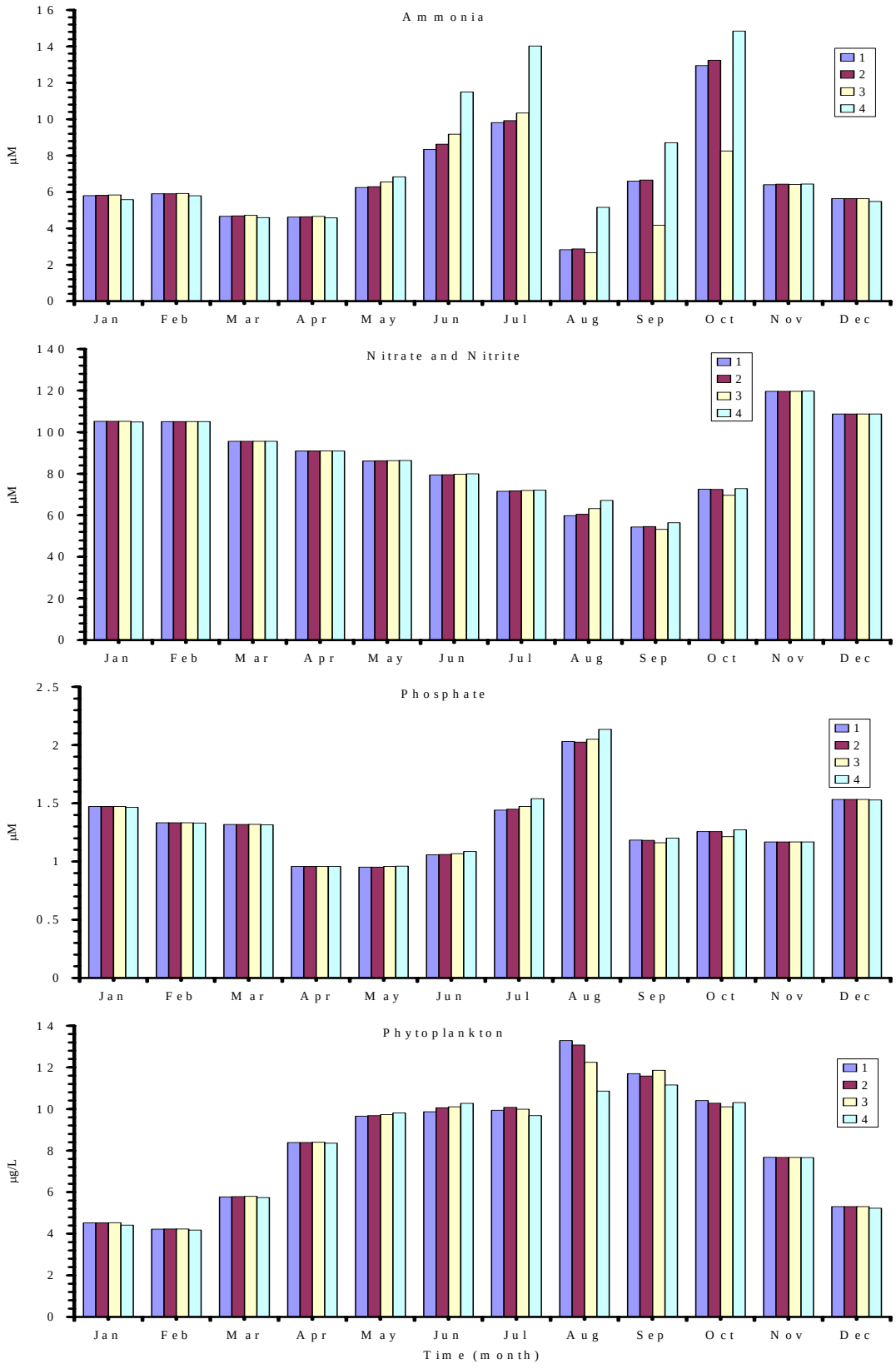

Figure 12 – Monthly average ammonium, nitrate+nitrite, phosphate and chlorophyll for the simulations (see text).

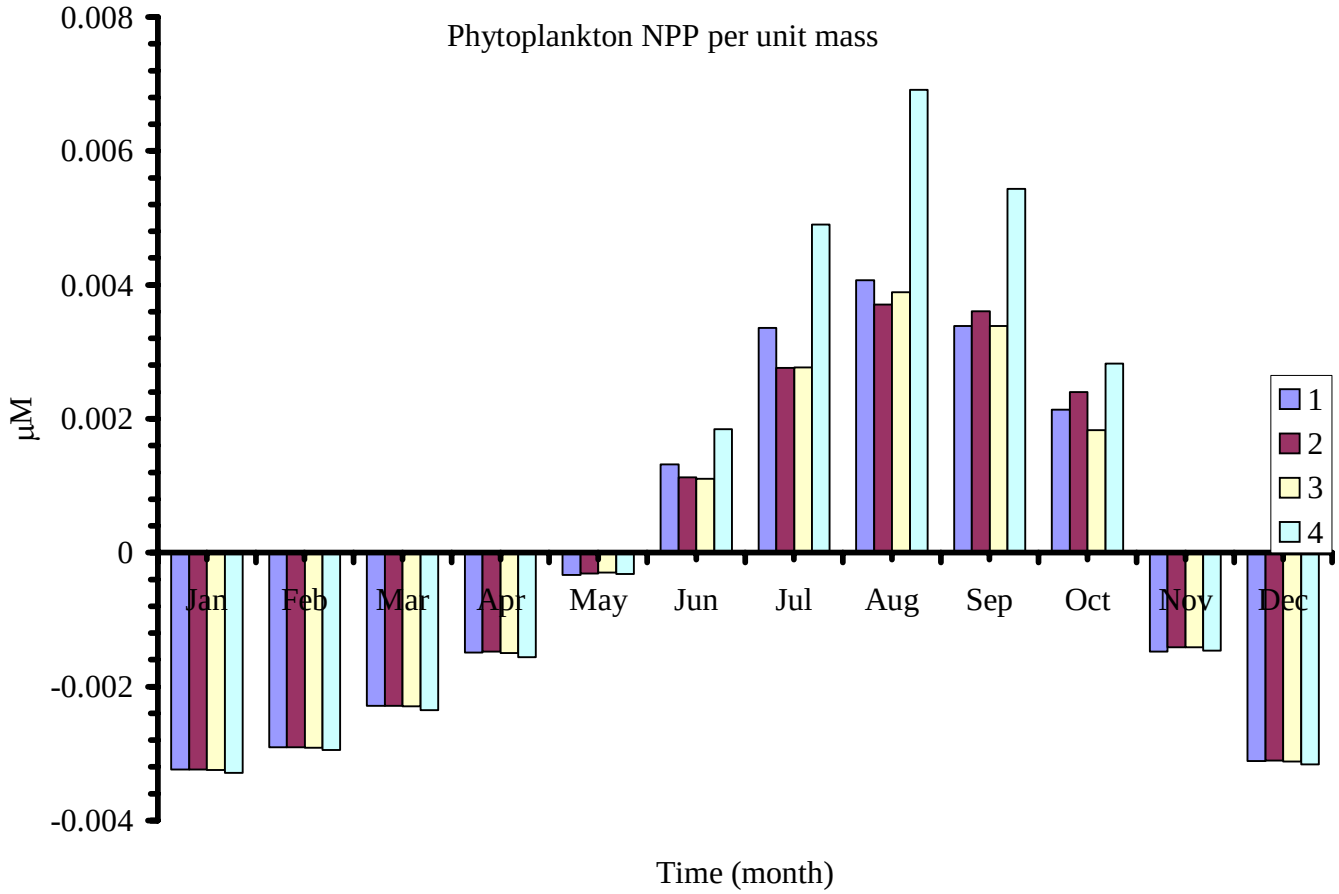

Figure 13 – Monthly average NPP for the simulations (see text).

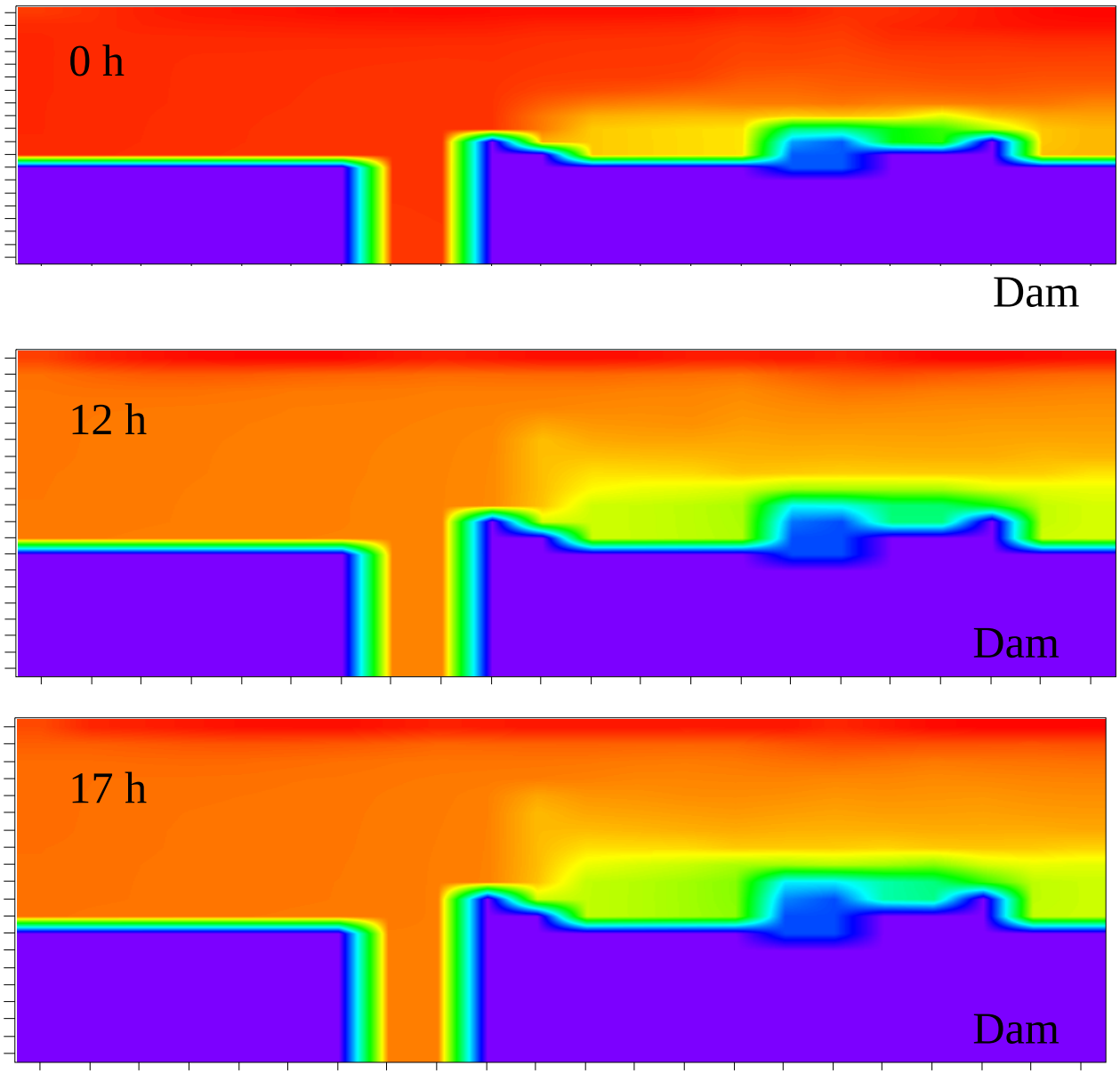

Fig. 14 – Horizontal and vertical temperature variation in simulation 1 at the third of July at 0 hours, 12 hours and 17 hours, over all model domain. Blue color represents bottom. Dam is located on the right limit of model domain. Vertical scale magnified to improve figure readability (see text).

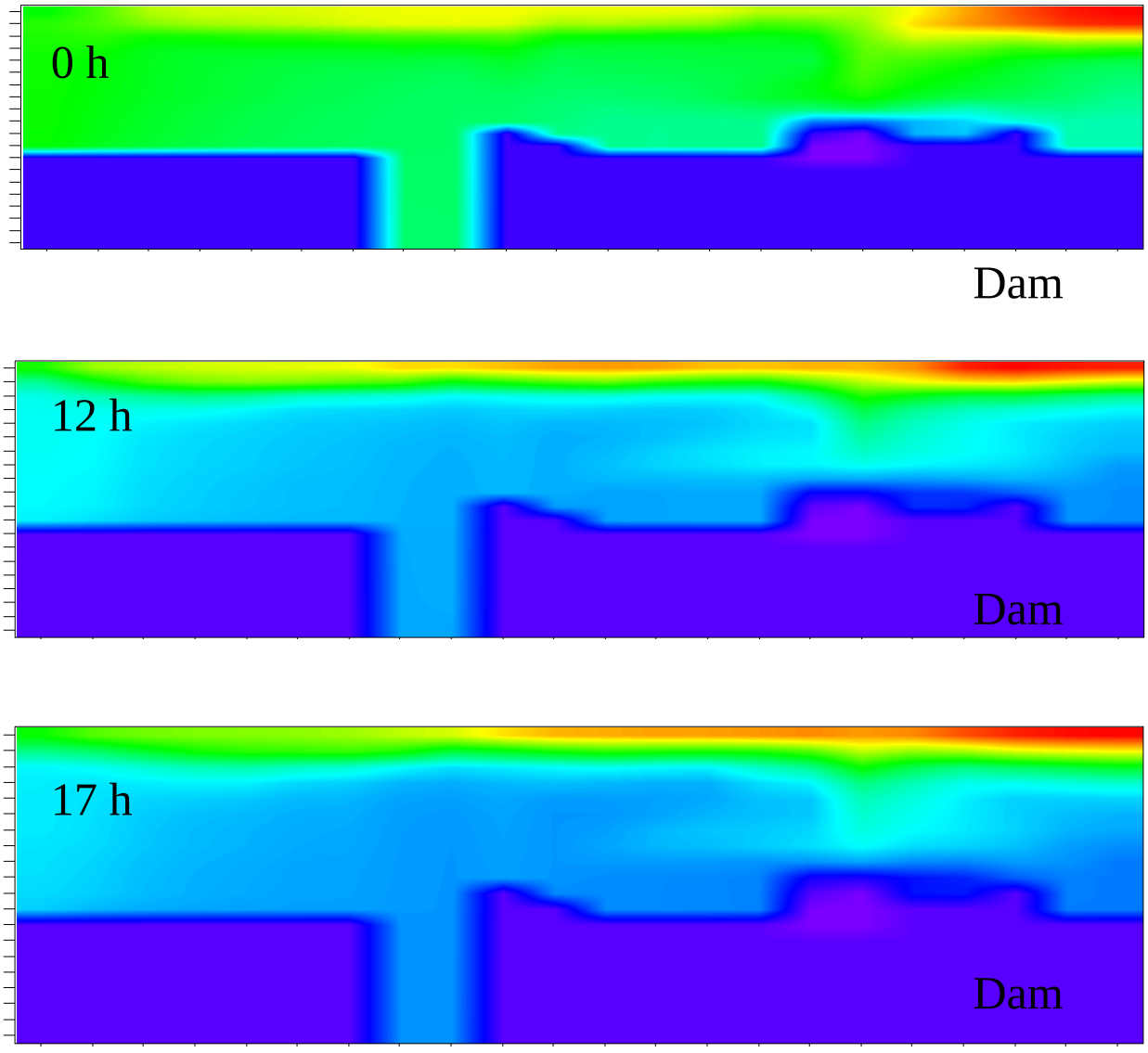

Fig. 15 – Horizontal and vertical chlorophyll variation in simulation 1 at the third of July at 0 hours, 12 hours and 17 hours, over all model domain. Blue color represents bottom. Dam is located on the right limit of model domain. Vertical scale magnified to improve figure readability (see text).

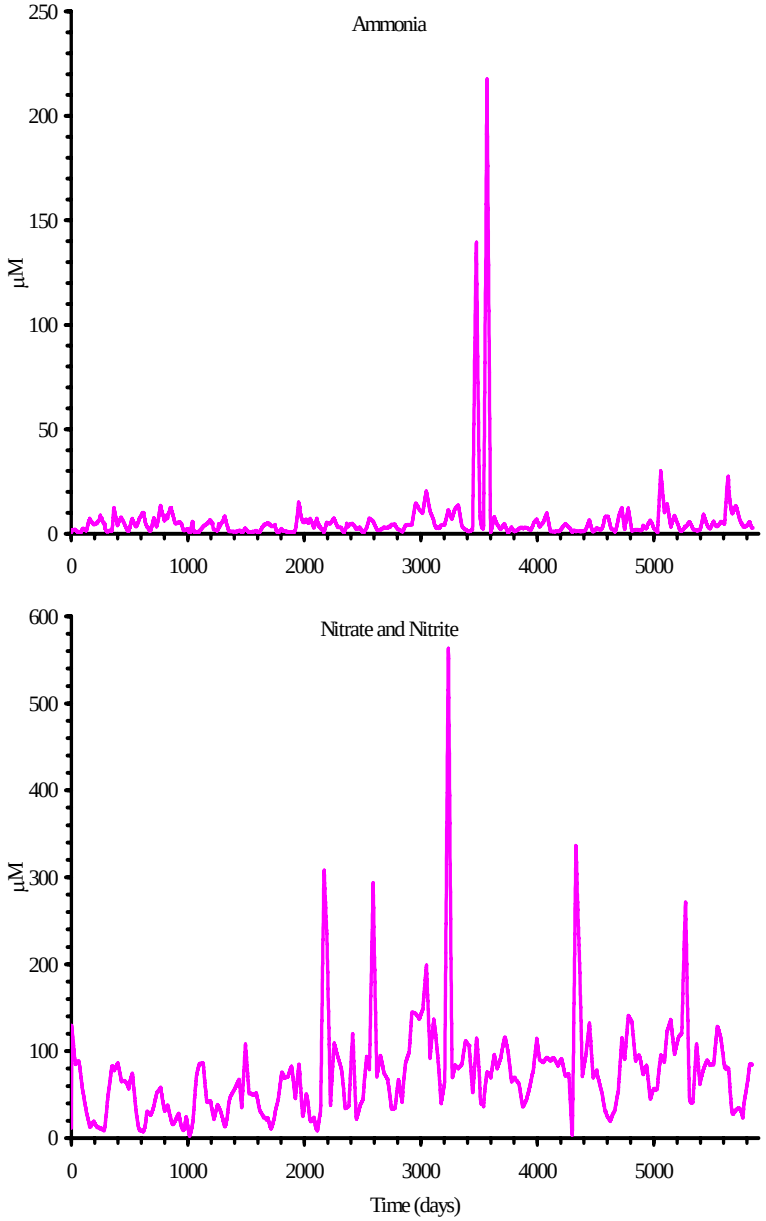

Fig. 16 – Sixteen years predictions to ammonia and nitrate + nitrite at station A shown in Fig. 1.

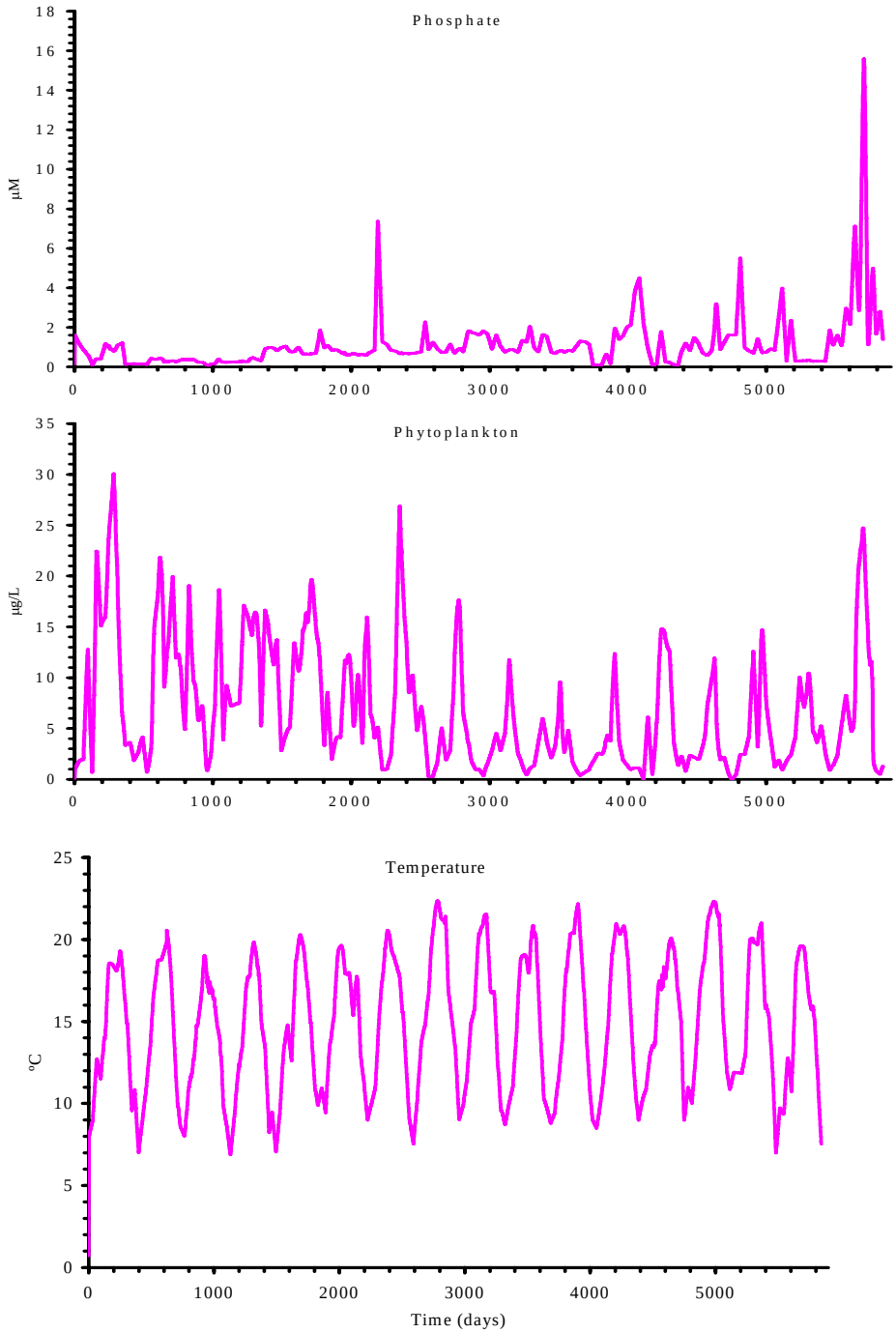

Fig. 17 – Sixteen years predictions to phosphate, chlorophyll and water temperature at station A shown in Fig. 1 (see text).

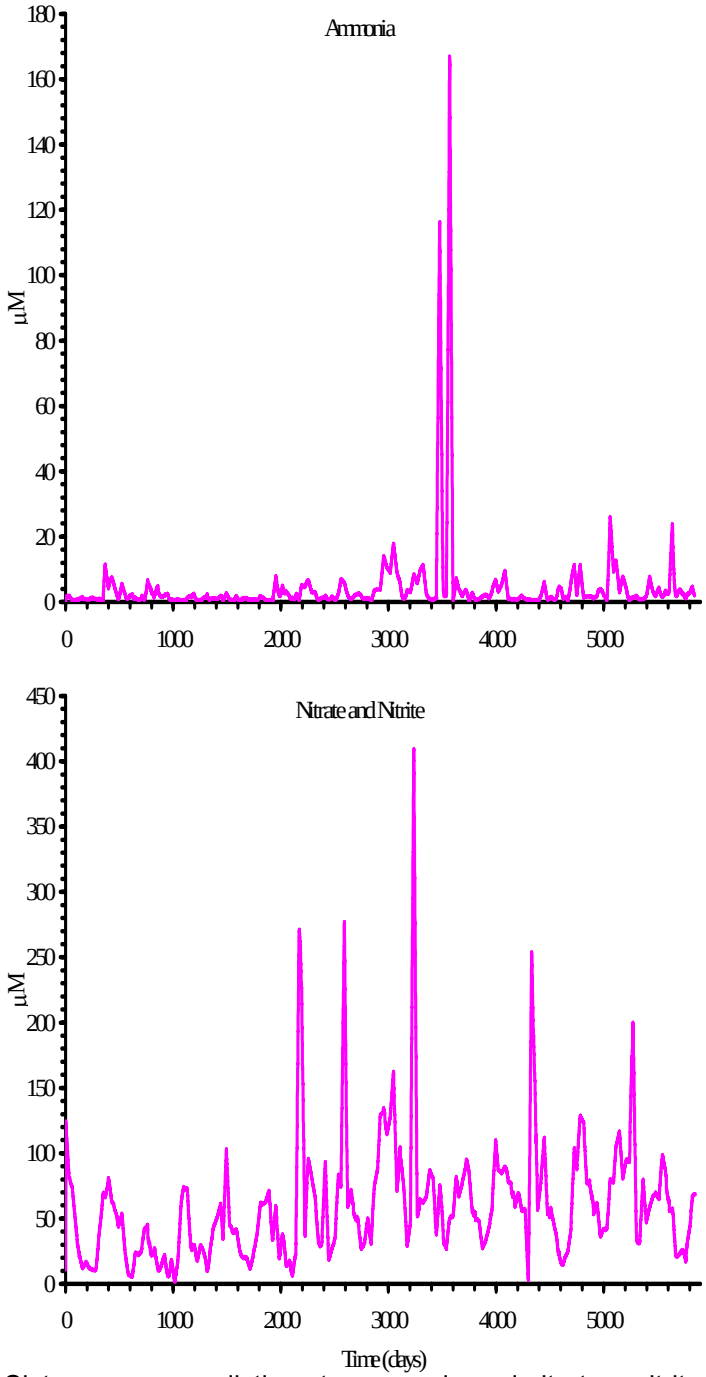

Fig. 18 – Sixteen years predictions to ammonia and nitrate + nitrite at station B shown in Fig. 1.

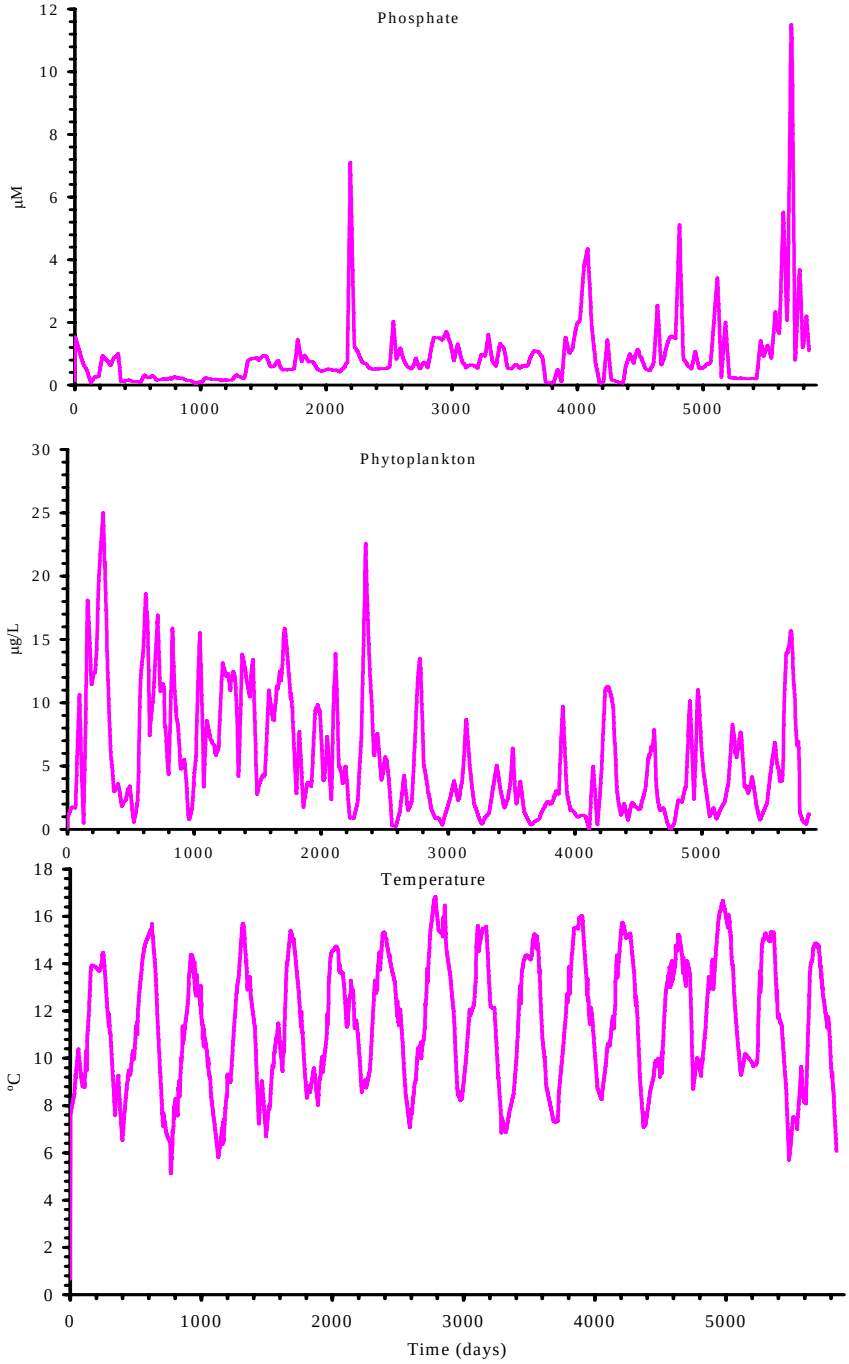

Fig. 19 – Sixteen years predictions to phosphate, chlorophyll and water temperature at station B shown in Fig. 1 (see text).

Indicadores de realização fisica

	Unidade: em número
A- Publicações	
Livros	
Artigos em revistas internacionais*	1
Artigos em revistas nacionais	1
B- Comunicações	
Em congressos científicos internacionais	
Em congressos científicos nacionais	
C- Relatórios	3
D- Organização de seminários e conferências	
E- Formação Avançada	
Teses de Doutoramento	
Teses de Mestrado	
Outra	2
F- Modelos	2
G- Aplicações computacionais	
H- Instalações Piloto	
I- Protótipos laboratoriais	
J- Patentes	
L- Outros (discriminar)	

* Additionally, two papers to be submitted soon, two others under preparation

Publicações

(listar as publicações com origem no projecto)

BORDALO A. A, TEIXEIRA, R. & WIEBE, W.J. 2006. A water quality index applied to an international shared river basin: the case of the River Douro*. Environmental Management* 38 910–920

AZEVEDO, B., DUARTE, P. & BORDALO, A.A. 2005. Análise e verificação de um modelo ecológico para a albufeira de Crestuma-Lever. *Revista da Faculdade de Ciência e Tecnologia da Universidade Fernando Pessoa*, 2: 8-25

* Additionally, two papers to be submitted soon, two others under preparation